# Development of Optical Metabolic Imaging for Pancreatic and Breast Cancer Precision Medicine

By

Joseph Thomas Sharick

Dissertation

Submitted to the Faculty of the

Graduate School of Vanderbilt University

in partial fulfillment of the requirements

for the degree of

DOCTOR OF PHILOSOPHY

in

Biomedical Engineering

March 31st, 2019

Nashville, Tennessee

Approved:

Melissa C. Skala, Ph.D.

Todd D. Giorgio, Ph.D.

Rebecca S. Cook, Ph.D.

Ethan S. Lippmann, Ph.D.

David E. Cliffel, Ph.D.

To my family and friends that have battled cancer

## ACKNOWLEDGMENTS

First, thank you to my advisor, Dr. Melissa Skala, for being generous with her time, guidance, and support. Her expertise in biophotonics and her mentorship made all of my work possible. She fostered a lab environment that always kept me motivated and excited about my work. Thank you as well to my committee members Dr. Rebecca Cook, Dr. Todd Giorgio, Dr. David Cliffel, and Dr. Ethan Lippmann, for sharing their valuable ideas and feedback from their unique perspectives.

Thank you to my many collaborators, which are too many to name, for their extensive efforts and contributions to all of my projects. I could not have done any of this research on my own. I would especially like to thank Dr. Alex Walsh, Dr. Amy Shah, Dr. Rebecca Cook, and Cheri Pasch for taking the time in the lab to teach me the many biology and microscopy skills that I needed to succeed.

I would like to thank all the members of Dr. Skala's lab, both past and present, for their assistance, feedback, and support. I am especially grateful for those that made the move from Nashville to Madison with me; they truly made the transition a smooth one. Thank you as well to everyone I crossed paths with in the Vanderbilt University and University of Wisconsin communities for making them such enjoyable places to learn and work.

I would like to thank the many funding sources that made this work possible, especially the NSF, for supporting me with a fellowship. I would also like to thank all of the patients that participated in my studies. I applaud their bravery and selflessness; it was motivating every day.

Finally, thank you to my partner, family, and friends that all supported me outside of the lab. They were infinitely understanding and encouraging, and I could not have done it on my own.

TABLE OF CONTENTS

Page

LIST OF TABLES

Table Page

LIST OF FIGURES

Figure Page

# CHAPTER 1

# Introduction

## 1.1 Motivation

Breast cancer is the most common cancer in women, with over 250,000 estimated new cases in the US in 2018 (1). Pancreatic cancer has one of the lowest 5-year survival rates of all cancer types (8%) (2), and is projected to be the second leading cause of cancer death by 2030 (3). An estimated 2.5 million new cases of breast and pancreatic cancer were diagnosed in 2018 worldwide (4). Standard of care for both cancer types often involves surgical tumor resection, with the option for chemotherapy and radiation either before surgery, to make a tumor more easily resectable, or after surgery, to prevent future recurrence and increase long-term survival. Unfortunately, each individual patient's tumor is unique, and there are no reliable methods to determine how they will respond to a particular treatment option. Current precision medicine approaches use the molecular profile of an individual tumor to guide treatment choices, but this often fails (5). Treatment response is identified by tracking tumor size or by monitoring tumor recurrence after surgery, which can take months to determine. At that point, alternative drugs can be given, but the tumor may have progressed on the ineffective treatment, and the patient likely experienced significant side effects. One major cause for this cancer treatment failure is intratumor heterogeneity, as drug-resistant cell subpopulations continue to proliferate even when a majority of the tumor appears to be drug-responsive (6, 7).

Patient-derived tumor organoids offer the ability to screen drugs directly on a patient's cells *in vitro* to determine drug effectiveness and guide therapeutic decisions in pancreatic (8, 9) and breast cancer (10, 11). Many organoids can be cultured from a single patient biopsy, enabling high-throughput studies of many treatment options. Unlike patient-derived xenograft (PDX)

models, which can take months to establish, organoids can be used for drug screening within days. However, we currently lack the tools to evaluate cellular subpopulations of response within organoids. Current methods to measure overall response, including cell viability assays, organoid diameter tracking, or pooling of proteins or genetic material from many organoids, ignore cellular heterogeneity. Methods to measure response in individual cells such as flow cytometry, single-cell sequencing, or immunolabeling require destruction of the organoid. Therefore, technology to guide cancer treatment decisions by non-invasively evaluating subpopulations of drug response in patient organoids is needed.

Optical metabolic imaging (OMI) leverages the intrinsic autofluorescence intensities and lifetimes of the metabolic coenzymes NAD(P)H and FAD to quantify the metabolic state of cells and tissues, and non-invasively provides single-cell resolution using two-photon excitation (12, 13). OMI-organoid technology has been validated as an accurate predictor of *in vivo* drug response in xenograft models generated from human breast cancer cell lines (11) and a mouse model of pancreatic cancer (9), but it is unclear whether OMI of primary human tumor organoids can be used to predict patient outcome. Furthermore, it has not been determined whether *in vitro* organoid heterogeneity accurately captures *in vivo* heterogeneity, and whether OMI endpoints are sensitive to certain key metabolic pathways that can drive treatment resistance.

The goal of this dissertation is to develop OMI for measuring drug-induced changes in metabolic heterogeneity in pancreatic and breast cancer organoids. This will provide novel insights into how individual patients respond to intervention at the single-cell level. The development of this technology will enable optimal treatment decisions for individual patients that minimize toxicity, while killing all subpopulations of cells within heterogeneous tumors.

## 1.2 Specific Aims

**Aim 1: Validate the sensitivity of the fluorescence lifetime of NAD(P)H to shifts in flux through key metabolic pathways.** Fluorescence imaging of NAD(P)H is useful for probing the metabolism of living cells because it is non-damaging and does not require exogenous labeling. However it remains unclear whether NAD(P)H FLIM can be used to detect metabolic alterations at other key enzymatic steps that control the path of carbon from glucose uptake to ETC activity. For the first time, NAD(P)H FLIM was used to accurately quantify the relative concentrations of two enzyme species in solution. FLIM of NAD(P)H was also performed on breast epithelial cells and pancreatic duct epithelial cells treated with metabolic inhibitors. Finally, NAD(P)H FLIM was measured in cells forced to metabolize lactate or pyruvate, thus modulating carbon flux through lactate dehydrogenase. This aim tested the hypothesis that NAD(P)H $\tau_2$ offers the ability to non-invasively quantify diversions of carbon away from the TCA cycle and electron transport chain. This sensitivity could be harnessed in order to identify the mechanisms that allow drug-resistant cell subpopulations to evade treatment, and to determine viable alternative drug targets in these subpopulations.

**Aim 2: Test the ability of OMI of *in vitro* breast tumor organoids to accurately quantify *in vivo* heterogeneous response to treatment.** This aim tested the hypothesis that OMI of primary breast cancer organoids can accurately represent *in vivo* changes in tumor heterogeneity in response to treatment, as well as predict overall tumor response in an immunocompetent model of breast cancer. FVB mice bearing orthotopic allografts of polyomavirus middle-T (PyVmT) tumors were treated with a combination of clinically-relevant anti-cancer drugs, and imaged using intravital OMI. In parallel, *in vitro* organoids were generated from the PyVmT model and treated with the same drugs. A novel weighted heterogeneity index (wH-index) was used to quantify the

degree of heterogeneity in organoid treatment groups and *in vivo* tumors, and test whether OMI of primary breast tumor organoids can re-capitulate treatment-induced *in vivo* changes in cell-level metabolic heterogeneity. Additionally, OMI predictions of global tumor response were validated using standard *in vivo* tumor volume in a separate cohort of mice over 14 days. Histology was used to evaluate potential causes behind divergent cell subpopulations in both tumors and organoids.

**Aim 3: Characterize OMI of drug response heterogeneity in human pancreatic cancer organoids.** Currently, oncologists must select drugs for individual pancreatic cancer patients without a dependable method for predicting response. This aim tested the hypothesis that OMI of pancreatic tumor organoids can be used to evaluate patient-specific response to treatment at the single-cell level. Organoids were generated from fresh patient tissue samples acquired during surgical tumor resection. These organoids were treated with the same drugs that the patient received following surgery, and OMI was used to measure cellular metabolic heterogeneity in response to this treatment. The degree of OMI-measured heterogeneity in drug-treated organoids were compared to patient recurrence-free survival, suggesting a high level of agreement.

### 1.3 Dissertation Outline

This dissertation has been organized in the following manner:

Chapter 1 includes the motivation behind the dissertation, as well as an outline of the specific aims.

Chapter 2 provides background information on the current state of breast and pancreatic cancer treatment, along with challenges associated with tumor heterogeneity. Background is also provided on the tools used to address these challenges, including organoid culture and optical imaging.

Chapter 3 describes experiments in both solutions and cells demonstrating that the fluorescence lifetime of enzyme-bound NAD(P)H is sensitive to alternative fates of glucose carbon before entry into the TCA cycle. This work offers a novel biochemical interpretation for changes in the fluorescence lifetime of NAD(P)H, connecting OMI measurements with shifts in flux through specific metabolic pathways which may contribute to anti-cancer drug resistance. This work was published in 2018 in *Scientific Reports* (14).

Chapter 4 contains a novel demonstration that metabolic heterogeneity in tumor-derived organoids accurately recapitulates that of the original tumor. OMI was performed *in vivo* in an immunocompetent mouse model of breast cancer, and also in organoids derived from the same tumor model. A novel weighted heterogeneity index was used to quantify and compare measurements in both settings. This work validates OMI of tumor-derived organoids as a platform to study tumor heterogeneity, when direct measurement *in vivo* is not feasible.

Chapter 5 characterizes OMI of heterogeneous drug responses in pancreatic cancer patient-derived organoids. First, interpatient variability in terms of overall treatment response to a panel of pancreatic cancer therapies was demonstrated across patient-derived organoids. Next, metabolic heterogeneity at the cellular level in patient organoids in response to treatment was compared to long-term patient outcome. This study demonstrates the feasibility of OMI of organoids as a high-throughput drug screening technology to quickly optimize treatment plans for individual pancreatic cancer patients.

Chapter 6 first provides a summary of the dissertation and its conclusions. This is followed by a discussion of potential future directions for this research. Finally, the scientific contributions of this dissertation and its broader impacts on society are outlined.

Appendices A, B, and C contain supplementary figures and tables from Chapters 3, 4, and 5, respectively.

### 1.4 References


[1] Cancer Facts & Figures 2018: American Cancer Society.

[2] Siegel RL, Miller KD, Jemal A. Cancer statistics, 2018. CA Cancer J Clin. 2018;68(1):7-30.

[3] Rahib L, Smith BD, Aizenberg R, Rosenzweig AB, Fleshman JM, Matrisian LM. Projecting cancer incidence and deaths to 2030: the unexpected burden of thyroid, liver, and pancreas cancers in the United States. Cancer Res. 2014;74(11):2913-21.

[4] Bray F, Ferlay J, Soerjomataram I, Siegel RL, Torre LA, Jemal A. Global cancer statistics 2018: GLOBOCAN estimates of incidence and mortality worldwide for 36 cancers in 185 countries. CA Cancer J Clin. 2018;68(6):394-424.

[5] Fountzilas E, Tsimberidou AM. Overview of precision oncology trials: challenges and opportunities. Expert Rev Clin Pharmacol. 2018;11(8):797-804.

[6] Marusyk A, Polyak K. Tumor heterogeneity: causes and consequences. Biochim Biophys Acta. 2010;1805(1):105-17.

[7] Fisher R, Pusztai L, Swanton C. Cancer heterogeneity: implications for targeted therapeutics. Br J Cancer. 2013;108(3):479-85.

[8] Boj SF, Hwang CI, Baker LA, Chio, II, Engle DD, Corbo V, et al. Organoid models of human and mouse ductal pancreatic cancer. Cell. 2015;160(1-2):324-38.

[9] Walsh AJ, Castellanos JA, Nagathihalli NS, Merchant NB, Skala MC. Optical Imaging of Drug-Induced Metabolism Changes in Murine and Human Pancreatic Cancer Organoids Reveals Heterogeneous Drug Response. Pancreas. 2016;45(6):863-9.

[10] Sachs N, de Ligt J, Kopper O, Gogola E, Bounova G, Weeber F, et al. A Living Biobank of Breast Cancer Organoids Captures Disease Heterogeneity. Cell. 2018;172(1-2):373-86 e10.

[11] Walsh AJ, Cook RS, Sanders ME, Aurisicchio L, Ciliberto G, Arteaga CL, et al. Quantitative optical imaging of primary tumor organoid metabolism predicts drug response in breast cancer. Cancer Res. 2014;74(18):5184-94.

[12] Chance B, Schoener B, Oshino R, Itshak F, Nakase Y. Oxidation-reduction ratio studies of mitochondria in freeze-trapped samples. NADH and flavoprotein fluorescence signals. J Biol Chem. 1979;254(11):4764-71.

[13] Georgakoudi I, Quinn KP. Optical Imaging Using Endogenous Contrast to Assess Metabolic State. Annu Rev Biomed Eng. 2012;14:351-67.

[14] Sharick JT, Favreau PF, Gillette AA, Sdao SM, Merrins MJ, Skala MC. Protein-bound NAD(P)H Lifetime is Sensitive to Multiple Fates of Glucose Carbon. Sci Rep. 2018;8(1):5456.

CHAPTER 2

# Background

## 2.1 Breast and pancreatic cancer personalized medicine

### 2.1.1 Breast cancer and treatment strategies

Breast cancer accounts for about 30% of all cancers in women globally (1). It has been estimated that about 266,000 women and 2,600 men will be diagnosed with invasive breast cancer in the United States in 2018, and 40,920 women and 480 men will die of the disease. The absolute number of women being diagnosed continues to increase as the "baby boomers" generation approaches the median age of breast cancer diagnosis, which is 62 years of age (2). Breast cancer confined to the breast or nearby lymph nodes does not cause mortalities; it is the metastatic spread of the disease to vital organs such as the liver, brain, or lungs that causes death (3). From 1989 to 2015, the female breast cancer death rate decreased by 39%, largely due to improvements in awareness and screening leading to earlier detection, yet breast cancer remains the second leading cause of cancer death in women (Fig. 2.1) (1).

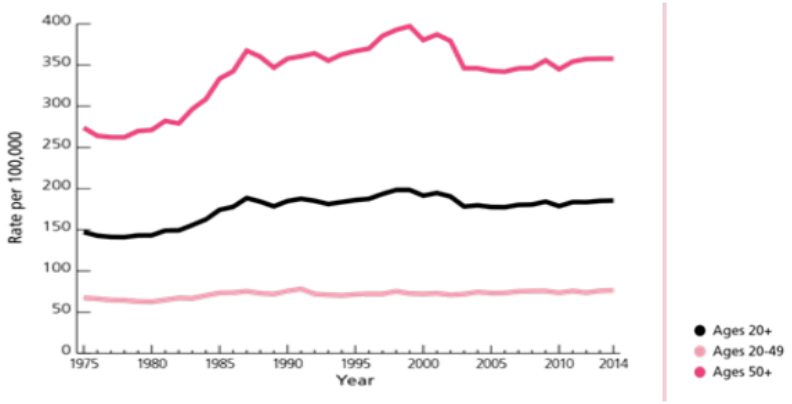


**Figure 2.1. Breast cancer incidence rates in the US by age.** Breast cancer incidence rates in the United States, stratified by patient age at diagnosis (2).

Most cases of breast cancer will require surgery to remove the tumor. Breast-conserving strategies include lumpectomy, in which only a small amount of normal tissue around the tumor

is removed along with the tumor, and partial mastectomy, in which more normal tissue is removed, possibly including the lining of the chest wall (4). A total mastectomy refers to the removal of the entire afflicted breast and some lymph nodes. Neoadjuvant therapy, or treatment before surgery with chemotherapy and/or other drugs to shrink the size of the tumor, is often given in hopes of making the operation less extensive.

Chemotherapy is used as a breast cancer treatment both before and after surgery, and also for treating metastatic lesions. Chemotherapy targets and kills cells that are dividing rapidly, which is true of most cancer cells. The most common chemotherapy drugs for breast cancer include the anthracyclines (doxorubicin and epirubicin) and the taxanes (docetaxel and paclitaxel), which can be combined with other chemotherapeutics such as cisplatin, carboplatin, or gemcitabine. Unfortunately, chemotherapy generally attacks healthy cells of the body, resulting in side effects that include hair loss, fatigue, nausea, susceptibility to infection, peripheral nerve damage, and permanent cardiomyopathy (5). Because of these toxic side effects, chemotherapy is often given in cycles of 2-3 weeks for a total of 3-6 months, depending on the drug and side effects experienced (5).

Hormone therapy is usually used in the adjuvant setting but can also be used in the neoadjuvant setting. This treatment is only useful for patients that have been classified as hormone receptor positive, which is true for 2 out of 3 breast cancers (5). Most types of hormone therapy lower estrogen levels or block the ability of estrogen to activate cancer cell growth. For example, tamoxifen is an antagonist of the estrogen receptor and is commonly given to women with early stage breast cancer that have not gone through menopause. Also, tamoxifen is frequently given to patients adjuvantly for up to 10 years following surgery. Tamoxifen use can have serious side effects including uterine cancer, blood clots, stroke, heart attacks, and bone thinning. Fulvestrant

is a hormone therapy used to treat late-stage breast cancer after other hormone therapies have lost efficacy. Fulvestrant is an estrogen receptor antagonist that also causes temporary receptor degradation, which also has significant side effects including bone thinning. Finally, aromatase inhibitors can be given to post-menopausal women to block the remaining production of estrogen in fatty tissue. These inhibitors generally have less side effects than tamoxifen and fulvestrant, but can still cause joint pain and bone thinning (5).

Therapies that target the HER2 receptor are prescribed for patients whose cancer over-expresses this protein. Trastuzumab is a monoclonal antibody which targets the human HER2 receptor to help slow the growth of these cancers and stimulate the immune system. Trastuzumab can be combined with chemotherapy in the neoadjuvant and adjuvant settings, and the combination tends to show more efficacy than chemotherapy alone (5). Pertuzumab is another monoclonal antibody that targets the HER2 receptor, and can be combined with trastuzumab and chemotherapy. It binds to a different location on the HER2 receptor than trastuzumab and prevents dimerization of the receptor. A major side effect of these antibodies is heart damage due to the presence of these receptors in the heart, which can lead to congestive heart failure. If chemotherapy and anti-HER2 antibodies have stopped working, lapatinib is a small molecule inhibitor of both the HER2 and epidermal growth factor receptor (EGFR) pathways that can be used as treatment, but can cause severe diarrhea and hand-foot syndrome (6). Everolimus is an inhibitor of the mTOR signaling pathway in cells, which is important in cell growth and survival. It is approved for use in hormone receptor-positive, HER2-negative post-menopausal women that are also taking an aromatase inhibitor, but can cause nausea, diarrhea, shortness of breath, and infection (5).

New targeted therapies are regularly being developed to treat breast cancer. Another therapeutic target being researched by drug developers are the PARP enzymes, which are involved

in the DNA repair mechanism known as base excision repair (BER). PARP enzymes bind to single-strand DNA breaks and recruit DNA repair proteins to fix the damage (7). PARP inhibitors block BER, but normal cells have other pathways to repair this damage. In cells that already have a separate DNA repair defect, cell death occurs. *BRCA1* and *BRCA2* mutations are examples of these defects, and PARP inhibitors are currently in clinical trials for these patients.

Clearly, there exist a large number of drug choices for patients undergoing neoadjuvant treatment, all of which can cause significant long-term side effects. A quick and reliable method for determining the optimal treatment plan for an individual patient's cancer would reduce the unnecessary toxicity, cost, and time associated with ineffective therapies.

### 2.1.2 Methods for predicting therapy response in breast cancer

The current standard of care involves testing for the expression of hormone receptors (ER and PR) as well as HER2 (Fig. 2.2). Hormone therapy drugs target these hormone receptors, and drugs such as trastuzumab and lapatinib target HER2. A number of additional methods have been investigated for predicting how an individual patient will respond to a neoadjuvant treatment regimen. While evaluation of tumor size change using MRI is not sensitive enough for evaluating treatment response until several doses of neoadjuvant therapy have taken place, dynamic contrast-enhanced MRI measurements of tumor permeability after one cycle of chemotherapy have been found to correlate with treatment response to further cycles of chemotherapy (8). While techniques such as this one may greatly reduce the treatment time required to determine whether a neoadjuvant treatment is having an effect, it requires an entire cycle of treatment to take place before evaluation, can only evaluate one treatment regimen at a time, and is expensive.

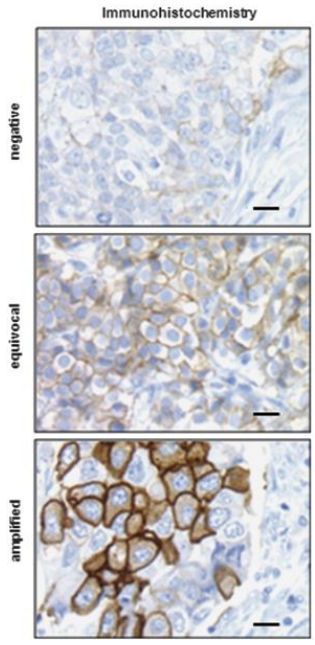


**Figure 2.2. HER2 immunohistochemistry of breast cancer.** Examples of HER2 staining in HER2 negative, equivocal, and amplified tumors. Breast cancer patients are routinely tested for HER2 to determine whether HER2-targeted therapy is recommended. Scale bar = 25μm. Re-printed with permission from Springer Nature Modern Pathology (9). Copyright 2010.

The rate of washout of $^{99m}$Tc-sestamibi radiotracer in a tumor as measured by scintimammography before treatment was found to predict tumor response to chemotherapy with 100% sensitivity and 80% specificity (10), but requires the intravenous injection of a radioactive substance and is also expensive. Other studies have aimed to find genetic biomarkers to predict response in patients, with limited success (11). For example, Chang *et al.* investigated a gene expression profile that could predict response to neoadjuvant docetaxel in breast cancer with 85% sensitivity and 90% specificity (12). Genetic tests such as these can only predict the success of treatment regimens for which a genetic predictor profile has been developed and can require significant time and money. Profiling of metabolites in serum has also been studied as a predictor of response to neoadjuvant chemotherapy. For example, the amounts of four metabolites (threonine, glutamine, isoleucine, and linolenic acid) were found to distinguish breast cancer patients that responded to neoadjuvant chemotherapy from those that did not (13). This method

along with all other aforementioned methods do not take into account the heterogeneous nature of breast tumors, which may allow for subclones within an otherwise drug-responsive tumor to evade treatment and cause eventual recurrence. Clearly, the need still exists for a quick, reliable, and cost-effective method to determine the optimal treatment plan for an individual breast cancer patient.

### 2.1.3 Pancreatic cancer and treatment strategies

Pancreatic cancer has one of the lowest 5-year survival rates of all cancer types (8%) (14), and is projected to be the second leading cause of cancer death by 2030 (15). Pancreatic cancer mortality has not improved over the last 25 years (Fig. 2.3). Even for those patients that are able to be diagnosed with local disease, the 5-year survival rate is still only 32%. A majority of patients are diagnosed at a distant stage, where the cancer has spread beyond the pancreas (1).

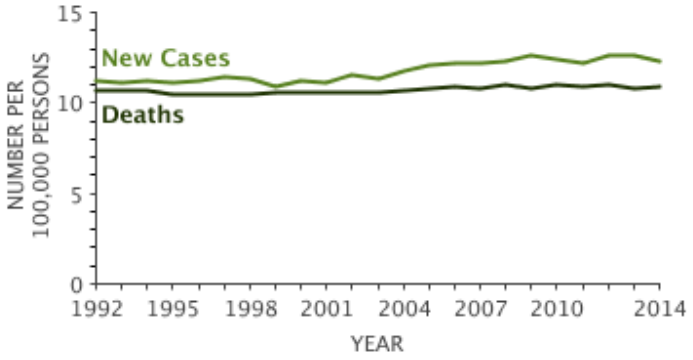


**Figure 2.3. Pancreatic cancer incidence and death rate trends in the US (2).**

One reason that pancreatic cancer is most often diagnosed at an advanced stage is the lack of symptoms associated with localized disease. Generally, patients do not experience symptoms until other organs are affected (16). Due to the location of the pancreas in the body (Fig. 2.4), early stage tumors are also generally not discovered during routine physical exams.

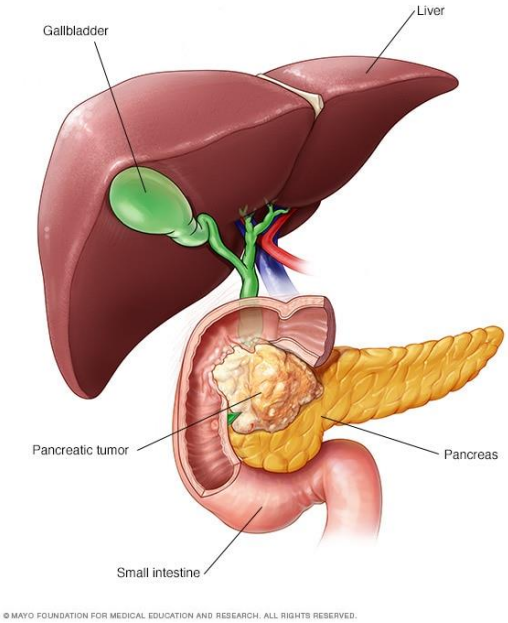


**Figure 2.4. Anatomical diagram of pancreatic cancer.** Most pancreatic cancers form in the cells that line pancreatic ducts. This is referred to as pancreatic adenocarcinoma (PDAC) (17). Used with permission of Mayo Foundation for Medical Education and Research, all rights reserved.

If the cancer is discovered prior to metastasis and is determined to be resectable, surgery may offer a chance at cure, but this only comprises 5-10% of cases (18). Surgical procedures for pancreatic cancer include the pancreaticoduodenectomy (Whipple procedure), and the less common distal pancreatectomy (16). The Whipple procedure involves removing part or all of the pancreas, along with surrounding portions of the small intestine, gall bladder, and stomach. Distal pancreatectomy, which is the partial removal of pancreas, can be performed when the tumor is confined to the tail segment.

Chemotherapy can be prescribed in the adjuvant setting to enhance survival, as well as in the neoadjuvant setting in order to shrink borderline resectable localized tumors and enhance the chance at successful surgery. Standard treatments in the adjuvant setting include gemcitabine and gemcitabine combined with capecitabine (5-fluorouracil (5-FU) pro-drug) (19). Additional promising adjuvant treatments include gemcitabine combined with abraxane (paclitaxel albumin-

stabilized nanoparticles), and FOLFIRINOX, the combination of folinic acid, 5-FU, irinotecan, and oxaliplatin (20). Side effects caused by these chemotherapy drugs are similar to those used for breast cancer, including nausea, diarrhea, increased risk of infection, bleeding, fatigue, and kidney damage. FOLFIRINOX can also cause liver and heart damage, problems swallowing, and allergic reactions. Chemotherapy can also be combined with radiation therapy, but brings additional side effects.

The stromal microenvironment of pancreatic cancer plays a major role in therapeutic response. Tumors are characterized by a very dense stroma containing stellate cells, collagen, and other ECM components. This fibrous stroma causes reduced blood flow and high interstitial pressure, which can impair drug delivery to tumor cells (21-23). The stroma can also promote tumorigenesis by preventing the surveillance and destruction of abnormal cells by the immune system (22).

### 2.1.4 Methods for predicting therapy response in pancreatic cancer

Currently, there are no dependable methods for predicting how an individual pancreatic cancer patient will respond to a particular drug or combination. Doctors weigh a number of factors when making treatment options, such as the patient's ability to withstand the associated side effects. They may also weigh the patient's expected life span, the stage and resectability of the tumor, and complications from the patient's other health issues. For example, the doctor may choose to prescribe more aggressive chemotherapy regimens such as FOLFIRINOX to certain patients simply because they are otherwise in better health and can endure the associated side effects (16).

Pancreatic tumor biopsies can be genetically sequenced with significant detail, but tailoring treatment based on genomic analysis alone has not shown success in pancreatic cancer. Despite being less genetically diverse than most cancers, targeted approaches to treating pancreatic cancer have failed in clinical trials. Most pancreatic tumors do not express a specific therapeutic target (24), and the driver mutations present in a patient's cancer usually do not predict their response to chemotherapy. One exception is in the case of the *BRCA1/2* driver mutations, which show an improved response to platinum-based chemotherapy (25). Using deep molecular genomics and transcriptomics, predictive gene signatures have been used to identify patients that may respond better to certain chemotherapies, but these signatures have not been evaluated in large numbers of patients (26).

### 2.2 Tumor heterogeneity

Not only do individual tumors have unique genetic expression patterns and resulting clinical outcomes (intertumor heterogeneity) (27), but there is also significant variability among the cancer cells that make up a tumor (intratumor heterogeneity) (28). These cells can vary in sensitivity to chemotherapy, gene expression, proliferation rate, metastatic potential, and morphology (29). The presence of multiple distinct clones poses a major challenge in both determining a prognosis as well as identifying an effective treatment plan (Fig. 2.5) (30). Pre-existing subpopulations of cells that are resistant to a certain drug can be selected for by that drug, which can lead to expansion of that resistant subpopulation and treatment failure. For this reason, predictive biomarkers of tumor treatment response that do not account for intratumor heterogeneity underestimate the importance of small yet dangerous drug-resistant subpopulations.

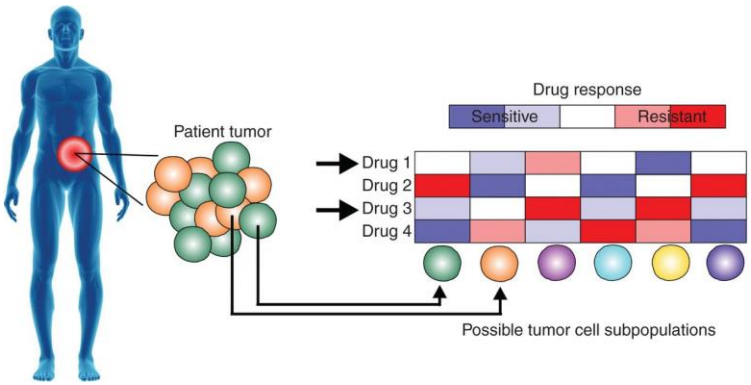


**Figure 2.5. The challenge of tumor heterogeneity.** In order to optimize therapies for individual patients with heterogeneous tumors, personalized medicine tools are needed to measure the drug sensitivity of each individual cell subpopulation. Reprinted from (31) with permission from AACR.

Tumor subpopulations can often be distinguished by their unique metabolic states. Single-cell genetic sequencing can identify mutant subclones within a tumor (32-36), and the number of subclonal driver mutations has predictive value for a patient's overall survival (37). However, additional factors affect drug sensitivity, which is a complex combination of both genetic and non-genetic factors (38). Each tumor subclone is also phenotypically heterogeneous itself due to non-genetic factors, including cellular metabolism. Cancer cells must reprogram their metabolism to fuel abnormally high proliferation rates, even in the absence of growth factor signals (39, 40). Individual cells adapt appropriately to maximize their survival in response to unique nutrients and signals in their microenvironment (41, 42). Metabolic adaptation also affect cell resistance to cytotoxic drugs and immunotherapies (43, 44), resulting in subpopulations of tumor cells with differing sensitivities to treatment. This highlights the need for personalized medicine tools which incorporate metabolic heterogeneity.

## 2.3 Patient-Derived Organoids

Organoid culture refers to the digestion and growth of tumor tissue in a 3D extracellular matrix. Organoids maintain the genetic profile, surface markers, and 3-dimensional organizational characteristics of breast tumors (Fig. 2.6) (45-48) and pancreatic tumors (26, 49), and contain all of the cell types present in the tissue sample, including the tumor cells, immune cells, and fibroblasts. The inclusion of non-tumor cells in the culture system improves the accuracy of treatment response because these cells are known to have effects on therapeutic resistance and tumor heterogeneity (50, 51). Additionally, 3D cell culture techniques are known to more accurately mimic *in vivo* tumor growth than 2D cell cultures (52, 53). This is partly due to the presence of oxygen, metabolites, nutrients, and pH gradients that mimic those in the *in vivo* tumor and cause cells in different regions of the organoid to experience very different microenvironment conditions. Gradients also form with regards to drug penetration throughout the organoid, which captures the heterogeneous drug delivery that occurs in bulk tumors. 3D cultures also allow for cell-to-cell contacts and signaling to occur between cells of different types in the same manner in which it would occur in the bulk tumor.

Organoids offer the ability to perform high-throughput drug screens directly on patient cells, and study single-cell metabolic responses (54). While PDX models also allow drug screening on patient cells in a relevant 3D microenvironment, they have not been routinely adopted due to the time and animal burden required for their establishment (55). A significant number of organoids can be established in hours to days, allowing for drug screening in a clinically relevant time frame.

In general, methods for measuring drug response in organoids have either involved tracking changes in organoid diameter, assays of overall cell viability, or pooling of proteins, DNA, and/or

RNA from many organoids. These methods ignore cellular heterogeneity and may overlook the influence of lethal drug-resistant cells. Other methods such as flow cytometry, immunofluorescence, or immunohistochemistry can be used to characterize individual cells within organoids, but required fixing or dissociating samples. New technologies are needed that can measure the response of individual cells within organoids, non-destructively.

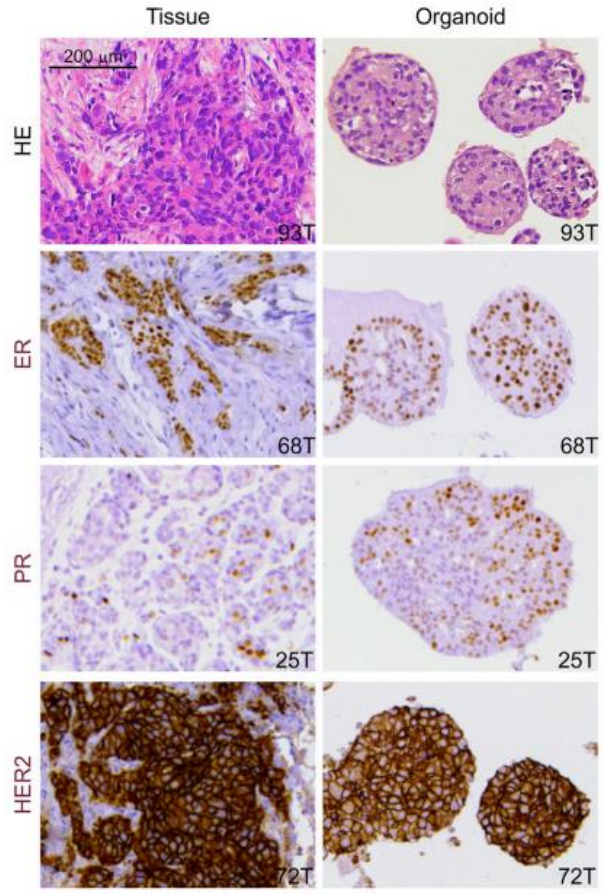


**Figure 2.6. Breast cancer organoids conserve the properties of the original tumor.** Immunohistochemistry demonstrates that the ER, PR, and HER2 status of breast cancers can be preserved in organoid lines. H&E staining shows similar epithelial structures and cell organization between tumors and organoids. Reprinted from (48) with permission from Elsevier. Copyright 2018.

### 2.4 Multiphoton microscopy

Imaging with multiphoton microscopy involves exciting a fluorophore with two or more photons simultaneously. This requires the absorbance of two photons that each have half the

energy, or twice the wavelength, of a photon required for single photon excitation (56). Since this simultaneous absorbance of two half-energy photons is required for fluorescence excitation, the amount of photon flux needed only occurs at the focal point of the microscope objective (Fig. 2.7). This eliminates excitation of fluorophores outside of the focal plane and provides very precise optical sectioning. Most endogenous fluorophores, including NAD(P)H and FAD, are excited by one photon of ultraviolet to visible light, or two photons of near-infrared light. Near-infrared light exhibits less scattering and absorption in tissue, and therefore two-photon excitation allows for deeper imaging penetration (57, 58). Two-photon excitation also allows for imaging and quantification of weaker fluorophores with subcellular resolution, and thus can be used in optical metabolic imaging to characterize metabolic changes at the single-cell level.

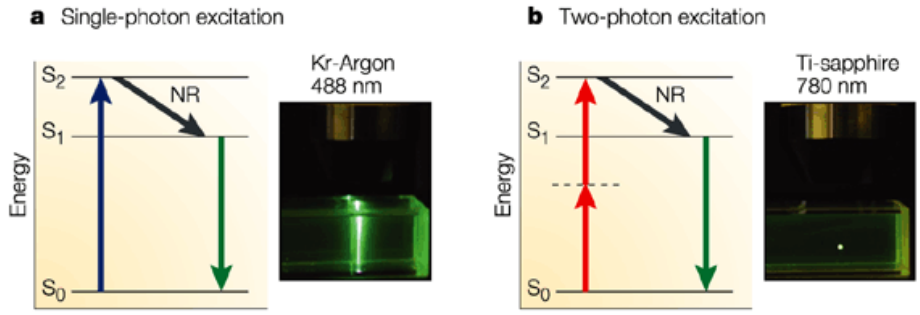


**Figure 2.7. Two-photon vs. one-photon fluorescence microscopy.** (a) Jablonski diagram of energy states involved in single-photon excitation. Single-photon fluorescence from blue light is emitted along the entire laser beam path. (b) Jablonski diagram of energy states involved in two-photon excitation. Light is only emitted at the focus of the NIR laser beam. Reprinted from (59) with permission from Springer Nature Reviews Immunology. Copyright 2002.

### 2.5 Cellular metabolism and autofluorescence

Nicotinamide adenine dinucleotide (NADH) and its phosphorylated form NADPH (together referred to as NAD(P)H) are metabolic coenzymes that donate electrons to reactions. They bind to at least 334 known proteins in cells (60). NAD(P)H, which is the reduced form of the coenzyme, is fluorescent, while the oxidized form, $NAD(P)^+$, is not. Flavin adenine dinucleotide (FAD) is another important metabolic coenzyme which is fluorescent in its oxidized form but not

in its reduced form ($FADH_2$). During cellular glycolysis, $NAD^+$ is reduced to NADH. In oxidative phosphorylation, NADH is oxidized to $NAD^+$, and $FADH_2$ is oxidized to FAD. By probing endogenous fluorophores such as NAD(P)H and FAD, biochemical and structural information about cells and tissues can be collected without the need for exogenous dyes or contrast agents (61).

The optical redox ratio, which is defined as the ratio of the fluorescence intensity of NAD(P)H to FAD, reflects the redox state of the cell (62-64). Due to the Warburg effect, the preference for glycolysis exhibited by many cancer cells (65), the optical redox ratio is a particularly useful tool for exploiting intrinsic contrast to study cancer metabolism, distinguishing cancer subtypes, monitoring cancer treatment response, and distinguishing precancerous cells from normal cells (63, 64, 66). Additionally, the optical redox ratio is correlated with oxygen consumption, a key metabolic process, in breast cancer cells (Fig. 2.8) (67, 68).

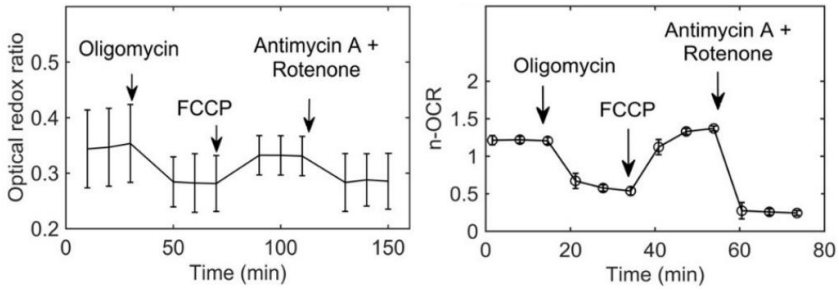


**Figure 2.8. The optical redox ratio is sensitive to changes in oxygen consumption.** (Left) The optical redox ratio in 4T1 breast cancer cells after sequential addition of indicated mitochondrial inhibitors. (Right) Quantification of the normalized oxygen consumption rate (n-OCR) in response to the same drugs as measured using a Seahorse XFp analyzer. The optical redox ratio reports dynamic changes in cellular oxygen consumption. Reprinted with permission from (67). Copyright 2016 Optical Society of America.

### 2.6 Fluorescence lifetime imaging

Fluorescence lifetime imaging microscopy (FLIM) is a technique which probes the amount of time that a fluorophore remains in the excited state before relaxing to the ground state and emitting a photon (58, 69). FLIM is sensitive to factors in the molecular environment of

fluorophores, such as oxygen, pH, temperature, and binding to other molecules. One method of measuring the fluorescence lifetime of molecules is through time-correlated single photon counting (TCSPC), in which individual lifetime events (in the picosecond to nanosecond range) are timed, plotted as a histogram, and fit with an exponential curve (Fig. 2.9) (70). This exponential curve is comprised of multiple decay components, each of which corresponds to an individual molecular species or binding configuration of the fluorophore. TCSPC fitting determines the relative abundance of each configuration in each pixel, as well as their individual lifetimes.

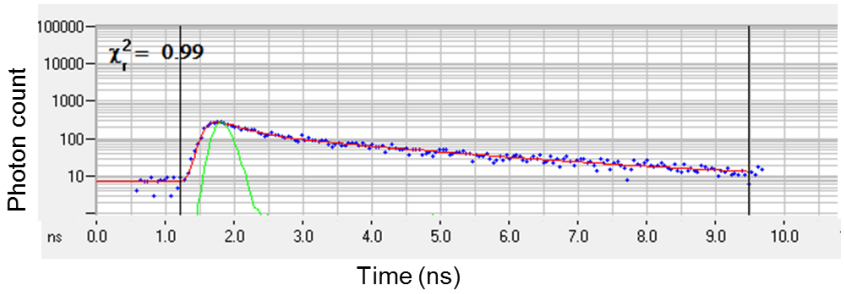


**Figure 2.9. TCSPC fluorescence lifetime decay curve.** The fluorescence lifetime in a pixel is calculated by fitting a histogram of measured lifetime events (blue) to an exponential decay function (red), after deconvolving the instrument response function (green). The chi-square value quantifies the goodness of fit.

FLIM of the metabolic coenzymes NAD(P)H and FAD in particular exploit endogenous autofluorescence to provide complimentary information to the optical redox ratio. NAD(P)H and FAD exist in free and protein-bound states which have distinct fluorescence lifetimes (represented as $\tau_1$ and $\tau_2$) (58). Free NAD(P)H and bound FAD ($\tau_1$) have short lifetimes due to dynamic self-quenching, while bound NAD(P)H and free FAD ($\tau_2$) have longer lifetimes (58, 71). Thus, FLIM can be used to quantify the relative abundance of each species within a cell (represented as $\alpha_1$ and $\alpha_2$, respectively, where $\alpha_1 + \alpha_2 = 1$), and probe changes in cell metabolism that affect coenzyme binding. This cannot be done with intensity measurements alone, due to the similar absorption and emission spectra of free and protein-bound NAD(P)H and free and protein-bound FAD. The

lifetime of protein-bound NAD(P)H also depends on which enzyme it is bound to (72), suggesting that NAD(P)H FLIM is sensitive to changes in cell metabolism that affect the distribution of NAD(P)H binding to various enzymes. For example, many studies have shown that NAD(P)H FLIM can detect changes in flux through glycolysis, the tricarboxylic acid (TCA) cycle and electron transport chain (ETC) (63, 73-81). The wide-ranging applications of NAD(P)H FLIM have been demonstrated in cell culture (63, 73, 82, 83), in animal models of cancer (66, 84, 85), and in pilot studies in human tissues *in vivo* (86-88) and *ex vivo* (89-91). Probing endogenous fluorophores using FLIM and high-resolution multiphoton microscopy allows cellular metabolic information to be quantified at the single-cell level, enabling studies of tumor heterogeneity.

## 2.7 References


[1] Cancer Facts & Figures 2018: American Cancer Society.

[2] Noone A, Howlader N, Krapcho M, Miller D, Brest A, Yu M, et al. SEER Cancer Statistics Review, 1975–2015. based on November 2017 SEER data submission, posted to the SEER web site, April 2018. National Cancer Institute Bethesda, MD. 2018.

[3] The Breast Cancer Landscape: Department of Defense Breast Cancer Research Program; 2018 [updated January 2018.

[4] PDQ Breast Cancer Treatment: National Cancer Institute. PDQ® Adult Treatment Editorial Board; [updated December 2018; cited 2018.

[5] Breast Cancer detailed guide: American Cancer Society; 2017 [updated October 2017.

[6] Higa GM, Abraham J. Lapatinib in the treatment of breast cancer. Expert Rev Anticancer Ther. 2007;7(9):1183-92.

[7] Rouleau M, Patel A, Hendzel MJ, Kaufmann SH, Poirier GG. PARP inhibition: PARP1 and beyond. Nat Rev Cancer. 2010;10(4):293-301.

[8] Padhani AR, Hayes C, Assersohn L, Powles T, Makris A, Suckling J, et al. Prediction of clinicopathologic response of breast cancer to primary chemotherapy at contrast-enhanced MR imaging: initial clinical results. Radiology. 2006;239(2):361-74.

[9] Theurillat JP, Dreier B, Nagy-Davidescu G, Seifert B, Behnke S, Zurrer-Hardi U, et al. Designed ankyrin repeat proteins: a novel tool for testing epidermal growth factor receptor 2 expression in breast cancer. Mod Pathol. 2010;23(9):1289-97.

[10] Sciuto R, Pasqualoni R, Bergomi S, Petrilli G, Vici P, Belli F, et al. Prognostic value of (99m)Tc-sestamibi washout in predicting response of locally advanced breast cancer to neoadjuvant chemotherapy. J Nucl Med. 2002;43(6):745-51.

[11] Sorlie T, Perou CM, Fan C, Geisler S, Aas T, Nobel A, et al. Gene expression profiles do not consistently predict the clinical treatment response in locally advanced breast cancer. Mol Cancer Ther. 2006;5(11):2914-8.

[12] Chang JC, Wooten EC, Tsimelzon A, Hilsenbeck SG, Gutierrez MC, Elledge R, et al. Gene expression profiling for the prediction of therapeutic response to docetaxel in patients with breast cancer. Lancet. 2003;362(9381):362-9.

[13] Wei S, Liu L, Zhang J, Bowers J, Gowda GA, Seeger H, et al. Metabolomics approach for predicting response to neoadjuvant chemotherapy for breast cancer. Mol Oncol. 2013;7(3):297-307.

[14] Siegel RL, Miller KD, Jemal A. Cancer statistics, 2018. CA Cancer J Clin. 2018;68(1):7-30.

[15] Rahib L, Smith BD, Aizenberg R, Rosenzweig AB, Fleshman JM, Matrisian LM. Projecting cancer incidence and deaths to 2030: the unexpected burden of thyroid, liver, and pancreas cancers in the United States. Cancer Res. 2014;74(11):2913-21.

[16] Pancreatic Cancer detailed guide: American Cancer Society; 2016 [updated May 2016.

[17] Pancreatic cancer: Mayo Clinic Staff; 2018. Available from: https://www.mayoclinic.org/diseases-conditions/pancreatic-cancer/symptoms-causes/syc-20355421.

[18] Spanknebel K, Conlon KC. Advances in the surgical management of pancreatic cancer. Cancer J. 2001;7(4):312-23.

[19] Neoptolemos JP, Palmer DH, Ghaneh P, Psarelli EE, Valle JW, Halloran CM, et al. Comparison of adjuvant gemcitabine and capecitabine with gemcitabine monotherapy in patients with resected pancreatic cancer (ESPAC-4): a multicentre, open-label, randomised, phase 3 trial. Lancet. 2017;389(10073):1011-24.

[20] PDQ Pancreatic Cancer Treatment: National Cancer Institute. PDQ® Adult Treatment Editorial Board; [updated May 2018; cited 2018.

[21] Provenzano PP, Cuevas C, Chang AE, Goel VK, Von Hoff DD, Hingorani SR. Enzymatic targeting of the stroma ablates physical barriers to treatment of pancreatic ductal adenocarcinoma. Cancer Cell. 2012;21(3):418-29.

[22] Ryan DP, Hong TS, Bardeesy N. Pancreatic adenocarcinoma. N Engl J Med. 2014;371(22):2140-1.

[23] Nagathihalli NS, Castellanos JA, Shi C, Beesetty Y, Reyzer ML, Caprioli R, et al. Signal Transducer and Activator of Transcription 3, Mediated Remodeling of the Tumor Microenvironment Results in Enhanced Tumor Drug Delivery in a Mouse Model of Pancreatic Cancer. Gastroenterology. 2015;149(7):1932-43 e9.

[24] Witkiewicz AK, Balaji U, Eslinger C, McMillan E, Conway W, Posner B, et al. Integrated Patient-Derived Models Delineate Individualized Therapeutic Vulnerabilities of Pancreatic Cancer. Cell Rep. 2016;16(7):2017-31.

[25] Golan T, Kanji ZS, Epelbaum R, Devaud N, Dagan E, Holter S, et al. Overall survival and clinical characteristics of pancreatic cancer in BRCA mutation carriers. Br J Cancer. 2014;111(6):1132-8.

[26] Tiriac H, Belleau P, Engle DD, Plenker D, Deschenes A, Somerville T, et al. Organoid profiling identifies common responders to chemotherapy in pancreatic cancer. Cancer Discov. 2018.

[27] Sorlie T, Perou CM, Tibshirani R, Aas T, Geisler S, Johnsen H, et al. Gene expression patterns of breast carcinomas distinguish tumor subclasses with clinical implications. Proc Natl Acad Sci U S A. 2001;98(19):10869-74.

[28] Campbell LL, Polyak K. Breast tumor heterogeneity: cancer stem cells or clonal evolution? Cell Cycle. 2007;6(19):2332-8.

[29] Heppner GH. Tumor heterogeneity. Cancer Res. 1984;44(6):2259-65.

[30] Michor F, Polyak K. The origins and implications of intratumor heterogeneity. Cancer Prev Res (Phila). 2010;3(11):1361-4.

[31] Fedele C, Tothill RW, McArthur GA. Navigating the challenge of tumor heterogeneity in cancer therapy. Cancer Discov. 2014;4(2):146-8.

[32] Suzuki Y, Ng SB, Chua C, Leow WQ, Chng J, Liu SY, et al. Multiregion ultra-deep sequencing reveals early intermixing and variable levels of intratumoral heterogeneity in colorectal cancer. Mol Oncol. 2017;11(2):124-39.

[33] Roerink SF, Sasaki N, Lee-Six H, Young MD, Alexandrov LB, Behjati S, et al. Intra-tumour diversification in colorectal cancer at the single-cell level. Nature. 2018;556(7702):457-62.

[34] Sievers CK, Zou LS, Pickhardt PJ, Matkowskyj KA, Albrecht DM, Clipson L, et al. Subclonal diversity arises early even in small colorectal tumours and contributes to differential growth fates. Gut. 2017;66(12):2132-40.

[35] Navin N, Kendall J, Troge J, Andrews P, Rodgers L, McIndoo J, et al. Tumour evolution inferred by single-cell sequencing. Nature. 2011;472(7341):90-4.

[36] Kim C, Gao R, Sei E, Brandt R, Hartman J, Hatschek T, et al. Chemoresistance Evolution in Triple-Negative Breast Cancer Delineated by Single-Cell Sequencing. Cell. 2018;173(4):879-93 e13.

[37] Kleppe M, Levine RL. Tumor heterogeneity confounds and illuminates: assessing the implications. Nat Med. 2014;20(4):342-4.

[38] Caiado F, Silva-Santos B, Norell H. Intra-tumour heterogeneity - going beyond genetics. FEBS J. 2016;283(12):2245-58.

[39] Vander Heiden MG, Cantley LC, Thompson CB. Understanding the Warburg effect: the metabolic requirements of cell proliferation. Science. 2009;324(5930):1029-33.

[40] Hanahan D, Weinberg RA. Hallmarks of cancer: the next generation. Cell. 2011;144(5):646-74.

[41] Cantor JR, Sabatini DM. Cancer cell metabolism: one hallmark, many faces. Cancer Discov. 2012;2(10):881-98.

[42] Vander Heiden MG. Targeting cancer metabolism: a therapeutic window opens. Nat Rev Drug Discov. 2011;10(9):671-84.

[43] Morandi A, Indraccolo S. Linking metabolic reprogramming to therapy resistance in cancer. Biochim Biophys Acta Rev Cancer. 2017;1868(1):1-6.

[44] Renner K, Singer K, Koehl GE, Geissler EK, Peter K, Siska PJ, et al. Metabolic Hallmarks of Tumor and Immune Cells in the Tumor Microenvironment. Front Immunol. 2017;8:248.

[45] Nguyen-Ngoc KV, Cheung KJ, Brenot A, Shamir ER, Gray RS, Hines WC, et al. ECM microenvironment regulates collective migration and local dissemination in normal and malignant mammary epithelium. Proc Natl Acad Sci U S A. 2012;109(39):E2595-604.

[46] Baibakov BA, Chipisheva TA, Guelstein VI, Ermilova VD, Polevaya EB, Vasiliev JM, et al. Organotypic growth and differentiation of human mammary gland in sponge-gel matrix supported histoculture. In Vitro Cell Dev Biol Anim. 1994;30A(8):490-5.

[47] Yang J, Guzman R, Richards J, Jentoft V, DeVault MR, Wellings SR, et al. Primary culture of human mammary epithelial cells embedded in collagen gels. J Natl Cancer Inst. 1980;65(2):337-43.

[48] Sachs N, de Ligt J, Kopper O, Gogola E, Bounova G, Weeber F, et al. A Living Biobank of Breast Cancer Organoids Captures Disease Heterogeneity. Cell. 2018;172(1-2):373-86 e10.

[49] Boj SF, Hwang CI, Baker LA, Chio, II, Engle DD, Corbo V, et al. Organoid models of human and mouse ductal pancreatic cancer. Cell. 2015;160(1-2):324-38.

[50] Junttila MR, de Sauvage FJ. Influence of tumour micro-environment heterogeneity on therapeutic response. Nature. 2013;501(7467):346-54.

[51] Majety M, Pradel LP, Gies M, Ries CH. Fibroblasts Influence Survival and Therapeutic Response in a 3D Co-Culture Model. PLoS One. 2015;10(6):e0127948.

[52] Hebner C, Weaver VM, Debnath J. Modeling morphogenesis and oncogenesis in three-dimensional breast epithelial cultures. Annu Rev Pathol. 2008;3:313-39.

[53] Sutherland RM. Cell and environment interactions in tumor microregions: the multicell spheroid model. Science. 1988;240(4849):177-84.

[54] Walsh AJ, Cook RS, Sanders ME, Aurisicchio L, Ciliberto G, Arteaga CL, et al. Quantitative optical imaging of primary tumor organoid metabolism predicts drug response in breast cancer. Cancer Res. 2014;74(18):5184-94.

[55] Tentler JJ, Tan AC, Weekes CD, Jimeno A, Leong S, Pitts TM, et al. Patient-derived tumour xenografts as models for oncology drug development. Nat Rev Clin Oncol. 2012;9(6):338-50.

[56] Denk W, Strickler JH, Webb WW. Two-photon laser scanning fluorescence microscopy. Science. 1990;248(4951):73-6.

[57] Helmchen F, Denk W. Deep tissue two-photon microscopy. Nat Methods. 2005;2(12):932-40.

[58] Lakowicz JR. Principles of fluorescence spectroscopy. 2nd ed. New York: Kluwer Academic/Plenum; 1999. xxiii, 698 p. p.

[59] Cahalan MD, Parker I, Wei SH, Miller MJ. Two-photon tissue imaging: seeing the immune system in a fresh light. Nat Rev Immunol. 2002;2(11):872-80.

[60] Berman HM, Westbrook J, Feng Z, Gilliland G, Bhat TN, Weissig H, et al. The Protein Data Bank. Nucleic Acids Res. 2000;28(1):235-42.

[61] Zipfel WR, Williams RM, Christie R, Nikitin AY, Hyman BT, Webb WW. Live tissue intrinsic emission microscopy using multiphoton-excited native fluorescence and second harmonic generation. Proc Natl Acad Sci U S A. 2003;100(12):7075-80.

[62] Chance B, Schoener B, Oshino R, Itshak F, Nakase Y. Oxidation-reduction ratio studies of mitochondria in freeze-trapped samples. NADH and flavoprotein fluorescence signals. J Biol Chem. 1979;254(11):4764-71.

[63] Walsh AJ, Cook RS, Manning HC, Hicks DJ, Lafontant A, Arteaga CL, et al. Optical metabolic imaging identifies glycolytic levels, subtypes, and early-treatment response in breast cancer. Cancer Res. 2013;73(20):6164-74.

[64] Ostrander JH, McMahon CM, Lem S, Millon SR, Brown JQ, Seewaldt VL, et al. Optical redox ratio differentiates breast cancer cell lines based on estrogen receptor status. Cancer Res. 2010;70(11):4759-66.

[65] Warburg O. On the origin of cancer cells. Science. 1956;123(3191):309-14.

[66] Skala MC, Riching KM, Gendron-Fitzpatrick A, Eickhoff J, Eliceiri KW, White JG, et al. In vivo multiphoton microscopy of NADH and FAD redox states, fluorescence lifetimes, and cellular morphology in precancerous epithelia. Proc Natl Acad Sci U S A. 2007;104(49):19494-9.

[67] Alhallak K, Rebello LG, Muldoon TJ, Quinn KP, Rajaram N. Optical redox ratio identifies metastatic potential-dependent changes in breast cancer cell metabolism. Biomed Opt Express. 2016;7(11):4364-74.

[68] Hou J, Wright HJ, Chan N, Tran R, Razorenova OV, Potma EO, et al. Correlating two-photon excited fluorescence imaging of breast cancer cellular redox state with seahorse flux analysis of normalized cellular oxygen consumption. J Biomed Opt. 2016;21(6):60503.

[69] Lakowicz JR, Szmacinski H, Nowaczyk K, Johnson ML. Fluorescence lifetime imaging of free and protein-bound NADH. Proc Natl Acad Sci U S A. 1992;89(4):1271-5.

[70] Becker W. Advanced time-correlated single photon counting techniques. Berlin ; New York: Springer; 2005. xix, 401 p. p.

[71] Maeda-Yorita K, Aki K. Effect of nicotinamide adenine dinucleotide on the oxidation-reduction potentials of lipoamide dehydrogenase from pig heart. J Biochem. 1984;96(3):683-90.

[72] Iweibo I. Protein fluorescence and electronic energy transfer in the determination of molecular dimensions and rotational relaxation times of native and coenzyme-bound horse liver alcohol dehydrogenase. Biochim Biophys Acta. 1976;446(1):192-205.

[73] Bird DK, Yan L, Vrotsos KM, Eliceiri KW, Vaughan EM, Keely PJ, et al. Metabolic mapping of MCF10A human breast cells via multiphoton fluorescence lifetime imaging of the coenzyme NADH. Cancer Res. 2005;65(19):8766-73.

[74] Yu Q, Heikal AA. Two-photon autofluorescence dynamics imaging reveals sensitivity of intracellular NADH concentration and conformation to cell physiology at the single-cell level. J Photochem Photobiol B. 2009;95(1):46-57.

[75] Yaseen MA, Sutin J, Wu W, Fu B, Uhlirova H, Devor A, et al. Fluorescence lifetime microscopy of NADH distinguishes alterations in cerebral metabolism in vivo. Biomed Opt Express. 2017;8(5):2368-85.

[76] Vergen J, Hecht C, Zholudeva LV, Marquardt MM, Hallworth R, Nichols MG. Metabolic imaging using two-photon excited NADH intensity and fluorescence lifetime imaging. Microsc Microanal. 2012;18(4):761-70.

[77] Schneckenburger H, Wagner M, Weber P, Strauss WS, Sailer R. Autofluorescence lifetime imaging of cultivated cells using a UV picosecond laser diode. J Fluoresc. 2004;14(5):649-54.

[78] Ghukasyan VV, Kao FJ. Monitoring Cellular Metabolism with Fluorescence Lifetime of Reduced Nicotinamide Adenine Dinucleotide. J Phys Chem C. 2009;113(27):11532-40.

[79] Evans ND, Gnudi L, Rolinski OJ, Birch DJ, Pickup JC. Glucose-dependent changes in NAD(P)H-related fluorescence lifetime of adipocytes and fibroblasts in vitro: potential for non-invasive glucose sensing in diabetes mellitus. J Photochem Photobiol B. 2005;80(2):122-9.

[80] Wang HW, Wei YH, Guo HW. Reduced nicotinamide adenine dinucleotide (NADH) fluorescence for the detection of cell death. Anticancer Agents Med Chem. 2009;9(9):1012-7.

[81] Stringari C, Nourse JL, Flanagan LA, Gratton E. Phasor fluorescence lifetime microscopy of free and protein-bound NADH reveals neural stem cell differentiation potential. PLoS One. 2012;7(11):e48014.

[82] Walsh A, Cook RS, Rexer B, Arteaga CL, Skala MC. Optical imaging of metabolism in HER2 overexpressing breast cancer cells. Biomed Opt Express. 2012;3(1):75-85.

[83] Guo HW, Chen CT, Wei YH, Lee OK, Gukassyan V, Kao FJ, et al. Reduced nicotinamide adenine dinucleotide fluorescence lifetime separates human mesenchymal stem cells from differentiated progenies. J Biomed Opt. 2008;13(5):050505.

[84] Walsh AJ, Poole KM, Duvall CL, Skala MC. Ex vivo optical metabolic measurements from cultured tissue reflect in vivo tissue status. J Biomed Opt. 2012;17(11):116015.

[85] Cheng S, Cuenca RM, Liu B, Malik BH, Jabbour JM, Maitland KC, et al. Handheld multispectral fluorescence lifetime imaging system for in vivo applications. Biomed Opt Express. 2014;5(3):921-31.

[86] Sun Y, Liu R, Elson DS, Hollars CW, Jo JA, Park J, et al. Simultaneous time- and wavelength-resolved fluorescence spectroscopy for near real-time tissue diagnosis. Opt Lett. 2008;33(6):630-2.

[87] Meier JD, Xie H, Sun Y, Sun Y, Hatami N, Poirier B, et al. Time-resolved laser-induced fluorescence spectroscopy as a diagnostic instrument in head and neck carcinoma. Otolaryngol Head Neck Surg. 2010;142(6):838-44.

[88] Butte PV, Fang Q, Jo JA, Yong WH, Pikul BK, Black KL, et al. Intraoperative delineation of primary brain tumors using time-resolved fluorescence spectroscopy. J Biomed Opt. 2010;15(2):027008.

[89] Dimitrow E, Riemann I, Ehlers A, Koehler MJ, Norgauer J, Elsner P, et al. Spectral fluorescence lifetime detection and selective melanin imaging by multiphoton laser tomography for melanoma diagnosis. Exp Dermatol. 2009;18(6):509-15.

[90] Galletly NP, McGinty J, Dunsby C, Teixeira F, Requejo-Isidro J, Munro I, et al. Fluorescence lifetime imaging distinguishes basal cell carcinoma from surrounding uninvolved skin. Br J Dermatol. 2008;159(1):152-61.

[91] Kennedy GT, Manning HB, Elson DS, Neil MA, Stamp GW, Viellerobe B, et al. A fluorescence lifetime imaging scanning confocal endomicroscope. J Biophotonics. 2010;3(1-2):103-7.

# CHAPTER 3

## Protein-bound NAD(P)H Lifetime is Sensitive to Multiple Fates of Glucose Carbon

Sharick, J.T., Favreau, P.F., Gillette, A.A., Sdao, S.M., Merrins, M.J., Skala, M.C. "Protein-bound NAD(P)H Lifetime is Sensitive to Multiple Fates of Glucose Carbon". *Scientific Reports*, 8(1), 5456. (2018).

### 3.1 Abstract

While NAD(P)H fluorescence lifetime imaging (FLIM) can detect changes in flux through the TCA cycle and electron transport chain (ETC), it remains unclear whether NAD(P)H FLIM is sensitive to other potential fates of glucose. Glucose carbon can be diverted from mitochondria by the pentose phosphate pathway (via glucose 6-phosphate dehydrogenase, G6PDH), lactate production (via lactate dehydrogenase, LDH), and rejection of carbon from the TCA cycle (via pyruvate dehydrogenase kinase, PDK), all of which can be upregulated in cancer cells. Here, we demonstrate that multiphoton NAD(P)H FLIM can be used to quantify the relative concentrations of recombinant LDH and malate dehydrogenase (MDH) in solution. In multiple epithelial cell lines, NAD(P)H FLIM was also sensitive to inhibition of LDH and PDK, as well as the directionality of LDH in cells forced to use pyruvate versus lactate as fuel sources. Among the parameters measurable by FLIM, only the lifetime of protein-bound NAD(P)H ($\tau_2$) was sensitive to these changes, in contrast to the optical redox ratio, mean NAD(P)H lifetime, free NAD(P)H lifetime, or the relative amount of free and protein-bound NAD(P)H. NAD(P)H $\tau_2$ offers the ability to non-invasively quantify diversions of carbon away from the TCA cycle/ETC, which may support mechanisms of drug resistance.

### 3.2 Introduction

Reduced nicotinamide adenine dinucleotide (NADH) is a fluorescent electron donor that

binds to metabolic enzymes in the cytoplasm and mitochondria. The spectral properties of NADH and its phosphorylated form, NADPH, overlap, thus their combined fluorescence is denoted NAD(P)H. NADH has a vital role in glycolysis, the tricarboxylic acid (TCA) cycle, and the electron transport chain (ETC) (1, 2). NADH and NADPH bind at least 334 known proteins in cells (3), including enzymes that are up-regulated in cancer such as lactate dehydrogenase (LDH) (4), pyruvate dehydrogenase (PDH) (5), and glucose 6-phosphate dehydrogenase (G6PDH) (6). Multiphoton fluorescence imaging of NAD(P)H is useful for probing the metabolism of living cells because it is non-damaging and does not require exogenous labeling.

Flavin adenine dinucleotide (FAD) is an electron acceptor in the cell, and is also fluorescent. The optical redox ratio, defined as the fluorescence intensity of NAD(P)H to that of FAD, reflects the redox balance of the cell (8). The optical redox ratio has been used to distinguish cancer subtypes, monitor cancer treatment response, distinguish pre-cancerous cells from normal cells, and detect stem cell differentiation (9-16). Changes in the optical redox ratio to specific metabolic perturbations have been studied as well (9, 16-19). For example, the optical redox ratio is correlated with oxygen consumption, a key metabolic process, in breast cancer cells (18, 19). There are benefits to using a ratiometric measurement versus separate NAD(P)H and FAD intensity measurements. Both noise and spatial variation in excitation light intensity common in both NAD(P)H and FAD intensity are mitigated by using the ratio of the two fluorophores. While powerful, ratiometric intensity-based measurements, such as the optical redox ratio, can be difficult to compare between samples with different optical properties. Additionally, intensity measurements cannot distinguish free from protein-bound NAD(P)H due to their similar absorption and emission spectra.

Fluorescence lifetime imaging microscopy (FLIM) probes an additional dimension of

NAD(P)H activity. The fluorescence lifetime is the time that a fluorophore remains in the excited state before returning to the ground state through photon emission. The fluorescence lifetime is sensitive to changes in the microenvironment of a fluorophore, including molecular conformation, binding, pH, temperature, and the presence of quenchers (20). On average, the fluorescence lifetime of free NAD(P)H is distinctly shorter than that of protein-bound NAD(P)H (represented as $\tau_1$ and $\tau_2$, respectively). This difference is likely due to the degree of motion of the excited nicotinamide ring, which is more restricted when NAD(P)H is enzyme-bound than when it is free (21). Due to these distinct lifetimes, FLIM can quantify the relative fractions of free and protein-bound NAD(P)H in the cell (represented as $\alpha_1$ and $\alpha_2$, respectively, where $\alpha_1 + \alpha_2 = 1$) (22). These parameters are measured by fitting a time-resolved fluorescence decay curve to a two-component exponential decay according to Equation 3.3 (see methods). FLIM of endogenous fluorophores including NAD(P)H has been used to study metabolism in disease pathology and progression (23), to monitor metabolic response to therapy (24, 25), and to distinguish cancerous from normal cells and tissues (9, 11, 26). FLIM of NAD(P)H has been applied to cell culture (9, 27-29), to animal models of disease progression (11, 30, 31), and in pilot studies in human tissues *in vivo* (32) and *ex vivo* (33-35).

Many studies have shown that NAD(P)H FLIM can detect changes in flux through glycolysis, the TCA cycle and ETC (9, 25, 27, 36-41). However, it remains unclear whether NAD(P)H FLIM can be used to detect metabolic alterations at other key enzymatic steps that control the path of carbon from glucose uptake to ETC activity. These carbon-diverting steps include the pentose phosphate pathway (PPP) via G6PDH, lactate production via LDH, and inhibited entry into the TCA cycle via pyruvate dehydrogenase kinase (PDK) (PDK inhibits PDH activity). These pathways can be upregulated in cancer to support tumor progression and drug

resistance (4-6, 42, 43). Additionally, it remains unclear which NAD(P)H FLIM variables are most sensitive to these carbon-diverting steps.

In this study, we tested whether multiphoton NAD(P)H FLIM is sensitive to key enzymatic steps that control the path of carbon from glucose uptake to ETC activity. Experiments in solutions characterized NAD(P)H lifetimes under controlled titrations of two enzymes. To determine whether NAD(P)H lifetime is sensitive to diversions of carbon away from mitochondria, FLIM of NAD(P)H was performed on breast epithelial cells and pancreatic duct epithelial cells treated with metabolic inhibitors. These inhibitors include FX11, which inhibits LDH (44, 45), and dichloroacetate (DCA), which allows carbon to enter the TCA cycle by relieving PDK inhibition on PDH (46). FX11 and DCA are under investigation as cancer therapies because LDH and PDH activities are dysregulated in cancer (4, 42, 44-47). In addition, NAD(P)H FLIM was measured in cells forced to metabolize lactate or pyruvate, thus modulating carbon flux through LDH. Our results indicate that the fluorescence lifetime of protein-bound NAD(P)H is more sensitive to these key enzymatic steps than the NAD(P)H intensity, free NAD(P)H lifetime, or relative amounts of free and protein-bound NAD(P)H.

## 3.3 Results

### 3.3.1 FLIM of NAD(P)H bound to enzymes in solution

Solutions of NAD(P)H and metabolic enzymes were generated to determine whether FLIM could accurately recover relative enzyme concentrations. First, separate solutions of 50 μM NADH and 50 μM NADPH were imaged to determine their free fluorescence lifetime. No difference in lifetime was found between the two species (Fig. 3.1A). Next, solutions of NADH or NADPH with varying concentrations of enzymes, MDH, LDH, and G6PDH, were generated and imaged.

As expected, the fraction of protein-bound NADH, $\alpha_2$, reflected the relative concentration of malate dehydrogenase (MDH) and LDH in solution (Fig. 3.1B-C). NADPH $\alpha_2$ reflected the relative concentration of G6PDH in solution (Fig. 3.1D). The measured value for the lifetime of NADH bound to MDH or LDH ($\tau_2$) was consistent between NADH-to-enzyme ratios ($p>0.05$), with an average lifetime of 1.2 ns or 1.6 ns, respectively (Fig. 3.1E-F). Likewise, the lifetime of NADPH bound to G6PDH ($\tau_2$) did not change between solutions ($p>0.05$), and had an average value of about 2.5 ns (Fig. 3.1G). Appendix A Fig. A.1 shows representative decay curves and the corresponding multi-exponential fits that were used to calculate the NAD(P)H lifetimes. Appendix A Fig. A.2 shows representative images of these solutions, demonstrating their homogeneity.

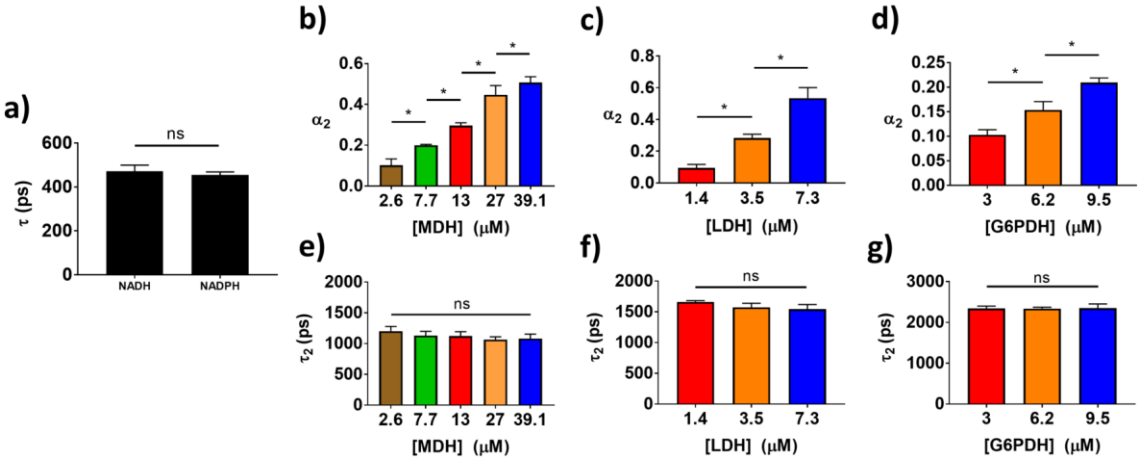


**Figure 3.1. FLIM of NADH bound to metabolic enzymes in solution.** (**a**) Mean and standard deviations of the fluorescence lifetime of 50 μM NADH and 50 μM NADPH from 3-5 experiments. ns = $p>0.05$. (**b-c**) Mean and standard deviations of the fraction of protein-bound NADH, or $\alpha_2$, measured in mixtures of 50 μM NADH with varied concentrations of (**b**) MDH or (**c**) LDH across triplicate experiments. * $p<0.05$. (**d**) Mean and standard deviations of NADPH $\alpha_2$ measured in mixtures of 50 μM NADPH with varied concentrations of G6PDH across triplicate experiments. (**e-g**) Mean and standard deviations of the protein-bound lifetime of NAD(P)H, or $\tau_2$, measured in the same solutions of NADH with MDH (**e**), NADH with LDH (**f**), and NADPH with G6PDH (**g**) across triplicate experiments.

Solutions containing a fixed concentration of 50 μM NADH and both LDH and MDH were generated to determine if FLIM could quantify the relative amounts NADH bound to two different

enzymes. The FLIM-measured proportion of protein-bound NADH attributed to LDH was compared to the actual proportion of LDH added to each mixture (Fig. 3.2). The $R^2$ was 0.95 ($p<0.0001$), indicating a strong correlation between FLIM-measured enzyme proportions and the actual enzyme proportions. Table 3.1 shows the concentrations of enzymes used to generate the mixtures shown in Figure 3.2, along with the proportion of free NADH ($\alpha_{NADH-Free}$, Eq. 3.4) measured in each solution. Examples of the three-exponential fits (Eq. 3.4) that were used to calculate these proportions are shown in Appendix A Fig. A.3.

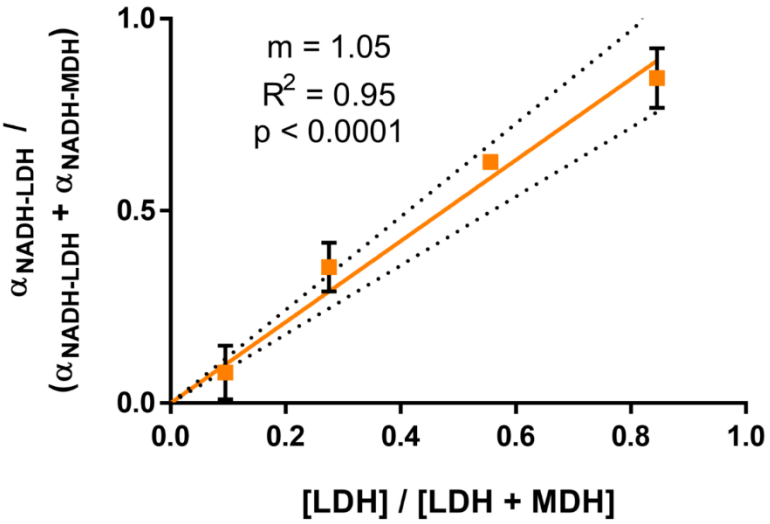


**Figure 3.2. FLIM of NADH quantifies a mixture of enzymes in solution.** The relationship between the relative concentration of LDH in a solution of NADH, LDH, and MDH, and the measured $\alpha_{NADH-LDH}$ value (Eq. 3.4). Error bars represent the standard deviation across triplicate experiments, and the dotted line represents the 95% confidence interval for the regression line. Error bars on one of the points is too small to display (SD = ±0.004). The linear regression is forced through 0,0, and the slope of the line is given as m. [LDH], concentration of LDH in the solution; [LDH+MDH], concentration of LDH plus MDH in the solution. $\alpha_{NADH-LDH}$ and $\alpha_{NADH-MDH}$ from Eq. 3.4.

**Table 3.1. NADH-MDH-LDH solution parameters.**

| | Mixture 1 | Mixture 2 | Mixture 3 | Mixture 4 |
|---|---|---|---|---|
| [LDH] (μM) | 4.9 | 14.2 | 1.4 | 10.0 |
| [MDH] (μM) | 13.0 | 2.6 | 13.0 | 8.0 |
| [LDH]/([LDH]+[MDH]) | 0.27 | 0.85 | 0.10 | 0.56 |
| Total Enzyme (μM) | 17.9 | 16.8 | 14.4 | 18.0 |
| Measured $\boldsymbol{\alpha_{NADH-Free}}$ (%) | 60.5 | 48.0 | 68.9 | 42.6 |

3.3.2 Effects of inhibitors on cell enzyme activities

Standard measures of enzyme activity after FX11 treatment confirmed a significant decrease in LDH activity ($p<0.05$, Fig. 3.3A), while DCA treatment caused a significant increase in PDH activity ($p<0.005$, Fig. 3.3A) compared to control in MCF10A breast epithelial cells. In HPDE6 pancreatic duct epithelial cells, FX11 had no effect on LDH activity (Fig. 3.3B), while DCA caused a significant increase in PDH activity ($p<0.05$, Fig. 3.3B). The absolute activity rates of LDH and PDH are shown in Appendix A Fig. A.4. The absolute activity of LDH at baseline was over one order of magnitude higher than PDH in both MCF10A and HPDE6 cells. Appendix A Fig. A.5 gives examples of the time-dependent enzyme reaction that was used to calculate the enzyme activity rates. The established mechanisms and targets of these metabolic inhibitors are diagrammed in Figure 3.4.

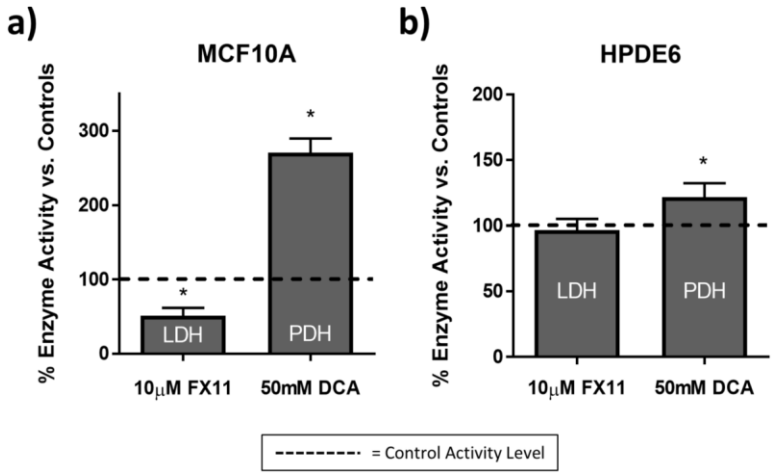


**Figure 3.3. Relative activities of LDH and PDH with FX11 and DCA treatment in cells.** Mean and standard deviations of the percent change in LDH and PDH activity after 48 hours of FX11 or 48 hours of DCA treatment, respectively in MCF10A cells (**a**) and HPDE6 cells (**b**) vs. vehicle. Dashed line represents enzyme activity level in vehicle-treated cells. * $p<0.05$ vs. control. n = 3-5 experiments.

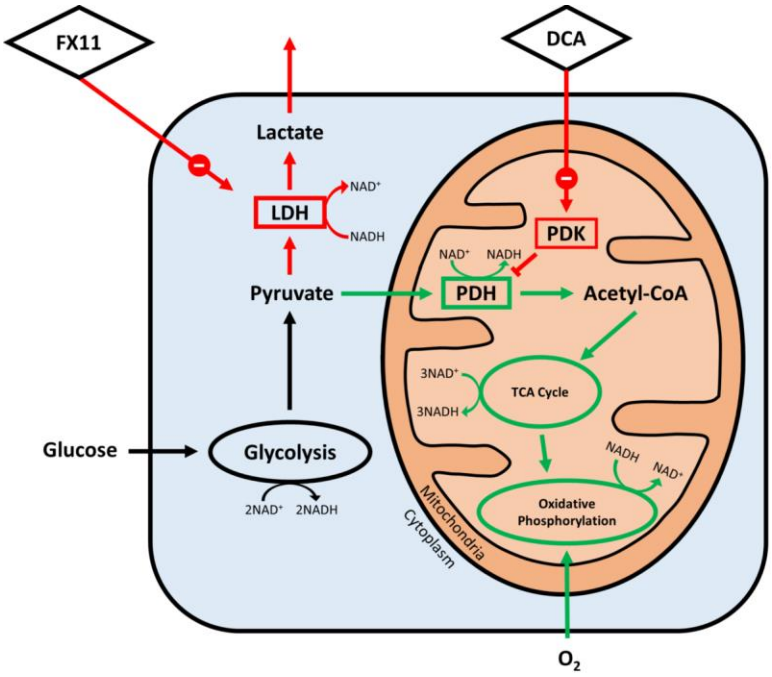


**Figure 3.4. Metabolic diagram of enzyme inhibition with DCA and FX11 treatment.** Summary of cellular metabolic pathways investigated using metabolic inhibitors DCA and FX11 (diamonds). Red arrows indicate a decrease in activity, while green arrows indicate an increase, and black arrows indicate no change. Enzymes are shown in boxes, enzyme-containing pathways such as glycolysis and oxidative phosphorylation are circled, while enzyme products and substrates are unboxed. Both FX11 and DCA result in an overall increase in oxygen consumption, but by acting on different enzymes. DCA inhibits PDK to increase the activity of PDH, allowing pyruvate to enter the mitochondria and fuel oxidative phosphorylation. FX11 has a similar effect, but acts by inhibiting the ability of LDH to convert pyruvate into lactate.

### 3.3.3 Optical redox ratio in cells with enzyme inhibitors

Multiphoton FLIM visualizes autofluorescence changes on an individual cell level in MCF10A cells (Fig. 3.5A,B). No changes in cell morphology were noted with drug treatment. Both FX11 and DCA significantly ($p<0.05$) decreased the optical redox ratio in MCF10A cells compared to control (Fig. 3.5C,D). The fluorescence intensities of NAD(P)H (Fig. 3.5E,F) and FAD (Fig. 3.5G,H) alone do not significantly change with treatment in MCF10A cells except for an increase in FAD intensity with FX11 treatment ($p<0.05$).

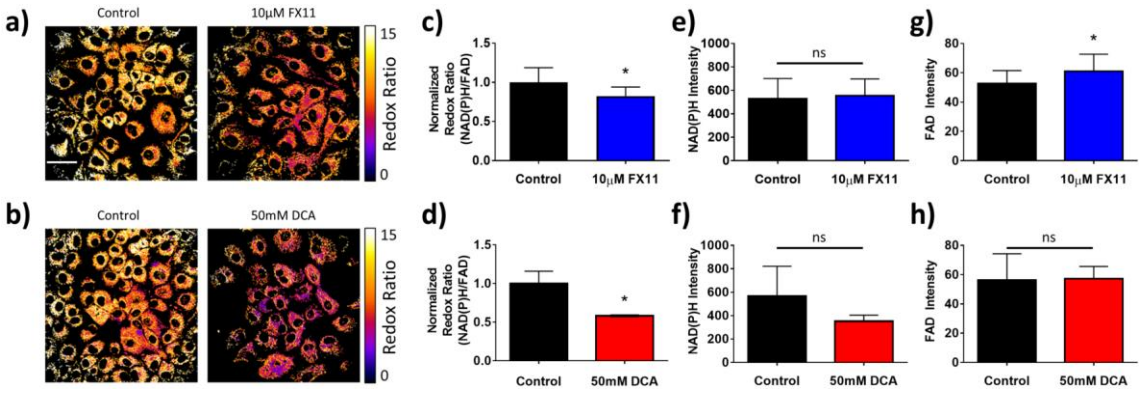


**Figure 3.5. Effects of FX11 and DCA on the optical redox ratio in MCF10A cells.** (**a-c**) Representative images of MCF10A cells after 48 hours of 10 μM FX11 (**a**) and 48 hours of 50mM DCA (**b**) treatment vs. vehicle, color-coded for the redox ratio. Scale bar = 50 μm. (**c-d**) Mean and standard deviations of the normalized redox ratio in MCF10A cells after 48 hours of 10 μM FX11 (**c**) and 48 hours of 50 mM DCA (**d**) treatment vs. vehicle. * $p<0.05$ vs. control. n = 3 experiments. (**e-f**) Mean and standard deviations of NAD(P)H fluorescence intensity in MCF10A cells after 48 hours of 10 μM FX11 (**e**) and 48 hours of 50 mM DCA (**f**) treatment vs. vehicle. ns = $p>0.05$ vs. control. n = 3 experiments. (**g-h**) Mean and standard deviations of FAD fluorescence intensity in MCF10A cells after 48 hours of 10 μM FX11 (**g**) and 48 hours of 50 mM DCA (**h**) treatment vs. vehicle. n = 3 experiments.

No changes in cell morphology were noted with drug treatment in HPDE6 cells (Fig. 3.6A,B). Additionally, neither FX11 nor DCA caused significant changes to the optical redox ratio (Fig. 3.6C,D), NAD(P)H fluorescence intensity (Fig. 3.6E,F), or FAD intensity (Fig. 3.6G,H) in HPDE6 cells.

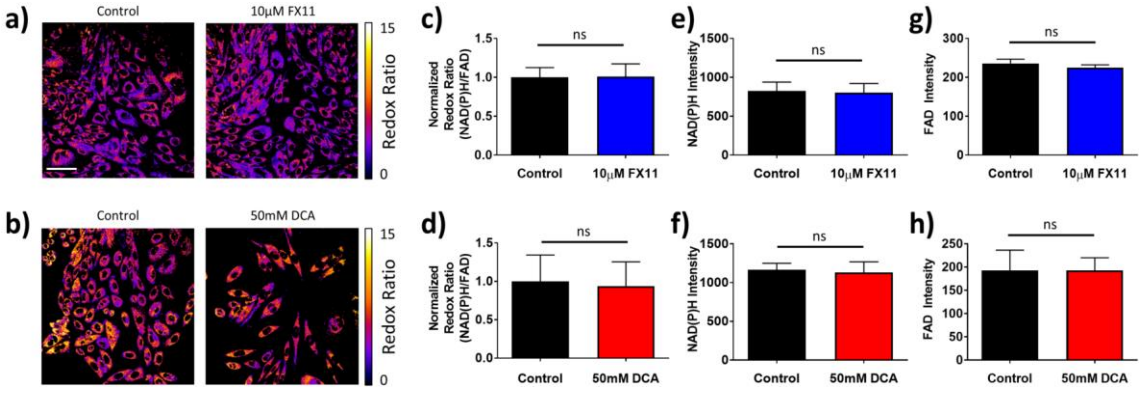


**Figure 3.6. Effects of FX11 and DCA on the optical redox ratio in HPDE6 cells.** (**a-b**) Representative images of HPDE6 cells after 48 hours of 10 μM FX11 (**a**) and 48 hours of 50 mM DCA (**b**) treatment vs. vehicle, color-coded for the redox ratio. Scale bar = 50 μm. (**c-d**) Mean and standard deviations of the normalized redox ratio in HPDE6 cells after 48 hours of 10 μM FX11 (**c**) and 48 hours of 50 mM DCA (**d**) treatment vs. vehicle. ns = $p>0.05$ vs. control. n = 3

experiments. (**e-f**) Mean and standard deviations of NAD(P)H fluorescence intensity in HPDE6 cells after 48 hours of 10 μM FX11 (**e**) and 48 hours of 50 mM DCA (**f**) treatment vs. vehicle. n = 3 experiments. (**g-h**) Mean and standard deviations of FAD fluorescence intensity in HPDE6 cells after 48 hours of 10 μM FX11 (**g**) and 48 hours of 50 mM DCA (**h**) treatment vs. vehicle. n = 3 experiments.

3.3.4 NAD(P)H fluorescence lifetime in cells with enzyme inhibitors

FX11 treatment significantly decreased NAD(P)H $\tau_2$ in MCF10A cells ($p<0.0001$, Fig. 3.7A,B). Conversely, DCA treatment significantly increased NAD(P)H $\tau_2$ ($p<0.01$, Fig. 3.7C,D). FX11 treatment did not have a significant effect on NAD(P)H $\tau_2$ in HPDE6 cells (Fig. 3.8A,B). DCA treatment significantly increased NAD(P)H $\tau_2$ in HPDE6 cells ($p<0.05$, Fig. 3.8C,D).

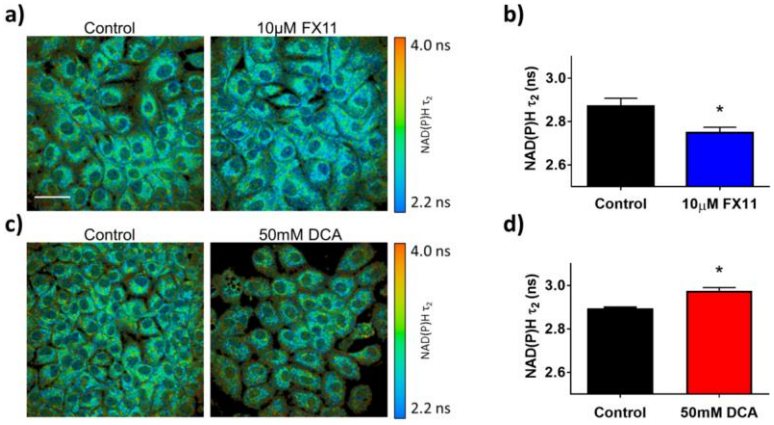


**Figure 3.7. Effects of FX11 and DCA on the fluorescence lifetime of protein-bound NAD(P)H in MCF10A cells.** (**a**) Representative images of MCF10A cells after 48 hours of 10 μM FX11 treatment vs. vehicle, color-coded for NAD(P)H $\tau_2$. Scale bar = 50 μm. (**b**) Mean and standard deviations of NAD(P)H $\tau_2$ in MCF10A cells after 48 hours of 10 μM FX11 treatment vs. vehicle. * $p<0.05$ vs. control. n = 3 experiments. (**c**) Representative images of MCF10A cells after 48 hours of 50 mM DCA treatment vs. vehicle color-coded for NAD(P)H $\tau_2$. (**d**) Mean and standard deviations of NAD(P)H $\tau_2$ in MCF10A cells after 48 hours of 50 mM DCA treatment vs. vehicle. n = 3 experiments.

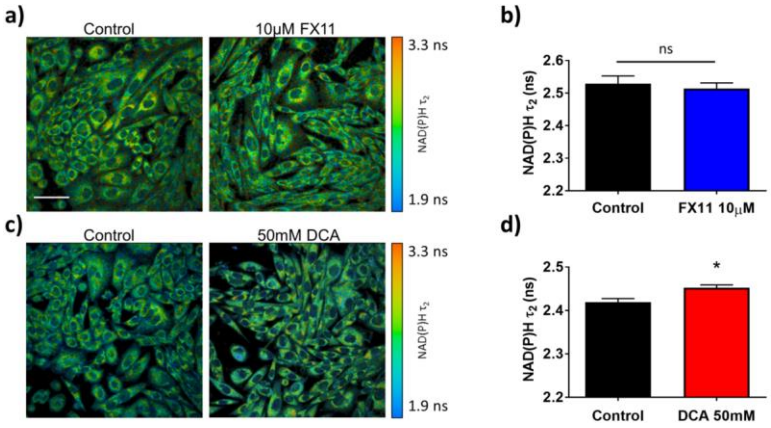


**Figure 3.8. Effects of FX11 and DCA on the fluorescence lifetime of protein-bound NAD(P)H in HPDE6 cells.** (**a**) Representative images of HPDE6 cells after 48 hours of 10 μM FX11 treatment vs. vehicle, color-coded for NAD(P)H $\tau_2$. Scale bar = 50 μm. (**b**) Mean and standard deviations of NAD(P)H $\tau_2$ in HPDE6 cells after 48 hours of 10 μM FX11 treatment vs. vehicle. * $p<0.05$ vs. control. n = 4 experiments. (**c**) Representative images of HPDE6 cells after 48 hours of 50 mM DCA treatment vs. vehicle color-coded for NAD(P)H $\tau_2$. (**d**) Mean and standard deviations of NAD(P)H $\tau_2$ in HPDE6 cells after 48 hours of 50 mM DCA treatment vs. vehicle. n = 4 experiments.

The effects of these inhibitors on the additional NAD(P)H lifetime parameters, $\alpha_1$, $\tau_1$, or $\tau_m$, were analyzed. Neither inhibitor had a significant effect on NAD(P)H $\alpha_1$, $\tau_1$, or $\tau_m$ in MCF10A cells (Fig. 3.9A,B). Most of these lifetime parameters did not change with inhibitor treatment in HPDE6 cells, other than a significant decrease in the proportion of free NAD(P)H and a significant increase in NAD(P)H $\tau_m$ with DCA treatment (Fig. 3.9C-D). Unlike NAD(P)H $\tau_2$, these additional NAD(P)H lifetime parameters do not consistently reflect changes in enzyme activity across both cell types and inhibitors. Representative decay curves and the corresponding multi-exponential fits that were used to calculate these NAD(P)H lifetime parameters are in Appendix A Fig. A.6.

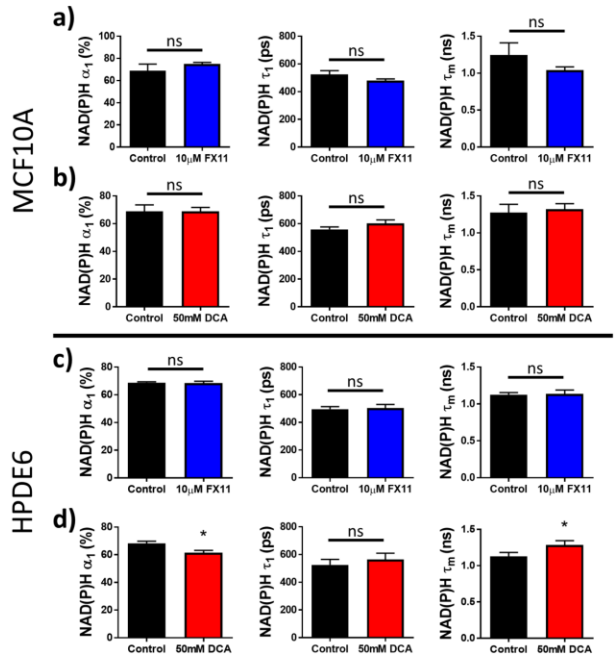


**Figure 3.9. Sensitivity of additional NAD(P)H fluorescence lifetime components to FX11 and DCA treatment in cells.** (**a**) Mean and standard deviations of NAD(P)H $\alpha_1$, $\tau_1$, and $\tau_m$ in MCF10A cells after 48 hours of 10 μM FX11 treatment vs. vehicle. (**b**) Mean and standard deviations of NAD(P)H $\alpha_1$, $\tau_1$, and $\tau_m$ in MCF10A cells after 48 hours of 50 mM DCA treatment vs. vehicle. (**c**) Mean and standard deviations of NAD(P)H $\alpha_1$, $\tau_1$, and $\tau_m$ in HPDE6 cells after 48 hours of 10 μM FX11 treatment vs. vehicle. (**d**) Mean and standard deviations of NAD(P)H $\alpha_1$, $\tau_1$, and $\tau_m$ in HPDE6 cells after 48 hours of 50 mM DCA treatment vs. vehicle. n = 3-4 experiments each.

3.3.5 Autofluorescence in cells with varying fuel sources

Like enzyme inhibitors, the fuel source available to the cell also alters carbon flux. Therefore, the effect of fuel source on autofluorescence in MCF10A cells was tested to complement the above enzyme inhibitor experiments. Specifically, the diversion of carbon from mitochondria can be modulated by forcing starved cells to use lactate versus pyruvate as a primary fuel source (Fig. 3.4). NAD(P)H $\tau_2$ increased significantly after MCF10A cells were supplied with an excess of pyruvate ($p<0.05$, Fig. 3.10A), while the optical redox ratio, NAD(P)H fluorescence intensity, $\alpha_1$, $\tau_1$, and $\tau_m$ did not change (Fig. 3.10B-F). When the cells were supplied with excess lactate, NAD(P)H $\tau_2$ decreased ($p<0.05$, Fig. 3.10G), while the optical redox ratio and NAD(P)H $\tau_m$ remained unchanged (Fig. 3.10H, L). The NAD(P)H fluorescence intensity and $\alpha_1$ decreased

slightly with lactate ($p<0.05$, Fig. 3.10I-J), while $\tau_1$ increased ($p<0.05$, Fig. 3.10K). NAD(P)H $\tau_2$ more robustly distinguishes the use of pyruvate or lactate as fuel sources in cells than the optical redox ratio, NAD(P)H $\tau_1$, $\alpha_1, \tau_m$ or intensity. Representative decay curves and the corresponding multi-exponential fits that were used to calculate these NAD(P)H lifetime parameters can be found in Appendix A Fig. A.7.

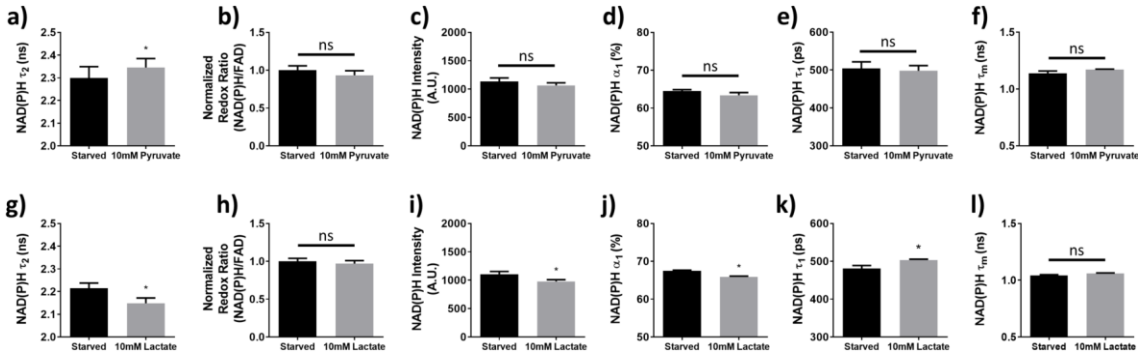


**Figure 3.10. NAD(P)H $\tau_2$ is sensitive to cellular fuel source.** (**a-f**) Mean and standard deviations of NAD(P)H $\tau_2$ (**a**), optical redox ratio (**b**), NAD(P)H intensity (**c**), NAD(P)H $\alpha_1$ (**d**), NAD(P)H $\tau_1$ (**e**), and NAD(P)H $\tau_m$ (**f**) of fuel-starved MCF10A cells before and after addition of 10mM sodium pyruvate. (**g-l**) Mean and standard deviations of NAD(P)H $\tau_2$ (**g**), optical redox ratio (**h**), NAD(P)H intensity (**i**), NAD(P)H $\alpha_1$ (**j**), NAD(P)H $\tau_1$ (**k**), and NAD(P)H $\tau_m$ (**l**) of fuel-starved MCF10A cells before and after addition of 10mM sodium lactate. ns = $p>0.05$ vs. control. * $p<0.05$ vs. control. n = 3 experiments each.

### 3.4 Discussion

FLIM of NAD(P)H can non-destructively measure changes in cellular metabolism, but these changes are difficult to interpret. In this study, we used NAD(P)H-enzyme solutions, metabolic inhibitors in cells, and alternate fuel sources for cells to determine if NAD(P)H FLIM is sensitive to key enzymatic steps that control the path of carbon from glucose uptake to ETC activity. This information will aid in the interpretation of changes in NAD(P)H lifetimes.

The measured lifetimes of NADH bound to LDH and MDH in solution were distinct from each other (Fig. 3.1) and only slightly different than previously reported values (22, 36). Deviations from previous values are likely due to differences in buffer conditions, different

fluorescence emission filter wavelengths, different numbers of exponential decays used for fitting, or differences in temporal resolution between previous single-point lifetime measurements and our FLIM measurements. Previous studies show that LDH and MDH have distinct effects on the fluorescence spectrum of NADH, which suggests unique molecular conformations and/or environments (48). We also found that the fluorescence lifetime of NADPH bound to the NADPH-dependent enzyme G6PDH was independent of enzyme concentration, and was distinct from the lifetimes of NADH bound to MDH or LDH. This agrees with the previous report that FLIM can be used to distinguish protein-bound NADH from protein-bound NADPH (49). The consistent protein-bound NADH lifetime across enzyme concentration within a single-enzyme solution (Fig. 3.1F-H) was expected because fluorescence lifetimes are independent of the fluorophore concentration (20, 50). Small differences in protein-bound NAD(P)H lifetime between enzyme concentrations within a single enzyme solution are likely due to time-correlated single photon counting (TCSPC) noise and fitting error (51). MDH, LDH, and G6PDH were chosen for this study because they are readily available in isolated form, can be dissolved *in vitro* in the same buffers as NADH, and have well-characterized binding affinities for NADH (52-54). Additionally, these experiments tested whether an enzyme in the TCA cycle (MDH) could be distinguished from key enzymes that modify the flow of carbon into the TCA cycle (LDH and G6PDH).

This is the first study to demonstrate that NAD(P)H $\tau_2$ can distinguish NADH bound to two different metabolic enzymes in a single solution, and thus quantify changes in the relative activities of two enzymes. We found a strong linear correlation between the relative amounts of LDH and MDH added to a solution of NADH, and the measured values of $\alpha_{NADH-LDH}$ and $\alpha_{NADH-MDH}$ (Fig. 3.2). Without further characterization, we cannot obtain the absolute ratio of NADH molecules bound to LDH vs. MDH using FLIM, but these results do indicate that $\alpha$ values

were sensitive to changes in this ratio. While it is doubtful that FLIM can distinguish all 334 known binding partners of NAD(P)H in cells (3), the summation of protein-bound NAD(P)H lifetimes within distinct metabolic pathways may differ. Thus, changes in protein-bound NAD(P)H lifetimes could be related back to groups of metabolic reactions, including those that divert carbon away from the mitochondria.

Decreases in the optical redox ratio with both DCA and FX11 treatment in MCF10A cells (Fig. 3.5) agree with previous reports that these inhibitors increase oxygen consumption in other cell types (18, 19, 44, 45). However, the redox ratio did not distinguish the different mechanisms of DCA and FX11 treatment in MCF10A cells. FX11 has been shown to increase the $NADH/NAD^+$ ratio in human lymphoma cells (44), but an increase in NAD(P)H intensity was not observed in our studies. An increase in the $NADH/NAD^+$ ratio does not necessarily result in a significant increase in NAD(P)H fluorescence intensity, because the total NAD pool may have decreased following FX11 treatment. Additionally, the effects of FX11 on NAD(P)H levels in MCF10A and HPDE6 cells have not been previously reported, and could differ from the effects on lymphoma cells. FX11 has also been shown to reduce the mitochondrial membrane potential of lymphoma cells (44), which could affect NAD(P)H FLIM values (20).

There was no change in the optical redox ratio for FX11 treatment in HPDE6 cells (Fig. 3.6C), which agrees with independent measurements of sustained LDH activity with FX11 treatment in HPDE6 cells (Fig. 3.3B). However, there was no change in the optical redox ratio with DCA treatment (Fig. 3.6D), which does not agree with independent measurements of significant changes in PDH activity with DCA treatment in HPDE6 cells (Fig. 3.3B). Like the MCF10A results, the insensitivity of the optical redox ratio to DCA treatment in HPDE6 cells suggests that the optical redox ratio is not robustly sensitive to changes in the activity of enzymes

such as PDH and LDH, which control the path of carbon from glucose uptake to the TCA cycle. The optical redox ratio is affected by changes in the concentrations of NAD(P)H and FAD, and by changes in the lifetimes of NAD(P)H and FAD (due to differences in quantum yield (20, 21, 55)).

Unlike the optical redox ratio, NAD(P)H $\tau_2$ distinguished between DCA and FX11 treatment in MCF10A cells (Fig. 3.7). This was expected because these inhibitors altered the activity of two different NADH-binding enzymes that influence the fate of cellular carbon (PDH and LDH) (Fig. 3.3A). We speculate that FX11 decreased $\tau_2$ because the lifetime of NADH bound to LDH is longer than the overall NAD(P)H $\tau_2$ (FX11 inhibits NADH-LDH binding). Similarly, we speculate that DCA increased $\tau_2$ because the lifetime of NAD(P)H bound to PDH is much longer than the overall NAD(P)H $\tau_2$ (DCA activates NADH-PDH binding). However, future work is needed to interpret the direction of these changes. While NADH bound to LDH in solution was found to have a much shorter lifetime (~1.6 ns, Fig. 3.1G) than cellular NAD(P)H $\tau_2$ (~2.4-2.9 ns, Figs. 3.7B,D & 3.8B,D), it is likely that the molecular environment of the cell cytoplasm ($pO_2$, pH, viscosity) significantly alters the lifetime of NADH bound to LDH (20). LDH inhibition and PDH activation cause opposite changes in NAD(P)H $\tau_2$, but both promote downstream TCA cycle and ETC activation. This suggests that the change in $\tau_2$ is due to distinct shifts in the activities of NAD(P)H-binding enzymes that control the flow of carbon to the TCA cycle, in addition to downstream activation of the TCA cycle and ETC.

FX11 and DCA treatment in HPDE6 cells provide further evidence that NAD(P)H $\tau_2$ is sensitive to changes in the activities NAD(P)H-binding enzymes that control the fate of carbon (Fig. 3.8). FX11 did not affect the activity of its target enzyme, LDH (Fig. 3.3B). There was also no change in NAD(P)H $\tau_2$ in HPDE6 cells treated with FX11 (Fig. 3.8B), which provides a negative control consistent with no change in LDH activity (Fig. 3.3B). Furthermore, DCA

increased PDH activity (Fig. 3.3), and caused a significant increase in NAD(P)H $\tau_2$ in both cell types (Figs. 3.7D & 3.8D). Other components of the NAD(P)H fluorescence lifetime (NAD(P)H intensity, $\alpha_1$, $\tau_1$, and $\tau_m$) were not consistently sensitive to changes in metabolic enzyme activities caused by inhibitors across both cell types (Fig. 3.9). This suggests that NAD(P)H $\tau_2$ is more sensitive to the NADH-binding activity of LDH and PDH than other NAD(P)H fluorescence intensity and lifetime parameters.

Finally, we tested whether NAD(P)H $\tau_2$ is sensitive to the fuel source of the cell. Like the enzyme inhibitor experiments, feeding starved cells pyruvate versus lactate can also alter the flow of cellular carbon into the mitochondria. For example, LDH is more active with lactate versus pyruvate as a fuel source because LDH must convert lactate to pyruvate. The protein-bound lifetime of NAD(P)H increased when starved cells were given pyruvate, but decreased when starved cells were given lactate (Fig. 3.10). Note that the baseline conditions for the enzyme inhibitor experiments (non-starved cells) are different from these fuel source experiments (starved cells). Thus, changes in enzyme activities in the two conditions are not directly comparable. For example, adding lactate to starved cells would not reduce glycolysis because glycolysis is already at a minimum. All other autofluorescence measurements including the optical redox ratio and NAD(P)H $\tau_m$ either showed no change with lactate or pyruvate as a fuel source, or only changed with lactate. Further work is needed to interpret changes in NAD(P)H $\alpha_1$, $\tau_1$ and intensity with lactate, but could be due to changes in quenchers such as $H^+$ and $pO_2$ (20). While NAD(P)H $\tau_1$ increased significantly with the addition of lactate, the relatively small magnitude of the change combined with a significant decrease in its fractional contribution ($\alpha_1$) to the overall fluorescence signal resulted in a non-significant increase in NAD(P)H $\tau_m$. Overall, Fig. 3.10 supports the conclusion that NAD(P)H $\tau_2$ is more sensitive to enzymes that control the flow of carbon into the

mitochondria, compared to other NAD(P)H fluorescence intensity and lifetime parameters. Forcing starved cells to use lactate versus pyruvate as fuel caused opposite changes in NAD(P)H $\tau_2$, like LDH inhibition and PDH activation. This is further evidence that changes in $\tau_2$ are not simply due to downstream TCA cycle and ETC activation.

There are additional methods to analyze TCSPC FLIM data, such as phasor analysis (56). For this study, we chose to fit our fluorescence decay data to the sum of exponentials. There are limitations to this method, such as the selection of the number of fit components and computational time. While the fit-free phasor approach eliminates the need for *a priori* knowledge of the number of lifetime components and simplifies FLIM analysis, we were specifically interested in measuring small changes in NAD(P)H $\tau_2$, which is not easily quantified from phasor plots of TCSPC data.

This study demonstrates that the fluorescence lifetime of protein-bound NAD(P)H is sensitive to alternative fates of glucose carbon before entry into the TCA cycle. While the optical redox ratio, mean NAD(P)H lifetime, free NAD(P)H lifetime, or relative amounts of free and protein-bound NAD(P)H can provide valuable information on changes in metabolic cofactors in the cell, NAD(P)H $\tau_2$ is most useful to quantify changes in the activity of enzymes that control the path of carbon into the TCA cycle. This is likely because NAD(P)H has unique lifetimes when bound to different enzymes (22, 36, 50) (Fig. 3.1). The results of this study confirm that a shift in the fluorescence lifetime of NAD(P)H cannot simply be interpreted as a change in glycolysis or oxidative phosphorylation rate, because pathways that control other fates of carbon must also be incorporated.

Currently, photon counts and acquisition time limits the discrimination of multiple protein-bound lifetimes, and thus most analysis of NAD(P)H lifetime in cells is performed using a two-exponential decay. More efficient photon collection methods are under development (51) that will

enable higher-order exponential fits. Future work is also required to further interpret changes in protein-bound NAD(P)H lifetimes in cells. Overall, a better understanding of NAD(P)H FLIM signals enables unique, non-destructive insights into cellular metabolism.

## 3.5 Materials and methods

### 3.5.1 Fluorescence lifetime imaging

Fluorescence intensity and lifetime images were acquired using a custom-built multiphoton fluorescence lifetime system (Bruker Fluorescence Microscopy, Middleton, WI), with a 40x oil-immersion objective (1.3 NA, Nikon, Tokyo, Japan) and an inverted microscope using epifluorescence illumination (TiE, Nikon). A titanium:sapphire laser (Chameleon Ultra II, Coherent, Santa Clara, CA) was tuned to 750 nm for two-photon excitation of NAD(P)H and tuned to 890 nm for two-photon excitation of FAD. A 440/80nm bandpass filter was used to collect NAD(P)H fluorescence emission, and a 550/100nm filter was used to collect FAD emission. A pixel dwell time of 4.8 μs collected 256x256 pixel images over a 270 μm x 270 μm field of view, with a total integration time of 60 seconds for cells and 120 seconds for solutions. A GaAsP PMT (H7422P-40, Hamamatsu Photonics, Hamamatsu, Japan) detected emitted photons. TCSPC electronics (SPC-150, Becker & Hickl, Berlin, Germany) were used to acquire fluorescence decay curves with 256 time bins. The second harmonic generated signal from urea crystals at 900 nm excitation was used to measure the instrument response function, which had a full width at half maximum of 220 ps. A fluorescent bead (Polysciences Inc., Warrington, PA) was imaged daily as a fluorescence lifetime validation. The single-component lifetime of the bead was stable (2.13 ± 0.03 ns, n=16), and consistent with published values (11, 24, 27, 30).

3.5.2 Enzyme solutions

Tris-buffered saline (di$H_20$, 50mM Tris, 150mM NaCl) at pH 7.6 and 21°C was used as the solvent for all solutions. LDH from porcine heart (#L7525, Sigma) or MDH from porcine heart (#M1567, Sigma) were mixed with 50 μM NADH (#43420, Sigma) to generate solutions with distinct free-to-bound ratios of NADH. G6PDH from *S. cerevisiae* (#G6378, Sigma) was mixed with 50 μM NADPH (#N7505) in a similar manner. Previous reports indicate that self-quenching of NADH occurs above 250 mg/L (~ 375 μM) (57) in Tris buffer. In our solution studies, 50 μM was used to minimize self-quenching. Desired concentrations of enzyme were calculated using the following equation to generate solutions with a range of free-to-bound NAD(P)H ratios:

$$[\text{Enzyme}] = \frac{[NAD(P)H] - (\alpha_1)}{F * S} \tag{3.1}$$

Here, $\alpha_1$ represents the desired fraction of unbound NAD(P)H, *S* represents the integer number of binding sites per enzyme molecule, and *F* is the fraction of enzyme binding sites to be occupied, calculated using the following equation:

$$F = \frac{\alpha_1 * [NAD(P)H]}{\alpha_1 * [NAD(P)H] + K_D} \tag{3.2}$$

Published values for the dissociation constants ($K_D$) of NAD(P)H to LDH, MDH, and G6PDH were used for these calculations, in addition to the number of NADH binding sites per enzyme (52-54, 58, 59). Solutions of only 50 μM NADH or NADPH were also imaged. Four mixtures of 50 μM NADH with both LDH and MDH were generated with varying amounts of the two enzymes as described in Table 3.1. Enzyme concentrations in this experiment were chosen that gave a wide range of LDH to MDH ratios. Following mixing, a 100 μl droplet of each solution was placed in a separate 35 mm glass-bottom imaging dish, and a glass coverslip was placed over each droplet to reduce evaporation. Solutions were imaged at room temperature.

3.5.3 Enzyme solution image analysis

A histogram of photon counts per temporal bin, or decay curve, was constructed for each image by binning all pixels together to increase photon counts for improved fitting accuracy (SNR >3000). This decay curve was deconvolved with the instrument response function using SPCImage. For solutions with one enzyme, decay curves were fit to a two-component exponential decay according to Equation 3.3, where $I(t)$ represents the fluorescence intensity measured at time t after the laser pulse, and C represents a constant level of background light (20, 60).

$$I(t) = \alpha_1 exp^{-t/\tau_1} + \alpha_2 exp^{-t/\tau_2} + C \quad (3.3)$$

A two-exponential model was chosen because the chi-squared goodness of fit value did not improve for a three-exponential model versus a two-exponential model. $\tau_1$ was fixed at 450 ps, the measured lifetime value of a pure NADH solution. For solutions with two enzymes, Equation 3.4 was used to fit decay curves to a three-exponential decay, with $\tau_1$ fixed at 450 ps (to represent free NADH), $\tau_2$ fixed at 1.2 ns (to represent NADH bound to MDH, or NADH-MDH) and $\tau_3$ was fixed at 1.6 ns (to represent NADH bound to LDH, or NADH-LDH).

$$I(t) = \alpha_{NADH-Free} exp^{-t/450\,ps} + \alpha_{NADH-MDH} exp^{-t/1.2ns} + \alpha_{NADH-LDH} exp^{-t/1.6ns} + C \quad (3.4)$$

The lifetime values of NADH used in our three-component fit (Eq. 3.4) were fixed based on our previous measurements in individual NADH-enzyme solutions (Fig. 3.1). Fixing these values reduces free fitting parameters and significantly improves the accuracy of their relative contributions (51). The relationship between actual [LDH] / [LDH + MDH] and measured $\alpha_{NADH-LDH}$ / ($\alpha_{NADH-LDH}$ + $\alpha_{NADH-MDH}$) was calculated with a regression line with y-intercept fixed at 0. A 95% confidence interval for this line was calculated, along with its coefficient of determination and p-value.

3.5.4 Cell culture, metabolic inhibition, and imaging

The MCF10A noncancerous mammary epithelial cell line (36 y.o. Caucasian female) was obtained from the American Type Culture Collection (#CRL-10317, Mannasas, VA) and grown in DMEM/F-12 (#11330, Gibco, Gaithersburg, MD) supplemented with 5% horse serum (#16050, Gibco), 20 ng/mL EGF (#AF-100-15, Peprotech, Rock Hill, NJ), 0.5 μg/mL hydrocortisone (#H0888, Sigma, St. Louis, MO), 100 ng/mL cholera toxin (#C8052, Sigma), 10 μg/mL insulin (#I1882, Sigma), and 1% penicillin/streptomycin (#15070, Gibco). The HPDE6 human pancreatic duct epithelial cells were obtained from ABM (#T0005, Richmond, BC, Canada) and grown in DMEM (#11965, Gibco) supplemented with 10% fetal bovine serum (#TMS-013-B, EMD Millipore) and 1% penicillin/streptomycin. For imaging, $1x10^5$ cells were seeded 24 hours prior to drug treatment in 35mm glass-bottom dishes (#P35G-1.5-14-C, MatTek Corp, Ashland, MA). After 24 hours, media was replaced with either standard media, media with DMSO vehicle (#D8418, Sigma), media with 10 μM FX11 (#427218, EMD Millipore, Billerica, MA) in 1% DMSO, or media with 50 mM DCA (#347795, Sigma). All cell culture media formulations contained glucose and glutamine. 48 hours after this treatment for FX11 and DCA, cells were imaged at 3-4 different locations in each dish for a total of 100-550 cells imaged per treatment group. NAD(P)H images were first acquired, followed immediately by an FAD image of the same field of view. All imaging experiments were performed after cells equilibrated to room temperature. To ensure cell viability and minimize time spent outside of the cell incubator, experiments were kept brief (<20 minutes). Cell viability was also confirmed following imaging. All cell metabolic inhibitor experiments were repeated in triplicate.

3.5.5 Enzyme activity assays

LDH (#MAK066) and PDH (#MAK183) Activity Assay Kits (Sigma) were used to quantify enzyme activities in MCF10A and HPDE6 cells. Enzymes were isolated from $1x10^6$ cells for each activity assay. Enzyme activity levels are reported in milliUnits, which corresponds to nanomoles of reaction product generated per minute. All enzyme activity experiments were repeated 3-5 times.

3.5.6 Cellular image analysis

NAD(P)H fluorescence lifetime images of cells were analyzed similarly to images of NADH-enzyme solutions using SPCImage software (Becker & Hickl). Binning of only 3x3 pixels was used to preserve spatial resolution (SNR >15). Equation 3.3 was used to extract the free and protein-bound configurations of NAD(P)H from decay curves. The lifetime of free NAD(P)H was not fixed in this analysis due to the heterogeneity of the intracellular environment in terms of pH, $O_2$, and viscosity. Again, a two-exponential model was chosen because the chi-squared goodness of fit value did not improve for a three-exponential model versus a two-exponential model. NAD(P)H $\tau_m$ is calculated by taking a weighted average of the free and protein-bound lifetimes:

$$\tau_m = \alpha_1 * \tau_1 + \alpha_2 * \tau_1 \quad (3.5)$$

An automated cell segmentation routine was written using CellProfiler to identify individual cells and extract average fluorescence intensity and fluorescence lifetime values for each cell in the field of view (minus background and nuclear signals) (61). Intensity values for each pixel were calculated by integrating the decay curve corresponding to that pixel. Optical redox ratio values were calculated for each pixel (without binning) by dividing the intensity of NAD(P)H by the intensity of FAD. Then, the average redox ratio across all pixels in each cell cytoplasm was

calculated. The redox ratio on a per-cell basis was used for all statistical comparisons. Reported mean redox ratios are normalized to control values. The mean lifetime ($\tau_m$) of NAD(P)H, which represents the weighted average of the free and protein-bound lifetimes, was calculated for each cell cytoplasm using Equation 3.5. For each imaging variable, values for all cells in a dish were averaged together. An analysis of the sources of variability in NAD(P)H FLIM signals in our cell experiments shows that error due to fitting of decay curves is far outweighed by biological variation (Appendix A Table A.1).

### 3.5.7 Cellular fuel sources

$1x10^5$ MCF10A cells were seeded 24 hours prior to starvation in 35mm glass-bottom dishes. Then, standard media was replaced with glucose-free, pyruvate-free, and serum-free DMEM (#11966, Gibco) overnight. FLIM images of NAD(P)H in three fields of view were taken in each dish immediately before and immediately after the replacement of media with fresh serum-free media containing either 10 mM sodium pyruvate or 10 mM sodium lactate (#P2256 and #L7022, Sigma). A total of 200-300 cells were imaged per condition, and individual cells were analyzed. This experiment was repeated in triplicate.

### 3.5.8 Statistical analysis

Differences in optical redox ratios, NAD(P)H intensities, and FAD intensities between treatment groups in cells were tested across 3 or more replicates using a ratio paired student's t-test. All standard deviations in figures are calculated across experimental replicates. Differences in NAD(P)H lifetime variables between solutions and differences in cellular NAD(P)H lifetime variables between treatment groups were tested across 3 or more replicates using an unpaired

student's t-test with Welch's correction for samples of unequal variance. Differences in enzyme activity levels between control and treated cells were tested across 3-5 experiments using the same test. A significance level of 0.05 was used to determine statistical significance in all tests.

### 3.6 Acknowledgments

The Skala laboratory is supported by grants from the NSF Graduate Research Fellowship (DGE-1445197; JTS), the NSF (CBET-1554027), the DOD Breast Cancer Research Program (W81XWH-13-1-0194), the Mary Kay Foundation (067-14), Stand Up to Cancer (SU2C-AACR-IG-08-16, Sharp Award) and the NIH (NCI R01 CA185747, NCI R01 CA205101, NCI R01 CA211082). The Merrins laboratory is supported by grants to M.J. Merrins from the NIH/NIA (R21 AG050135), the NIH/NIDDK (K01 DK101683), the American Diabetes Association (1-16-IBS-212), and the Wisconsin Partnership Program.

### 3.7 References

[1] Heikal AA. Intracellular coenzymes as natural biomarkers for metabolic activities and mitochondrial anomalies. Biomark Med. 2010;4(2):241-63.

[2] Uppal A, Gupta PK. Measurement of NADH concentration in normal and malignant human tissues from breast and oral cavity. Biotechnol Appl Biochem. 2003;37(Pt 1):45-50.

[3] Berman HM, Westbrook J, Feng Z, Gilliland G, Bhat TN, Weissig H, et al. The Protein Data Bank. Nucleic Acids Res. 2000;28(1):235-42.

[4] Fantin VR, St-Pierre J, Leder P. Attenuation of LDH-A expression uncovers a link between glycolysis, mitochondrial physiology, and tumor maintenance. Cancer Cell. 2006;9(6):425-34.

[5] McFate T, Mohyeldin A, Lu H, Thakar J, Henriques J, Halim ND, et al. Pyruvate dehydrogenase complex activity controls metabolic and malignant phenotype in cancer cells. J Biol Chem. 2008;283(33):22700-8.

[6] Patra KC, Hay N. The pentose phosphate pathway and cancer. Trends Biochem Sci. 2014;39(8):347-54.

[7] Bergmann A. SPCImage: data analysis software for fluorescence lifetime imaging microscopy. Becker & Hickl GmbH, available on www becker-hickl com. 2003.

[8] Chance B, Schoener B, Oshino R, Itshak F, Nakase Y. Oxidation-reduction ratio studies of mitochondria in freeze-trapped samples. NADH and flavoprotein fluorescence signals. J Biol Chem. 1979;254(11):4764-71.

[9] Walsh AJ, Cook RS, Manning HC, Hicks DJ, Lafontant A, Arteaga CL, et al. Optical metabolic imaging identifies glycolytic levels, subtypes, and early-treatment response in breast cancer. Cancer Res. 2013;73(20):6164-74.

[10] Ostrander JH, McMahon CM, Lem S, Millon SR, Brown JQ, Seewaldt VL, et al. Optical redox ratio differentiates breast cancer cell lines based on estrogen receptor status. Cancer Res. 2010;70(11):4759-66.

[11] Skala MC, Riching KM, Gendron-Fitzpatrick A, Eickhoff J, Eliceiri KW, White JG, et al. In vivo multiphoton microscopy of NADH and FAD redox states, fluorescence lifetimes, and cellular morphology in precancerous epithelia. Proc Natl Acad Sci U S A. 2007;104(49):19494-9.

[12] Xu HN, Nioka S, Glickson JD, Chance B, Li LZ. Quantitative mitochondrial redox imaging of breast cancer metastatic potential. J Biomed Opt. 2010;15(3):036010.

[13] Varone A, Xylas J, Quinn KP, Pouli D, Sridharan G, McLaughlin-Drubin ME, et al. Endogenous two-photon fluorescence imaging elucidates metabolic changes related to enhanced glycolysis and glutamine consumption in precancerous epithelial tissues. Cancer Res. 2014;74(11):3067-75.

[14] Mujat C, Greiner C, Baldwin A, Levitt JM, Tian F, Stucenski LA, et al. Endogenous optical biomarkers of normal and human papillomavirus immortalized epithelial cells. Int J Cancer. 2008;122(2):363-71.

[15] Quinn KP, Sridharan GV, Hayden RS, Kaplan DL, Lee K, Georgakoudi I. Quantitative metabolic imaging using endogenous fluorescence to detect stem cell differentiation. Sci Rep. 2013;3:3432.

[16] Alhallak K, Jenkins SV, Lee DE, Greene NP, Quinn KP, Griffin RJ, et al. Optical imaging of radiation-induced metabolic changes in radiation-sensitive and resistant cancer cells. J Biomed Opt. 2017;22(6):60502.

[17] Rice WL, Kaplan DL, Georgakoudi I. Two-photon microscopy for non-invasive, quantitative monitoring of stem cell differentiation. PLoS One. 2010;5(4):e10075.

[18] Alhallak K, Rebello LG, Muldoon TJ, Quinn KP, Rajaram N. Optical redox ratio identifies metastatic potential-dependent changes in breast cancer cell metabolism. Biomed Opt Express. 2016;7(11):4364-74.

[19] Hou J, Wright HJ, Chan N, Tran R, Razorenova OV, Potma EO, et al. Correlating two-photon excited fluorescence imaging of breast cancer cellular redox state with seahorse flux analysis of normalized cellular oxygen consumption. J Biomed Opt. 2016;21(6):60503.

[20] Lakowicz JR. Principles of fluorescence spectroscopy. 2nd ed. New York: Kluwer Academic/Plenum; 1999. xxiii, 698 p. p.

[21] Blacker TS, Marsh RJ, Duchen MR, Bain AJ. Activated barrier crossing dynamics in the non-radiative decay of NADH and NADPH. Chemical Physics. 2013;422:184-94.

[22] Lakowicz JR, Szmacinski H, Nowaczyk K, Johnson ML. Fluorescence lifetime imaging of free and protein-bound NADH. Proc Natl Acad Sci U S A. 1992;89(4):1271-5.

[23] Conklin MW, Provenzano PP, Eliceiri KW, Sullivan R, Keely PJ. Fluorescence lifetime imaging of endogenous fluorophores in histopathology sections reveals differences between normal and tumor epithelium in carcinoma in situ of the breast. Cell Biochem Biophys. 2009;53(3):145-57.

[24] Walsh AJ, Cook RS, Sanders ME, Aurisicchio L, Ciliberto G, Arteaga CL, et al. Quantitative optical imaging of primary tumor organoid metabolism predicts drug response in breast cancer. Cancer Res. 2014;74(18):5184-94.

[25] Ghukasyan VV, Kao FJ. Monitoring Cellular Metabolism with Fluorescence Lifetime of Reduced Nicotinamide Adenine Dinucleotide. J Phys Chem C. 2009;113(27):11532-40.

[26] Skala MC, Riching KM, Bird DK, Gendron-Fitzpatrick A, Eickhoff J, Eliceiri KW, et al. In vivo multiphoton fluorescence lifetime imaging of protein-bound and free nicotinamide adenine dinucleotide in normal and precancerous epithelia. J Biomed Opt. 2007;12(2):024014.

[27] Bird DK, Yan L, Vrotsos KM, Eliceiri KW, Vaughan EM, Keely PJ, et al. Metabolic mapping of MCF10A human breast cells via multiphoton fluorescence lifetime imaging of the coenzyme NADH. Cancer Res. 2005;65(19):8766-73.

[28] Walsh A, Cook RS, Rexer B, Arteaga CL, Skala MC. Optical imaging of metabolism in HER2 overexpressing breast cancer cells. Biomed Opt Express. 2012;3(1):75-85.

[29] Guo HW, Chen CT, Wei YH, Lee OK, Gukassyan V, Kao FJ, et al. Reduced nicotinamide adenine dinucleotide fluorescence lifetime separates human mesenchymal stem cells from differentiated progenies. J Biomed Opt. 2008;13(5):050505.

[30] Walsh AJ, Poole KM, Duvall CL, Skala MC. Ex vivo optical metabolic measurements from cultured tissue reflect in vivo tissue status. J Biomed Opt. 2012;17(11):116015.

[31] Cheng S, Cuenca RM, Liu B, Malik BH, Jabbour JM, Maitland KC, et al. Handheld multispectral fluorescence lifetime imaging system for in vivo applications. Biomed Opt Express. 2014;5(3):921-31.

[32] Sun Y, Phipps JE, Meier J, Hatami N, Poirier B, Elson DS, et al. Endoscopic fluorescence lifetime imaging for in vivo intraoperative diagnosis of oral carcinoma. Microsc Microanal. 2013;19(4):791-8.

[33] Dimitrow E, Riemann I, Ehlers A, Koehler MJ, Norgauer J, Elsner P, et al. Spectral fluorescence lifetime detection and selective melanin imaging by multiphoton laser tomography for melanoma diagnosis. Exp Dermatol. 2009;18(6):509-15.

[34] Galletly NP, McGinty J, Dunsby C, Teixeira F, Requejo-Isidro J, Munro I, et al. Fluorescence lifetime imaging distinguishes basal cell carcinoma from surrounding uninvolved skin. Br J Dermatol. 2008;159(1):152-61.

[35] Kennedy GT, Manning HB, Elson DS, Neil MA, Stamp GW, Viellerobe B, et al. A fluorescence lifetime imaging scanning confocal endomicroscope. J Biophotonics. 2010;3(1-2):103-7.

[36] Yu Q, Heikal AA. Two-photon autofluorescence dynamics imaging reveals sensitivity of intracellular NADH concentration and conformation to cell physiology at the single-cell level. J Photochem Photobiol B. 2009;95(1):46-57.

[37] Yaseen MA, Sutin J, Wu W, Fu B, Uhlirova H, Devor A, et al. Fluorescence lifetime microscopy of NADH distinguishes alterations in cerebral metabolism in vivo. Biomed Opt Express. 2017;8(5):2368-85.

[38] Vergen J, Hecht C, Zholudeva LV, Marquardt MM, Hallworth R, Nichols MG. Metabolic imaging using two-photon excited NADH intensity and fluorescence lifetime imaging. Microsc Microanal. 2012;18(4):761-70.

[39] Schneckenburger H, Wagner M, Weber P, Strauss WS, Sailer R. Autofluorescence lifetime imaging of cultivated cells using a UV picosecond laser diode. J Fluoresc. 2004;14(5):649-54.

[40] Wang HW, Wei YH, Guo HW. Reduced nicotinamide adenine dinucleotide (NADH) fluorescence for the detection of cell death. Anticancer Agents Med Chem. 2009;9(9):1012-7.

[41] Stringari C, Nourse JL, Flanagan LA, Gratton E. Phasor fluorescence lifetime microscopy of free and protein-bound NADH reveals neural stem cell differentiation potential. PLoS One. 2012;7(11):e48014.

[42] Xian ZY, Liu JM, Chen QK, Chen HZ, Ye CJ, Xue J, et al. Inhibition of LDHA suppresses tumor progression in prostate cancer. Tumour Biol. 2015;36(10):8093-100.

[43] Kim JW, Tchernyshyov I, Semenza GL, Dang CV. HIF-1-mediated expression of pyruvate dehydrogenase kinase: a metabolic switch required for cellular adaptation to hypoxia. Cell Metab. 2006;3(3):177-85.

[44] Le A, Cooper CR, Gouw AM, Dinavahi R, Maitra A, Deck LM, et al. Inhibition of lactate dehydrogenase A induces oxidative stress and inhibits tumor progression. Proc Natl Acad Sci U S A. 2010;107(5):2037-42.

[45] Cairns RA, Papandreou I, Sutphin PD, Denko NC. Metabolic targeting of hypoxia and HIF1 in solid tumors can enhance cytotoxic chemotherapy. Proc Natl Acad Sci U S A. 2007;104(22):9445-50.

[46] Michelakis ED, Webster L, Mackey JR. Dichloroacetate (DCA) as a potential metabolic-targeting therapy for cancer. Br J Cancer. 2008;99(7):989-94.

[47] Rellinger EJ, Craig BT, Alvarez AL, Dusek HL, Kim KW, Qiao J, et al. FX11 inhibits aerobic glycolysis and growth of neuroblastoma cells. Surgery. 2017;161(3):747-52.

[48] Maltas J, Amer L, Long Z, Palo D, Oliva A, Folz J, et al. Autofluorescence from NADH Conformations Associated with Different Metabolic Pathways Monitored Using Nanosecond-Gated Spectroscopy and Spectral Phasor Analysis. Anal Chem. 2015;87(10):5117-24.

[49] Blacker TS, Mann ZF, Gale JE, Ziegler M, Bain AJ, Szabadkai G, et al. Separating NADH and NADPH fluorescence in live cells and tissues using FLIM. Nat Commun. 2014;5:3936.

[50] Gafni A, Brand L. Fluorescence decay studies of reduced nicotinamide adenine dinucleotide in solution and bound to liver alcohol dehydrogenase. Biochemistry. 1976;15(15):3165-71.

[51] Walsh AJ, Sharick JT, Skala MC, Beier HT. Temporal binning of time-correlated single photon counting data improves exponential decay fits and imaging speed. Biomed Opt Express. 2016;7(4):1385-99.

[52] Lodola A, Spragg SP, Holbrook JJ. Malate dehydrogenase of the cytosol. Preparation and reduced nicotinamide-adenine dinucleotide-binding studies. Biochem J. 1978;169(3):577-88.

[53] Torikata T, Forster LS, O'Neal CC, Jr., Rupley JA. Lifetimes and NADH quenching of tryptophan fluorescence in pig heart lactate dehydrogenase. Biochemistry. 1979;18(2):385-90.

[54] Kanji MI, Toews ML, Carper WR. A kinetic study of glucose-6-phosphate dehydrogenase. J Biol Chem. 1976;251(8):2258-62.

[55] Ma N, Digman MA, Malacrida L, Gratton E. Measurements of absolute concentrations of NADH in cells using the phasor FLIM method. Biomed Opt Express. 2016;7(7):2441-52.

[56] Digman MA, Caiolfa VR, Zamai M, Gratton E. The phasor approach to fluorescence lifetime imaging analysis. Biophys J. 2008;94(2):L14-6.

[57] Wos M, Pollard P. Sensitive and meaningful measures of bacterial metabolic activity using NADH fluorescence. Water Res. 2006;40(10):2084-92.

[58] Deng H, Zhadin N, Callender R. Dynamics of protein ligand binding on multiple time scales: NADH binding to lactate dehydrogenase. Biochemistry. 2001;40(13):3767-73.

[59] Shore JD, Evans SA, Holbrook JJ, Parker DM. NADH binding to porcine mitochondrial malate dehydrogenase. J Biol Chem. 1979;254(18):9059-62.

[60] Becker W. Advanced time-correlated single photon counting techniques. Berlin ; New York: Springer; 2005. xix, 401 p. p.

[61] Walsh AJ, Skala MC. An automated image processing routine for segmentation of cell cytoplasms in high-resolution autofluorescence images. SPIE Proceedings. 2014;8948.

# CHAPTER 4

## Cellular Metabolic Heterogeneity *In Vivo* is Recapitulated in Tumor Organoids

Sharick, J.T., Jeffery, J.J., Karim, M.R., Walsh, C.M., Esbona, K., Cook, R.S., Skala, M.C. "Cellular metabolic heterogeneity *in vivo* is recapitulated in tumor organoids." In review.

### 4.1 Abstract

Heterogeneous populations within a tumor have varying metabolic profiles, which can muddle the interpretation of bulk tumor imaging studies of treatment response. Although methods to study tumor metabolism at the cellular level are emerging, these methods provide a single time point 'snap-shot' of tumor metabolism, and require a significant time and animal burden, while failing to capture the longitudinal metabolic response of a single tumor to treatment. Here, we investigated a novel method for longitudinal, single-cell imaging of metabolism across heterogeneous tumor cell populations using optical metabolic imaging (OMI), which measures autofluorescence of metabolic co-enzymes as a report of metabolic activity. We also investigated whether *in vivo* cellular metabolic heterogeneity can be accurately captured using tumor-derived three-dimensional organoids in a genetically engineered mouse model of breast cancer. OMI measurements of response to paclitaxel and the phosphatidylinositol-3-kinase (PI3K) inhibitor XL147 in tumors and organoids taken at single cell resolution revealed parallel shifts in metabolic heterogeneity. Interestingly, these previously unappreciated heterogeneous metabolic responses in tumors and organoids could not be attributed to tumor cell fate or varying leukocyte content within the microenvironment, suggesting that heightened metabolic heterogeneity upon treatment is largely due to heterogeneous metabolic shifts within tumor cells. Together, these studies show that OMI revealed remarkable heterogeneity in response to treatment, which could provide a novel approach to predict the presence of potentially unresponsive tumor cell subpopulations lurking

within a largely responsive bulk tumor population, which might otherwise be overlooked by traditional measurements.

## 4.2 Introduction

There is accumulating evidence that tumor cell populations are heterogeneous, enabling heterogeneous responses to treatments that may either enhance or inhibit treatment sensitivity (1-4). Minority populations of tumor cells with innate treatment resistance have been identified, such as $CD24^+$ breast cancer cells, which exhibit resistance to certain chemotherapies (5, 6). The presence of minority tumor cell subpopulations with innate resistance to treatment can ultimately result in tumor recurrence, even under circumstances when the original tumor, comprised mainly of treatment sensitive cells, responds to treatment. Clinicians lack the tools necessary to assess this heterogeneity and to recommend optimal treatment plans for each individual patient. It is also difficult to study the process by which tumors evolve to obtain variability in cellular treatment sensitivity. Current techniques to perform high-throughput *in vivo* drug screens and assess heterogeneity are destructive to the cells and require enormous animal burden. These limitations not only hinder our understanding of the mechanisms behind tumor heterogeneity and recurrence, but also obstruct the discovery of novel drugs and drug combinations that combat the emergence of therapy-resistant subpopulations of cells. To address these problems, a platform is needed that faithfully recapitulates and quantifies *in vivo* cellular heterogeneity *in vitro.*

Next-generation single-cell sequencing can be used to characterize genetic diversity by identifying mutant subclones (7-11), and the number of subclonal driver mutations has predictive value for a patient's overall survival (12). However, the predictive ability of single cell sequencing in the clinical setting relies on genetic mutations that are already known. Therefore, the remarkable

advances provided by single cell sequencing still cannot provide a true predictive analysis of treatment-resistance tumor cell subpopulations that may lurk within a larger tumor cell population. Further, the sensitivity of a cell to a specific drug is a complex combination of both genetic and non-genetic factors, including cellular metabolism (13, 14). To fuel aberrant proliferation rates, cancer cells are able to reprogram their metabolic machinery to incorporate nutrients into required pathways, even in the absence of growth factor signals (15, 16). However, not all cells in a tumor alter their metabolism in the same manner. In response to unique levels of oxygen, glucose, pH, cytokines, and extracellular matrix proteins in their microenvironment, individual cells adapt appropriately to maximize their survival (14, 17). These mechanisms of adaptation also affect cell resistance to cytotoxic drugs and immunotherapies (18, 19), resulting in subpopulations of tumor cells with differing sensitivities to treatment. This highlights the need for a functional readout of heterogeneity that is based on cell metabolism.

Given the limitations of genetic testing on predicting treatment response, alternative approaches which directly measure drug response in tumor cells are under investigation. For example, testing treatment response in mouse patient-derived xenograft (PDX) models captures the influence of *in vivo* genetic heterogeneity, and can be used to predict patient response to many therapies *ex vivo* (20), but require enormous numbers of animals for high-throughput drug screening, and cannot be performed in a clinically beneficial time frame. Alternatively, *in vitro* cancer organoids can be used to screen drugs directly on patient cells, alleviating the burdens of time, animals, and cost (21). Organoids maintain the genetic, histopathological, functional surface markers, and 3-dimensional characteristics of the original tumor for a variety of cancer types (22-25). Additionally, organoids contain stromal cells that can facilitate therapeutic resistance (26). Many organoids can be cultured from a single patient biopsy, supporting the feasibility of

screening patient-derived tumor organoids for sensitivity to a variety of treatments.

Optical metabolic imaging (OMI) is a label-free two-photon microscopy technique that quantifies single-cell metabolic changes with treatment, both in tumors *in vivo* (27) and in tumor-derived organoids (28). OMI uses the endogenous fluorescent properties of metabolic coenzymes NAD(P)H and FAD. The optical redox ratio, or the ratio of the fluorescence intensity of NAD(P)H to that of FAD, reflects the redox state of the cell (29-31). The fluorescence lifetimes of NAD(P)H and FAD are distinct for the free-and protein-bound conformations of both molecules, and thus reflect enzyme binding (32-34). These OMI endpoints, integrated to form a composite OMI index, reflect early metabolic shifts and thus can evaluate drug response prior to changes in cell viability or tumor size (21, 35, 36). The non-destructive nature of this technique allows heterogeneity to be tracked in organoids over time to analyze the potential for drug resistance evolution in the original tumor. This is not possible with other methods for measuring heterogeneity (e.g. flow cytometry, single-cell sequencing, or immunolabeling) because these standard methods are destructive.

OMI of cancer organoids has been validated as an accurate predictor of *in vivo* drug response in xenograft models generated from human breast cancer and head and neck cancer cell lines (21, 35) and a mouse model of pancreatic cancer (36), but it is unclear whether the heterogeneity measured in organoids also accurately mirrors the original tumor. Here, we investigate the feasibility of studying *in vivo* heterogeneity using OMI measurements in organoids derived from the polyomavirus middle T (PyVmT) mouse model, which closely models the stages and progression of human breast cancer, exhibits more heterogeneity than human cell line xenografts, and can develop in a fully immunocompetent mouse (37). This study demonstrates that OMI of *in vitro* tumor organoids accurately captures *in vivo* heterogeneous response to treatment in a relevant breast cancer model.

## 4.3 Materials and methods

### 4.3.1 Orthotopic PyVmT tumors

Animal research was approved by the Institutional Animal Care and Use Committees at Vanderbilt University and the University of Wisconsin-Madison. Orthotopic tumors were initially generated by injecting $10^6$ PyVmT cell line suspended in 100 µl of a chilled 1:1 mixture of DMEM (Gibco #11965) and Matrigel (Corning #354234) into the 4$^{th}$ inguinal mammary fat pads of 6-week old FVB female mice (The Jackson Laboratory #001800) using a 26 gauge needle. The PyVmT cell line was derived from tumors isolated from transgenic FVB MMTV-PyVmT mice (The Jackson Laboratory #002374). Tumors were passaged by mechanically dissociating an existing tumor, passing the tumor cell suspension through a 70 µm strainer, and injecting the cells into a new 6-week old FVB mouse.

### 4.3.2 FDG-PET/CT imaging

Mice were randomized and imaged prior to treatment (when tumors grew to >200 mm$^3$), and then imaged weekly over a 14-day time course at the University of Wisconsin Small Animal Imaging and Radiotherapy Facility by trained staff (J.J.J., J.T.S.). 10 mg/kg paclitaxel (Vanderbilt University pharmacy/University of Wisconsin pharmacy) was diluted in 150 µl PBS and injected i.p. twice weekly. 50 mg/kg XL147 (Selleckchem) was suspended in 100 µl 1% DMSO and delivered by oral gavage daily. Control mice received 100 µl 1% DMSO by o.g. daily and 150 µl PBS by i.p. injection twice weekly. Prior to PET/CT imaging, mice were fasted for 12 hours. One hour prior to imaging, ~9.25 MBq of [$^{18}$F]FDG was delivered by tail vein injection, and mice were immediately anesthetized under 4% isoflurane, maintained at 1.5%, and warmed with a heated bed until the end of the imaging procedure. The mice were scanned using an Inveon microPET/CT

(Siemens Medical Solutions, Knoxville, TN) in the prone position. Forty-million counts per mouse were collected for the PET scan to obtain adequate signal-to-noise. PET data were histogrammed in to one static frame and subsequently reconstructed using ordered-subset expectation maximization (OSEM) of three dimensions followed by the maximum *a posteriori* algorithm, and CT attenuation and scatter correction were applied based on the NEMA NU 4 image-quality parameters (38). Inveon Research Workplace software (Siemens Medical Solution, Knoxville, TN) was used to measure tumor volume and glucose uptake. PET and CT images were co-registered, and manual regions-of-interest (ROIs) were drawn around each tumor. FDG uptake was measured as the decay corrected percent injected dose normalized by the mass of the tissue ($\%ID/g_{tissue}$) assuming the density of the ROI tissue is equal to water. Five tumors from five mice were imaged per treatment group.

4.3.3 Fluorescence lifetime imaging

A custom multiphoton fluorescence lifetime system (Bruker Fluorescence Microscopy) was used to acquire fluorescence images. A titanium:sapphire laser (Chameleon Ultra II, Coherent) was used for excitation, while GaAsP photomultiplier tubes (H7422P-40, Hamamatsu) was used to detect emission photons. A 40x water immersion objective (Nikon, 1.15 NA) was used with an inverted microscope (Nikon, TiE). Two-photon excitation of NAD(P)H and FAD was performed with 750 nm and 890 nm light, respectively. A 440/80 nm filter was used to isolate NAD(P)H fluorescence emission, and a 550/100 nm filter for FAD fluorescence emission. 256x256 pixel images were acquired using a pixel dwell time of 4.8 μs and a 60 second collection time. Time-correlated single photon counting electronics (SPC-150, Becker & Hickl) were used to acquire fluorescence lifetime data with 256 time bins. A single Fluoresbrite YG microsphere

(Polysciences) was imaged each day as a fluorescence lifetime standard. The measured lifetime (2.15 ± 0.08 ns, n=7) was stable and consistent with previously published values (27, 33, 35, 39, 40). For each field of view, an NAD(P)H image was acquired first followed immediately by an FAD image.

4.3.4 Intravital OMI

48 hours after initial treatment, and 1 hour following final treatment, mice were anesthetized using isoflurane, and a small portion of skin was removed to expose the underlying tumor. OMI was performed on at least four fields of view and at least 450 total cells per tumor. Following imaging, mice were euthanized while under anesthesia, and tumors were extracted and fixed. Five tumors from five different mice were imaged per treatment group.

4.3.5 Tissue processing and organoid culture

Excised tumors were rinsed in PBS and thoroughly minced in DMEM with dissecting scissors. The resulting cell macro-suspension was chilled on ice and mixed with Matrigel at a 1:2 ratio, and 100 µl of the resulting mixture was pipetted into 35 mm glass-bottom dishes (#P35G-1.5-14-C, MatTek). Gels were allowed to solidify slowly at room temperature for 30 minutes, and then placed in a 37°C, 5% $CO_2$ incubator for 1 hour before being overlaid with DMEM supplemented with 10% FBS and 1% penicillin-streptomycin (Gibco).

4.3.6 Organoid imaging

24 hours prior to imaging, organoid media was replaced with fresh media containing 500 nM paclitaxel, 25 nM XL147, or 0.1% DMSO vehicle. These doses were chosen to replicate *in*

*vivo* doses (21). Organoids were imaged after 24, 48, and 72 hours of treatment. At least six organoids from each treatment group were imaged at each time point, containing at least 290 cells total for each treatment group.

4.3.7 OMI endpoint images

The optical redox ratio was computed from NAD(P)H and FAD lifetime images. First, the fluorescence intensities of NAD(P)H and FAD are determined by the total number of photons detected over the collection time. Then, the intensity of NAD(P)H is divided by the intensity of FAD in each pixel. SPCImage software was used to analyze fluorescence lifetime images (Becker & Hickl) (41). First, fluorescence decay curves for NAD(P)H and FAD are generated for each pixel by assigning all photon events into 256 temporal bins. Detected photons from the 8 neighboring pixels are also included in each curve to increase photon counts. This decay curve is deconvolved with the measured instrument response function, and fit with a two-component exponential decay (Equation 4.1).

$$I(t) = \alpha_1 exp^{-t/\tau_1} + \alpha_2 exp^{-t/\tau_2} + C \quad (4.1)$$

$I(t)$ represents the fluorescence intensity measured at time $t$ following a laser pulse, $\alpha_1$ and $\alpha_2$ represent the percentage of the overall signal made up by the short and long lifetime components respectively, $\tau_1$ and $\tau_2$ are the short and long lifetime components respectively, and $C$ represents background light. The use of a two-component fit was chosen in order to differentiate the free ($\tau_1$) and bound ($\tau_2$) states of NAD(P)H and the free ($\tau_2$) and bound ($\tau_1$) states of FAD (32, 42). The mean lifetime ($\tau_m$) of NAD(P)H and FAD for each pixel is the weighted average of the free and bound lifetimes (Equation 4.2).

$$\tau_m = \alpha_1 * \tau_1 + \alpha_2 * \tau_2 \quad (4.2)$$

A CellProfiler routine was written to automatically distinguish between individual cell cytoplasms and the nuclei they encircle (43, 44). For each cytoplasm detected, values for the redox ratio and all NAD(P)H and FAD lifetime variables were calculated by averaging the incorporated pixels within the cytoplasm.

### 4.3.8 OMI index

The redox ratio, NAD(P)H $\tau_m$, and FAD $\tau_m$ were normalized to average values in control cells for the OMI index calculation. *In vivo,* values are normalized to averages of all cells imaged in all control mice on the same day. *In vitro,* values are normalized to averages of all cells from all control organoids imaged on the same day. In both cases, the OMI index is calculated for each cell using a linear combination of the control-normalized redox ratio, NAD(P)H $\tau_m$, and FAD $\tau_m$ with coefficients of (1,1,-1), respectively. A decrease in OMI index correlates with drug sensitivity (21).

### 4.3.9 Heterogeneity analysis

Histograms were generated for all cells within a group using individual cell OMI indices. The histogram is fit to Gaussian mixture distribution models containing one, two, or three components, using an iterative expectation maximization algorithm. Each component represents a distinct subpopulation of cells. Goodness of fit for each model was evaluated using the Akaike information criterion (45), and only the model with best fit was implemented. For each group, this process is repeated 1,000 times. For visual comparison, example distributions are normalized to have equal areas under the curve. Similar numbers of cells were imaged in each tumor and in each organoid treatment group to provide similar power to identify subpopulations in each distribution (46). The heterogeneity index is a validated metric for quantifying heterogeneity in a population

(27, 47). Here we present a modified version, the weighted heterogeneity index (wH-index), which also takes into account the standard deviations of all subpopulations.

$$\text{wH-index} = \sum\ (1 - p_i ln(p_i + 1)) * (\sigma_i + d_i) \tag{4.3}$$

Here, $i$ represents each subpopulation, $d$ represents the distance between the median of each subpopulation and the median of the entire distribution, $p$ represents the proportion of all cells belonging to that subpopulation, and $\sigma$ is the standard deviation.

4.3.10 Histological analysis

Immediately following *in vivo* tumor imaging, tumors were collected and fixed in 10% neutral buffered formalin for 48 hours. Tumors were oriented and paraffin embedded such that 5 μm slices were taken from the imaged portion of the tumor. Also immediately following imaging, Matrigel droplets containing organoids were detached from glass coverslips and encased in agarose. These agarose gels were placed in 10% neutral buffered formalin for 48 hours, paraffin embedded, and sliced into 5 μm sections starting from the center. Organoid histology experiments were duplicated and results were combined. Tumors and organoid sections were stained using immunohistochemistry for CD45 (ab10558, Abcam, 32 min.), vimentin (ab92547, Abcam, 32 min.), alpha smooth muscle actin (αSMA) (ab5694, Abcam, 32 min.), wide spectrum cytokeratin (ab9377, Abcam, 28 min.), polyoma virus middle T antigen (sc-53481, SantaCruz, 60 min.), Ki67 (ab15580, Abcam, 28 min.), cleaved caspase 3 (9661, Cell Signaling, 28 min.), phospho-histone H3 (9701, Cell Signaling, 16 min.), and phospho-PRAS40 (2997, Cell Signaling, 12 min.). Positive staining was visualized with diaminobenzidine (DAB) and counter-stained with hematoxylin.

4.3.11 Histology imaging and quantification

Multispectral image cubes were acquired using a Nuance multispectral imaging microscope and software (Perkin Elmer) (48). Images of transmitted light were taken from 420 nm to 720 nm with 20 nm steps and converted to optical densities using a blank reference image. Image cubes were unmixed using a spectral library to isolate individual stains and exclude background signals. Individual cells (stained with DAB and counterstained with hematoxylin) in tumor and organoid images were automatically segmented using InForm software (Perkin Elmer). In organoid images, machine learning algorithms were trained to distinguish between individual cellular organoids, extracellular matrix, and background. For tumors, algorithms were trained to separate tumor and stromal compartments. All algorithms had precision >92%. Only cells in tumor or organoid compartments were quantified. Individual cells were scored as positive or negative for a particular target antibody by thresholding for the mean value within that cell. At least 4 random fields of view were acquired per stain per tumor, for a total of at least 23 images per stain per treatment group. Organoids containing less than 5 cells were rejected from analysis, and at least 35 organoids were quantified per stain per treatment group.

4.3.12 Statistical analysis

Normalized tumor volumes and glucose uptake values were compared using a student t-test with Bonferroni correction for multiple comparisons. Significant differences in OMI variables, wH-indices, and IHC percentages between treatment groups were tested using a Wilcoxon rank-sum test. Treatment effect size was calculated with Glass's $\Delta$ (49), with directionality determined by the response of HER2+ cell line xenografts to trastuzumab (21).

## 4.4 Results

### 4.4.1 PET/CT measures *in vivo* treatment response

Response to treatment with paclitaxel and XL147 was measured in orthotopic PyVmT allograft tumors and tumor organoids. Paclitaxel is an FDA-approved chemotherapy for breast cancer that has been shown to reduce tumor growth rates in orthotopic PyVmT tumors (50). XL147, an inhibitor of the phosphatidylinositol-3 kinase family (PI3K), was also chosen due to the dependence of the PyVmT model on PI3K activity (51-53), and for its use in clinical trials for breast cancer. To verify response to treatment, FDG-PET measurements were taken of tumors treated with paclitaxel, XL147, and combination (P+X) over 14 days (Fig. 4.1). Subsequent CT measurements were also taken in order to better visualize the tumor in the mammary fat pad and distinguish tumor-associated signal from background (Fig. 4.1A). While XL147 alone and paclitaxel alone did not affect tumor growth after 2 weeks, the combination of both drugs significantly decreased tumor growth vs. vehicle ($p<0.05$, Fig. 4.1B). No differences in FDG-uptake were observed with treatment (Fig. 4.1C). A reduction in pPRAS40 staining in XL147 treated tumors and organoids confirms successful PI3K inhibition (Appendix B Fig. B.1).

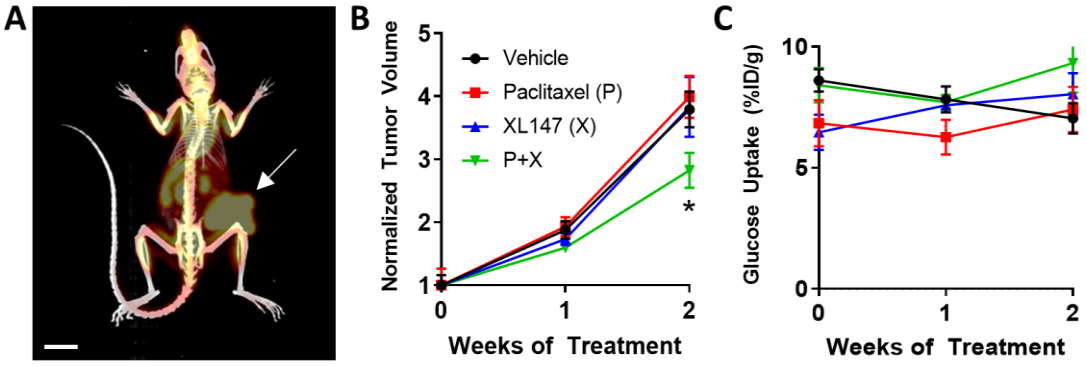


**Figure 4.1. FDG-PET/CT of PyVmT *in vivo* treatment response. A,** Example PET/CT image showing glucose uptake in an orthotopic PyVmT tumor (arrow) growing on the right mammary fat pad. Scale bar = 1 cm. **B,** The effect of drug treatment on tumor growth. All volumes are normalized to pre-treatment volume. N=5 tumors per treatment group. * $p<0.05$ vs. vehicle. **C,** Glucose uptake did not change with drug treatment.

4.4.2 OMI of cellular metabolic heterogeneity *in vivo*

Intravital OMI was performed to determine how treatment affects tumor metabolic heterogeneity *in vivo* at a cellular level. Representative images demonstrate that OMI can visualize single-cell metabolic properties in these tumors (Fig. 4.2A). Response was quantified using the OMI index after 48 hours of treatment with either vehicle or P+X in 5 mice per group (Fig. 4.2B). Across all cells from all tumors, P+X treated cells had a significantly lower OMI index compared with vehicle controls ($p<0.0001$, Fig. 4.2C). Histograms of cell OMI indices were fit to Gaussian mixture distribution models (Fig.4.2D, plotted separately in Appendix B Fig. B.2). Vehicle treated tumors exhibited higher degrees of variance in their single-cell OMI index distributions compared to P+X treated tumors. The smallest subpopulation detected in tumors represented 29.0% of the overall population (vehicle). The degree of heterogeneity in each tumor is quantified using a modified form of the heterogeneity index (27, 47) with an additional term added for the standard deviation of each individual subpopulation (wH-index). P+X treatment was found to significantly decrease the *in vivo* wH-index vs. vehicle ($p<0.05$, Fig. 4.2E).

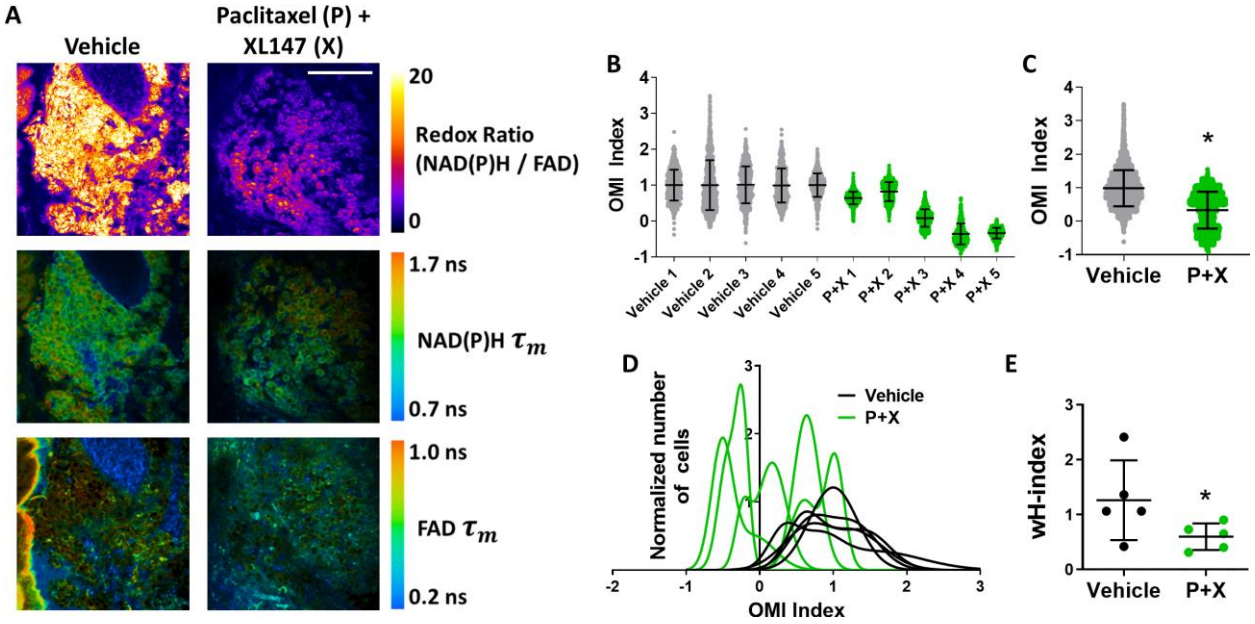


**Figure 4.2. OMI of drug response heterogeneity *in vivo.* A,** Representative images of the redox ratio, NAD(P)H mean lifetime ($\tau_m$) and FAD $\tau_m$ *in vivo* in PyVmT tumors treated with vehicle or paclitaxel + XL147 (P+X) for 48 hours. Scale bar = 100 μm. **B,** OMI Index quantified at the single cell level 48 hours after treatment *in vivo* for each tumor. Each dot represents one cell. A decrease in the OMI index indicates drug response. Error bars indicate mean ± SD. N>450 cells/tumor. **C,** Decrease in average OMI Index with treatment across all cells from all tumors. Error bars indicate mean ± SD. * p<0.0001 vs. vehicle. N>3,300 cells/group. **D,** Population density distributions of drug response at the single-cell level for each tumor. **E,** The effect of treatment on the degree of OMI Index heterogeneity per tumor quantified by the wH-index. Error bars indicate mean ± SD. N=1000 fits/tumor. Each dot represents one tumor. *p<0.05 vs. vehicle.

4.4.3 OMI of cellular metabolic heterogeneity in organoids

Next, responses to the same therapies were measured in PyVmT tumor-derived organoids to determine if organoid heterogeneity is similar to PyVmT tumors *in vivo.* Representative images demonstrate the size and morphology of the organoids and the OMI endpoint spatial distributions (Fig. 4.3A). Single therapies were tested in parallel to P+X combined therapy, and OMI index was calculated at the single-cell level after 24, 48, and 72 hours of treatment. Organoids treated with P+X had a lower mean OMI index compared to control organoids (p<0.0001, Fig. 4.3B and Appendix B Fig. B.3A,B), in agreement with the *in vivo* results. Examples of Gaussian mixture modeling showed multiple subpopulations in the control organoids, and only a single population

with smaller overall variance in the P+X treated organoids (Fig. 4.3C). The degree of heterogeneity was significantly decreased in P+X treated organoids vs. control organoids at 72 hours ($p<0.0001$, Fig. 4.3D), just as it was *in vivo* at 48 hours. The mean wH-index values were higher at 48 hours *in vivo* (1.26 and 0.60 for vehicle and P+X treated respectively) compared to 72 hours *in vitro* (0.90 and 0.08 for vehicle and P+X treated respectively). Similar wH-indices were found between treatment groups in organoids at 24 and 48 hours of treatment (Fig. 4.3D, example distributions in Appendix B Fig. B.3C,D). The smallest subpopulation detected in organoids represented 12.2% of the overall population (paclitaxel, 24 hours). The optical redox ratio, NAD(P)H $\tau_m$, and FAD $\tau_m$ also change significantly with P+X treatment in both organoids and tumors (Appendix B Fig. B.4). Coefficients of variation for the optical redox ratio, NAD(P)H $\tau_m$, and FAD $\tau_m$ showed similar trends within organoids and *in vivo* tumors (Appendix B Fig. B.5).

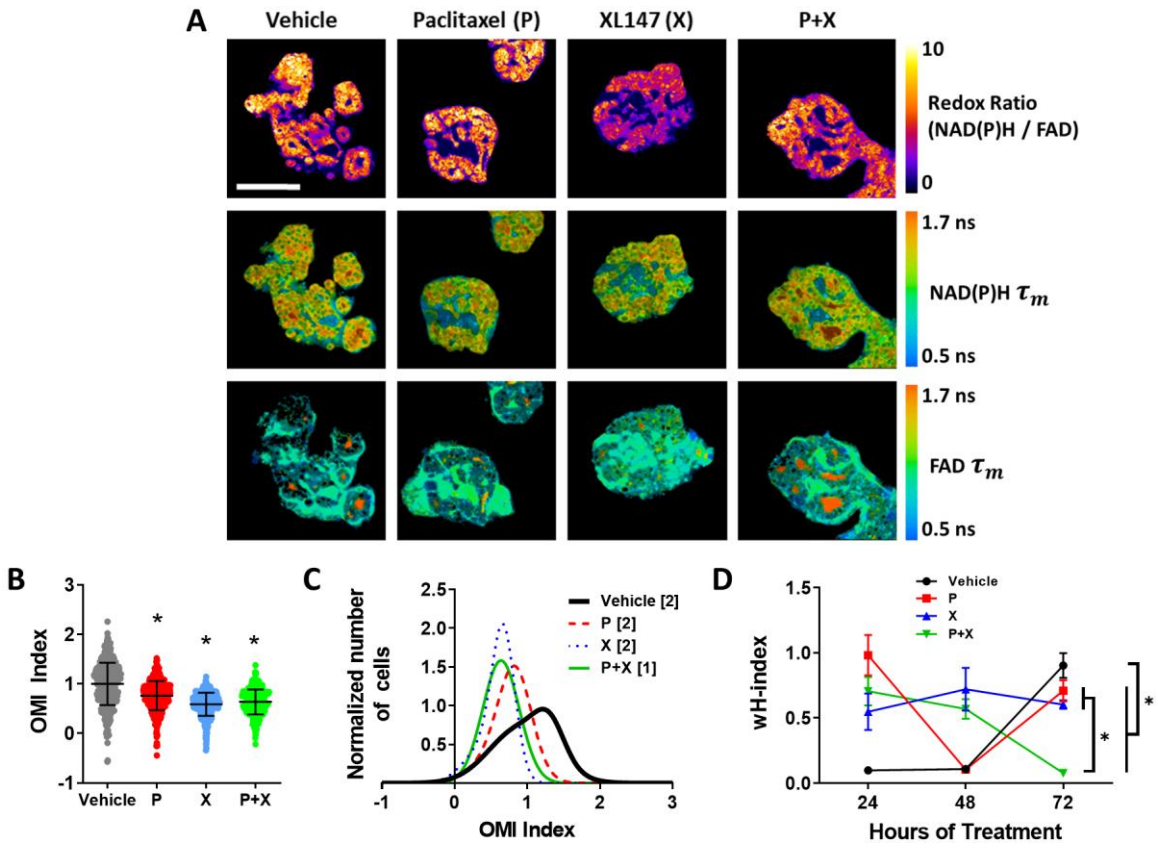


**Figure 4.3. OMI of drug response heterogeneity in PyVmT organoids. A,** Representative images of the redox ratio, NAD(P)H $\tau_m$ and FAD $\tau_m$ in organoids at 72 hours of treatment. Scale bar = 100 μm. **B,** OMI index quantified at the single cell level. N=6 organoids/group. N>300 cells/group. Each dot represents one cell. Error bars indicate mean ± SD. * p<0.0001 vs. vehicle. **C,** Example subpopulation analysis of the OMI index in all organoid cells. Brackets in legend indicate number of subpopulations for each group. **D,** The effect of treatment on the degree of OMI index heterogeneity per tumor quantified by the wH-index. Error bars indicate mean ± SD. N=1000 fits/group for all 6 organoids/group. * p<0.0001.

4.4.4 Comparison of drug treatment effect sizes on OMI variables

The effect size of drug treatment on individual OMI variables was calculated for all cells in tumors and organoids using Glass's Δ (49) (Fig. 4.4). P+X treatment had large effects (Δ>0.75) on the redox ratio and OMI index at 24, 48, and 72 hours in organoids (Fig. 4.4A-C), and in tumors at 48 hours (Fig. 4.4D). P+X did not have a large effect on individual lifetime variables, except at 48 hours in tumor-derived organoids. XL147 alone also had a large effect on the OMI index and redox ratio at all time points in organoids. Paclitaxel alone had a large effect on the redox ratio at

only 24 hours in organoids, and did not have a large effect on OMI index at any time point. The correlation between Glass's Δ values with P+X treatment *in vivo* at 48 hours versus organoids at 24, 48, and 72 hours was significant at all time points ($p<0.05$, Pearson's correlation), indicating that changes in OMI variables with P+X treatment in organoids faithfully mirror *in vivo* changes.

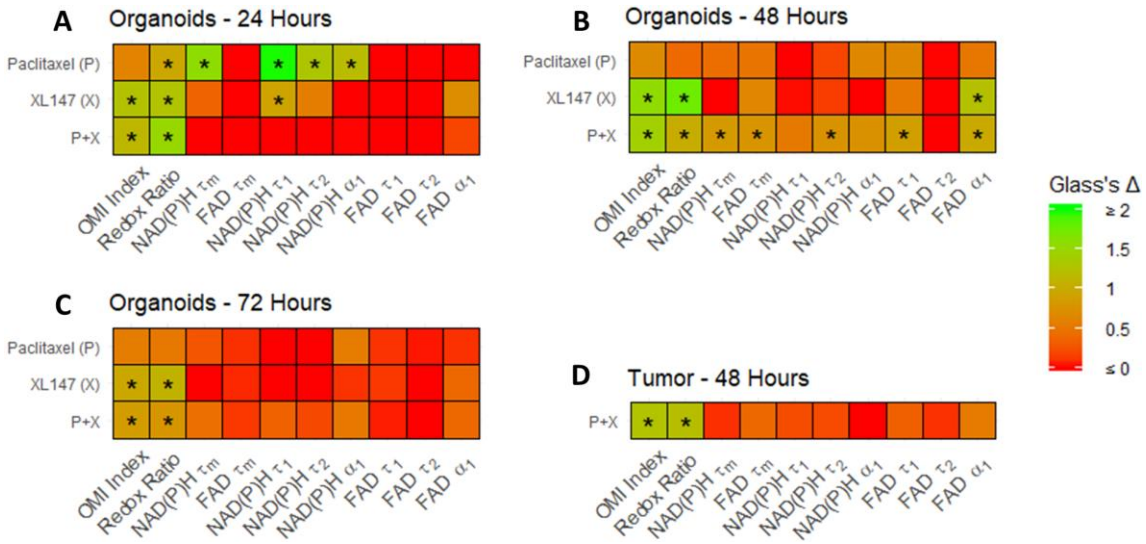


**Figure 4.4. Effect sizes of treatment on OMI variables in PyVmT tumors and organoids. A-C,** Glass's Δ effect size of treatment on OMI variables across all PyVmT tumor-derived organoid cells at (**A**) 24, (**B**) 48, and (**C**) 72 hours. * Δ > 0.75. **D,** Glass's Δ effect size of treatment on OMI variables across all PyVmT tumor cells.

4.4.5 Characterization of cell types in PyVmT tumors and organoids

Histology of PyVmT tumors and organoids was performed to determine if the distinct cell subpopulations measured in Figures 4.2 and 4.3 were comprised of different cell types, cells undergoing apoptosis or proliferation, or cells simply employing unique metabolic strategies. Expression of vimentin and αSMA and loss of wide spectrum cytokeratin expression in all tumors and organoids indicate that cells had undergone epithelial to mesenchymal transition prior to imaging (Fig. 4.5). Expression of PyVmT antigen in both tumors and organoids (Fig. 4.5) confirm that cells matched the tumors of origin.

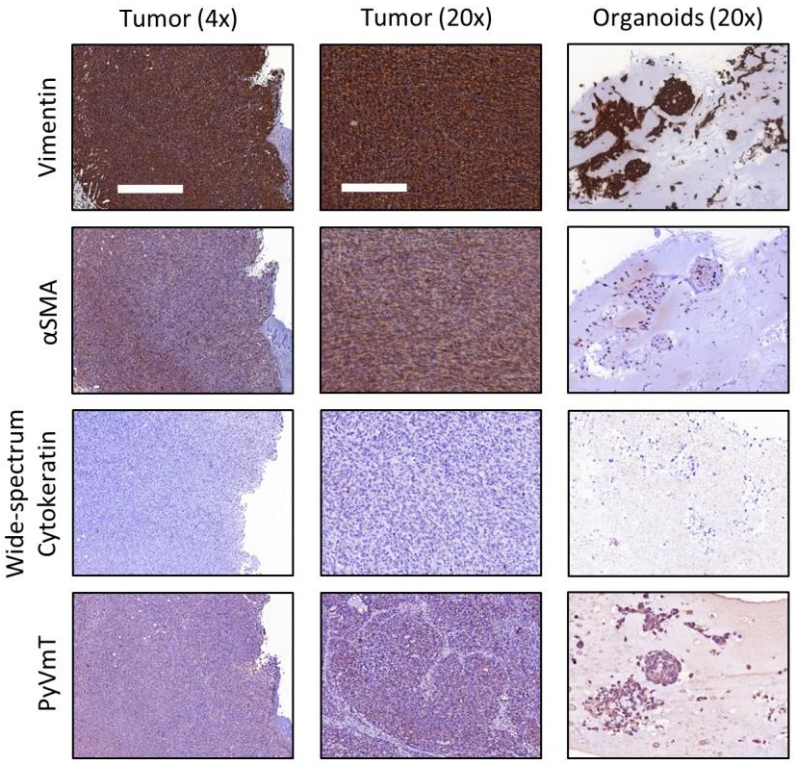


**Figure 4.5. Characterization of tumors and organoid cells.** Example images demonstrate that tumor and organoid cells express vimentin and α-smooth muscle actin, and do not express cytokeratins. Cells are confirmed positive for PyVmT antigen. 4x scale bar = 1 mm. 20x scale bar = 200 μm.

4.4.6 Quantification of potential sources of heterogeneity in PyVmT tumors and organoids

Machine learning algorithms were trained using inForm software to distinguish between individual cellular organoids in histology images, and to identify cells and quantify expression both in organoids and *in vivo*. The expression of Ki67 and phospho-histone H3 (pHH3), two proliferation markers, was quantified along with cleaved caspase 3 (CC3), a marker of apoptosis. Ki67 is expressed in the S, G2, and M phases of the cell cycle, while pHH3 is specific to cells in M phase (54). The percentage of cells expressing Ki67 was similar between tumors and organoids and also did not change after 48 hours of treatment in either setting (Fig. 4.6A). The percentage of cells in apoptosis was similar between tumors and organoids (both <20%), but did not change after 48 hours of treatment in either setting (Fig. 4.6B and Appendix B Fig. B.6A). pHH3 was expressed

in significantly fewer cells in tumors and organoids compared to Ki67 (Fig. 4.6C and Appendix B Fig. B.6B). Significantly fewer of these cells in M-phase were found in P+X treated tumors compared to vehicle controls ($p<0.05$), but treatment did not significantly change the number of M-phase cells in organoids. Small subpopulations of $CD45^+$ leukocytes were present in both tumors and organoids (Fig. 4.6D and Appendix B Fig. B.6C). A smaller percentage of $CD45^+$ leukocytes were present in organoids compared to the original tumors, and fewer were present in P+X treated organoids compared to vehicle ($p<0.05$). A majority of cells in organoids and tumors were positive for αSMA (Fig. 4.6E and Appendix B Fig. B.6D). The percentage of $\alpha SMA^+$ cells was not significantly different between organoids and tumors, and did not significantly change with treatment in either setting. The variance of positive staining of all markers across all FOV and organoids was not affected by treatment. These cell fates and cell types are unlikely to be responsible for the decrease in OMI index and its heterogeneity with P+X treatment because none of the positive percentages of these markers significantly changed with treatment in both tumors and organoids.

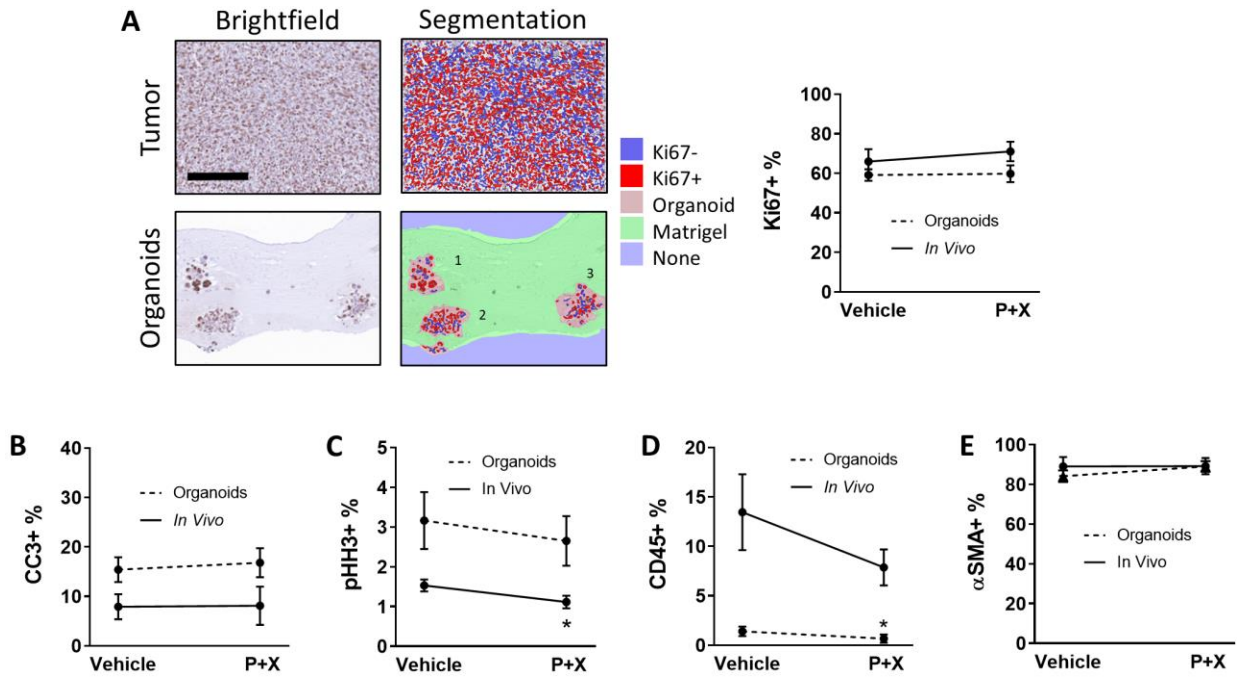


**Figure 4.6. Quantification of heterogeneity and treatment response in PyVmT tumors and organoids with histology. A,** Automatic cell segmentation and quantification of Ki67 expression in 20x images of PyVmT tumor and organoids. Scale bar = 200 μm. N>4 FOV per tumor, 5 tumors per group. N>39 organoids per group. **B,** CC3 expression in tumors and organoids. N=5 FOV per tumor, 5 tumors per group. N>44 organoids per group. **C,** pHH3 expression in tumors and organoids. N=5 FOV per tumor, 5 tumors per group. N>60 organoids per group. **D,** CD45 expression in tumors and organoids. N>4 FOV per tumor, 5 tumors per group. N>45 organoids per group. **E,** αSMA expression in tumors and organoids. N>4 FOV per tumor, N>5 tumors per group. N>20 organoids per group. Error bars indicate mean ± SD. * $p<0.05$ vs. control.

### 4.5 Discussion

To optimize a treatment plan for an individual cancer patient, a clinician must understand how various drug options will affect all the cells in a patient's uniquely heterogeneous tumor. While recent technological advances have improved our fundamental understanding of intratumoral heterogeneity, we still lack tools for cancer treatment planning that incorporate distinct metabolic subpopulations. Cancer organoids allow for rapid, high-throughput drug screening directly on tumor cells in a relevant 3-dimensional microenvironment (21, 23, 35, 36, 55). Current methods for evaluating drug response in organoids either damage the sample, overlook cellular heterogeneity, or do not directly screen drugs on patient-derived cells. To address

these limitations, we have developed OMI to non-invasively quantify metabolic heterogeneity within living organoids using the fluorescent properties of metabolic coenzymes NAD(P)H and FAD (21, 35). OMI detects minority metabolic subpopulations of drug-resistant cells within organoids, and this information can predict long-term tumor drug response. These capabilities have been confirmed in breast (21, 46) and head and neck (35) cell line xenografts, and in a pancreatic cancer mouse model (36). However, cell line tumors in immunocompromised mice do not capture the cellular heterogeneity of primary human tumors, and it remains unclear whether metabolic heterogeneity in primary tumor-derived organoids mirrors the heterogeneity of the original tumor. In this study, OMI was used to compare subpopulations of cell metabolism in tumors and tumor-derived organoids of the immunocompetent PyVmT breast cancer model. We confirm that organoids accurately capture *in vivo* metabolic heterogeneity, demonstrating the feasibility of using organoids to study tumor response to treatment.

CT images confirmed that P+X treatment reduced PyVmT tumor volume *in vivo* over 14 days in immunocompetent allografts (Fig. 4.1). Tumor volume did not change over the first week of treatment, and FDG uptake did not change with therapy over two weeks. However, OMI was sensitive to metabolic treatment response in only 48 hours (Fig. 4.2). This highlights the enhanced sensitivity of OMI to early metabolic changes compared to traditional methods of measuring treatment response, in agreement with previous reports in immunocompromised xenografts (27).

Intravital OMI was performed in mice treated with vehicle or P+X for 48 hours (Fig. 4.2), and the degree of heterogeneity within each tumor was characterized by the wH-index. P+X treated tumors exhibited a significantly lower degree of heterogeneity compared to control tumors ($p<0.05$), further suggesting that this treatment combination could be beneficial. OMI was also used to measure response to P+X in PyVmT tumor-derived organoids (Fig. 4.3). Paclitaxel and

XL147 single therapies were also screened with low additional effort and cost, underlining the high-throughput nature of organoid versus animal drug screens. Additionally, due to the non-invasive nature of OMI, measurement of response was performed at 24, 48, and 72 hours in the same set of organoids. OMI measurements at 72 hours in organoids, of all the time points acquired, most accurately replicated *in vivo* heterogeneity. This agrees with previous reports that early metabolic drug response at 72 hours in organoids predicts long-term *in vivo* tumor drug response (21). The higher degree of heterogeneity in organoids at 72 hours post-treatment for single agent treatments compared to P+X treatment (Fig. 4.3) may explain why single therapies alone did not reduce overall tumor growth (Fig. 4.1), despite a decrease in mean OMI index. It is possible that only a subpopulation of the cells were sensitive, which led to disease progression. In contrast, P+X treated organoids exhibited a lower wH-index at 72 hours compared to controls and single therapies (Fig. 4.3D), which suggests that this drug combination worked synergistically to overcome the resistance to single agent treatments. The higher fold change in wH-index with P+X treatment in organoids compared to *in vivo* tumors may be due to differences in efficiency of drug delivery. While drug gradients caused by drug diffusion do exist in large organoids, this may not completely capture the irregularity of drug diffusion throughout solid tumors. Evaluating the degree of drug response heterogeneity in organoids using the wH-index was a better predictor of long-term tumor growth than the average response across all cells. P+X treatment also had similar effects on individual OMI variables in tumors and organoids, including a large effect on the optical redox ratio, and small effects on FAD lifetime variables (Fig. 4.4). These parallels suggest that cellular level drug response in tumor-derived organoids can be used to analyze heterogeneous responses to treatment in the tumor of origin.

We next assessed potential sources of the shifts in heterogeneity found in tumors after 48

hours of treatment and in organoids after 72 hours of treatment using IHC (Fig. 4.5). These results indicate that PyVmT tumors in this study progressed to a mesenchymal phenotype at the time of imaging, closely resembling basal-like human breast cancer (56). Organoid cultures successfully captured these mesenchymal properties of the original tumor (Fig. 4.5).

Traditional IHC measures of therapeutic response (CC3, Ki67, pHH3), were also evaluated as potential sources of metabolic heterogeneity (Fig. 4.6) because metabolic activities are linked to apoptosis and proliferation (57, 58). PyVmT tumor allografts incorporate the host's acquired immune system, which is an advantage over cell line xenografts grown in athymic nude mice. Immune cells and tumor cells have distinct metabolic properties (19, 59), and thus could also contribute to OMI heterogeneity. A small subset of $CD45^+$ leukocytes were found in both tumors and organoids using IHC, and P+X treatment significantly reduced the percentage of leukocytes in organoids, but not *in vivo*. This may be because organoid culture conditions were not optimized to maintain mouse leukocytes. Finally, mesenchymal transition can also affect cellular drug response and metabolism (60), but our IHC results indicate that this mesenchymal phenotype is nearly homogenous and consistent with treatment, and thus not the cause of OMI index heterogeneity.

None of the markers tested changed significantly in both tumors and organoids, indicating that apoptosis, proliferation, and the presence of immune cells and $\alpha SMA^+$ cells are unlikely to be responsible for the decrease in OMI index and its heterogeneity with P+X treatment. These markers are likely not associated with the high OMI index subpopulations in control organoids at 72 hours and control tumors, which were affected by P+X treatment. Overall, we did not identify a marker of cell type or cell fate that accounted for the metabolic heterogeneity detected with OMI. These results suggest that the subpopulations identified with OMI are likely due to metabolic

differences between cells. Future studies could confirm this finding using emerging single-cell mass spectrometry on dissociated tumors and organoids, but these techniques are still in development (61, 62). Single cell RNA analysis of dissociated tumors and organoids could also support our findings, but does not offer a comparable measure to the more downstream metabolic activity of cells that OMI provides. Similarly, fluorescent reporters can quantify metabolic properties within single live cells that are correlated with the optical metabolic variables reported here (e.g., glucose uptake (63), pH (64), membrane potential (65), hypoxia (66), NADH/$NAD^+$ redox state (67)). Overall, comparison of OMI with IHC highlights that OMI provides an early measure of tumor response compared to traditional markers, consistent with previous results (35).

This study validates OMI of primary tumor-derived organoids as a unique, powerful tool to study *in vivo* tumor metabolic heterogeneity. This tool could also improve clinical treatment decisions, because minority subpopulations of treatment-resistant cells within an otherwise responsive tumor can initiate patient recurrence (2, 3, 21). These results are the first to show that *in vitro* organoids capture the early metabolic changes in heterogeneity that occur *in vivo* with treatment in an immunocompetent tumor. OMI of organoids quantifies single-cell response to many drugs in a relevant three-dimensional microenvironment, using a single tissue sample, and can be performed longitudinally to track the evolution of heterogeneity over time. This technology could provide a personalized medicine platform to perform high-throughput screening of drugs directly on patient cells, and detect metabolic heterogeneity. This would allow clinicians to quickly analyze cellular heterogeneity in response to numerous treatment options for an individual patient to more robustly inform on treatment decisions. Additionally, this technique could reduce the animals and time required to develop new therapeutic strategies that overcome tumor heterogeneity and achieve better outcomes in patients.

## 4.6 Acknowledgments

Thank you to the UW Translational Research Initiatives in Pathology laboratory and UW Small Animal Imaging and Radiotherapy Facility (both supported by the UWCCC grant P30 CA014520) for use of their facilities and services. Thank you to Sophie Mancha for assistance with organoid culture. Thank you to Dr. Dustin Deming and Dr. Suzanne Ponik for helpful conversations about organoids and cancer cell heterogeneity. The Skala laboratory is supported by grants from the NSF Graduate Research Fellowship (DGE-1445197; JTS), the NSF (CBET-1642287), Stand Up to Cancer (SU2C-AACR-IG-08-16, SU2C-AACR-PS-18) and the NIH (R01 CA185747, R01 CA205101, R01 CA211082, R21 CA224280, U01 TR002383).

## 4.7 References

[1] Greaves M. Evolutionary determinants of cancer. Cancer Discov. 2015;5(8):806-20.

[2] Marusyk A, Polyak K. Tumor heterogeneity: causes and consequences. Biochim Biophys Acta. 2010;1805(1):105-17.

[3] Fisher R, Pusztai L, Swanton C. Cancer heterogeneity: implications for targeted therapeutics. Br J Cancer. 2013;108(3):479-85.

[4] Gerlinger M, Swanton C. How Darwinian models inform therapeutic failure initiated by clonal heterogeneity in cancer medicine. Br J Cancer. 2010;103(8):1139-43.

[5] Almendro V, Cheng YK, Randles A, Itzkovitz S, Marusyk A, Ametller E, et al. Inference of tumor evolution during chemotherapy by computational modeling and in situ analysis of genetic and phenotypic cellular diversity. Cell Rep. 2014;6(3):514-27.

[6] Deng X, Apple S, Zhao H, Song J, Lee M, Luo W, et al. CD24 Expression and differential resistance to chemotherapy in triple-negative breast cancer. Oncotarget. 2017;8(24):38294-308.

[7] Suzuki Y, Ng SB, Chua C, Leow WQ, Chng J, Liu SY, et al. Multiregion ultra-deep sequencing reveals early intermixing and variable levels of intratumoral heterogeneity in colorectal cancer. Mol Oncol. 2017;11(2):124-39.

[8] Roerink SF, Sasaki N, Lee-Six H, Young MD, Alexandrov LB, Behjati S, et al. Intra-tumour diversification in colorectal cancer at the single-cell level. Nature. 2018;556(7702):457-62.

[9] Sievers CK, Zou LS, Pickhardt PJ, Matkowskyj KA, Albrecht DM, Clipson L, et al. Subclonal diversity arises early even in small colorectal tumours and contributes to differential growth fates. Gut. 2017;66(12):2132-40.

[10] Navin N, Kendall J, Troge J, Andrews P, Rodgers L, McIndoo J, et al. Tumour evolution inferred by single-cell sequencing. Nature. 2011;472(7341):90-4.

[11] Kim C, Gao R, Sei E, Brandt R, Hartman J, Hatschek T, et al. Chemoresistance Evolution in Triple-Negative Breast Cancer Delineated by Single-Cell Sequencing. Cell. 2018;173(4):879-93 e13.

[12] Kleppe M, Levine RL. Tumor heterogeneity confounds and illuminates: assessing the implications. Nat Med. 2014;20(4):342-4.

[13] Caiado F, Silva-Santos B, Norell H. Intra-tumour heterogeneity - going beyond genetics. FEBS J. 2016;283(12):2245-58.

[14] Cantor JR, Sabatini DM. Cancer cell metabolism: one hallmark, many faces. Cancer Discov. 2012;2(10):881-98.

[15] Vander Heiden MG, Cantley LC, Thompson CB. Understanding the Warburg effect: the metabolic requirements of cell proliferation. Science. 2009;324(5930):1029-33.

[16] Hanahan D, Weinberg RA. Hallmarks of cancer: the next generation. Cell. 2011;144(5):646-74.

[17] Vander Heiden MG. Targeting cancer metabolism: a therapeutic window opens. Nat Rev Drug Discov. 2011;10(9):671-84.

[18] Morandi A, Indraccolo S. Linking metabolic reprogramming to therapy resistance in cancer. Biochim Biophys Acta Rev Cancer. 2017;1868(1):1-6.

[19] Renner K, Singer K, Koehl GE, Geissler EK, Peter K, Siska PJ, et al. Metabolic Hallmarks of Tumor and Immune Cells in the Tumor Microenvironment. Front Immunol. 2017;8:248.

[20] Bruna A, Rueda OM, Greenwood W, Batra AS, Callari M, Batra RN, et al. A Biobank of Breast Cancer Explants with Preserved Intra-tumor Heterogeneity to Screen Anticancer Compounds. Cell. 2016;167(1):260-74 e22.

[21] Walsh AJ, Cook RS, Sanders ME, Aurisicchio L, Ciliberto G, Arteaga CL, et al. Quantitative optical imaging of primary tumor organoid metabolism predicts drug response in breast cancer. Cancer Res. 2014;74(18):5184-94.

[22] Boj SF, Hwang CI, Baker LA, Chio, II, Engle DD, Corbo V, et al. Organoid models of human and mouse ductal pancreatic cancer. Cell. 2015;160(1-2):324-38.

[23] Sachs N, de Ligt J, Kopper O, Gogola E, Bounova G, Weeber F, et al. A Living Biobank of Breast Cancer Organoids Captures Disease Heterogeneity. Cell. 2018;172(1-2):373-86 e10.

[24] van de Wetering M, Francies HE, Francis JM, Bounova G, Iorio F, Pronk A, et al. Prospective derivation of a living organoid biobank of colorectal cancer patients. Cell. 2015;161(4):933-45.

[25] Vlachogiannis G, Hedayat S, Vatsiou A, Jamin Y, Fernandez-Mateos J, Khan K, et al. Patient-derived organoids model treatment response of metastatic gastrointestinal cancers. Science. 2018;359(6378):920-6.

[26] Majety M, Pradel LP, Gies M, Ries CH. Fibroblasts Influence Survival and Therapeutic Response in a 3D Co-Culture Model. PLoS One. 2015;10(6):e0127948.

[27] Shah AT, Diggins KE, Walsh AJ, Irish JM, Skala MC. In Vivo Autofluorescence Imaging of Tumor Heterogeneity in Response to Treatment. Neoplasia. 2015;17(12):862-70.

[28] Walsh AJ, Cook RS, Skala MC. Functional Optical Imaging of Primary Human Tumor Organoids: Development of a Personalized Drug Screen. J Nucl Med. 2017;58(9):1367-72.

[29] Georgakoudi I, Quinn KP. Optical Imaging Using Endogenous Contrast to Assess Metabolic State. Annu Rev Biomed Eng. 2012;14:351-67.

[30] Chance B, Schoener B, Oshino R, Itshak F, Nakase Y. Oxidation-reduction ratio studies of mitochondria in freeze-trapped samples. NADH and flavoprotein fluorescence signals. J Biol Chem. 1979;254(11):4764-71.

[31] Walsh A, Cook RS, Rexer B, Arteaga CL, Skala MC. Optical imaging of metabolism in HER2 overexpressing breast cancer cells. Biomed Opt Express. 2012;3(1):75-85.

[32] Lakowicz JR. Principles of fluorescence spectroscopy. 2nd ed. New York: Kluwer Academic/Plenum; 1999. xxiii, 698 p. p.

[33] Bird DK, Yan L, Vrotsos KM, Eliceiri KW, Vaughan EM, Keely PJ, et al. Metabolic mapping of MCF10A human breast cells via multiphoton fluorescence lifetime imaging of the coenzyme NADH. Cancer Res. 2005;65(19):8766-73.

[34] Sharick JT, Favreau PF, Gillette AA, Sdao SM, Merrins MJ, Skala MC. Protein-bound NAD(P)H Lifetime is Sensitive to Multiple Fates of Glucose Carbon. Sci Rep. 2018;8(1):5456.

[35] Shah AT, Heaster TM, Skala MC. Metabolic Imaging of Head and Neck Cancer Organoids. PLoS One. 2017;12(1):e0170415.

[36] Walsh AJ, Castellanos JA, Nagathihalli NS, Merchant NB, Skala MC. Optical Imaging of Drug-Induced Metabolism Changes in Murine and Human Pancreatic Cancer Organoids Reveals Heterogeneous Drug Response. Pancreas. 2016;45(6):863-9.

[37] Guy CT, Cardiff RD, Muller WJ. Induction of mammary tumors by expression of polyomavirus middle T oncogene: a transgenic mouse model for metastatic disease. Mol Cell Biol. 1992;12(3):954-61.

[38] Disselhorst JA, Brom M, Laverman P, Slump CH, Boerman OC, Oyen WJ, et al. Image-quality assessment for several positron emitters using the NEMA NU 4-2008 standards in the Siemens Inveon small-animal PET scanner. J Nucl Med. 2010;51(4):610-7.

[39] Skala MC, Riching KM, Gendron-Fitzpatrick A, Eickhoff J, Eliceiri KW, White JG, et al. In vivo multiphoton microscopy of NADH and FAD redox states, fluorescence lifetimes, and cellular morphology in precancerous epithelia. Proc Natl Acad Sci U S A. 2007;104(49):19494-9.

[40] Walsh AJ, Cook RS, Manning HC, Hicks DJ, Lafontant A, Arteaga CL, et al. Optical metabolic imaging identifies glycolytic levels, subtypes, and early-treatment response in breast cancer. Cancer Res. 2013;73(20):6164-74.

[41] Bergmann A. SPCImage: data analysis software for fluorescence lifetime imaging microscopy. Becker & Hickl GmbH, available on www becker-hickl com. 2003.

[42] Nakashima N, Yoshihara K, Tanaka F, Yagi K. Picosecond fluorescence lifetime of the coenzyme of D-amino acid oxidase. J Biol Chem. 1980;255(11):5261-3.

[43] Walsh AJ, Skala MC. An automated image processing routine for segmentation of cell cytoplasms in high-resolution autofluorescence images. SPIE Proceedings. 2014;8948.

[44] Carpenter AE, Jones TR, Lamprecht MR, Clarke C, Kang IH, Friman O, et al. CellProfiler: image analysis software for identifying and quantifying cell phenotypes. Genome Biol. 2006;7(10):R100.

[45] Akaike H. A new look at the statistical model identification. IEEE transactions on automatic control. 1974;19(6):716-23.

[46] Walsh AJ, Skala MC. Optical metabolic imaging quantifies heterogeneous cell populations. Biomed Opt Express. 2015;6(2):559-73.

[47] Almendro V, Kim HJ, Cheng YK, Gonen M, Itzkovitz S, Argani P, et al. Genetic and phenotypic diversity in breast tumor metastases. Cancer Res. 2014;74(5):1338-48.

[48] Mansfield JR, Hoyt C, Levenson RM. Visualization of microscopy-based spectral imaging data from multi-label tissue sections. Curr Protoc Mol Biol. 2008;Chapter 14:Unit 14 9.

[49] Glass GV. Primary, secondary, and meta-analysis of research. Educational researcher. 1976;5(10):3-8.

[50] DeNardo DG, Brennan DJ, Rexhepaj E, Ruffell B, Shiao SL, Madden SF, et al. Leukocyte complexity predicts breast cancer survival and functionally regulates response to chemotherapy. Cancer Discov. 2011;1(1):54-67.

[51] Sai J, Owens P, Novitskiy SV, Hawkins OE, Vilgelm AE, Yang J, et al. PI3K Inhibition Reduces Mammary Tumor Growth and Facilitates Antitumor Immunity and Anti-PD1 Responses. Clin Cancer Res. 2017;23(13):3371-84.

[52] Cook RS, Garrett JT, Sanchez V, Stanford JC, Young C, Chakrabarty A, et al. ErbB3 ablation impairs PI3K/Akt-dependent mammary tumorigenesis. Cancer Res. 2011;71(11):3941-51.

[53] Webster MA, Hutchinson JN, Rauh MJ, Muthuswamy SK, Anton M, Tortorice CG, et al. Requirement for both Shc and phosphatidylinositol 3' kinase signaling pathways in polyomavirus middle T-mediated mammary tumorigenesis. Mol Cell Biol. 1998;18(4):2344-59.

[54] Lee LH, Yang H, Bigras G. Current breast cancer proliferative markers correlate variably based on decoupled duration of cell cycle phases. Sci Rep. 2014;4:5122.

[55] Friedman AA, Letai A, Fisher DE, Flaherty KT. Precision medicine for cancer with next-generation functional diagnostics. Nat Rev Cancer. 2015;15(12):747-56.

[56] Sarrio D, Rodriguez-Pinilla SM, Hardisson D, Cano A, Moreno-Bueno G, Palacios J. Epithelial-mesenchymal transition in breast cancer relates to the basal-like phenotype. Cancer Res. 2008;68(4):989-97.

[57] Andersen JL, Kornbluth S. The tangled circuitry of metabolism and apoptosis. Mol Cell. 2013;49(3):399-410.

[58] Vander Heiden MG, Lunt SY, Dayton TL, Fiske BP, Israelsen WJ, Mattaini KR, et al. Metabolic pathway alterations that support cell proliferation. Cold Spring Harb Symp Quant Biol. 2011;76:325-34.

[59] Gentric G, Mieulet V, Mechta-Grigoriou F. Heterogeneity in Cancer Metabolism: New Concepts in an Old Field. Antioxid Redox Signal. 2017;26(9):462-85.

[60] Fischer KR, Durrans A, Lee S, Sheng J, Li F, Wong ST, et al. Epithelial-to-mesenchymal transition is not required for lung metastasis but contributes to chemoresistance. Nature. 2015;527(7579):472-6.

[61] Spitzer MH, Nolan GP. Mass Cytometry: Single Cells, Many Features. Cell. 2016;165(4):780-91.

[62] Duncan KD, Fyrestam J, Lanekoff I. Advances in mass spectrometry based single-cell metabolomics. Analyst. 2018.

[63] O'Neil RG, Wu L, Mullani N. Uptake of a fluorescent deoxyglucose analog (2-NBDG) in tumor cells. Mol Imaging Biol. 2005;7(6):388-92.

[64] Tantama M, Hung YP, Yellen G. Imaging intracellular pH in live cells with a genetically encoded red fluorescent protein sensor. J Am Chem Soc. 2011;133(26):10034-7.

[65] Poburko D, Santo-Domingo J, Demaurex N. Dynamic regulation of the mitochondrial proton gradient during cytosolic calcium elevations. J Biol Chem. 2011;286(13):11672-84.

[66] Howard SS, Straub A, Horton N, Kobat D, Xu C. Frequency Multiplexed In Vivo Multiphoton Phosphorescence Lifetime Microscopy. Nat Photonics. 2013;7(1):33-7.

[67] Hung YP, Albeck JG, Tantama M, Yellen G. Imaging cytosolic NADH-NAD(+) redox state with a genetically encoded fluorescent biosensor. Cell Metab. 2011;14(4):545-54.

# CHAPTER 5

## Optical Metabolic Imaging of Heterogeneous Drug Response in Pancreatic Cancer Patient Organoids

Sharick, J.T., Walsh, C.M., Sprackling, C.M., Pasch, C.A., Parikh, A.A., Matkowskyj, K.A., Deming, D.A., Skala, M.C. "Optical metabolic imaging of heterogeneous drug response in pancreatic cancer patient organoids." In review.

### 5.1 Abstract

New tools are needed to match pancreatic cancer patients with effective treatments. Patient-derived organoids offer a high-throughput platform to personalize treatments and discover novel therapies. Currently, methods to evaluate drug response in organoids are limited because they cannot be completed in a clinically relevant time frame, only evaluate response at one time point, and most importantly, overlook cellular heterogeneity. In this study, non-invasive optical metabolic imaging (OMI) of cellular heterogeneity in organoids was evaluated as a predictor of clinical treatment response. Organoids were generated from fresh patient tissue samples acquired during surgery and treated with the same drugs as the patient's prescribed adjuvant treatment. OMI measurements of heterogeneity in response to this treatment were compared to later patient response, specifically to the time to recurrence following surgery. OMI was sensitive to patient-specific treatment response in as little as 24 hours. OMI distinguished subpopulations of cells with divergent and dynamic responses to treatment in living organoids without the use of labels or dyes. OMI of organoids agreed with long-term therapeutic response in patients. With these capabilities, OMI could serve as a sensitive high-throughput tool to identify optimal therapies for individual pancreatic cancer patients, and to develop new effective therapies that address cellular heterogeneity in pancreatic cancer.

## 5.2 Introduction

Pancreatic cancer has one of the lowest 5-year survival rates of all cancer types (8%) (1), and is projected to be the second leading cause of cancer death by 2030 (2). Surgery is required to cure pancreatic cancer (3), but can only be performed in 5-10% of cases, and only offers a 10.4% 5-year survival rate (4). Chemotherapy can enhance survival after surgery and standard treatments in the adjuvant setting include gemcitabine and gemcitabine combined with capecitabine (5-fluorouracil (5-FU) pro-drug) (5). Promising treatments for early-stage pancreatic cancer following surgery include gemcitabine combined with nab-paclitaxel, and FOLFIRINOX. Currently, oncologists must weigh these drug treatment options for individual patients based solely on potential side effects and have no *a priori* indication of whether a pancreatic cancer patient will respond to standard therapies. There is a need for a predictive tool to screen and identify alternative therapies that would benefit individual patients with either resectable or more advanced unresectable pancreatic cancer. Such a tool would minimize the needless costs and side effects accompanying ineffective treatment, while maximizing long-term survival rates. Additionally, the discovery of novel therapies would be accelerated by the ability to rapidly investigate the clinical efficacy of many drug candidates for many patients.

Tailoring treatment based on genomic analysis alone is insufficient due to poor understanding of the connections between pancreatic tumor driver mutations and drug response. Despite being less genetically diverse than most cancers, targeted approaches to treating pancreatic cancer have failed in clinical trials and drug treatment is limited to cytotoxic chemotherapies. Most pancreatic tumors do not express a specific therapeutic target (6), and the driver mutations present in a patient's cancer do not predict their response to chemotherapy. Alternatively, pancreatic organoids have emerged as an appealing method to tailor treatments by performing high-

throughput drug screening directly on a patient's tumor cells (7-9). *In vitro* organoids recapitulate the genetic and histopathological characteristics of the original pancreatic tumor, along with its complex 3-dimensional organization (10-14). Organoid cultures also preserve interactions between tumor cells, immune cells (15), and fibroblasts (16), which can influence tumor drug response and are potential drug targets (17, 18). Generally, methods for measuring drug response in organoids have involved either cell viability assays, pooling of proteins, DNA, and RNA from many organoids, or tracking of organoid diameter changes. These methods homogenize the response of an entire organoid or many organoids and ignore cellular heterogeneity, which drives tumor treatment resistance (19-22). It is possible that minority subpopulations of lethal drug-resistant cells go completely undetected without more advanced assessment tools. Additionally, these methods generally neglect cellular metabolism, which is a major factor determining cellular drug response and heterogeneity (23-25).

Optical metabolic imaging (OMI) is a non-destructive, high-resolution fluorescence microscopy technique that quantifies the metabolic state of individual cells within a single organoid using cellular autofluorescence (26, 27). The fluorescence properties of NADH and NADPH overlap and are referred to as NAD(P)H. NAD(P)H, an electron donor, and FAD, an electron acceptor, are fluorescent metabolic co-enzymes present in all living cells. The optical redox ratio, defined as the ratio of the fluorescence intensity of NAD(P)H to that of FAD, reflects the redox state of the cell (28-30), and is sensitive to shifts in metabolic pathways (27, 31, 32). The fluorescence lifetimes of NAD(P)H and FAD are both two-exponential with distinct lifetimes for the free-and protein-bound conformations, and thus reflect the protein-binding activities of NAD(P)H and FAD (33-35). The optical redox ratio, NAD(P)H, and FAD fluorescence lifetimes all provide complimentary information, and can be combined into a composite endpoint called the

OMI index (36). This metric distinguishes drug-resistant and responsive cells by their metabolic states and is robust and sensitive in pancreatic organoids (7).

OMI of organoids could improve predictions of patient outcomes for several reasons. First, drug-induced changes in cell metabolism precede changes in tumor size or overall cell viability (7, 27, 36, 37), and thus can measure drug response faster than conventional methods such as apoptosis and proliferation assays. Second, OMI analysis of cell subpopulations identifies and quantifies tumor heterogeneity (37, 38), which is vital to accurately capture patient drug response. Finally, OMI is non-invasive and does not require exogenous labels, so treatment response can be tracked over time in the same organoids. This is not possible with standard techniques which, by necessity, destroy samples. Therefore, OMI provides a fast, dynamic method to evaluate heterogeneous drug response at the organoid and single-cell level, integrating tumor heterogeneity into treatment planning and drug discovery. OMI of organoids has been validated as an accurate predictor of *in vivo* drug response in mouse models of pancreatic cancer (7), but has not yet been evaluated in humans. This study is the first to demonstrate that OMI of cellular metabolic heterogeneity in pancreatic tumor organoids provide an early measure of long-term *in vivo* drug response for individual patients.

## 5.3 Materials and methods

### 5.3.1 Tissue processing and organoid culture

Human tissue was collected with informed consent from all patients, and all studies were approved by the Institutional Review Board at the University of Wisconsin-Madison. Surgically resected tissue was placed in cold chelation buffer on ice for one hour. Tissues were washed with PBS and digested at 37°C in DMEM/F12 medium (Invitrogen) containing 1 mg/mL collagenase

(Sigma), 0.125 mg/mL dispase (Invitrogen), 10% FBS (Gibco), and 1% pen-strep (Gibco) for 2-3 hours with intermittent shaking. The resulting cell macro-suspension was rinsed in PBS, re-suspended in 1:1 DMEM/F12:Matrigel, plated in 50 µl droplets, and allowed to solidify at 37°C, 5% $CO_2$ in a cell incubator. Once solidified, droplets were overlaid with DMEM/F12 supplemented with 7% FBS, 20 µM Y-27632 (Sigma), 50 ng/ml EGF (Invitrogen), RSPO-conditioned medium (homemade) and 1% penicillin-streptomycin (Gibco). FBS, Y-27632, and RSPO-conditioned medium were removed from cultures if fibroblasts were out-growing tumor cells.

5.3.2 Drug screening

24 hours prior to imaging, media was replaced with fresh media containing 85 µM gemcitabine (39), 10 µM 5-FU, 200 nM TAK-228 (40, 41), 250 nM ABT-263 (42, 43), 5 µM oxaliplatin, 10 µM nab-paclitaxel, 50 nM SN-38 or combinations of each. Doses were selected to replicate clinically relevant peak plasma concentrations. FOLFIRINOX treatment was comprised of 5-FU, oxaliplatin, and SN-38. After the first imaging time point (24 hours), gemcitabine, nab-paclitaxel, SN-38, and oxaliplatin were removed from cultures to simulate single bolus delivery, while 5-FU, TAK-228, and ABT-263 exposure was maintained throughout the experiment (to simulate daily oral delivery). Chemotherapy drugs were obtained from the University of Wisconsin Carbone Cancer Center Pharmacy. TAK-228 was obtained from LC Laboratories, and ABT-263 was obtained from Apex Bio.

### 5.3.3 Multiphoton imaging

Fluorescence imaging was performed using a custom multiphoton fluorescence lifetime system (Bruker Fluorescence Microscopy). A 40x water immersion objective (Nikon, 1.15 NA) was used with an inverted microscope (Nikon, TiE). A titanium:sapphire laser (Spectra-Physics InSight DS+) was used for excitation, while GaAsP photomultiplier tubes (H7422P-40, Hamamatsu) detected emission light. 750 nm and 890 nm light were used for two-photon excitation of NAD(P)H and FAD, respectively. A 440/80 nm filter was used to collect NAD(P)H fluorescence emission, and a 550/100 nm filter was used to collect FAD fluorescence emission. Images were acquired over 60 seconds, with a pixel dwell time of 4.8 μs for 256x256 pixel images. Fluorescence lifetime data with 256 time bins was acquired using time-correlated single photon counting electronics (SPC-150, Becker & Hickl). A Fluoresbrite YG microsphere (Polysciences) was imaged daily as a fluorescence lifetime standard, which had a stable lifetime (2.09 ± 0.05 ns, n=61), consistent with previously published values (26, 33, 35).

### 5.3.4 Organoid imaging

Imaging of organoids was performed in 35 mm glass-bottom dishes (#P35G-1.5-14-C, MatTek). At least five representative organoids were imaged in each treatment group at each time point. At least two additional images of the fibroblast monolayer on the coverslip were taken, if present. Images were acquired 1, 2, 3, 5, and 7 days after initial treatment.

### 5.3.5 Cyanide experiment

Four previously untreated organoids from Patient 1 underwent OMI immediately before and after the addition of media containing 12 mM NaCN (Sigma), for a final concentration of

6 mM. OMI endpoints were quantified at the single-cell level, at least 60 cells per group. Redox ratio values were normalized to the pre-treatment average.

5.3.6 Image analysis

NAD(P)H and FAD fluorescence lifetime images were analyzed using SPCImage software (Becker & Hickl) (44). Briefly, a histogram of photon counts per temporal bin, or decay curve, is generated for each pixel by binning the photon counts of all 9 surrounding pixels. This decay curve is deconvolved with the instrument response function, and then fit to a two-component exponential decay (Equation 5.1).

$$I(t) = \alpha_1 exp^{-t/\tau_1} + \alpha_2 exp^{-t/\tau_2} + C \quad (5.1)$$

Here, $I(t)$ represents the fluorescence intensity measured at time $t$, $\alpha_1$ and $\alpha_2$ represent the fractional contributions of the short and long lifetime components to the overall signal respectively, $\tau_1$ and $\tau_2$ are the short and long lifetime components respectively, and $C$ represents background light. The two lifetime components are used to distinguish between the free and bound forms of NAD(P)H and FAD (45, 46). The mean lifetime ($\tau_m$) is a weighted average of the free and bound lifetimes, and is calculated for both NAD(P)H and FAD in each pixel using Equation 5.2.

$$\tau_m = \alpha_1 * \tau_1 + \alpha_2 * \tau_2 \quad (5.2)$$

The optical redox ratio was calculated for each pixel by dividing the intensity of NAD(P)H by the intensity of FAD. A customized CellProfiler (v1.0.6025) routine was written to mask individual cell cytoplasms and extract average NAD(P)H and FAD intensities and lifetime components for each cell cytoplasm (47, 48). All reported redox ratios are normalized to average control values of the same patient and time point.

5.3.7 OMI index calculation

The OMI index, in this study, is a linear combination of three independent OMI endpoints (redox ratio, NAD(P)H $\tau_m$, and FAD $\tau_m$), each centered around the average value measured in control cells within each patient at the same experimental time point. This differs from previous descriptions (7, 36) where the end points are mean-centered across all cells in all treatment groups. This modification allows drug responses to be compared between patients in this study. As before, the redox ratio, NAD(P)H $\tau_m$, and FAD $\tau_m$ are given coefficients of (1,1,-1). A decrease in OMI index relative to control correlates with drug response, while an increase or lack of change indicates drug resistance.

5.3.8 Subpopulation analysis

A Gaussian mixture distribution model was used to assess heterogeneity of cellular metabolism (7, 36, 38, 49). OMI values for all cells within a treatment group and time point are input into this model described by Equation 5.3.

$$f(y;\Phi_g) = \sum_{i=1}^{g} \pi_i \phi(y;\mu_i,V_i) \tag{5.3}$$

Here, $g$ represents the number of subpopulations in the model, $\phi(y;\mu_i,V_i)$ is a normal probability density function where $\mu_i$ represents the mean and $V_i$ represents variance, and $\pi_i$ is the mixing proportion. Models containing $g$ = 1, 2, and 3 subpopulations are fit to the data, and the goodness of fit for each model is assessed using the Akaike information criterion (AIC) (50). The best fit of the three models, equivalent to the lowest AIC, is used to evaluate heterogeneity. For comparison, distributions are normalized such that all have an area under the curve of 1. The weighted heterogeneity index (wH-index, Eq. 5.4) is based on the Gaussian distribution models described by Eq. 5.3, and  is a modified form of the Shannon diversity index used to quantify the

degree of heterogeneity (37, 51).

$$\text{wH-index} = \sum\ (1 - p_i ln(p_i + 1)) * (\sigma_i + d_i) \tag{5.4}$$

Here, $i$ represents each subpopulation in the Gaussian distribution model, $d$ represents the distance between the median of each subpopulation and the median of the entire distribution, $p$ represents the proportion of all cells belonging to that subpopulation, and $\sigma$ is the standard deviation.

5.3.9 Organoid immunofluorescence

Organoids were rinsed in PBS and fixed for 20 minutes in 4% paraformaldehyde (VWR). Fixed organoids were rinsed and stored in PBS at 4°C until stained. Organoids were blocked for one hour in PBS with 10% goat serum and 0.3% Triton-X 100 (Sigma) at room temperature followed by co-incubation with Ki67 antibody conjugated to AlexaFluor 488 (1:50, Cell Signaling #11882S) and CC3 antibody conjugated to AlexaFluor 555 (1:50, Cell Signaling #9604S). Organoids were then washed in PBS and mounted to a slide using ProLong™ Diamond Antifade Mountant with DAPI (Molecular Probes). DAPI was imaged on the multiphoton microscope at 40x magnification using 750 nm for excitation and 440/80 nm bandpass filter for emission. AlexaFluor 488 was imaged using 965 nm for excitation and 550/100 nm filter for emission. AlexaFluor 555 was imaged using 1050 nm excitation and a 585/65 nm filter. Six or more organoids per treatment group were imaged and the percentage of Ki67-positive cells and cleaved caspase-3 positive cells in each organoid were quantified.

5.3.10 Patient-derived xenografts

Animal research was approved by the UW-Madison Institutional Animal Care and Use Committee. Organoids from Patient 13 were pelleted, re-suspended in media, and mixed 1:1 with Matrigel. This mixture was subsequently injected (100 µl) subcutaneously into bilateral flanks of female NOD *scid* gamma mice at 6 weeks old (NOD.Cg-*Prkdc*$^{scid}$ *Il2rg*$^{tm1Wjl}$/SzJ, The Jackson Laboratory) for initial PDX establishment. For treatment experiments, extracted tumors were mechanically minced to form a cell suspension, which was then mixed with Matrigel for injection into experimentally naïve female athymic nude mice at 6 weeks old (Hsd:Athymic nude-Foxn1$^{nu/nu}$, Envigo). Tumor volume was measured with calipers using the formula 0.5*length*width$^2$. When average tumor volume reached ~150 mm$^3$, mice were randomized into two groups. 20 mice received 100 mg/kg gemcitabine and 100 mg/kg nab-paclitaxel weekly via intraperitoneal injection while 23 control mice received only PBS weekly. Tumor volume was measured twice weekly. Mice were euthanized and tumors were collected when humane endpoints were reached.

5.3.11 High-depth targeted gene sequencing

Patient 13 organoids were sequenced using the Qiagen Comprehensive Cancer Panel and molecular barcode technology, with greater than 500x median coverage.

5.3.12 UMAP clustering

UMAP (Uniform Manifold Approximation and Projection) was performed on metabolic imaging data from all organoid cells (control and treated) from all patients and time points (N ~ 45,000) using the UMAP.py package (52). Nine metabolic measures: redox ratio, NAD(P)H $\tau_m$,

NAD(P)H $\alpha_1$, NAD(P)H $\tau_1$, NAD(P)H $\tau_2$, FAD $\tau_m$, FAD $\tau_1$, FAD $\tau_2$, and FAD $\alpha_1$ were reduced to two components. Points could have 10 neighbors in the manifold structure, and cosine was used to measure distance in the multivariate space. The two resulting components were visually displayed using the CRAN package ggplots2 (53).

### 5.3.13 Statistics

Differences in OMI index, optical redox ratio, NAD(P)H $\tau_m$, FAD $\tau_m$, CC3+%, and Ki67+% between treatment groups were tested using a Wilcoxon rank-sum test. Normalized tumor volumes were compared using a student t-test and a D'agostino-Pearson normality test. Treatment effect size was calculated with Glass's Δ (54).

## 5.4 Results

### 5.4.1 Organoid generation, drug screening, and optical metabolic imaging

Organoids were generated from fresh patient tissue samples acquired during distal pancreatectomy or pancreaticoduodenectomy (Whipple resection) surgeries. The overall rate of successful organoid formation was 67% (12 of 18 patients) (Fig. 5.1A), including mostly pancreatic tumors (pancreatic ductal adenocarcinomas (PDAC) and anaplastic carcinoma of the pancreas), along with two pancreatic intraepithelial neoplasia (PanIN) lesions and one ampullary adenocarcinoma (Appendix C Table C.1). 50% of the successfully cultured patient samples underwent neoadjuvant treatment prior to resection, including one patient that was downgraded from PDAC to PanIN following a complete pathologic response to chemotherapy (Patient 5). Neoadjuvant treatment did not impede organoid formation (75% and 60% success rates for pretreated and non-pretreated samples respectively). Viability and OMI were validated for

pancreatic organoids by quantifying metabolic inhibition to cyanide, a known inhibitor of the electron transport chain (Appendix C Fig. C.1). The effects of cyanide on OMI endpoints agreed with previous reports (27). After an establishment period, organoids were treated with a panel of standard and experimental pancreatic cancer therapies and imaged over a time course (Fig. 5.1B). This drug panel included 5-FU and gemcitabine chemotherapy, along with an experimental combination of TAK-228 (mTORC1/2 inhibitor) and ABT-263 (Bcl-2 and Bcl-xL inhibitor). Strategies to inhibit mTOR kinase activity could potentially induce apoptosis (55, 56), but this process is inhibited by antiapoptotic proteins of the Bcl-2 family (57). Thus, the combination of an mTORC1/2 inhibitor (TAK-228) with a Bcl-2 and Bcl-xL inhibitor (ABT-263) could strongly induce apoptosis in pancreatic cancer. Additional standard drugs were tested on organoids from Patients 6, 13, and 18 at later time points after patient treatment plans were obtained. The length of the organoid establishment period varied by patient between 4 and 12 days (Fig. 5.1C), and ended when organoids were clearly visible and proliferating with rounded edges. Differences in size and cellular quality of patient tumor samples likely contributed to the variance in time to maturation for organoid lines. One line (Patient 6) was thawed after being frozen, requiring additional time to re-establish a usable culture. Representative images demonstrate that multiphoton microscopy measures OMI endpoints with high resolution (Fig. 5.1D-F). This allows endpoints to be quantified in individual cells by masking each cell nucleus and cytoplasm using NAD(P)H fluorescence intensity (Fig. 5.1G). Tumor cells often grew as 3-dimensional hollow spheres (Fig. 5.1H), but other morphologies such as solid spheres were noted. The effects of drugs on the three OMI endpoints at 72 hours is summarized by comparing the mean values across all cells (Fig. 5.1I-K). A decrease in the mean optical redox ratio or NAD(P)H $\tau_m$ (see Equation 5.2), or an increase in the mean FAD $\tau_m$ is considered an indicator of response to that treatment, based

on previous studies in breast organoids (36). The OMI index combines the complimentary information provided by the three endpoints for each individual cell (Fig. 5.1L), and a decrease in the mean OMI index with treatment indicates a metabolic response. At the cellular level, Patient 14 organoids did not respond to 5-FU on average, but did respond to gemcitabine and targeted therapy (all $p<0.05$ vs. control).

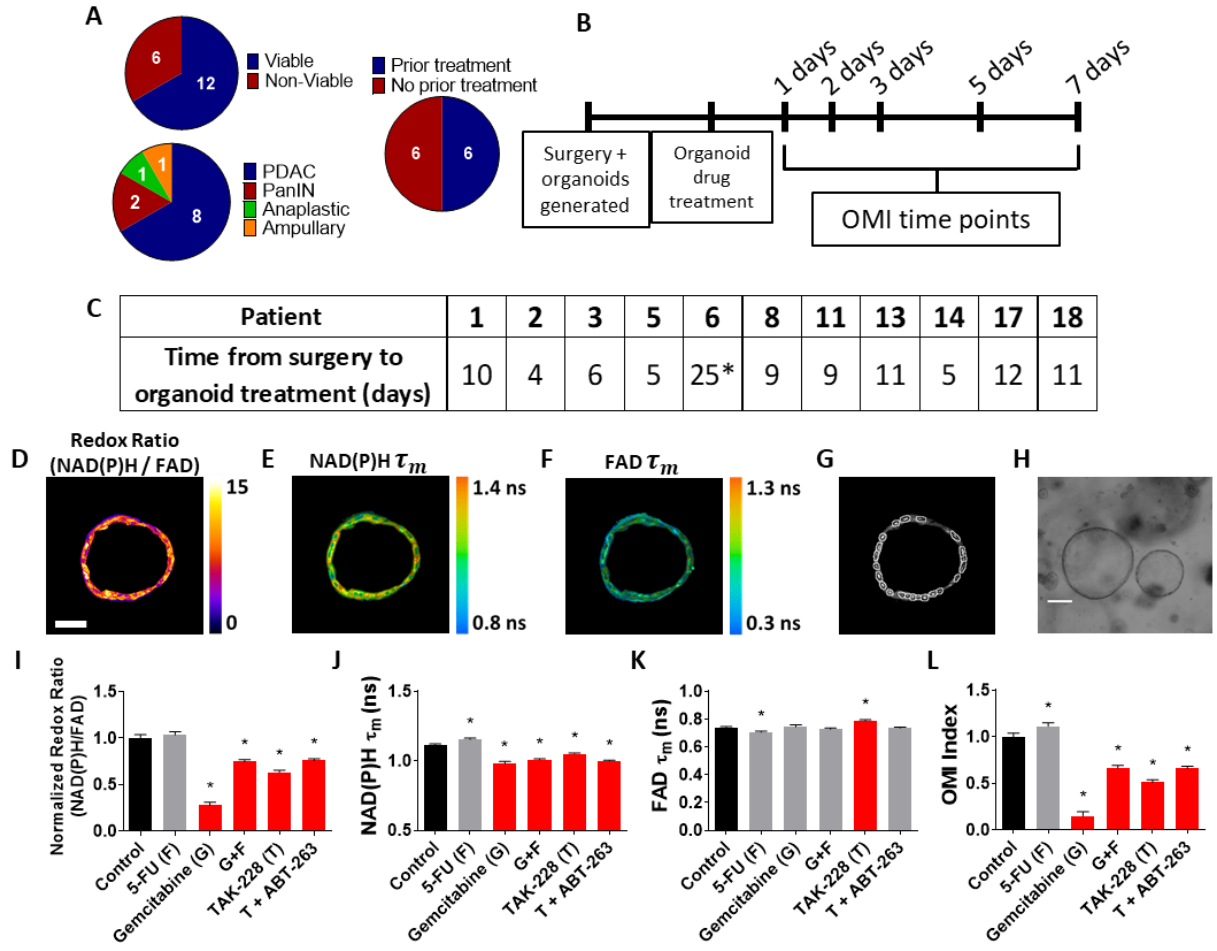


C

| Patient | 1 | 2 | 3 | 5 | 6 | 8 | 11 | 13 | 14 | 17 | 18 |
|---|---|---|---|---|---|---|---|---|---|---|---|
| Time from surgery to organoid treatment (days) | 10 | 4 | 6 | 5 | 25* | 9 | 9 | 11 | 5 | 12 | 11 |




**Figure 5.1. Pancreatic organoid generation, drug screening, and optical metabolic imaging.** **A,** Pie charts depicting the success rate for generating viable organoids from patient pancreatic lesions (top left), the distribution of PDAC, PanIN, anaplastic cancer, and ampullary cancer among successfully generated organoids (bottom left), and the distribution of previously treated versus untreated tumors among successfully generated organoids (right). **B,** Experimental workflow begins with a brief period where organoids are allowed to expand after initial generation, followed by drug treatment, and a series of time points where OMI is performed to track dynamic organoid drug responses. **C,** Time between organoid generation and drug treatment for each individual patient in the study. * Patient 6 organoids were thawed from frozen stocks and required additional

time in culture. Representative redox ratio (**D**), NAD(P)H $\tau_m$ (**E**), and FAD $\tau_m$ (**F**) images of an untreated pancreatic organoid taken 6 days after surgical resection (Patient 14). Scale bar is 50 μm. **G**, Masks of individual cell cytoplasms overlaid onto NAD(P)H intensity image. **H,** Representative brightfield image of pancreatic organoids (Patient 14). Scale bar is 200 μm. The effect of 72 hours of drug treatment on the redox ratio (**I**), NAD(P)H $\tau_m$ (**J**), and FAD $\tau_m$ (**K**) of pancreatic organoids quantified at the single-cell level (Patient 14). **L,** The effect of 72 hours of drug treatment on OMI index, a composite metric of metabolic drug response (Patient 14). Error bars indicate mean ± SEM. * $p<0.05$ vs. control. Red bar indicates response to treatment (significant reduction in mean redox ratio, NAD(P)H $\tau_m$, or OMI index, or significant increase in mean FAD $\tau_m$).

5.4.2 OMI of organoids resolves differential sensitivities to relevant drug treatments

A wide variety of OMI index responses were elicited across treatment conditions and patient samples. In addition to statistical significance of these drug responses, treatment effect sizes were calculated on all OMI measurements in order to determine their magnitude. A heatmap of OMI index treatment effect size, calculated using Glass's Δ at 72 hours post-treatment, shows significant inter-patient heterogeneity for drug response in organoids (Fig. 5.2A; additional drugs and time points in Appendix C Fig. C.2). In a subset of patient samples, a significant fibroblast population (co-cultured with organoids) migrated from the 3D matrix and adhered to the 2D glass coverslip. Heterogeneity in these fibroblasts has been shown in organoid models of murine pancreatic cancer (7, 58). A heatmap of OMI index treatment effect size, calculated using Glass's Δ at 72 hours post-treatment, also shows inter-patient drug response heterogeneity in co-cultured fibroblasts (Fig. 5.2B; Appendix C Fig. C.3). Not all drugs were tested on every patient's cells for the full time-course. Drug choices were made based on the availability of viable organoids and the clinical treatment plans (or lack thereof) for individual patients. All organoids were initially treated with the drug panel in Figure 5.1 because gemcitabine and 5-FU combination therapy was most likely to be prescribed after surgery (excluding Patient 6; it was known in advance that they would receive oxaliplatin rather than gemcitabine). When additional drugs were prescribed for a patient such as nab-paclitaxel or the FOLFIRINOX regimen, their panels were expanded to incorporate

those treatments. Responses to a chemotherapy drug (5-FU) and an experimental targeted therapy combination (TAK-228 and ABT-263) at days 1, 3, and 7 demonstrate how OMI can track single-cell drug responses over time within organoids (Fig. 5.2C; additional drugs and time points in Appendix C Fig. C.4) and co-cultured fibroblasts (Fig. 5.2D; Appendix C Fig. C.5). For example, response data show an increased response to TAK-228 and ABT-263 combination targeted therapy over time, while 5-FU remained ineffective for most patients.

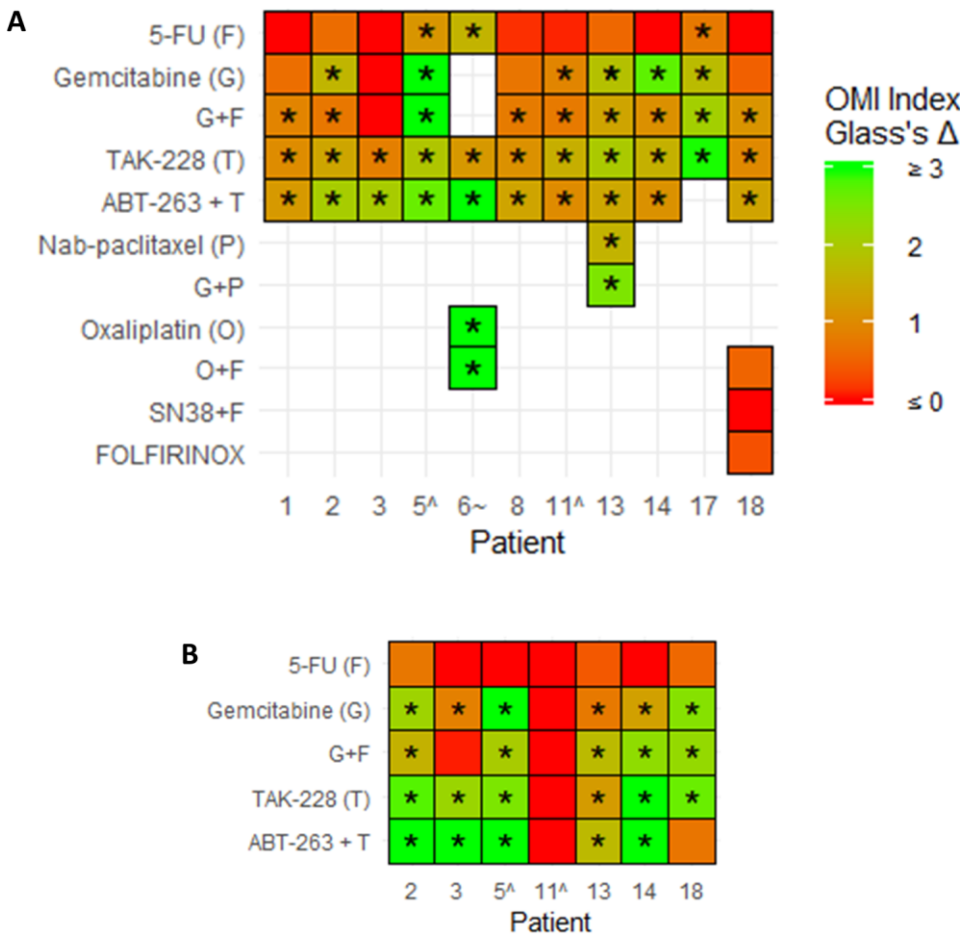

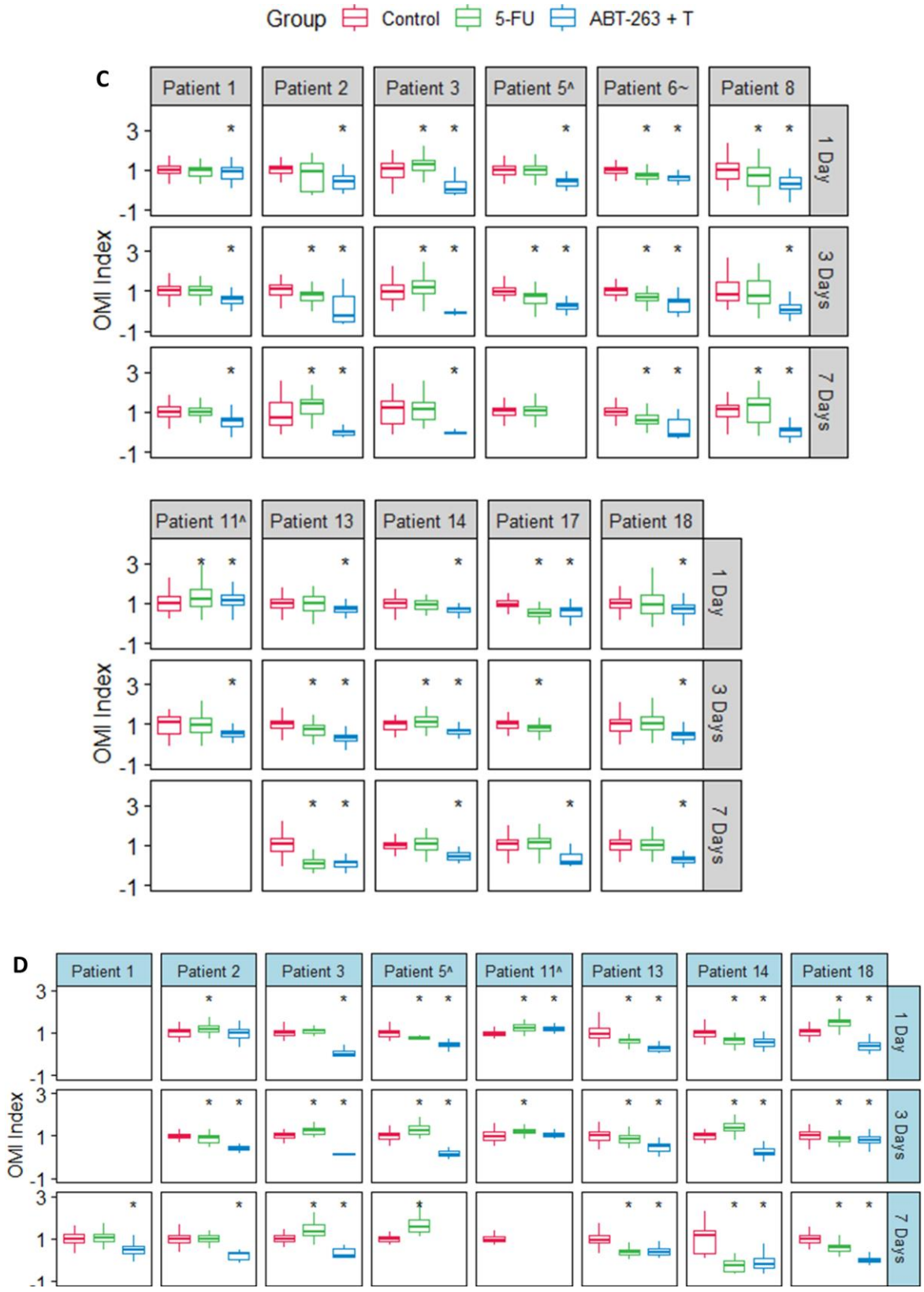
Group
Control
5-FU
ABT-263 + T
C
Patient 1
Patient 2
Patient 3
Patient 5^
Patient 6~
Patient 8
Patient 11^
Patient 13
Patient 14
Patient 17
Patient 18
OMI Index
1 Day
3 Days
7 Days
D

**Figure 5.2. OMI of organoids resolves differential sensitivities to relevant drug treatments.** **A** and **B,** Heatmap representation of the OMI index treatment effect size (Glass's Δ) at 72 hours in organoids (**A**) and fibroblasts co-cultured with organoids (**B**). * Glass's $\Delta \geq 0.75$. **C** and **D,** Boxplot comparing metabolic responses to 5-FU and ABT-263 combined with TAK-228 (A+T) between patients and time points in organoids (**C**) and fibroblasts co-cultured with organoids (**D**). Response is measured using OMI index at the single-cell level. A decrease in OMI index versus control indicates response to treatment. Center line indicates median, box indicates interquartile range (IQR), and whiskers indicate most extreme data point within 1.5*IQR. '^' and '~' indicate the patient lesion was diagnosed as PanIN or ampullary cancer, respectively. * $p<0.05$ vs. control.

5.4.3 OMI captures non-genetic cellular heterogeneity in pancreatic organoids

Additional analysis was performed on Patient 13 organoids to evaluate the utility of OMI. The combination of gemcitabine and nab-paclitaxel was used in addition to the standard treatment panel on Patient 13's organoids to mimic the treatment received prior to sample collection (Fig. 5.3A). Population density modeling was used to determine whether cellular subpopulations of metabolic response were present in organoids for each treatment condition at 72 hours (Fig. 5.3B; additional drugs in Appendix C Fig. C.6). Metabolic subpopulations were observed in controls and organoids treated with gemcitabine and nab-paclitaxel (G+P) combination. Patient 13 responded poorly to this treatment prior to surgery and organoid generation. OMI of organoids treated with the experimental combination of TAK-228 and ABT-263 resulted in a single, homogeneous drug-responsive population.

High-depth targeted gene sequencing was performed on untreated Patient 13 organoids to determine whether subclonal populations could be resolved to explain the metabolic heterogeneity (Fig. 5.3C). A mutation in *TP53* tumor-suppressor gene (stop-gain Gln165*) and a mutation in the *KRAS* oncogene (G12V) were found with allele frequencies of 100% and 52%, respectively, indicating a single population of cells with homogeneous driver mutations. Mutations with allele frequencies between 10-30% are indicative of potential subclonal populations (59). Only 4 alterations were found to occur within this range, with 3 of the 4 at frequencies just below the top

of this range. None of the alterations identified are pathogenic or known to alter tumor biology. This indicates that this patient sample was quite homogeneous on a genetic level and the treatment subpopulations identified are likely related to metabolic changes and not differing mutation profiles. To test whether OMI agreed with traditional cell markers, a subset of organoids were fixed at 72 hours of treatment and dual-stained using immunofluorescence for cleaved caspase-3 (CC3) and Ki67 to quantify apoptosis and proliferation rates, respectively (Fig. 5.3D,E; Appendix C Fig. C.7). Three treatments caused both a significant increase ($p<0.05$ vs. control) in apoptosis and a significant decrease in proliferation: gemcitabine, gemcitabine and nab-paclitaxel, and TAK-228 and ABT-263. When averages were compared, proliferation rates correlated with changes in cell metabolism measured by OMI index ($p<0.001$), but apoptosis rates did not (Appendix C Fig. C.8). A patient-derived xenograft line was generated and athymic nude mice were treated with combination therapy of gemcitabine and nab-paclitaxel (Appendix C Fig. C.9) to determine if *in vivo* treatment response correlates with that seen in organoids. Tumor growth was tracked by direct caliper measurement and an early reduction was observed over the first 7 days ($p<0.05$); however, the effect was not sustained.

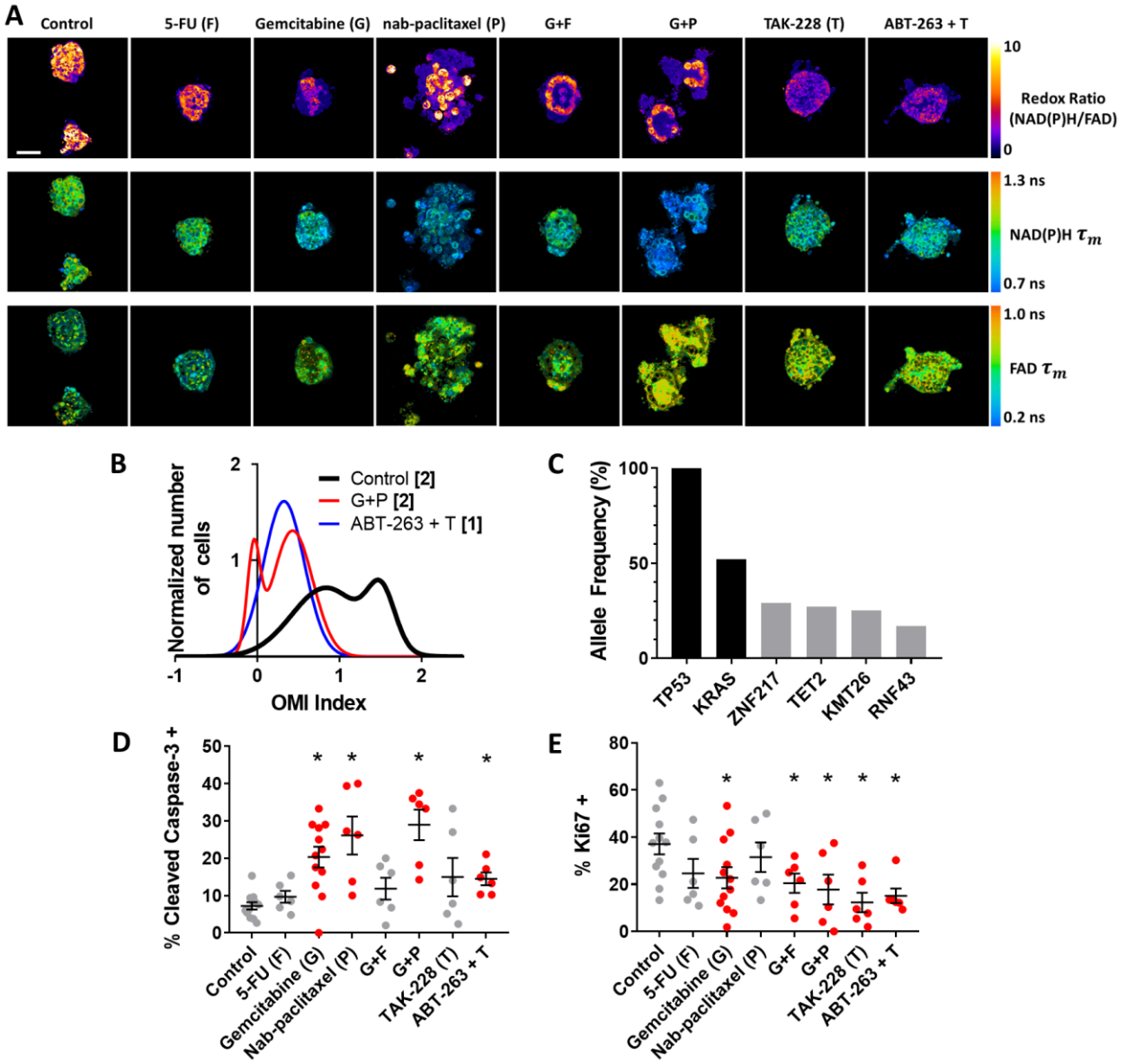


**Figure 5.3. OMI captures non-genetic cellular heterogeneity in pancreatic organoids. A,** Representative images of the redox ratio, NAD(P)H $\tau_m$, and FAD $\tau_m$ in organoids generated from Patient 13 (anaplastic carcinoma of the pancreas), treated with standard chemotherapies and experimental targeted therapies for 72 hours. Scale bar is 50 μm. **B,** Normalized density distributions of the OMI index of individual cells contain subpopulations with G+P treatment, but not ABT-263 +T treatment after 72 hours. Bracketed number indicates number of subpopulations. **C,** High-depth targeted cancer gene sequencing of Patient 13 organoids. Allele frequencies of ~50% for *KRAS* and 100% for *TP53* were found (black bars). Alterations with allele frequencies of 10-30% were detected (gray bars), but none of these alterations were pathogenic. **D,** Cleaved caspase-3 staining of organoids shows differences in apoptosis between treatment conditions after 72 hours of treatment. **E,** Ki67 staining of organoids shows differences in proliferation between treatment conditions after 72 hours. Each dot represents one organoid (mean ± SEM), and red indicates significant response to treatment. *p<0.05 vs. control.

5.4.4 Heterogeneity of drug response in organoids agrees with later patient recurrence during adjuvant therapy

Seven patients received adjuvant drug treatment following surgical resection of their tumor. Clinical treatment efficacy was tracked and compared to the OMI prediction of drug response at 72 hours post-treatment in patient-matched organoids. Four patients whose organoids exhibited a homogeneous response to the patient's prescribed therapy were classified as "predicted responders" (Fig. 5.4). Representative redox ratio, NAD(P)H $\tau_m$, and FAD $\tau_m$ images demonstrate the morphological variety as well as a decrease in size or structural integrity with treatment of organoids generated from these patients (1, 2, 6, and 14) (Fig. 5.4A-D). Representative images of collapsed organoids that lose their hollow morphology (Fig. 5.4C,D), are the result of treatment sensitivity and are generally not present in untreated cultures. Furthermore, the OMI index reflects an organoid response to the prescribed treatment for these patients ($p<0.0001$) (Fig. 5.4E-H). Glass's $\Delta$ effect size was calculated for each treatment's OMI index value in addition to statistical significance, and was found to be consistently greater than 0.75 for these patients. Cellular population density modeling of organoids from Patients 1, 2, 6, and 14 did not reveal distinct metabolic subpopulations of response (Fig. 5.4I-L). In each case, one homogeneous population of response was found. Fibroblasts co-cultured with organoids from Patients 2 and 14 also showed homogeneous response to the patient's prescribed therapy (Appendix C Fig. C.10).

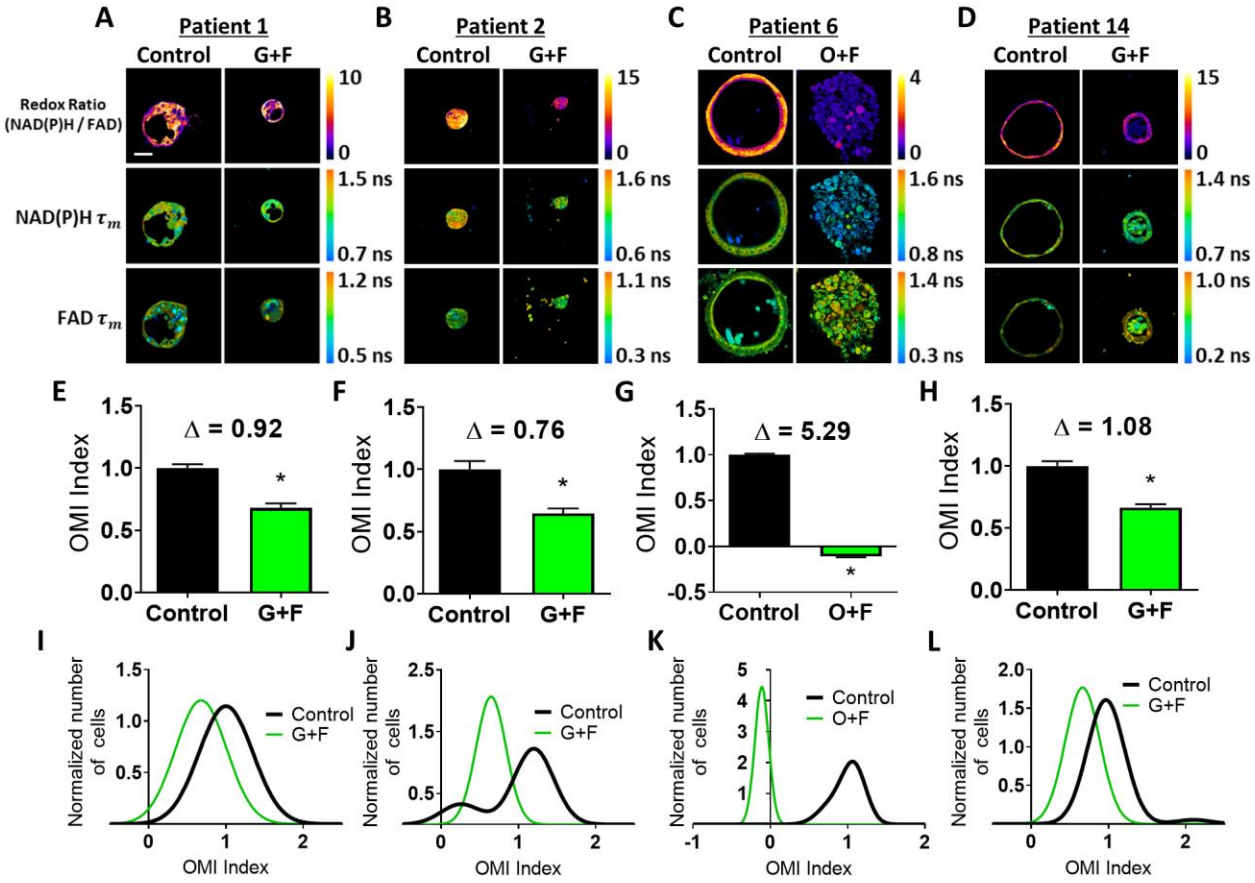


**Figure 5.4. Organoids of Patients 1, 2, 6, and 14 exhibit homogeneous response to patient therapy. A-D,** Representative redox ratio, NAD(P)H $\tau_m$, and FAD $\tau_m$ images of pancreatic organoids from Patients 1 (**A**), 2 (**B**), 6 (**C**), and 14 (**D**). Left columns indicate control organoids, and right columns indicate organoids treated with the same drugs as the patient adjuvant treatment. Scale bar is 50 μm. **E-H,** The effect of the same drugs on the OMI index averaged across all cells in organoids derived from Patient 1 (**E**), 2 (**F**), 6 (**G**), and 14 (**H**). Error bars indicate mean ± SEM. * p<0.0001. **I-L,** Single-cell OMI index subpopulation analysis of treatment response in organoids from Patient 1 (**I**), 2 (**J**), 6 (**K**), and 14 (**L**).

Three patients (3, 8, and 18) whose organoids exhibited treatment response heterogeneity were classified as "predicted non-responders" (Fig. 5.5). Representative images show a lack of apparent response in terms of OMI endpoints (Fig. 5.5A-C). On average, cells from Patient 3 and 8 organoids did not respond to the patient's prescribed treatment ($p<0.05$ increase in OMI index and no significant change, respectively, Fig. 5.5D,E). Unlike 3 and 8, the OMI index of Patient 18's organoid cells significantly decreased with treatment ($p<0.0001$, Fig. 5.5F), but further OMI analysis also predicts poor response for this patient. The treatment effect size was small (Glass's

$\Delta < 0.3$) in organoids for all three patients, and all exhibited multiple subpopulations of tumor cells post-treatment, some of which overlapped completely with control distributions or contained OMI index values above control (Fig. 5.5G-I). Patient 3 organoids treated with gemcitabine and 5-FU exhibited a drug-responsive minority subpopulation with a smaller OMI index than the mean of the control population (yet still within the control distribution), but also a larger drug-resistant subpopulation that had a higher OMI index than the mean of the control population (Fig. 5.5G). Patient 8 organoids contained high and low OMI index subpopulations that were not affected by 5-FU treatment beyond a small increase in the percentage of cells falling in the high OMI index group (Fig. 5.5H). A majority of cells from Patient 18 treated with FOLFIRINOX showed response to treatment, but two FOLFIRINOX-resistant subpopulations remained (Fig. 5.5I). Fibroblasts co-cultured with organoids from Patient 3 also showed a lack of response to gemcitabine and 5-FU, along with treatment-induced metabolic heterogeneity (Appendix C Fig. C.10).

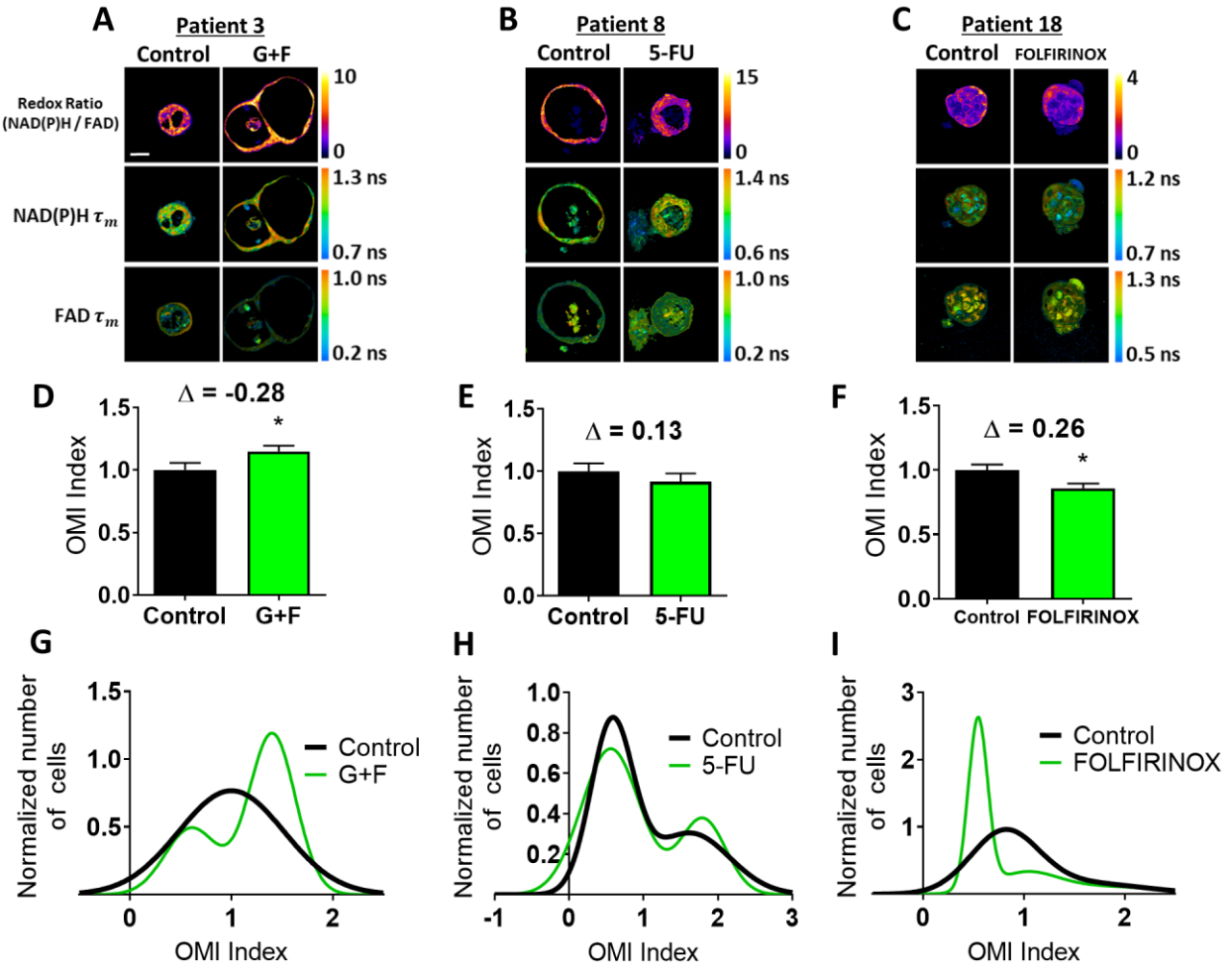


**Figure 5.5. Organoids of Patients 3, 8, and 18 exhibit partial or no response to patient therapy. A-C,** Representative redox ratio, NAD(P)H $\tau_m$, and FAD $\tau_m$ images of pancreatic organoids from Patients 3 (**A**), 8 (**B**), and 18 (**C**). Left columns indicate control organoids, and right columns indicate organoids treated with the same drugs as the patient adjuvant treatment. Scale bar is 50 μm. **D-F,** The effect of the same drugs on the OMI index averaged across all cells in organoids derived from Patient 3 (**D**), 8 (**E**), and 18 (**F**). Error bars indicate mean ± SEM. * $p<0.05$. **G-I,** Single-cell OMI index subpopulation analysis of treatment response in organoids from Patient 3 (**G**), 8 (**H**), and 18 (**I**).

The time between surgical resection and the first evidence of recurrence, or recurrence free survival (RFS) time, was plotted for these seven patients (Fig. 5.6A). One year of follow-up data is available for Patients 1, 2, 3, 6, 8, and 14. Patients 3 and 8, classified as predicted non-responders, experienced recurrences within one year. Patients 1, 2, 6, and 14, classified as predicted responders, each survived at least one year after surgery without a recurrence. One year

of follow-up data is not yet available for 18. Patients 1, 6, 14, and 18 have no signs or symptoms of disease at the time of this writing. Patients with a RFS >12 months had a higher OMI index Glass's Δ in organoids at 72 hours post-treatment than patients with a RFS <12 months (Fig. 5.6B). The degree of heterogeneity, quantified by the wH-index, decreased in treated vs. control organoids in patients with a RFS >12 months, and increased in treated vs. control organoids in patients with a RFS <12 months (Fig. 5.6C).

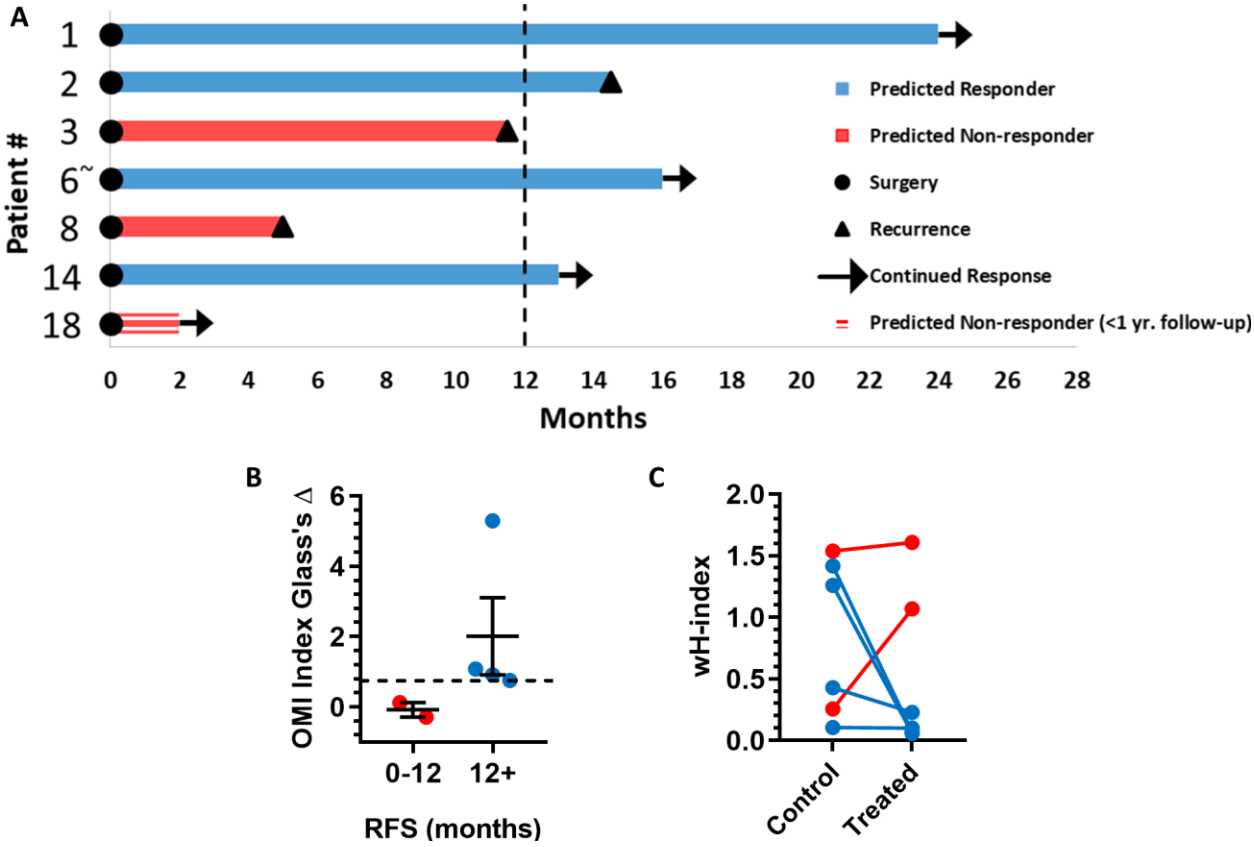


**Figure 5.6. Patient clinical outcomes while on adjuvant therapy. A,** Swimmer plot indicating the number of months without recurrence following surgical resection of the tumor and adjuvant treatment. Patients are classified as predicted responders and non-responders based on organoid response profiles. Arrows indicate that the patient continues to survive without recurrence at the time of publication. '~' indicates the patient's lesion was diagnosed as ampullary cancer. **B,** Patients with RFS > 12 months had higher OMI index effect sizes at 72 hours (Glass's Δ) than patients with RFS < 12 months (mean ± SEM). Dotted line represents proposed cutoff of Δ = 0.75. **C,** Patients with RFS > 12 months show a decrease in wH-index with treatment compared to control organoids. Patients with RFS < 12 months show an increase in wH-index with treatment compare to control organoids. Error bars not visible. N=1000 fits/group.

5.4.5 Dimensional reduction of single-cell OMI data reveals organoid cell clustering by patient of origin

UMAP dimensional reduction analysis was performed on the OMI variables of organoid cells imaged at all time points (45,752 cells) to determine whether cells from different patients exhibited unique metabolic profiles (Fig. 5.7). Cells from the same patient generally clustered together (Fig. 5.7A). Some patients (e.g. 6, 13, 17) formed a primary cluster and a secondary, smaller cluster. Plotting control and treated cells separately revealed that these secondary clusters occurred due to drug treatment (Fig. 5.7B,C).

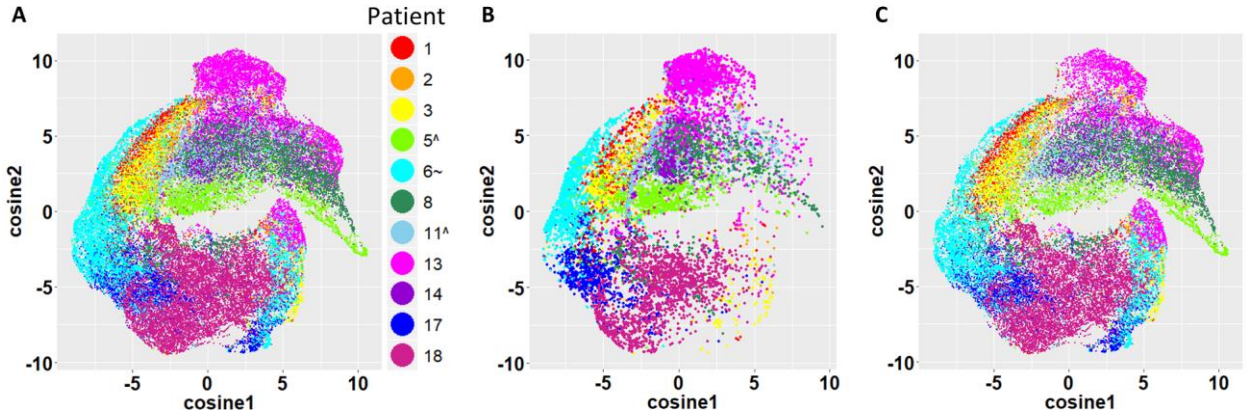


**Figure 5.7. UMAP dimensional reduction analysis of organoid cell metabolism reveals clustering by patient. A,** UMAP of all organoid cells from all time points color-coded post-analysis by patient of origin. **B,** Untreated cells only. **C,** Drug-treated cells only. '^' and '~' indicate the patient lesion was diagnosed as PanIN or ampullary cancer, respectively.

## 5.5 Discussion

Pancreatic organoids can be used for drug screens directly on patient cells, which could enable rational treatment planning for individual patients (7-9). Organoids also provide a platform to discover new drugs and drug combinations to treat pancreatic cancer patients, who currently suffer from a severe lack of effective treatment options. Existing methods to evaluate drug response in organoids ignore cellular heterogeneity, which can lead to patient relapse. Thus, our group developed OMI as a single-cell analysis tool to detect minority subpopulations of drug-

resistant cells existing within living organoids that would otherwise appear responsive. We have previously shown that OMI detects subpopulations of drug response in murine PDAC organoids and early treatment responses in human pancreatic organoids (7). Here, we investigate for the first time whether OMI measurements of early drug response heterogeneity in organoids can capture meaningful treatment responses in individual pancreatic cancer patients.

Organoids were successfully generated from PDAC, precancerous PanIN, anaplastic carcinoma of the pancreas, and ampullary adenocarcinoma tissue samples, with equal success for both pre-treated and treatment-naïve samples. While some time is required to establish healthy organoids for drug screening, OMI measurements began within a 4-12 day window of the patient's surgery. This is crucial for generating individualized treatment plans because pancreatic cancer is often advanced at diagnosis, and any delay to receiving effective therapy may increase mortality. Three independent OMI endpoints (redox ratio, NAD(P)H $\tau_m$, and FAD $\tau_m$) were quantified in response to panels of standard drugs (gemcitabine and 5-FU) and experimental targeted therapies that have shown promise in pancreatic cancer (TAK-228 and ABT-263) (Fig. 5.1). Each OMI endpoint captures unique metabolic information (27), and quantitatively combining these three independent measurements into the OMI index provides a technique to evaluate early metabolic response to treatment. An oncologist could use this technology to quickly determine if a patient would benefit from experimental targeted therapies over standard chemotherapies, rather than waiting for standard chemotherapy to fail while exposing the patient to unnecessary toxicities.

OMI was used to track drug response at the single-cell level over a time course of treatment for 11 pancreatic cancer, PanIN, and ampullary cancer patients (Fig. 5.2). Time courses are vital to evaluate response, because cells often evolve mechanisms of drug resistance that are not immediately apparent. For example, Patient 17 organoids initially responded to 5-FU ($p<0.05$ vs.

control, Glass's $\Delta = 1.66$ at 24 hours), but became resistant at day 7 ($p>0.05$ vs. control, Glass's $\Delta = -0.04$). This is a major advantage of OMI over methods that destroy the sample. Drug response was also evaluated using OMI in patient-derived fibroblasts, which grew along with organoids for most patients. The dense fibrotic extracellular matrix surrounding pancreatic tumors can hinder drug delivery by reducing blood flow and raising interstitial fluid pressure (60, 61). Thus, it may be vital to evaluate whether drugs can target both the tumor and its stromal microenvironment to enhance delivery (16, 17). For example, Patient 18's organoids showed response to the combination of TAK-228 and ABT-263 (Glass's $\Delta > 0.75$) at 72 hours while co-cultured Patient 18 fibroblasts did not, suggesting that this drug regimen could successfully kill tumor cells but may have difficulty reaching them. This highlights the need for OMI-organoid technology to aid in the discovery of new treatment strategies to target both a tumor and its stroma. Additionally, there were multiple instances of novel drug combinations outperforming standard chemotherapies. For instance, TAK-228 and ABT-263 elicited a more significant metabolic response in both Patient 3 organoids and fibroblasts than the prescribed standard gemcitabine and 5-FU regimen.

Our group has shown that OMI non-invasively distinguishes unique groups of cells by their metabolic properties in human breast cancer (36, 38), human head and neck cancer (37), and murine PDAC (7). Here, we performed subpopulation analysis on Patient 13 organoid cells to evaluate whether OMI could distinguish cells with distinct drug responses in human pancreatic cancer (Fig. 5.3; Appendix C Fig. C.6). Indeed, many treatments caused two distinct subpopulations to form in organoids within 72 hours post-treatment, including the standard chemotherapy regimen given to the patient prior to surgery and organoid generation (gemcitabine with nab-paclitaxel). This suggests that a drug-resistant cell subpopulation persisted throughout

the patient's neoadjuvant treatment, and was captured in the organoids. Accordingly, pathology of the patient's resected tumor indicated a poor response to gemcitabine with nab-paclitaxel.

Conversely, targeted therapies induced single populations of homogenous response in Patient 13 organoids. While the combination of gemcitabine and nab-paclitaxel caused a similar average reduction in OMI index as the combination of TAK-228 and ABT-263, the former showed heterogeneity and a drug-resistant population, while the latter showed a homogeneous response. This suggests that this targeted therapy combination (TAK-228 and ABT-263) may have been a beneficial alternative for Patient 13. One month after surgery, metastasis in the liver was found on an ultrasound, and the patient died less than two weeks later. This highlights the need for a technology that can rapidly evaluate drug sensitivity in patient cells.

Untreated Patient 13 organoids were also deep-sequenced to determine if genetic heterogeneity could be the source of metabolic subpopulations in untreated organoids. Our metabolic imaging data shows greater heterogeneity than predicted by deep sequencing, as no subclonal populations with pathogenic mutations were found in these organoids. This suggests that the OMI index heterogeneity is likely not genetic in nature, and that OMI is more effective for detecting divergent populations in organoid cultures than destructive sequencing techniques. This work also highlights the importance of metabolic heterogeneity within cancer samples to capture therapeutic response. At 72 hours, a subset of Patient 13 organoids were fixed and stained for proliferation and apoptosis markers. In some cases, OMI detected shifts in metabolism with treatment that had not triggered apoptosis, suggesting that metabolic changes can precede Ki67/CC3 indicators of cell fate, and are an earlier indicator of drug efficacy.

The combination of gemcitabine and nab-paclitaxel was evaluated *in vivo* in a PDX line established from Patient 13 organoids. A small but transient response in average tumor growth was

detected (Appendix C Fig. C.9). This poor response is in agreement with the heterogeneous effect found in organoids using OMI. While the PDX model accurately captured the presence of drug resistance in Patient 13's cells, it required months to first establish the PDX line, expand it, and then assess a time course of treatment. While PDX models are an important tool, our studies show that drug screens on organoids can provide more detailed response information with increased cost effectiveness in a clinically meaningful time frame.

OMI of organoids generated from tissues collected at surgery agreed with patient outcome on adjuvant therapy (Fig. 5.4-5.6). Treatment response in organoids was evaluated on the basis of both metabolic heterogeneity in treated organoids, as well as the effect size of the OMI index response. For Patients 1, 2, 3, 6, 8, and 14, OMI of organoid heterogeneity predicted whether or not the patient survived one year post-surgery without a recurrence. Based on data from this initial patient cohort, a proposed OMI index effect size cutoff of 0.75, in parallel with a decrease in wH-index could classify patients as predicted responders vs. non-responders. We cannot yet evaluate our prediction that Patient 18 will experience a recurrence within one year of surgery. Overall, our results suggest that early metabolic responses in pancreatic organoids can successfully capture the response of tumor cells *in vivo* that are not removed during surgery. In all cases, organoid viability yielded sufficient material to measure heterogeneity in response to the patient's prescribed drug treatment and evaluate multiple alternative drug options, highlighting the potential of OMI of organoids to aid in drug discovery and development within diverse patient populations. While many other factors beyond tumor cell treatment response affect pancreatic cancer survival in the adjuvant setting (i.e. surgical margins, stage, grade, etc.), the organoid-OMI platform can be used to identify drug resistance and eliminate objectively poor drug options.

Finally, we used a dimensionality reduction approach to determine the influence of patient of origin on cellular metabolism in pancreatic organoids (Fig. 5.7). UMAP analysis was performed on metabolic parameters from all 45,000+ cells, completely naïve to patient of origin. These organoid cells clearly clustered by patient, but also show clear heterogeneity within each patient. This reinforces the fact that cells from a patient are metabolically heterogeneous, but more metabolically similar to each other than cells from other patients. This metabolic diversity between patients as well as within patients underlines the need for personalized medicine approaches to cancer treatment that incorporate single-cell metabolic measurements.

Organoids offer a compelling platform for the interrogation of a variety of drugs *ex vivo*. This platform provides an extracellular matrix that can support co-culture of both patient-derived cancer cells and fibroblasts, thus creating a more robust model of human disease. OMI has many benefits over existing methods to assess drug response in organoids, in part because it is completely non-destructive and it measures unique features of cell metabolism. OMI can measure response on the single-cell level to assess heterogeneity as quickly as 24 hours post-treatment and can track dynamic responses over time. We used these optical imaging tools to show that organoid drug screens can assess heterogeneous drug responses in pancreatic cancer patients (and one rare ampullary cancer patient) within a clinically meaningful time frame. Additionally, the ability to detect a drug-resistant subpopulation of cells following neoadjuvant treatment failure was demonstrated with OMI, and alternative treatment options were evaluated. In cases where multiple treatment options are likely beneficial, clinicians could use this platform to select the regimen that presents the fewest side effects for the patient, significantly improving quality of life. Taken together, OMI of organoids is a sensitive, high-throughput tool to select the best treatments for

individual pancreatic cancer patients based on single-cell metabolic response, which could improve patient outcomes and enable new drug discovery.

### 5.6 Acknowledgments

Thank you to the patients that graciously donated tissue to this study. Thank you to the Translation Science BioCore BioBank and its staff at the University of Wisconsin Carbone Cancer Center for the collection of donated tissue. Thank you to Amani Gillette and Mohammad Karim for their time, expertise, and assistance acquiring OMI images. The Skala laboratory is supported by grants from the NSF Graduate Research Fellowship (DGE-1445197; JTS), the NSF (CBET-1642287), Stand Up to Cancer (SU2C-AACR-IG-08-16, SU2C-AACR-PS-18) and the NIH (R01 CA185747, R01 CA205101, R01 CA211082, R21 CA224280, U01 TR002383). The Deming laboratory is supported by the NIH (R37 CA226526) and the University of Wisconsin Carbone Cancer Center (Support Grant P30 CA014520 and the UWCCC Pancreatic Cancer Taskforce).

### 5.7 References

[1] Siegel RL, Miller KD, Jemal A. Cancer statistics, 2018. CA Cancer J Clin. 2018;68(1):7-30.

[2] Rahib L, Smith BD, Aizenberg R, Rosenzweig AB, Fleshman JM, Matrisian LM. Projecting cancer incidence and deaths to 2030: the unexpected burden of thyroid, liver, and pancreas cancers in the United States. Cancer Res. 2014;74(11):2913-21.

[3] Spanknebel K, Conlon KC. Advances in the surgical management of pancreatic cancer. Cancer J. 2001;7(4):312-23.

[4] Oettle H, Neuhaus P, Hochhaus A, Hartmann JT, Gellert K, Ridwelski K, et al. Adjuvant chemotherapy with gemcitabine and long-term outcomes among patients with resected pancreatic cancer: the CONKO-001 randomized trial. JAMA. 2013;310(14):1473-81.

[5] Neoptolemos JP, Palmer DH, Ghaneh P, Psarelli EE, Valle JW, Halloran CM, et al. Comparison of adjuvant gemcitabine and capecitabine with gemcitabine monotherapy in patients with resected pancreatic cancer (ESPAC-4): a multicentre, open-label, randomised, phase 3 trial. Lancet. 2017;389(10073):1011-24.

[6] Witkiewicz AK, Balaji U, Eslinger C, McMillan E, Conway W, Posner B, et al. Integrated Patient-Derived Models Delineate Individualized Therapeutic Vulnerabilities of Pancreatic Cancer. Cell Rep. 2016;16(7):2017-31.

[7] Walsh AJ, Castellanos JA, Nagathihalli NS, Merchant NB, Skala MC. Optical Imaging of Drug-Induced Metabolism Changes in Murine and Human Pancreatic Cancer Organoids Reveals Heterogeneous Drug Response. Pancreas. 2016;45(6):863-9.

[8] Moreira L, Bakir B, Chatterji P, Dantes Z, Reichert M, Rustgi AK. Pancreas 3D Organoids: Current and Future Aspects as a Research Platform for Personalized Medicine in Pancreatic Cancer. Cell Mol Gastroenterol Hepatol. 2018;5(3):289-98.

[9] Wolff RA, Wang-Gillam A, Alvarez H, Tiriac H, Engle D, Hou S, et al. Dynamic changes during the treatment of pancreatic cancer. Oncotarget. 2018;9(19):14764-90.

[10] Boj SF, Hwang CI, Baker LA, Chio, II, Engle DD, Corbo V, et al. Organoid models of human and mouse ductal pancreatic cancer. Cell. 2015;160(1-2):324-38.

[11] Tiriac H, Belleau P, Engle DD, Plenker D, Deschenes A, Somerville T, et al. Organoid profiling identifies common responders to chemotherapy in pancreatic cancer. Cancer Discov. 2018.

[12] Huang L, Holtzinger A, Jagan I, BeGora M, Lohse I, Ngai N, et al. Ductal pancreatic cancer modeling and drug screening using human pluripotent stem cell- and patient-derived tumor organoids. Nat Med. 2015;21(11):1364-71.

[13] Romero-Calvo I, Weber C, Ray M, Brown M, Kirby K, Nandi RK, et al. Human Organoids Share Structural and Genetic Features with Primary Pancreatic Adenocarcinoma Tumors. Mol Cancer Res. 2018.

[14] Tsai S, McOlash L, Palen K, Johnson B, Duris C, Yang Q, et al. Development of primary human pancreatic cancer organoids, matched stromal and immune cells and 3D tumor microenvironment models. BMC Cancer. 2018;18(1):335.

[15] Jenkins RW, Aref AR, Lizotte PH, Ivanova E, Stinson S, Zhou CW, et al. Ex Vivo Profiling of PD-1 Blockade Using Organotypic Tumor Spheroids. Cancer Discov. 2018;8(2):196-215.

[16] Majety M, Pradel LP, Gies M, Ries CH. Fibroblasts Influence Survival and Therapeutic Response in a 3D Co-Culture Model. PLoS One. 2015;10(6):e0127948.

[17] Micke P, Ostman A. Tumour-stroma interaction: cancer-associated fibroblasts as novel targets in anti-cancer therapy? Lung Cancer. 2004;45 Suppl 2:S163-75.

[18] Junttila MR, de Sauvage FJ. Influence of tumour micro-environment heterogeneity on therapeutic response. Nature. 2013;501(7467):346-54.

[19] Marusyk A, Polyak K. Tumor heterogeneity: causes and consequences. Biochim Biophys Acta. 2010;1805(1):105-17.

[20] Burrell RA, McGranahan N, Bartek J, Swanton C. The causes and consequences of genetic heterogeneity in cancer evolution. Nature. 2013;501(7467):338-45.

[21] Gerlinger M, Swanton C. How Darwinian models inform therapeutic failure initiated by clonal heterogeneity in cancer medicine. Br J Cancer. 2010;103(8):1139-43.

[22] Fisher R, Pusztai L, Swanton C. Cancer heterogeneity: implications for targeted therapeutics. Br J Cancer. 2013;108(3):479-85.

[23] Hanahan D, Weinberg RA. Hallmarks of cancer: the next generation. Cell. 2011;144(5):646-74.

[24] Rahman M, Hasan MR. Cancer Metabolism and Drug Resistance. Metabolites. 2015;5(4):571-600.

[25] Cantor JR, Sabatini DM. Cancer cell metabolism: one hallmark, many faces. Cancer Discov. 2012;2(10):881-98.

[26] Skala MC, Riching KM, Gendron-Fitzpatrick A, Eickhoff J, Eliceiri KW, White JG, et al. In vivo multiphoton microscopy of NADH and FAD redox states, fluorescence lifetimes, and cellular morphology in precancerous epithelia. Proc Natl Acad Sci U S A. 2007;104(49):19494-9.

[27] Walsh AJ, Cook RS, Manning HC, Hicks DJ, Lafontant A, Arteaga CL, et al. Optical metabolic imaging identifies glycolytic levels, subtypes, and early-treatment response in breast cancer. Cancer Res. 2013;73(20):6164-74.

[28] Georgakoudi I, Quinn KP. Optical Imaging Using Endogenous Contrast to Assess Metabolic State. Annu Rev Biomed Eng. 2012;14:351-67.

[29] Chance B, Schoener B, Oshino R, Itshak F, Nakase Y. Oxidation-reduction ratio studies of mitochondria in freeze-trapped samples. NADH and flavoprotein fluorescence signals. J Biol Chem. 1979;254(11):4764-71.

[30] Walsh A, Cook RS, Rexer B, Arteaga CL, Skala MC. Optical imaging of metabolism in HER2 overexpressing breast cancer cells. Biomed Opt Express. 2012;3(1):75-85.

[31] Alhallak K, Rebello LG, Muldoon TJ, Quinn KP, Rajaram N. Optical redox ratio identifies metastatic potential-dependent changes in breast cancer cell metabolism. Biomed Opt Express. 2016;7(11):4364-74.

[32] Hou J, Wright HJ, Chan N, Tran R, Razorenova OV, Potma EO, et al. Correlating two-photon excited fluorescence imaging of breast cancer cellular redox state with seahorse flux analysis of normalized cellular oxygen consumption. J Biomed Opt. 2016;21(6):60503.

[33] Sharick JT, Favreau PF, Gillette AA, Sdao SM, Merrins MJ, Skala MC. Protein-bound NAD(P)H Lifetime is Sensitive to Multiple Fates of Glucose Carbon. Sci Rep. 2018;8(1):5456.

[34] Lakowicz JR. Principles of fluorescence spectroscopy. 2nd ed. New York: Kluwer Academic/Plenum; 1999. xxiii, 698 p. p.

[35] Bird DK, Yan L, Vrotsos KM, Eliceiri KW, Vaughan EM, Keely PJ, et al. Metabolic mapping of MCF10A human breast cells via multiphoton fluorescence lifetime imaging of the coenzyme NADH. Cancer Res. 2005;65(19):8766-73.

[36] Walsh AJ, Cook RS, Sanders ME, Aurisicchio L, Ciliberto G, Arteaga CL, et al. Quantitative optical imaging of primary tumor organoid metabolism predicts drug response in breast cancer. Cancer Res. 2014;74(18):5184-94.

[37] Shah AT, Diggins KE, Walsh AJ, Irish JM, Skala MC. In Vivo Autofluorescence Imaging of Tumor Heterogeneity in Response to Treatment. Neoplasia. 2015;17(12):862-70.

[38] Walsh AJ, Skala MC. Optical metabolic imaging quantifies heterogeneous cell populations. Biomed Opt Express. 2015;6(2):559-73.

[39] Shibata T, Ebata T, Fujita K, Shimokata T, Maeda O, Mitsuma A, et al. Optimal dose of gemcitabine for the treatment of biliary tract or pancreatic cancer in patients with liver dysfunction. Cancer Sci. 2016;107(2):168-72.

[40] Garcia-Garcia C, Ibrahim YH, Serra V, Calvo MT, Guzman M, Grueso J, et al. Dual mTORC1/2 and HER2 blockade results in antitumor activity in preclinical models of breast cancer resistant to anti-HER2 therapy. Clin Cancer Res. 2012;18(9):2603-12.

[41] Infante JR, Tabernero J, Cervantes A, Jalal S, Burris HA, Macarulla T, et al. Abstract C252: A phase 1, dose-escalation study of MLN0128, an investigational oral mammalian target of rapamycin complex 1/2 (mTORC1/2) catalytic inhibitor, in patients (pts) with advanced non-hematologic malignancies. Molecular Cancer Therapeutics. 2013;12(11 Supplement):C252-C.

[42] Gandhi L, Camidge DR, Ribeiro de Oliveira M, Bonomi P, Gandara D, Khaira D, et al. Phase I study of Navitoclax (ABT-263), a novel Bcl-2 family inhibitor, in patients with small-cell lung cancer and other solid tumors. J Clin Oncol. 2011;29(7):909-16.

[43] Shoemaker AR, Mitten MJ, Adickes J, Ackler S, Refici M, Ferguson D, et al. Activity of the Bcl-2 family inhibitor ABT-263 in a panel of small cell lung cancer xenograft models. Clin Cancer Res. 2008;14(11):3268-77.

[44] Bergmann A. SPCImage: data analysis software for fluorescence lifetime imaging microscopy. Becker & Hickl GmbH, available on www becker-hickl com. 2003.

[45] Lakowicz JR, Szmacinski H, Nowaczyk K, Johnson ML. Fluorescence lifetime imaging of free and protein-bound NADH. Proc Natl Acad Sci U S A. 1992;89(4):1271-5.

[46] Nakashima N, Yoshihara K, Tanaka F, Yagi K. Picosecond fluorescence lifetime of the coenzyme of D-amino acid oxidase. J Biol Chem. 1980;255(11):5261-3.

[47] Walsh AJ, Skala MC. An automated image processing routine for segmentation of cell cytoplasms in high-resolution autofluorescence images. SPIE Proceedings. 2014;8948.

[48] Carpenter AE, Jones TR, Lamprecht MR, Clarke C, Kang IH, Friman O, et al. CellProfiler: image analysis software for identifying and quantifying cell phenotypes. Genome Biol. 2006;7(10):R100.

[49] Pan W, Lin J, Le CT. Model-based cluster analysis of microarray gene-expression data. Genome Biol. 2002;3(2):1-8.

[50] Akaike H. A new look at the statistical model identification. IEEE transactions on automatic control. 1974;19(6):716-23.

[51] Almendro V, Kim HJ, Cheng YK, Gonen M, Itzkovitz S, Argani P, et al. Genetic and phenotypic diversity in breast tumor metastases. Cancer Res. 2014;74(5):1338-48.

[52] McInnes L, Healy J. Umap: Uniform manifold approximation and projection for dimension reduction. arXiv preprint arXiv:180203426. 2018.

[53] Wickham H. ggplot2: Elegant Graphics for Data Analysis. New York: Springer-Verlag; 2016.

[54] Glass GV. Primary, secondary, and meta-analysis of research. Educational researcher. 1976;5(10):3-8.

[55] Driscoll DR, Karim SA, Sano M, Gay DM, Jacob W, Yu J, et al. mTORC2 Signaling Drives the Development and Progression of Pancreatic Cancer. Cancer Res. 2016;76(23):6911-23.

[56] Morran DC, Wu J, Jamieson NB, Mrowinska A, Kalna G, Karim SA, et al. Targeting mTOR dependency in pancreatic cancer. Gut. 2014;63(9):1481-9.

[57] Jin J, Xiong Y, Cen B. Bcl-2 and Bcl-xL mediate resistance to receptor tyrosine kinase-targeted therapy in lung and gastric cancer. Anticancer Drugs. 2017;28(10):1141-9.

[58] Ohlund D, Handly-Santana A, Biffi G, Elyada E, Almeida AS, Ponz-Sarvise M, et al. Distinct populations of inflammatory fibroblasts and myofibroblasts in pancreatic cancer. J Exp Med. 2017;214(3):579-96.

[59] Sievers CK, Zou LS, Pickhardt PJ, Matkowskyj KA, Albrecht DM, Clipson L, et al. Subclonal diversity arises early even in small colorectal tumours and contributes to differential growth fates. Gut. 2017;66(12):2132-40.

[60] Ryan DP, Hong TS, Bardeesy N. Pancreatic adenocarcinoma. N Engl J Med. 2014;371(22):2140-1.

[61] Nagathihalli NS, Castellanos JA, Shi C, Beesetty Y, Reyzer ML, Caprioli R, et al. Signal Transducer and Activator of Transcription 3, Mediated Remodeling of the Tumor Microenvironment Results in Enhanced Tumor Drug Delivery in a Mouse Model of Pancreatic Cancer. Gastroenterology. 2015;149(7):1932-43 e9.

# CHAPTER 6

## Conclusions and Future Directions

### 6.1 Summary and Conclusions

The goal of this dissertation is to develop and characterize OMI of patient-derived organoids to quantify drug-induced changes in cellular metabolic heterogeneity for breast and pancreatic cancer personalized medicine. Selecting optimal treatment plans for individual patients is hindered by intratumor heterogeneity, as small cell subpopulations evade treatment and re-establish a potentially more aggressive tumor (1, 2). Tumor organoids offer a platform for high-throughput drug screening on breast and pancreatic cancer cells *ex vivo* to guide therapeutic decisions (3, 4). In order to account for heterogeneity, new technology to non-invasively evaluate subpopulations of drug response in patient organoids is needed. Current methods for examining subpopulations include flow cytometry, sequencing, histology, and immunolabeling, but these techniques require fixing or dissociating the organoids. OMI could provide an alternative that uses endogenous contrast to detect functional metabolic changes at the single-cell level. The combination of tumor organoids and OMI will enable optimal treatment decisions for individual patients that effectively target all subpopulations of cells within heterogeneous tumors.

Chapter 2 provides background information to contextualize the work presented in this dissertation. This chapter begins by describing treatment options for breast and pancreatic cancer as well as standard treatment decision-making procedures. Next, the problem of tumor heterogeneity is defined and its clinical implications are discussed, along with the significance of cell metabolism. Additionally, the advantages of using tumor-derived organoid culture for patient-specific drug screening are given. Finally, the chapter introduces the main technological

components that OMI comprises, including multiphoton microscopy, fluorescence lifetime imaging, and endogenous metabolic contrast.

Chapter 3 addresses Aim 1 by characterizing previously unidentified relationships between FLIM signals and flux through key cellular metabolic pathways. Experiments in solution demonstrate that NAD(P)H FLIM can accurately quantify the relative concentration of multiple enzyme species in a mixture. NAD(P)H FLIM also detects changes in key metabolic pathways that control the path of carbon from glucose uptake to the electron transport chain in breast and pancreatic epithelial cell lines. The main conclusion of this chapter is that NAD(P)H FLIM is sensitive to changes in flux through the pentose phosphate pathway, changes in flux through the lactate production pathway, and rejection of carbon from the TCA cycle. These pathways can be upregulated in cancer to support tumor progression and drug resistance (5-9). This improves our ability to interpret the biochemical causes behind shifts in NAD(P)H FLIM measurements, and to non-invasively investigate mechanisms that allow drug-resistant cell subpopulations to evade treatment. Using OMI, oncologists can personalize treatment plans that target the resistance mechanisms in these subpopulations.

Chapter 4 addresses Aim 2 by comparing OMI measurements of heterogeneity in tumors and tumor-derived organoids in response to therapy. Immunocompetent FVB mice harboring allografts of the PyVmT breast cancer model were treated with a clinically relevant chemotherapy and targeted inhibitor and imaged *in vivo*. Organoids derived from PyVmT allografts were treated likewise and imaged. A novel weighted heterogeneity index (wH-index) was used to quantify and compare cellular diversity in both settings. The main conclusion of this chapter is that OMI of *in vitro* tumor organoids accurately captures *in vivo* heterogeneous response to treatment. Additionally, IHC of tumors and organoids was performed to pinpoint potential sources of

metabolic heterogeneity. This work supports the translation of OMI of tumor-derived organoids as a platform to study the effect of drugs on *in vivo* tumor heterogeneity, both for clinical treatment planning as well as basic cancer biology studies. This is an important result because standard methods of measuring heterogeneity in tumors require significant animal burden, are destructive to the cells, and do not measure metabolism in a relevant 3D microenvironment.

The objective of Chapter 5 is to compare OMI measurements of drug-induced heterogeneity in organoids with long-term treatment response in pancreatic cancer patients. An oncologist could use this technology to quickly determine the most beneficial treatment regimen for an individual patient, rather than waiting for standard drugs to fail and exposing the patient to unnecessary toxicities. Additionally, this tool could accelerate the discovery of new treatment options for pancreatic cancer, which are urgently needed. To address Aim 3, organoids were generated from surgically resected pancreatic lesions, and treated with a panel of relevant therapies. For a subset of tumor samples, this panel included the same drugs that the patient received following surgery. The main conclusion of this study is that OMI of early heterogeneous drug responses in organoids was strongly associated with patient recurrence-free survival, suggesting that OMI-based insights into how drugs affect the degree of cellular heterogeneity could be clinically relevant. Currently, oncologists do not have any *a priori* indications as to whether an individual patient will respond to a standard therapy, and thus would greatly benefit from this technology.

This dissertation characterizes OMI for monitoring heterogeneous drug responses in breast and pancreatic cancer patient-derived organoids. OMI utilizes endogenous metabolic contrast to non-invasively resolve treatment response in individual cells. This provides novel insights into drug effects that are not obtainable using prevailing technologies, which are inherently destructive

or low-resolution. These include the differentiation of responsive and non-responsive cell subpopulations, as well as longitudinal tracking of these subpopulations over time. These benefits make OMI of organoids an attractive platform for basic science, drug discovery, and personalized breast and pancreatic cancer treatment planning.

## 6.2 Future Directions

OMI to Guide Neoadjuvant Treatment in Breast Cancer

New technologies are needed to match newly diagnosed breast cancer patients with the best treatment options for neoadjuvant therapy. This platform could allow oncologists to quickly optimize individualized treatment plans which successfully target and kill all cancer cell subpopulations with minimal toxicities. We have begun to test the hypothesis that OMI of cellular heterogeneity in organoids derived from diagnostic core needle biopsies can accurately predict patient response to their neoadjuvant therapy. OMI drug screen predictions of treatment efficacy will be validated using standard surgical pathology. An independent pathologist will evaluate surgical specimens and assign each patient a residual cancer burden (RCB) score and class. This score is based on the extent of remaining visible tumor following neoadjuvant therapy, with zero indicating pathological complete response (pCR), and higher scores corresponding with greater degrees of residual cancer.

Viable organoids have been generated from core needle biopsies of a variety of subtypes of breast tumors (Table 6.1). These organoids exhibit a variety of morphologies, including hollow, cystic organoids and dense, solid organoids (Fig. 6.1). CellProfiler is used to mask individual cytoplasms and analyze cellular heterogeneity, as described in Chapters 4 and 5.

**Table 6.1. Receptor expression and treatment status of biopsied patients.** Samples from patients #1-22 were used to develop and optimize organoid generation and imaging protocols.

| Study # | Receptor Status | Neoadjuvant Treatment Regimen | RCB score | RCB class |
|---|---|---|---|---|
| 23 | ER+/PR+/HER2- | None | - | - |
| 24 | ER+/PR+/HER2- | None | - | - |
| 25 | ER-/PR-/HER2+ | Paclitaxel + Trastuzumab + Pertuzumab | *pending* | |
| 26 | TN | Doxorubicin + Cyclophosphamide + Paclitaxel | *pending* | |
| 27 | ER+/PR+/HER2- | None | - | - |
| 28 | ER+/PR+/HER2- | None | - | - |

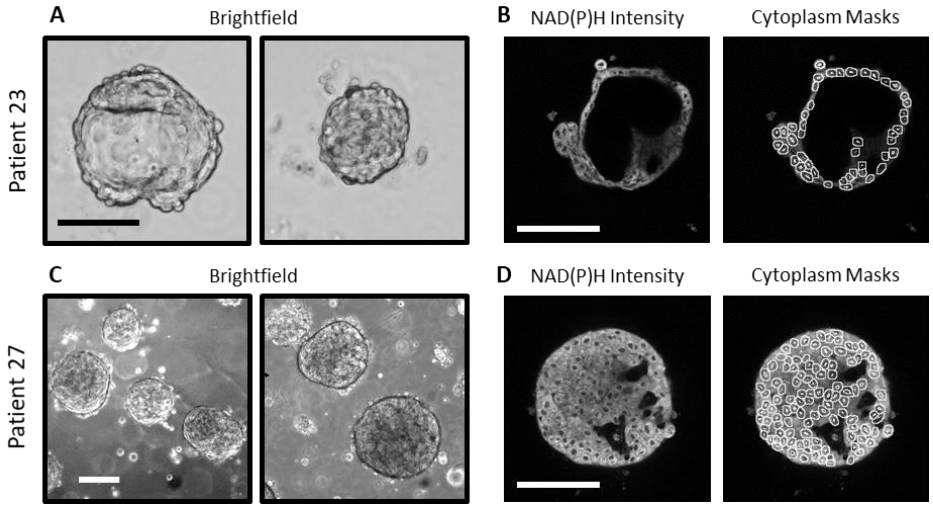


**Figure 6.1. Breast tumor biopsy organoid culture and imaging. A,** Brightfield images of Patient 23 organoids, featuring a hollow morphology. Scale bar = 100 μm. **B,** Representative NAD(P)H intensity image of a Patient 23 organoid (left) and masks of individual cell cytoplasms overlaid onto the image (right). Scale bar = 100 μm. **C,** Brightfield images of Patient 27 organoids, featuring a dense and solid morphology. Scale bar = 250 μm. **D,** Representative NAD(P)H intensity image of a Patient 27 organoid (left) and masks of individual cell cytoplasms overlaid onto the image (right). Scale bar = 100 μm.

Breast tumor biopsy organoids are treated with a variety of standard therapies, including the patient's prescribed neoadjuvant regimen, if applicable. These include trastuzumab for HER2+ patients, and chemotherapy combinations such as paclitaxel, doxorubicin, and cyclophosphamide for HER2- and triple negative patients. Treatment response is evaluated with single-cell resolution

in the organoids using OMI (Fig. 6.2).

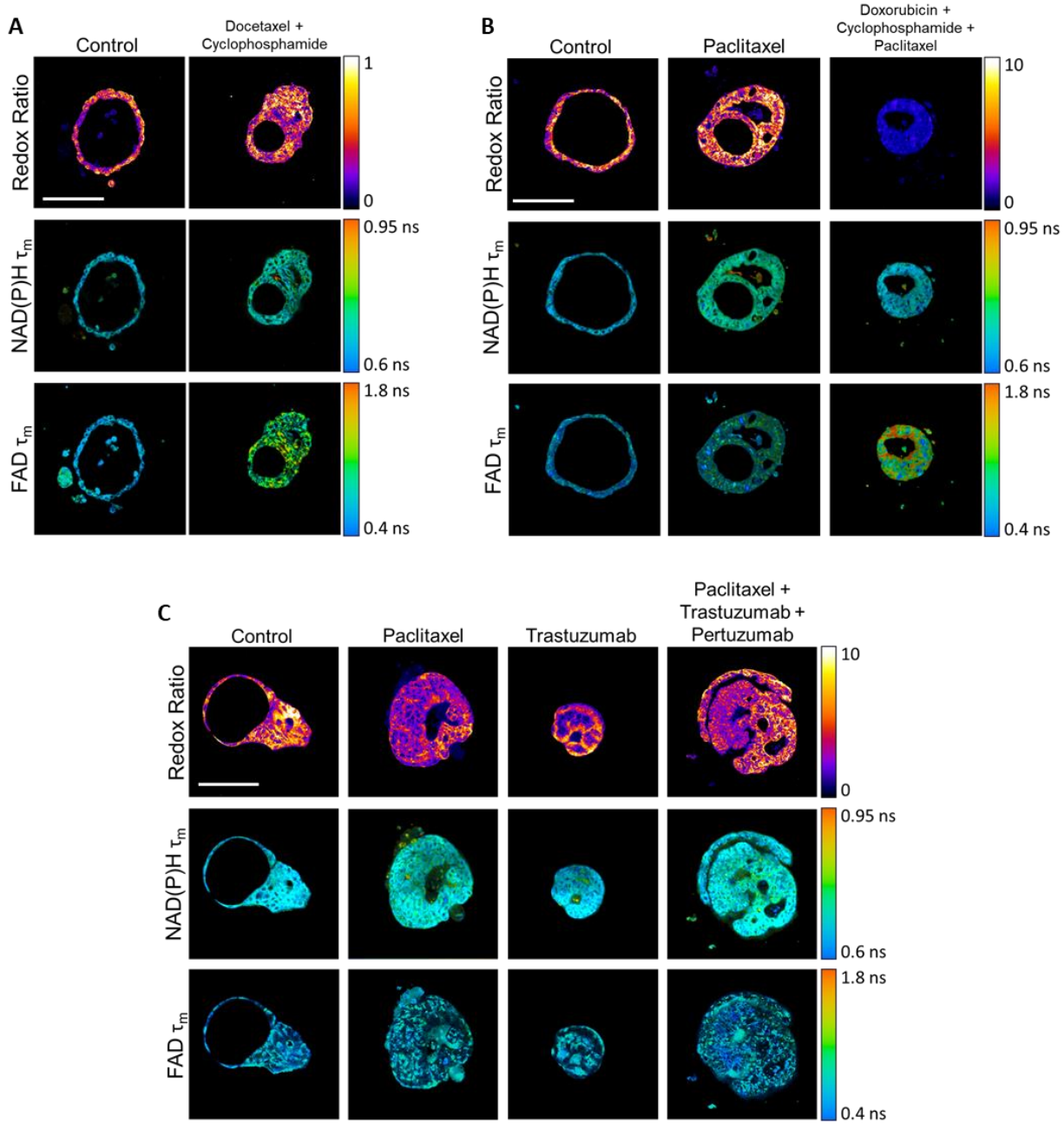

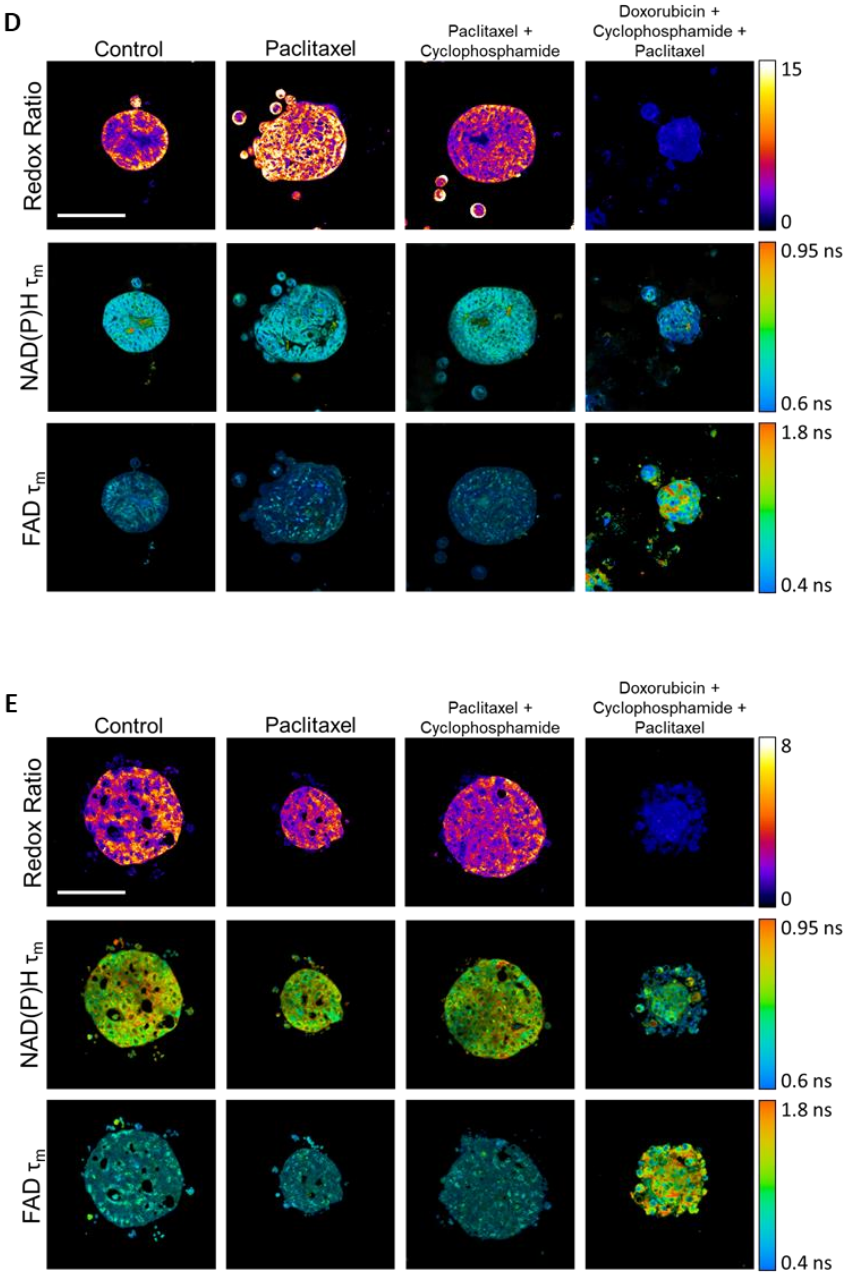


**Figure 6.2. OMI of patient breast tumor biopsy organoids.** Representative images of the optical redox ratio, NAD(P)H $\tau_m$, and FAD $\tau_m$ in organoids generated from (**A**) Patient 23, (**B**) Patient 24, (**C**) Patient 25, (**D**) Patient 26, and (**E**) Patient 27 breast tumor biopsies. Scale bar = 100 μm.

In Patient 26 organoids, the patient's neoadjuvant treatment regimen of doxorubicin, cyclophosphamide, and paclitaxel (A+C+T) significantly reduced the mean OMI index after 72 hours (Fig 6.3A). A+C+T treatment also reduced the degree of metabolic heterogeneity present in

the organoids, as quantified by the wH-index described in Chapters 4 and 5 (Fig. 6.3B,C). Together, this suggests that this treatment is likely to be beneficial for the patient. Based on this data, we predict Patient 26 to experience an RCB of zero (pCR) on A+C+T treatment. Standard markers of proliferation (Ki67) and apoptosis (cleaved caspase-3) were quantified at the single cell level in organoids in response to A+C+T, which agreed with the OMI measurements of response (Fig 6.3D-G).

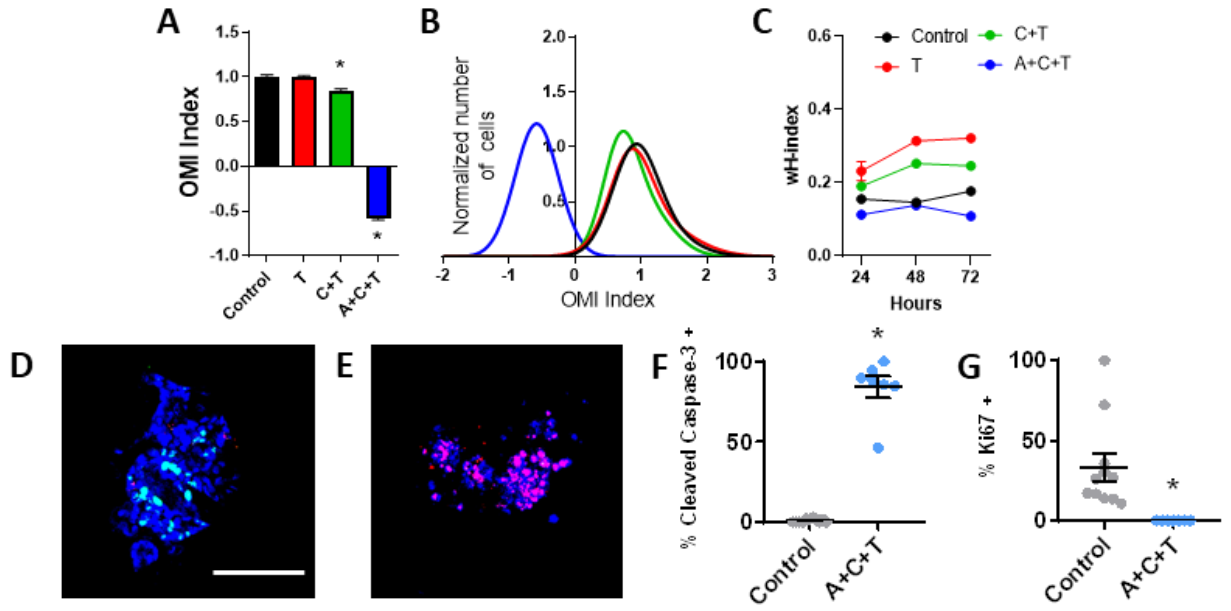


**Figure 6.3. OMI of Patient 26 breast tumor biopsy organoids agrees with standard markers . A,** OMI index of Patient 26 organoids at 72 hours decreased with C+T and A+C+T treatment. **B,** OMI index cell subpopulation analysis of Patient 26 organoids at 72 hours. **C,** The effect of treatment on OMI index heterogeneity quantified by the wH-index in Patient 26 organoids. **D-E,** Representative images of control (**D**) and A+C+T treated (**E**) organoids stained for Ki67 (green, proliferation), cleaved caspase-3 (red, apoptosis), and DAPI (blue, nuclei). Scale bar = 100 μm. **F,** Cleaved caspase-3 staining of organoids shows differences in apoptosis between treatment conditions after 72 hours of treatment. **G,** Ki67 staining of organoids shows differences in proliferation between treatment conditions after 72 hours. Each dot represents one organoid. Error bars indicate mean ± SEM. * $p<0.05$ vs. control.

These early results in a diverse cohort of patients demonstrate the feasibility of making biologically relevant measurements of single-cell drug response in biopsy-derived organoids with OMI. Future studies will continue to accrue a large cohort of patients planning neoadjuvant

therapy. Early heterogeneous metabolic changes with treatment in organoids will be compared to patient treatment response to validate OMI of organoids as a predictive tool for breast cancer personalized medicine.

Increase OMI Imaging Speed

A limitation of OMI for high-throughput organoid drug screening is the time required. In order to be clinically beneficial, future work will need to address this concern. Potential solutions will likely involve both: 1) automating the process of locating and focusing on organoids for OMI, and 2) reducing FLIM acquisition time. The former could be addressed by adding lower magnification widefield fluorescence microscopy to automatically detect the coordinates of organoids for subsequent OMI. A microscope stage-compatible environmental chamber could be used to maintain ideal culture conditions. The latter issue, the reduction of FLIM acquisition time, is a topic of great importance in the field, with many solutions being pursued. For example, data analysis techniques to accurately report lifetimes using fewer photon counts are being established (10), but these have not yet been evaluated specifically for organoid OMI. Additionally, multiphoton FLIM systems that employ analog measurements have been developed to increase imaging speed (11, 12), and were recently applied to NAD(P)H metabolic imaging (13). Widefield microscopy techniques with a large field of view, such as structured illumination microscopy (14, 15), could also potentially be optimized to rapidly perform single-cell OMI in organoids. Reduction of overall experimental time would also facilitate the screening of additional drug combinations, doses, and schedules.

Large Scale Clinical Study of Organoid-OMI Response Prediction

To confirm clinical utility, organoid-OMI predictions of patient-specific drug response need to be validated in a larger cohort of breast and pancreatic cancer patients. To increase enrollment, multiple institutions would ideally collaborate to share fresh tissue samples and clinical follow-up data. Initial studies would continue to be prospective and observational in nature, where individual patient-drug pairs are classified into categories of predicted response. With a larger dataset in hand, the methodology for classification can be optimized. For example, the current formulas for calculating the OMI index or the treatment effect size may require fine-tuning to improve patient response classification.

Once validated using a sufficient number of patients, a clinical trial would be designed to confirm that guiding treatment choices in patients with OMI of organoids improves patient outcome over standard of care. In one arm, high-throughput drug screens would be performed on patient organoids and evaluated with OMI to select the optimal treatment. In the control arm, patients would be treated by the current standard of care. Clinical outcome data would be analyzed to determine whether this personalized medicine approach can improve response rate and overall survival while reducing toxicity.

Tracking Metabolism of Individual Cells Over Time

OMI is non-destructive, and thus could be used to track how an individual tumor or organoid cell responds metabolically to treatment over time. By acquiring repeated OMI images of the same field of view over time and registering cells between images, cells could be individually classified based on their temporal profile of response. This could distinguish between cells that: respond gradually, respond acutely, are consistently resistant, or have an initial response

followed by consistent resistance. For example, this analysis could be used to determine whether a cell which appears to be responding to treatment, initially had more metabolic activity which decreased with treatment, or had low baseline metabolic activity independent of treatment. Tracking time-courses of response in individual cells could provide novel insights into how individual subpopulations of cells in tumors and organoids react when a stress is applied.

Additional Characterization of Metabolic Subpopulations in Organoids

OMI detects treatment-resistant subpopulations of cells within intact organoids. The unique biological characteristics that allow these cells to evade treatment is important to understand, in order to design additional treatment plans to target them. Results from Chapter 4 suggest that subpopulations identified with OMI in PyVmT mouse tumor organoids represent metabolic differences between tumor cells, but additional studies are required to further characterize heterogeneity. These studies would involve imaging organoids with OMI and subsequently characterizing individual cells using established techniques. Examples include flow cytometry, mass cytometry, immunofluorescence, and immunohistochemistry. Additionally, the ability of OMI to correctly identify subpopulations has been validated using mixtures of 2D breast cancer cell lines (16), but this should also been confirmed in 3D. These studies could also take advantage of exogenous fluorescent reporters to quantify metabolic properties of single live cells, such as glucose uptake (17), pH (18), membrane potential (19), hydrogen peroxide (20), hypoxia (21), and NADH/$NAD^+$ redox state (22).

OMI of Organoids for Personalized Cancer Immunotherapy

Patient-derived organoids also provide a platform to guide the optimal selection of

immunotherapies and study tumor-immune interactions (23). However, previous studies have used live and dead cell fluorescent labels and immunofluorescence to evaluate response. OMI could be used to non-destructively observe the activation and behavior of individual immune cells in response to treatment in organoids based on their unique metabolic profiles (24, 25). Future studies in immunocompetent animal models could validate OMI of organoids as an accurate predictor of *in vivo* immunotherapy response.

Prediction of Therapy Response in Additional Cancer Types

Future studies will validate the ability of OMI to predict long-term therapy response in other cancers, such as lung, colorectal, prostate, ovarian, and skin, and neuroendocrine tumors, among others. Applying OMI to diseases other than cancer may be beneficial as well, especially where quantifying cellular metabolism is advantageous. For example, late-onset Alzheimer's disease is associated with defective mitochondria, abnormal redox potential, and increased glycolysis (26).

Further Biochemical Interpretation of NAD(P)H and FAD Fluorescence Lifetimes

The free and bound states of NAD(P)H and FAD have unique fluorescence lifetimes which can be distinguished by fitting time-resolved photon count data with multiple exponentials decays. Changes in $\alpha_1$ and $\alpha_2$ can thus be interpreted as changes in the ratio of free to bound molecules. NAD(P)H and FAD $\tau_1$ and $\tau_2$ are known to be affected by temperature, pH, protein-binding, and quenching by molecules such as $O_2$ (27). NAD(P)H $\tau_2$ is unique to the enzyme that it is bound to. On one hand, a key benefit of these measurements is that they are highly sensitive to many specific metabolic perturbations in cells. On the other hand, interpreting the specific biochemical origin

behind a change in $\tau_1$ or $\tau_2$ remains difficult. Additional experiments in cells similar to those in Chapter 3 will continue to increase our understanding of how changes in flux through certain metabolic pathways affect FLIM variables. A model could then be constructed that works in the reverse direction, to take changes in NAD(P)H and FAD lifetime data and determine the most likely metabolic underpinnings. Such a model could help identify potential pathways driving treatment resistance.

### 6.3 Contribution to the Field and Societal Impact

Contributions to Biophotonics

The research in this dissertation has led to a number of contributions to the field of biophotonics. First, the work described in Chapter 3 addresses an ongoing need to enhance the biochemical interpretation of autofluorescence FLIM data. Experiments using metabolic inhibitors demonstrate the sensitivity of NAD(P)H FLIM to key enzymatic steps that control the path of carbon from glucose uptake to ETC activity. It is also shown that NAD(P)H $\tau_2$ is more sensitive to these key enzymatic steps than the NAD(P)H intensity, free NAD(P)H lifetime, or relative amounts of free and protein-bound NAD(P)H. This is the first study to demonstrate that NAD(P)H $\tau_2$ can distinguish NADH bound to two different metabolic enzymes in a single solution, and thus quantify changes in the relative activities of unique enzymes. In total, this work enhances the interpretability of NAD(P)H FLIM signals, bolstering OMI as a clinically relevant tool to non-invasively probe cellular metabolism.

Studies presented in Chapter 4 are the first to compare *in vivo* OMI measurements of drug response with FDG-PET imaging of glucose uptake in an immunocompetent breast cancer model. OMI endpoints were sensitive to treatment response in as few as 48 hours, while FDG-PET

imaging was not, even after 2 weeks. This provides evidence, in a relevant tumor model, that biophotonics techniques can be used to detect treatment response prior to standard radiology. For the first time, parallel treatment effects between *in vivo* tumor cells and organoids were demonstrated in an immunocompetent cancer model using OMI. This further validates that endogenous fluorescence signals in organoids are sensitive to physiologically relevant metabolic alterations. Previously, studies of cell metabolism have been primarily performed *in vivo*, which either requires significant animal burden to achieve large sample sizes, or in some cases may not even be feasible at all. However, these results suggest that the combination of optical technology and organoid culture provides a more practical and advantageous methodology.

Chapter 5 presents the first in-depth characterization of the optical redox ratio and NAD(P)H and FAD lifetimes in patient-derived pancreatic cancer organoids. This work provides key information strengthening the interpretation of these OMI endpoints by comparing drug responses in organoids to standard measures such as cell death, cell proliferation, long term tumor growth in xenografts, and clinical treatment outcomes in patients. The sensitivity of OMI endpoints to many clinically approved pancreatic cancer drugs has not been previously demonstrated in organoids, including nab-paclitaxel, 5-fluorouracil, oxaliplatin, SN-38, and the FOLFIRINOX regimen.

Contribution to Cancer Biology

This work has a number of implications for improving future basic science research in cancer biology. Deregulated cellular metabolism is an emerging hallmark of cancer and expanding area of study (28). In order to support neoplastic proliferation, cells must reprogram their metabolism to effectively incorporate available nutrients (29). This dissertation provides

substantial evidence that OMI delivers novel insights into cancer cell metabolism to characterize metabolic treatment effects and identify new drugs to target metabolic deficiencies (30). For example, in Chapter 3, NAD(P)H FLIM was used to probe changes in the activity of LDH and PDH, which are key metabolic enzymes that can contribute to cancer progression and treatment resistance (6-9).

Unlike standard techniques for probing cell metabolism, such as metabolite analysis, RNA expression, proteomics, and FDG-PET imaging, OMI can resolve the functional metabolic states of individual cells. In Chapter 4, OMI of heterogeneous treatment response in tumor organoids was shown to accurately capture *in vivo* changes. This platform has the potential to greatly accelerate basic studies of tumor heterogeneity, which currently have a number of limitations. First, OMI can be used to evaluate tumor heterogeneity directly *in vivo* under many experimental conditions with many replicates, but this requires an enormous number of animals. Also, extraction of animal model tumors for standard techniques such as flow cytometry, single-cell genetic sequencing, or histology prevents longitudinal studies of cellular heterogeneity evolution over time. Finally, even in cases where patient tumors are accessible for OMI imaging directly *in vivo*, the heterogeneous effect of only one treatment can be evaluated.

Results presented here show that OMI of organoids can overcome these limitations. This technology could provide new insights into the causes and development of cancer and intratumor heterogeneity. The complex influences of specific genes, signaling pathways, and metabolic status on tumor heterogeneity and progression could be investigated using knock-out models. Three-dimensional co-cultures of tumor cells with fibroblasts, immune cells, and other cells could be used to study tumor-microenvironment interactions and understand how these interactions drive cellular diversity. High-throughput screening can be performed on organoids to analyze how drug

treatment itself can drive the emergence of drug-resistant subpopulations, and identify new treatment strategies to prevent this emergence. For example, adaptive treatment strategies, which involve alternating between classes of drugs or modifying doses over time, could be tested to maintain a stable, drug-responsive tumor and prolong progression-free survival (31, 32).

Chapter 4 demonstrated that PyVmT immunocompetent organoids also maintain very similar levels of proliferation and apoptosis as compared to the tumor of origin, along with expression of epithelial markers, mesenchymal markers, and the PyVmT antigen. $CD45^+$ immune cells were present in organoids as well, which can affect tumor treatment response (33). In all, this work provides support for using organoids to model complex tumors in a relevant microenvironment.

In order to quantify the degree of heterogeneity measured in a sample and compare between experimental conditions, the wH-index was developed as a novel analysis tool to quantify the degree of metabolic heterogeneity present in a distribution of cells. This index incorporates the number of cell subpopulations, the variance of each subpopulation, their separation, and their relative proportions. In Chapter 4, the wH-index in drug-treated organoids predicted long term PyVmT tumor growth. In Chapter 5, a decrease in the wH-index with treatment in the pancreas organoids was associated with longer recurrence free survival. These relationships provide evidence that OMI-based insights into the effect of drugs on cellular heterogeneity could be clinically relevant.

Impacts on Clinical Cancer Treatment

Along with the aforementioned studies of *in vivo* tumor metabolism and heterogeneity, the development of OMI for measuring drug response in organoids could also transform preclinical

drug development. Long-term studies of drug efficacy require an enormous number of animals and other resources to complete, and yet a majority of drug candidates fail by late clinical trial stages (34). Alternatively, OMI can be used in a high-throughput manner to screen large libraries of potential drug candidates on *in vitro* organoids, and make longitudinal measurements of drug response. Rather than requiring mice for every experimental condition and time point of interest, organoid culture can be used to test every condition with only a small amount of tumor tissue. Chapter 4 & 5 also demonstrate that early changes in metabolism, measured with OMI, significantly precede changes in *in vivo* tumor growth. This suggests that drug candidates could be evaluated in a fraction of the time compared to current methods. Additionally, the analysis methods presented in this dissertation incorporate single-cell heterogeneity, which is key to determining drug efficacy. OMI could be used to more efficiently select the most promising drug candidates for clinical trials, significantly reducing the time and cost required to develop new cancer drugs.

In particular, pancreatic cancer treatment suffers from a lack of approved drug treatment options, none of which have been demonstrated to cure cancer on their own. In Chapter 5, a novel combination of targeted therapies, TAK-228 (mTORC1/2 inhibitor) and ABT-263 (Bcl-2 and Bcl-xL inhibitor), was tested on patient-derived pancreatic cancer organoids for the first time. This combination induced significant metabolic responses to treatment across all patient organoid lines, and exhibited a low degree of single-cell heterogeneity. This combination shows promise for use in patients, demonstrating the ability of OMI to accelerate the discovery of novel treatment strategies.

An estimated 2.5 million new cases of breast and pancreatic cancer were diagnosed in 2018 worldwide (35). Development of OMI for high-throughput drug evaluation could also revolutionize personalized medicine for these diseases. Organoids would be generated from tumor

biopsies or surgical resections, and a library of drug treatment options would be screened to identify the optimal choice for an individual patient. The ability to analyze heterogeneous responses allows drugs or drug combinations that kill all cell subpopulations to be identified and recommended. These studies characterize OMI measurements of drug response in primary tumor organoids, which accurately predicted long-term tumor response in a human-like breast cancer model, and agreed with long-term recurrence-free survival in pancreatic cancer patients. This work advances the development of OMI as a personalized medicine tool to improve patient outcomes and minimize unnecessary side-effects in breast and pancreatic cancer.

### 6.4 References


[1] Marusyk A, Polyak K. Tumor heterogeneity: causes and consequences. Biochim Biophys Acta. 2010;1805(1):105-17.

[2] Fisher R, Pusztai L, Swanton C. Cancer heterogeneity: implications for targeted therapeutics. Br J Cancer. 2013;108(3):479-85.

[3] Sachs N, de Ligt J, Kopper O, Gogola E, Bounova G, Weeber F, et al. A Living Biobank of Breast Cancer Organoids Captures Disease Heterogeneity. Cell. 2018;172(1-2):373-86 e10.

[4] Boj SF, Hwang CI, Baker LA, Chio, II, Engle DD, Corbo V, et al. Organoid models of human and mouse ductal pancreatic cancer. Cell. 2015;160(1-2):324-38.

[5] Patra KC, Hay N. The pentose phosphate pathway and cancer. Trends Biochem Sci. 2014;39(8):347-54.

[6] Xian ZY, Liu JM, Chen QK, Chen HZ, Ye CJ, Xue J, et al. Inhibition of LDHA suppresses tumor progression in prostate cancer. Tumour Biol. 2015;36(10):8093-100.

[7] Fantin VR, St-Pierre J, Leder P. Attenuation of LDH-A expression uncovers a link between glycolysis, mitochondrial physiology, and tumor maintenance. Cancer Cell. 2006;9(6):425-34.

[8] McFate T, Mohyeldin A, Lu H, Thakar J, Henriques J, Halim ND, et al. Pyruvate dehydrogenase complex activity controls metabolic and malignant phenotype in cancer cells. J Biol Chem. 2008;283(33):22700-8.

[9] Kim JW, Tchernyshyov I, Semenza GL, Dang CV. HIF-1-mediated expression of pyruvate dehydrogenase kinase: a metabolic switch required for cellular adaptation to hypoxia. Cell Metab. 2006;3(3):177-85.

[10] Walsh AJ, Sharick JT, Skala MC, Beier HT. Temporal binning of time-correlated single photon counting data improves exponential decay fits and imaging speed. Biomed Opt Express. 2016;7(4):1385-99.

[11] Giacomelli MG, Sheikine Y, Vardeh H, Connolly JL, Fujimoto JG. Rapid imaging of surgical breast excisions using direct temporal sampling two photon fluorescent lifetime imaging. Biomed Opt Express. 2015;6(11):4317-25.

[12] Ryu J, Kang U, Kim J, Kim H, Kang JH, Kim H, et al. Real-time visualization of two-photon fluorescence lifetime imaging microscopy using a wavelength-tunable femtosecond pulsed laser. Biomed Opt Express. 2018;9(7):3449-63.

[13] Bower AJ, Li J, Chaney EJ, Marjanovic M, Spillman DR, Boppart SA. High-speed imaging of transient metabolic dynamics using two-photon fluorescence lifetime imaging microscopy. Optica. 2018;5(10):1290-6.

[14] Gustafsson MG. Surpassing the lateral resolution limit by a factor of two using structured illumination microscopy. J Microsc. 2000;198(Pt 2):82-7.

[15] Gustafsson MG. Nonlinear structured-illumination microscopy: wide-field fluorescence imaging with theoretically unlimited resolution. Proc Natl Acad Sci U S A. 2005;102(37):13081-6.

[16] Walsh AJ, Skala MC. Optical metabolic imaging quantifies heterogeneous cell populations. Biomed Opt Express. 2015;6(2):559-73.

[17] O'Neil RG, Wu L, Mullani N. Uptake of a fluorescent deoxyglucose analog (2-NBDG) in tumor cells. Mol Imaging Biol. 2005;7(6):388-92.

[18] Tantama M, Hung YP, Yellen G. Imaging intracellular pH in live cells with a genetically encoded red fluorescent protein sensor. J Am Chem Soc. 2011;133(26):10034-7.

[19] Poburko D, Santo-Domingo J, Demaurex N. Dynamic regulation of the mitochondrial proton gradient during cytosolic calcium elevations. J Biol Chem. 2011;286(13):11672-84.

[20] Belousov VV, Fradkov AF, Lukyanov KA, Staroverov DB, Shakhbazov KS, Terskikh AV, et al. Genetically encoded fluorescent indicator for intracellular hydrogen peroxide. Nat Methods. 2006;3(4):281-6.

[21] Howard SS, Straub A, Horton N, Kobat D, Xu C. Frequency Multiplexed In Vivo Multiphoton Phosphorescence Lifetime Microscopy. Nat Photonics. 2013;7(1):33-7.

[22] Hung YP, Albeck JG, Tantama M, Yellen G. Imaging cytosolic NADH-NAD(+) redox state with a genetically encoded fluorescent biosensor. Cell Metab. 2011;14(4):545-54.

[23] Jenkins RW, Aref AR, Lizotte PH, Ivanova E, Stinson S, Zhou CW, et al. Ex Vivo Profiling of PD-1 Blockade Using Organotypic Tumor Spheroids. Cancer Discov. 2018;8(2):196-215.

[24] Szulczewski JM, Inman DR, Entenberg D, Ponik SM, Aguirre-Ghiso J, Castracane J, et al. In Vivo Visualization of Stromal Macrophages via label-free FLIM-based metabolite imaging. Sci Rep. 2016;6:25086.

[25] Michalek RD, Gerriets VA, Jacobs SR, Macintyre AN, MacIver NJ, Mason EF, et al. Cutting edge: distinct glycolytic and lipid oxidative metabolic programs are essential for effector and regulatory CD4+ T cell subsets. J Immunol. 2011;186(6):3299-303.

[26] Sonntag KC, Ryu WI, Amirault KM, Healy RA, Siegel AJ, McPhie DL, et al. Late-onset Alzheimer's disease is associated with inherent changes in bioenergetics profiles. Sci Rep. 2017;7(1):14038.

[27] Lakowicz JR. Principles of fluorescence spectroscopy. 2nd ed. New York: Kluwer Academic/Plenum; 1999. xxiii, 698 p. p.

[28] Hanahan D, Weinberg RA. Hallmarks of cancer: the next generation. Cell. 2011;144(5):646-74.

[29] Vander Heiden MG, Lunt SY, Dayton TL, Fiske BP, Israelsen WJ, Mattaini KR, et al. Metabolic pathway alterations that support cell proliferation. Cold Spring Harb Symp Quant Biol. 2011;76:325-34.

[30] Vander Heiden MG. Targeting cancer metabolism: a therapeutic window opens. Nat Rev Drug Discov. 2011;10(9):671-84.

[31] Gatenby RA, Silva AS, Gillies RJ, Frieden BR. Adaptive therapy. Cancer Res. 2009;69(11):4894-903.

[32] Enriquez-Navas PM, Kam Y, Das T, Hassan S, Silva A, Foroutan P, et al. Exploiting evolutionary principles to prolong tumor control in preclinical models of breast cancer. Sci Transl Med. 2016;8(327):327ra24.

[33] Junttila MR, de Sauvage FJ. Influence of tumour micro-environment heterogeneity on therapeutic response. Nature. 2013;501(7467):346-54.

[34] Paul SM, Mytelka DS, Dunwiddie CT, Persinger CC, Munos BH, Lindborg SR, et al. How to improve R&D productivity: the pharmaceutical industry's grand challenge. Nat Rev Drug Discov. 2010;9(3):203-14.

[35] Bray F, Ferlay J, Soerjomataram I, Siegel RL, Torre LA, Jemal A. Global cancer statistics 2018: GLOBOCAN estimates of incidence and mortality worldwide for 36 cancers in 185 countries. CA Cancer J Clin. 2018;68(6):394-424.

# APPENDIX A

## Supplementary Material for Chapter 3

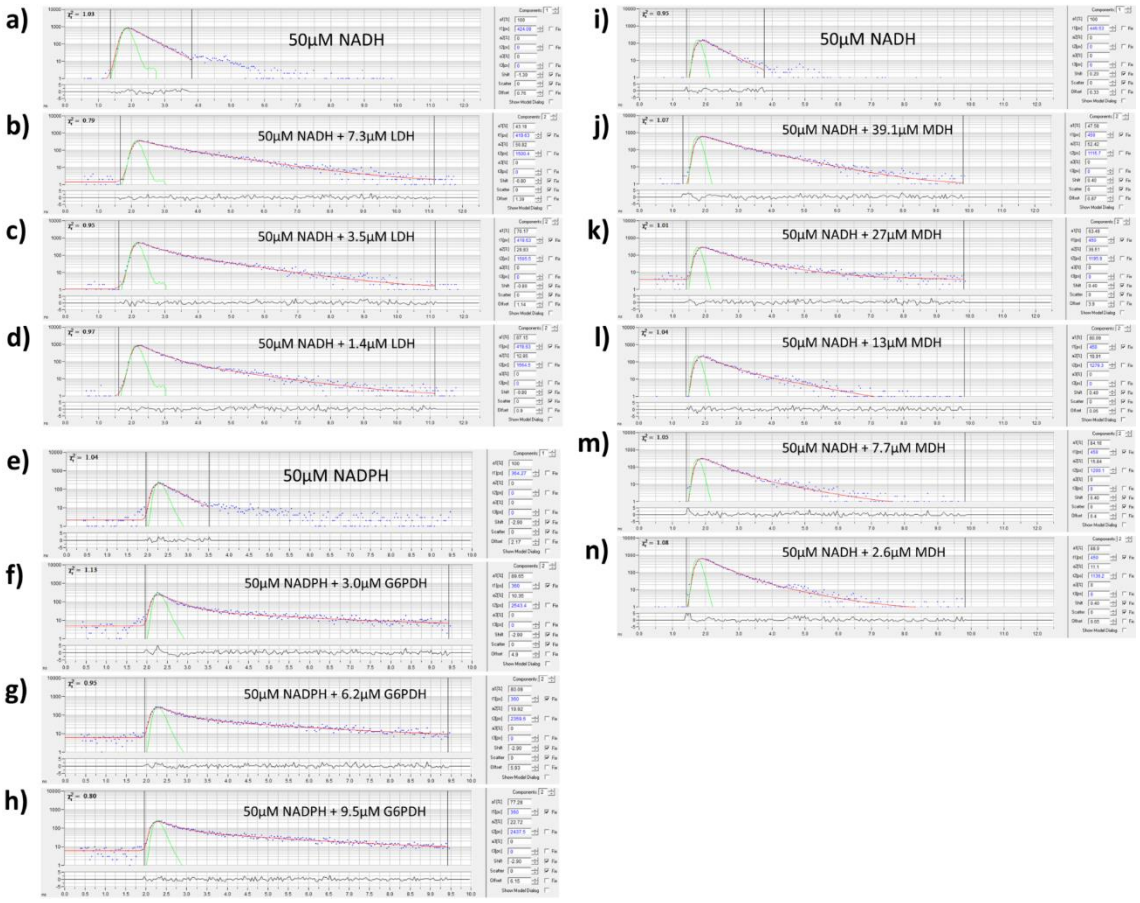


**Figure A.1. NAD(P)H fluorescence lifetime decay curve and fitting examples from single-enzyme binding experiments in solution.** (A-D) NADH fluorescence lifetime decay curves from a representative 1x1 binned pixel of solutions of 50 μM NADH alone or mixed with the indicated concentration of LDH. (E-H) NADPH fluorescence lifetime decay curves from a representative 1x1 binned pixel of solutions of 50 μM NADPH alone or mixed with the indicated concentration of G6PDH. (I-N) NADH fluorescence lifetime decay curves from a representative 1x1 binned pixel of solutions of 50 μM NADH alone or mixed with the indicated concentration of MDH (experiments from Fig. 3.1). Screengrabs taken from SPCImage software (Becker & Hickl). Blue dots represent lifetime decay histogram data (y-axis = number of photons, logarithmic scale). Green line represents the instrument response function (IRF). Red line indicates exponential decay fit. t1, t2, a1, and a2, refer to $\tau_1$, $\tau_2$, $\alpha_1$, and $\alpha_2$ respectively (Equation 3.3). The "components" box determines whether decay curves are fit using the sum of 1, 2, or 3 exponential decays. The "shift" box gives the number of time channels between the IRF and rising edge of the fluorescence curve. The "scatter" box represents the contribution of signal from scattering photons, which is set to zero in these experiments. The "offset" box (in number of photons) represents the constant baseline level of light (parameter C in Eq. 3.3), and is calculated from time channels before the rising part of the fluorescence decay. The $\chi^2$ goodness of fit values are close to 1 in all experiments,

indicating excellent fits to the lifetime decay curves. Deviations between fit and photon count data are represented by a weighted residual plot below the decay plot.

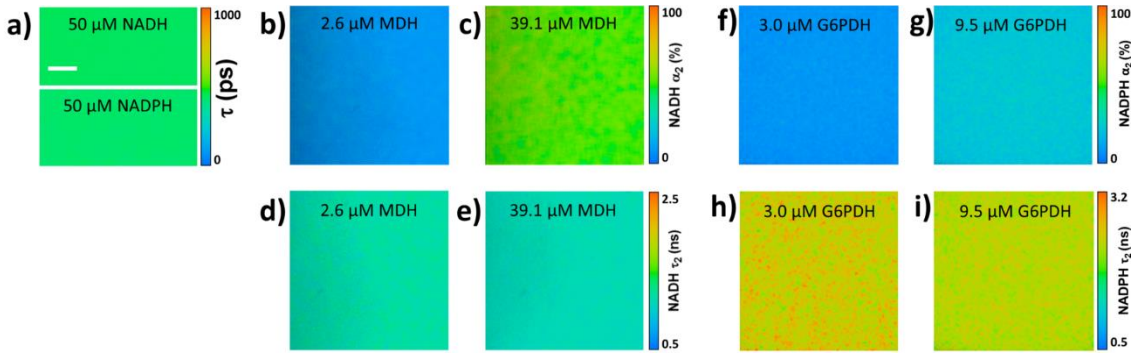


**Figure A.2. NAD(P)H fluorescence lifetime example images from enzyme mixture binding experiments in solution.** (**a**) Fluorescence lifetime images of 50 µM NADH and 50 µM NADPH. (**b,c**) Representative images, color-coded for $\alpha_2$, of mixtures containing 50 µM NADH and 2.6 µM MDH (**b**), and 50 µM NADH and 39.1 µM MDH (**c**). (**d,e**) Representative images, color-coded for $\tau_2$, of NADH-MDH mixtures containing 50 µM NADH and 2.6 µM MDH (**d**), and 50 µM NADH and 39.1 µM MDH (**e**). (**f,g**) Representative images, color-coded for $\alpha_2$, of NADPH-G6PDH mixtures containing 50 µM NADPH and 6.0 µM G6PDH (**f**), and 50 µM NADPH and 18.9 µM G6PDH (**g**). (**h,i**) Representative images, color-coded for $\tau_2$, of NADPH-G6PDH mixtures containing 50 µM NADPH and 6.0 µM G6PDH (**h**), and 50 µM NADPH and 18.9 µM G6PDH (**i**). Scale bar = 50 µm. All images binned 5x5 pixels for clarity.

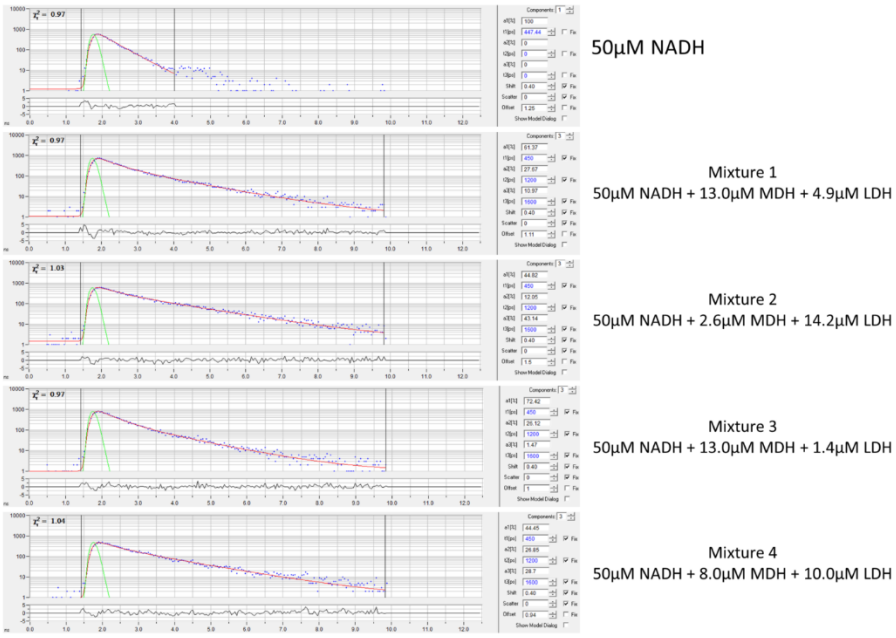


**Figure A.3. NADH fluorescence lifetime decay curve and fitting examples from enzyme mixture binding experiments in solution.** NADH fluorescence lifetime decay curves from a representative 1x1 binned pixel of 50 μM NADH alone or mixed with the indicated concentrations of LDH and MDH (experiments in Fig. 3.2). See Figure A.1 legend for explanation of SPCImage parameters. t1-3 refer to $\tau_1$, $\tau_2$, and $\tau_3$ respectively and are fixed according to Equation 3.4. a1-3 refer to $\alpha_{NADH-Free}$, $\alpha_{NADH-MDH}$, and $\alpha_{NADH-LDH}$ respectively (Eq. 3.4).

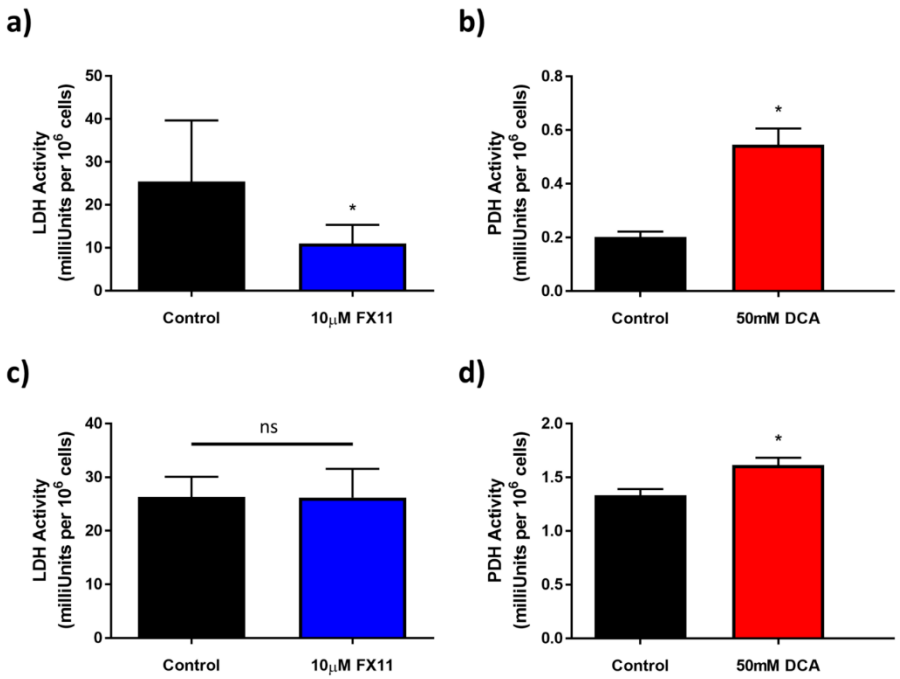


**Figure A.4. Absolute activities of PDH and MDH in cells.** (A-B) Mean and standard deviations of the absolute LDH (A) and PDH (B) activities in $10^6$ MCF10A cells after 48 hours of 10μM FX11 and 48 hours of 50mM DCA treatment vs. vehicle, respectively. * $p<0.05$ vs. control. n = 3-4 experiments. (C-D) Mean and standard deviations of the absolute LDH (C) and PDH (D) activities in $10^6$ HPDE6 cells after 48 hours of 10μM FX11 and 48 hours of 50mM DCA treatment vs. vehicle, respectively. n = 3-5 experiments.

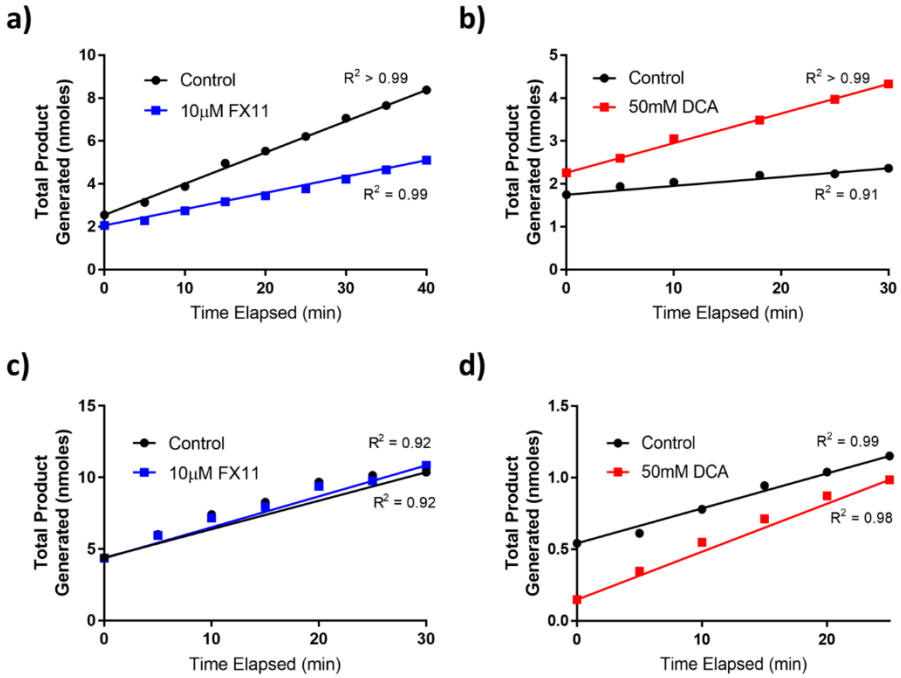


**Figure A.5. Examples of time-dependent LDH and PDH activity with fitting.** (A-B) NADH generated over time by LDH (A) and PDH (B) isolated from $10^6$ MCF10A cells after 48 hours of 10μM FX11 and 48 hours of 50mM DCA treatment vs. vehicle, respectively. Example data is from one single reaction from one experiment. Linear fits are calculated using first and last points in each reaction. The coefficient of determination ($R^2$) accounts for all time points. (C-D) NADH generated over time by LDH (C) and PDH (D) isolated from $10^6$ HPDE6 cells after 48 hours of 10μM FX11 and 48 hours of 50mM DCA treatment vs. vehicle, respectively. Example data shown from one single reaction per line.

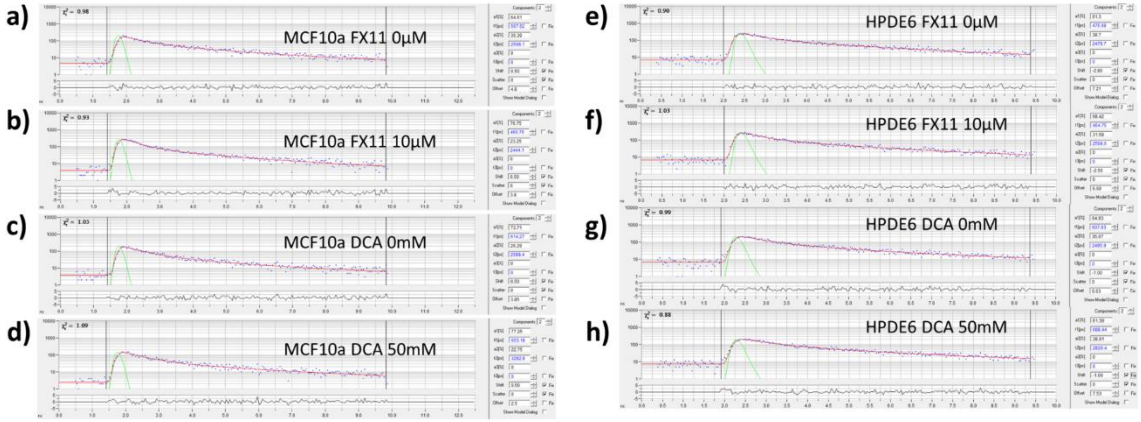


**Figure A.6. NAD(P)H fluorescence lifetime decay curve and fitting examples from MCF10A and HPDE6 cells.** (A-D) NAD(P)H fluorescence lifetime decay curves from a representative 1x1 binned pixel in the cytoplasm of MCF10A cells under each of the indicated metabolic inhibitor treatment conditions. (E-H) NAD(P)H fluorescence lifetime decay curves from a representative 1x1 binned pixel in the cytoplasm of HPDE6 cells under each of the indicated metabolic inhibitor treatment conditions (experiments in Fig. 3.3-3.9). See Figure A.1 legend for explanation of SPCImage parameters.

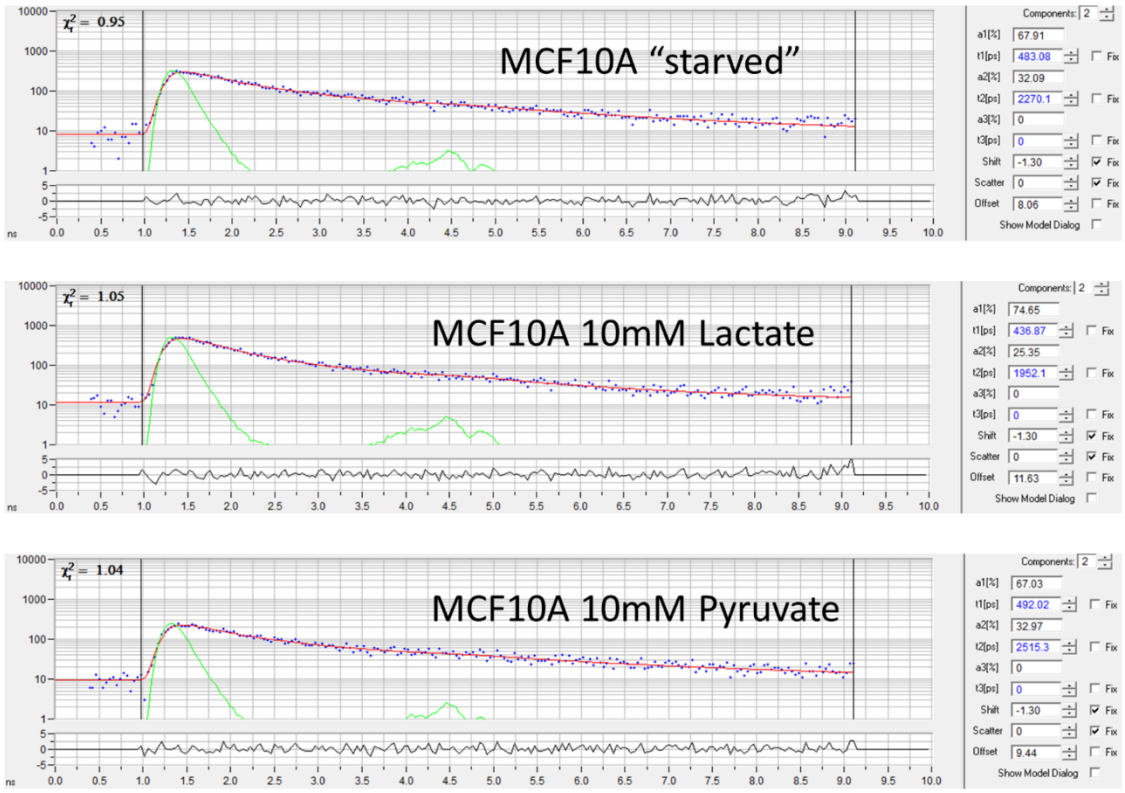


**Figure A.7. NAD(P)H fluorescence lifetime decay curve and fitting examples from starved MCF10A fed with pyruvate or lactate.** NAD(P)H fluorescence lifetime decay curves from a representative 1x1 binned pixel in the cytoplasm of MCF10A cells that have been starved or fed the indicated fuel source (experiments in Fig. 3.10). See Figure A.1 legend for explanation of SPCImage parameters.

**Table A.1. Sources of variability in NAD(P)H FLIM measurements.** Coefficients of variation and proportion of variation due to fitting uncertainty for NAD(P)H $\tau_2$, $\tau_1$, and $\alpha_1$ for each treatment condition in both cell types. The variation of NAD(P)H $\tau_1$, $\tau_2$, and $\alpha_1$ in each cell/treatment group within an individual pixel due to fitting was calculated by simulating decay curves with $\tau_1$, $\tau_2$, and $\alpha_1$ values that represented the measured values in each cell/treatment group (Fig. 3.7-3.9). For each of the 8 conditions, 65,536 curves were simulated using MATLAB (MathWorks) and random Poisson noise (square root of the number of photons) was added to each curve. The number of photons and the SNR of the simulated curves represent those acquired in our cell experiments. Each curve was fit in SPCImage (Becker & Hickl) and the standard deviation of the new fitted parameters was used to determine the coefficient of variation of fitting within a pixel. Coefficients of variation between experimental replicates, between cells within an experiment, and between pixels within a single cell (all factors that make up biological variation) were also quantified for each condition by calculating the coefficient of variation (ratio of standard deviation to mean). The proportion of total variance (sum of squared coefficients of variance) of a lifetime parameter that can be attributed to variability within a pixel (squared coefficient of variance within a pixel) was calculated and is displayed for each treatment condition and cell type.

| | | MCF10A | | | | HPDE6 | | | |
|---|---|---|---|---|---|---|---|---|---|
| | | FX11 Ctrl | FX11 10μM | DCA Ctrl | DCA 50mM | FX11 Ctrl | FX11 10μM | DCA Ctrl | DCA 50mM |
| NAD(P)H $\tau_2$ Coefficient of Variation (%) | Experimental Replicates | 1.3 | 0.9 | 0.2 | 0.5 | 1.9 | 1.3 | 0.7 | 0.5 |
| | Cell | 3.6 | 2.9 | 3.1 | 4.4 | 2.4 | 2.3 | 2.8 | 2.8 |
| | Pixel | 13.0 | 16.0 | 18.1 | 16.8 | 8.2 | 8.5 | 10.8 | 11.2 |
| | Within a pixel | 2.0 | 2.0 | 2.2 | 2.4 | 2.0 | 2.0 | 2.2 | 2.2 |
| | **Proportion due to uncertainty within a pixel (%)** | **2.1** | **1.5** | **1.4** | **1.9** | **5.0** | **4.9** | **3.6** | **3.5** |
| NAD(P)H $\tau_1$ Coefficient of Variation (%) | Experimental Replicates | 5.0 | 2.4 | 3.1 | 4.2 | 3.7 | 5.1 | 7.4 | 8.1 |
| | Cell | 5.8 | 5.7 | 5.2 | 6.6 | 3.1 | 3.6 | 4.1 | 5.5 |
| | Pixel | 20.7 | 29.6 | 24.8 | 25.5 | 11.5 | 14.1 | 16.0 | 16.4 |
| | Within a pixel | 4.4 | 3.5 | 4.4 | 4.4 | 4.4 | 4.4 | 4.5 | 5.6 |
| | **Proportion due to uncertainty within a pixel (%)** | **3.8** | **1.3** | **2.9** | **2.6** | **10.9** | **7.6** | **5.8** | **7.8** |
| NAD(P)H $\alpha_1$ Coefficient of Variation (%) | Experimental Replicates | 8.6 | 1.8 | 6.7 | 4.0 | 0.9 | 2.1 | 2.5 | 2.5 |
| | Cell | 2.9 | 1.7 | 2.2 | 2.5 | 3.5 | 2.9 | 3.0 | 4.9 |
| | Pixel | 9.4 | 5.6 | 9.0 | 8.8 | 4.8 | 7.7 | 9.8 | 10.3 |
| | Within a pixel | 1.7 | 1.2 | 1.8 | 2.0 | 1.8 | 1.9 | 2.1 | 2.9 |
| | **Proportion due to uncertainty within a pixel (%)** | **1.7** | **3.7** | **2.4** | **3.9** | **8.2** | **4.5** | **3.7** | **5.8** |

## APPENDIX B

### Supplementary Material for Chapter 4

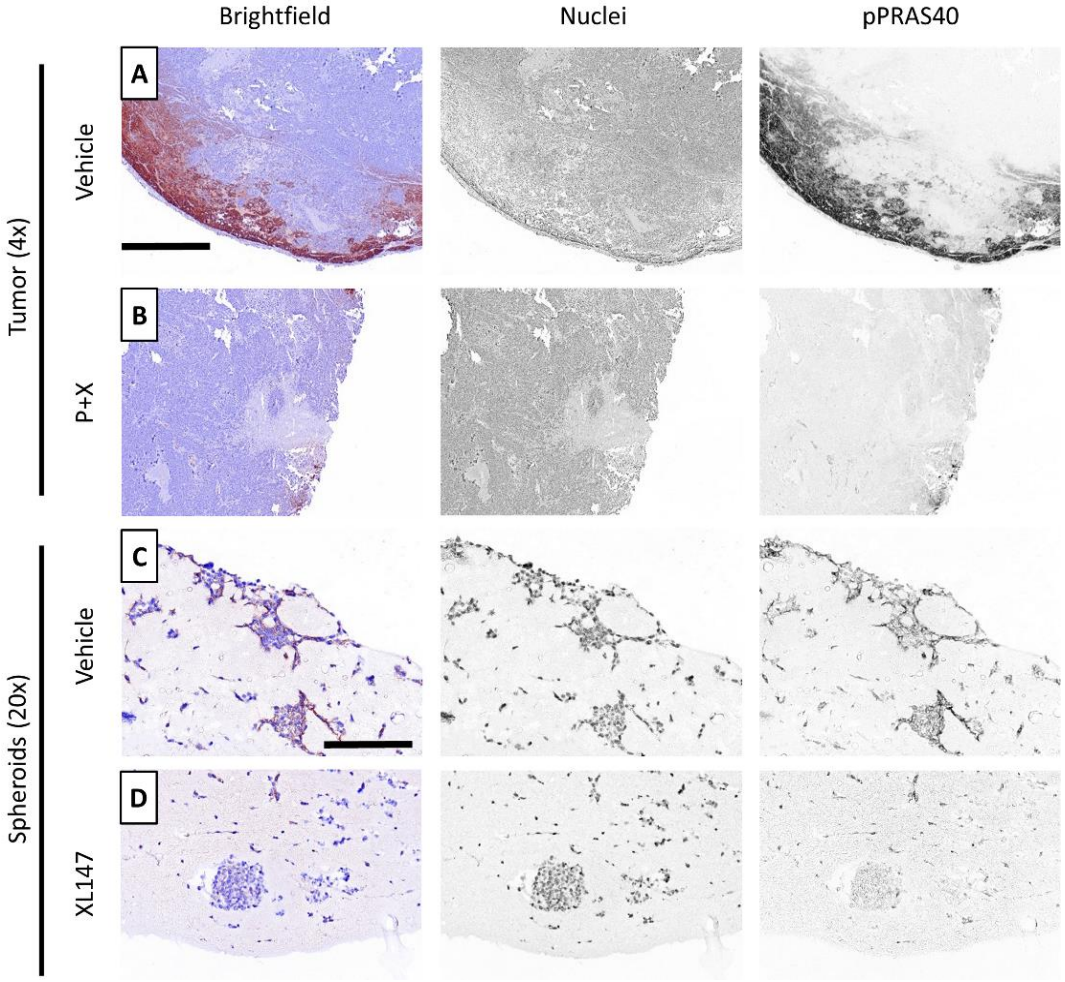


**Figure B.1. Decreased expression of pPRAS40 with treatment in PyVmT tumors and organoids. A-B,** Example histology and spectral unmixing of pPRAS40 expression in PyVmT tumors treated with vehicle (**A**) and paclitaxel and XL147 (P+X) for 48 hours (**B**). **C-D**, Examples of pPRAS40 expression in PyVmT organoids treated with vehicle (**C**) and XL147 for 72 hours (**D**). 4x scale bar = 1 mm. 20x scale bar = 200 μm.

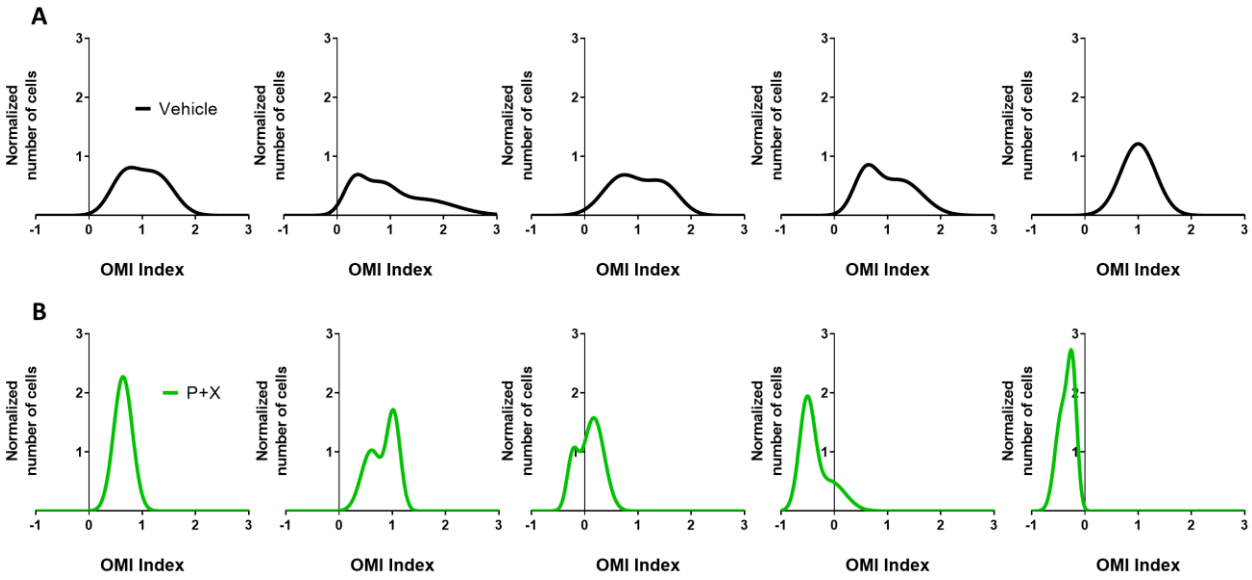


**Figure B.2. OMI index heterogeneity in individual PyVmT tumors.** Distributions of drug response at the single-cell level for (**A**) vehicle and (**B**) P+X treated tumors.

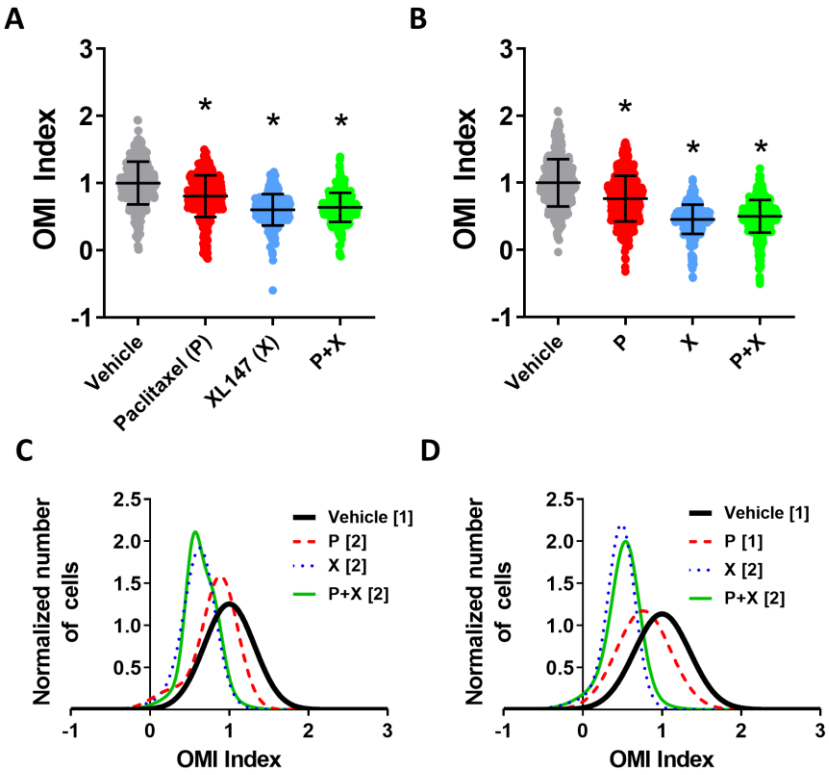


**Figure B.3. OMI of drug response heterogeneity in PyVmT organoids at additional time points. A-B,** OMI index quantified at the single cell level at (**A**) 24 hours and (**B**) 48 hours of treatment. N=6 organoids/group. N>290 cells/group. Error bars indicate mean ± SD. * p<0.0001 vs. vehicle. **C-D,** Example subpopulation analysis of the OMI index in all organoid cells at (**C**) 24 hours and (**D**) 48 hours of treatment. Brackets in legend indicate number of subpopulations for each group.

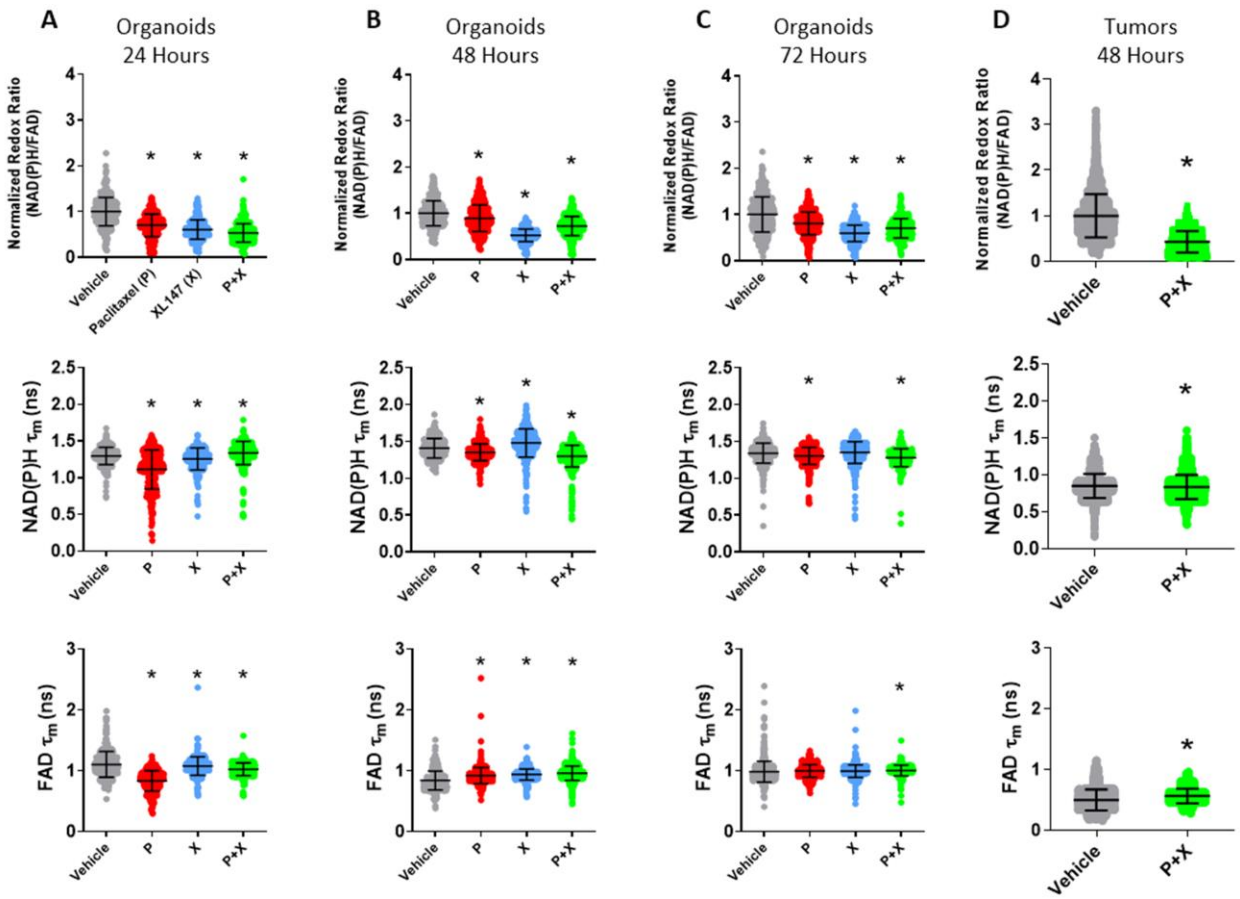


**Figure B.4. OMI endpoints of drug response in single cells.** Normalized redox ratio, NAD(P)H $\tau_m$, and FAD $\tau_m$ at (**A**) 24 hours, (**B**) 48 hours, (**C**) 72 hours in PyVmT organoids, and at (D) 48 hours in PyVmT tumors. Error bars indicate mean ± SD. * p<0.0001 vs. vehicle. Each dot represents one cell.

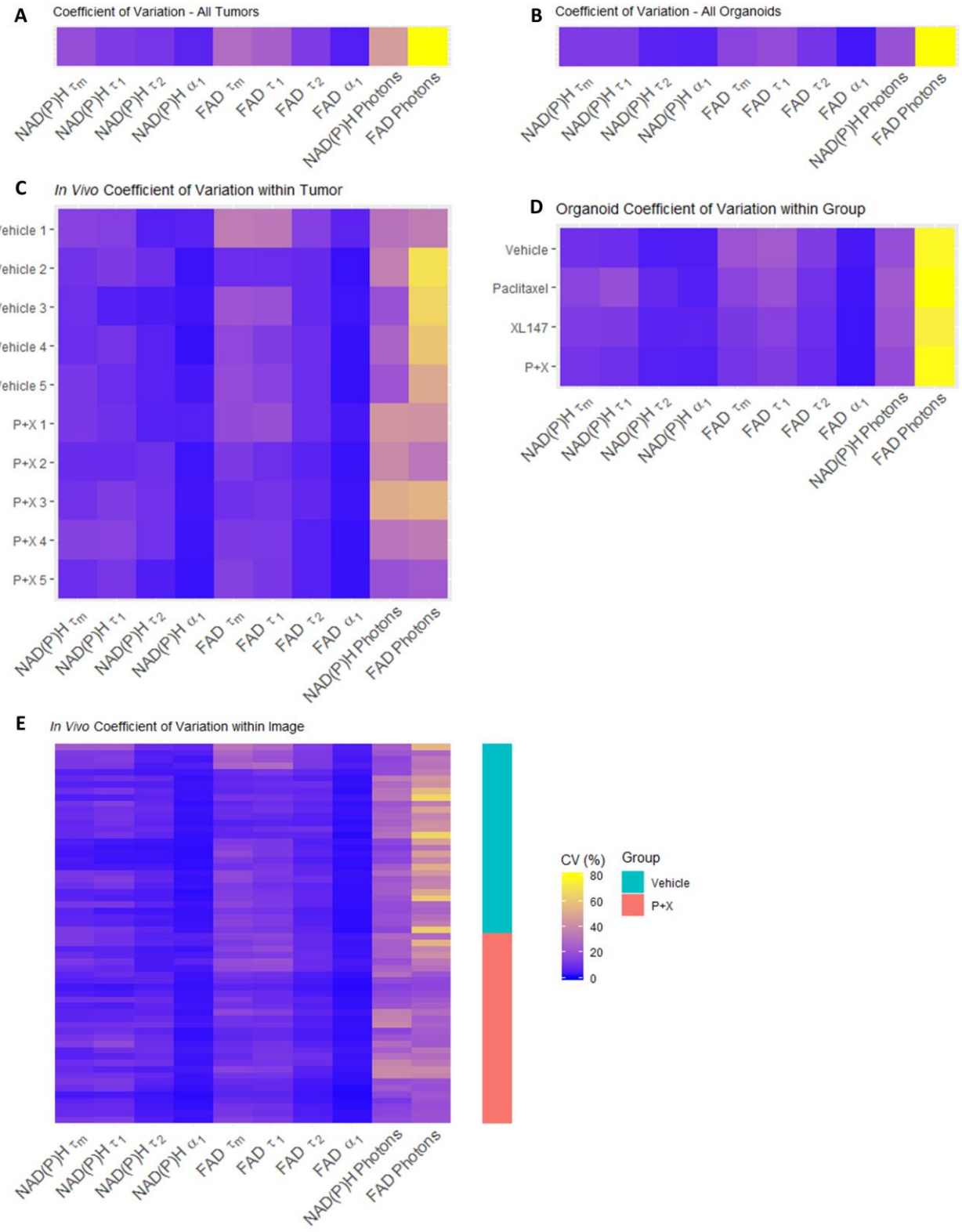
A
Coefficient of Variation - All Tumors
B
Coefficient of Variation - All Organoids
C
In Vivo Coefficient of Variation within Tumor
Vehicle 1
Vehicle 2
Vehicle 3
Vehicle 4
Vehicle 5
P+X 1
P+X 2
P+X 3
P+X 4
P+X 5
D
Organoid Coefficient of Variation within Group
Vehicle
Paclitaxel
XL147
P+X
E
In Vivo Coefficient of Variation within Image
CV (%)
80
60
40
20
0
Group
Vehicle
P+X
NAD(P)H τm
NAD(P)H τ1
NAD(P)H τ2
NAD(P)H α1
FAD τm
FAD τ1
FAD τ2
FAD α1
NAD(P)H Photons
FAD Photons

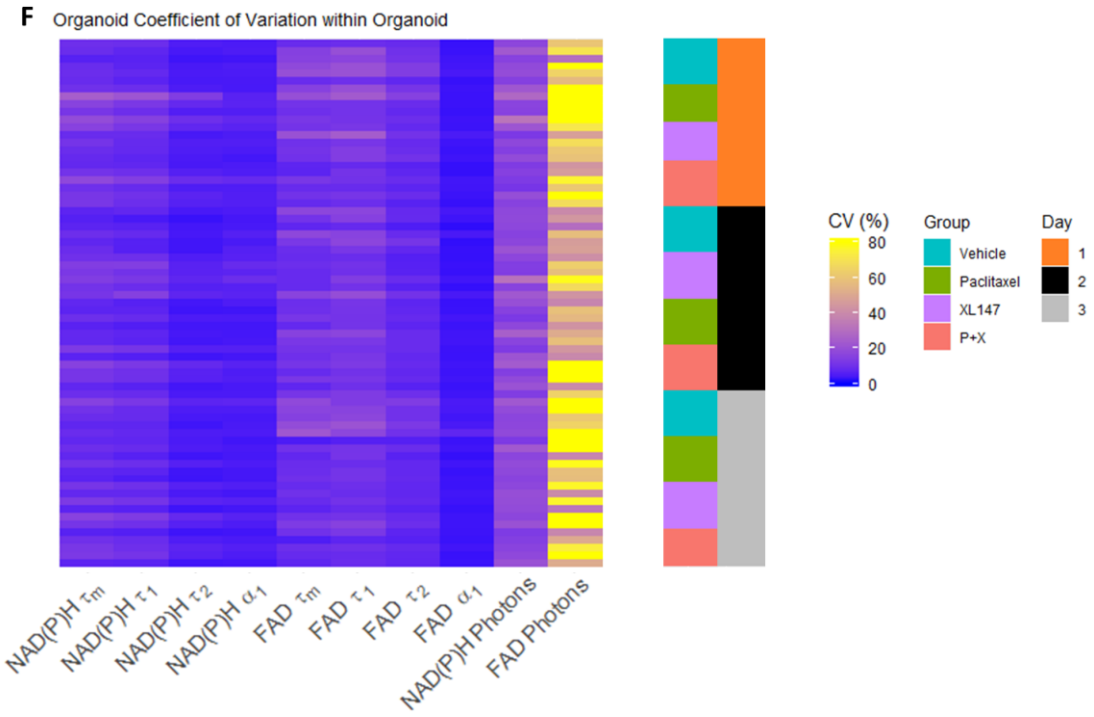


**Figure B.5. Coefficients of variation of OMI variables across individual cells. A-B,** Coefficients of variation (standard deviation divided by the mean, CV) of each OMI variable across all cells imaged (**A**) *in vivo* and (**B**) in tumor-derived organoids. **C,** CV of each OMI variable within each tumor *in vivo*. Each row represents a tumor. **D,** CVs of each OMI variable within each treatment group in organoids. Each row represents a treatment group. **E,** CVs of each OMI variable within each field of view (FOV) imaged *in vivo*. Each row represents a FOV. **F,** CVs of each OMI variable within each organoid. Each row represents an organoid.

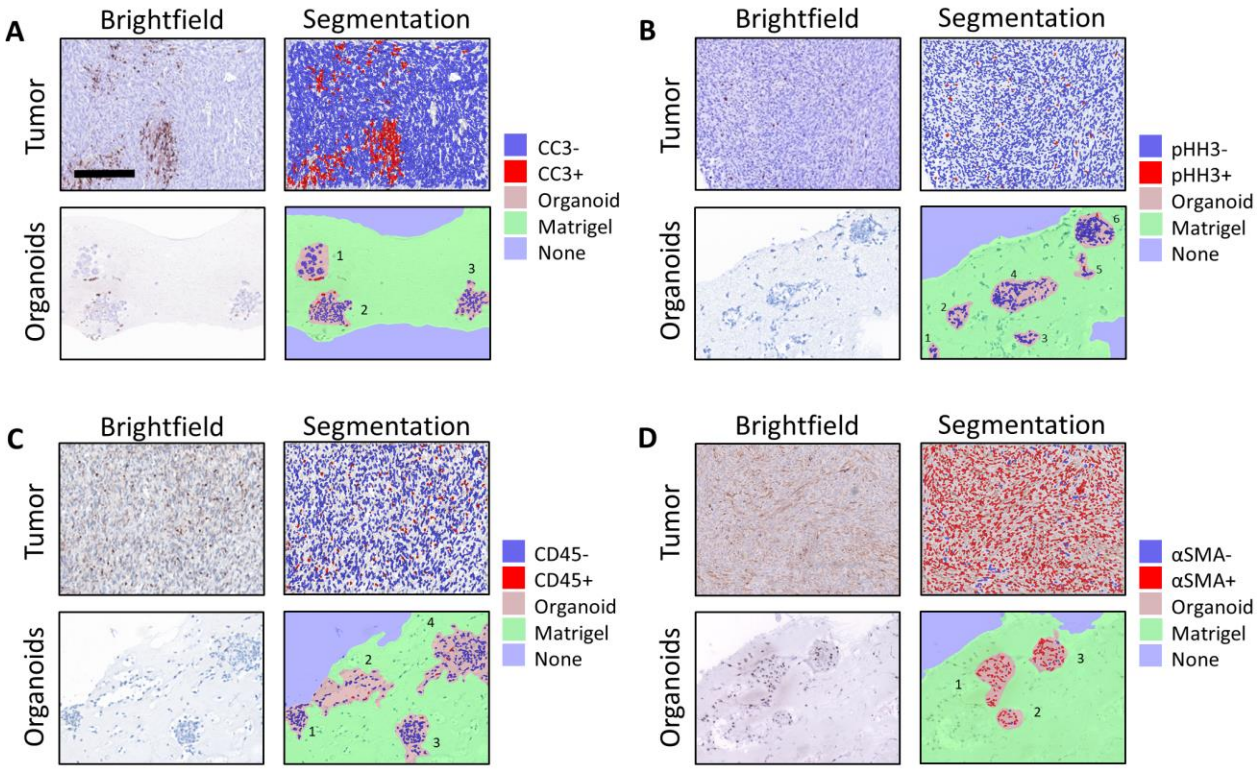


**Figure B.6. Automatic cell segmentation and quantification in PyVmT tumors and organoids with histology.** Examples images of (**A**) CC3, (**B**) pHH3, (**C**) CD45, and (**D**) αSMA expression in 20x histology images of PyVmT tumor and organoids. Scale bar = 200 μm.

# APPENDIX C

## Supplementary Material for Chapter 5

**Table C.1. Characteristics of patient tissue samples acquired from surgical resection of pancreatic lesions.** RFS, recurrence-free survival. Asterisk indicates that a recurrence has occurred.

| Patient # | Drug treatment before surgery | Neoadjuvant Treatment Response | Post-treatment Diagnosis | Residual Tumor Size | Stage | Viable Organ-oids | Drug treatment after surgery | Known RFS (months) |
|---|---|---|---|---|---|---|---|---|
| 1 | 5-FU | Partial response, score 2 | PDAC, well-differentiated | 3.5x1.8x1.7 cm | ypT3N0 | Yes | Gemcitabine + 5-FU | >24 |
| 2 | None | N/A | PDAC, poorly-differentiated | 4.8x3.5x2 cm | pT3N1 | Yes | Gemcitabine + 5-FU | 14.5* |
| 3 | 5-FU | Poor or no response, score 3 | PDAC, poorly-differentiated | 2x2x1.5 cm | ypT3N1 | Yes | Gemcitabine + 5-FU | 11.5* |
| 4 | None | N/A | Mucinous adenocarcinoma | 4x3x2.9 cm | pT3N1 | No | Gemcitabine + 5-FU | >20 |
| 5 | FOLFIRINOX | Complete response, score 0 | No residual cancer | N/A | ypT0N0 | Yes | None | N/A |
| 6 | None | N/A | Ampullary adenocarcinoma, moderately-differentiated | 2x2x1.2 cm | pT2N1 | Yes | Oxaliplatin + 5-FU | >16 |
| 7 | None | N/A | PDAC, moderately-differentiated (arising in IPMN) | 0.5 cm | pT1N0 | No | None | >14 |
| 8 | Gemcitabine + nab-paclitaxel | Partial response, score 2 | PDAC, moderately-differentiated | 3.0 cm | ypT3N1 | Yes | 5-FU | 5* |
| 9 | Gemcitabine + nab-paclitaxel + FOLFIRINOX | Poor or no response, score 3 | PDAC, moderately-differentiated | 3.1x2.5x2.3 cm | ypT4N1 | No | None | 4* |
| 10 | None | N/A | PDAC, moderately-differentiated | 3.5x2x2 cm | pT3N1 | No | Unknown | 2* |
| 11 | None | N/A | Chronic pancreatitis and PanIN-1 | N/A | N/A | Yes | None | N/A |
| 12 | None | N/A | PDAC, poorly-differentiated | 1.2x1.1x1.1 cm | pT1N1 | Yes | FOLFIRINOX | 2* |
| 13 | Gemcitabine + nab-paclitaxel | Poor or no response, score 3 | Undifferentiated (anaplastic) carcinoma of pancreas | 4.9x4.3x4.1 cm | ypT3N1 | Yes | None | 0.5* |
| 14 | None | N/A | PDAC, moderately-differentiated | 3.5 cm | pT3pN1 | Yes | Gemcitabine + 5-FU | >13 |
| 15 | None | N/A | PDAC, moderately-differentiated | 3x2.5x2.5 cm | pT2N1 | No | Gemcitabine + 5-FU | >7 |
| 16 | Gemcitabine + nab-paclitaxel | Partial response, score 2 | Ampullary adenocarcinoma, well-differentiated | 2.5x2.5x1.4 cm | ypT3bN1 | No | None | >3 |
| 17 | FOLFIRINOX | Partial response, score 2 | PDAC, well-differentiated | 2.0x2.0x1.5 cm | ypT2N0 | Yes | None | 4* |
| 18 | None | N/A | PDAC, poorly-differentiated | 4.7x4.3x3.5 cm | pT3N2 | Yes | FOLFIRINOX | >2 |

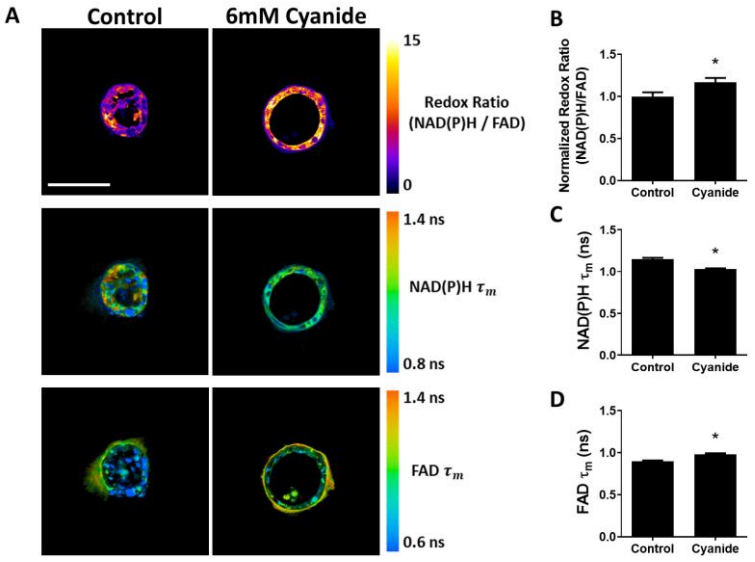


**Figure C.1. Metabolic perturbation with cyanide validates OMI and organoid viability. A,** Representative redox ratio, NAD(P)H $\tau_m$, and FAD $\tau_m$ images of Patient 1 pancreatic organoids before and after 6mM cyanide treatment. Scale bar is 100 μm. **B,** Optical redox ratio increases with cyanide. **C,** NAD(P)H mean lifetime decreases with cyanide. **D,** FAD mean lifetime increases with cyanide treatment. Error bars indicate mean ± SD. * $p<0.05$. N=4 pancreatic organoids comprising 64 cells.

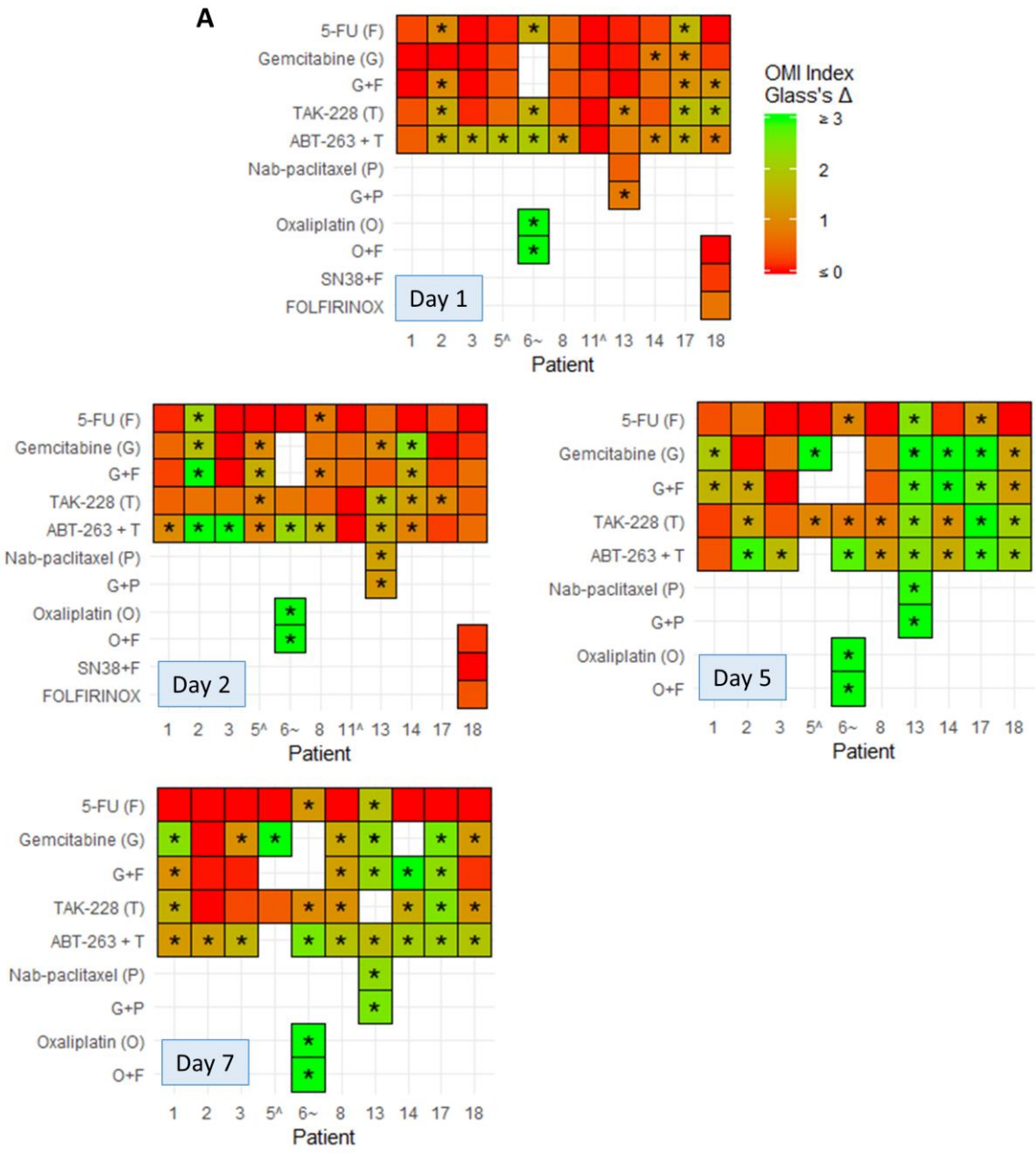
A
5-FU (F)
Gemcitabine (G)
G+F
TAK-228 (T)
ABT-263 + T
Nab-paclitaxel (P)
G+P
Oxaliplatin (O)
O+F
SN38+F
FOLFIRINOX
Day 1
Day 2
Day 5
Day 7
1 2 3 5^ 6~ 8 11^ 13 14 17 18
Patient
OMI Index
Glass's Δ
≥ 3
2
1
≤ 0

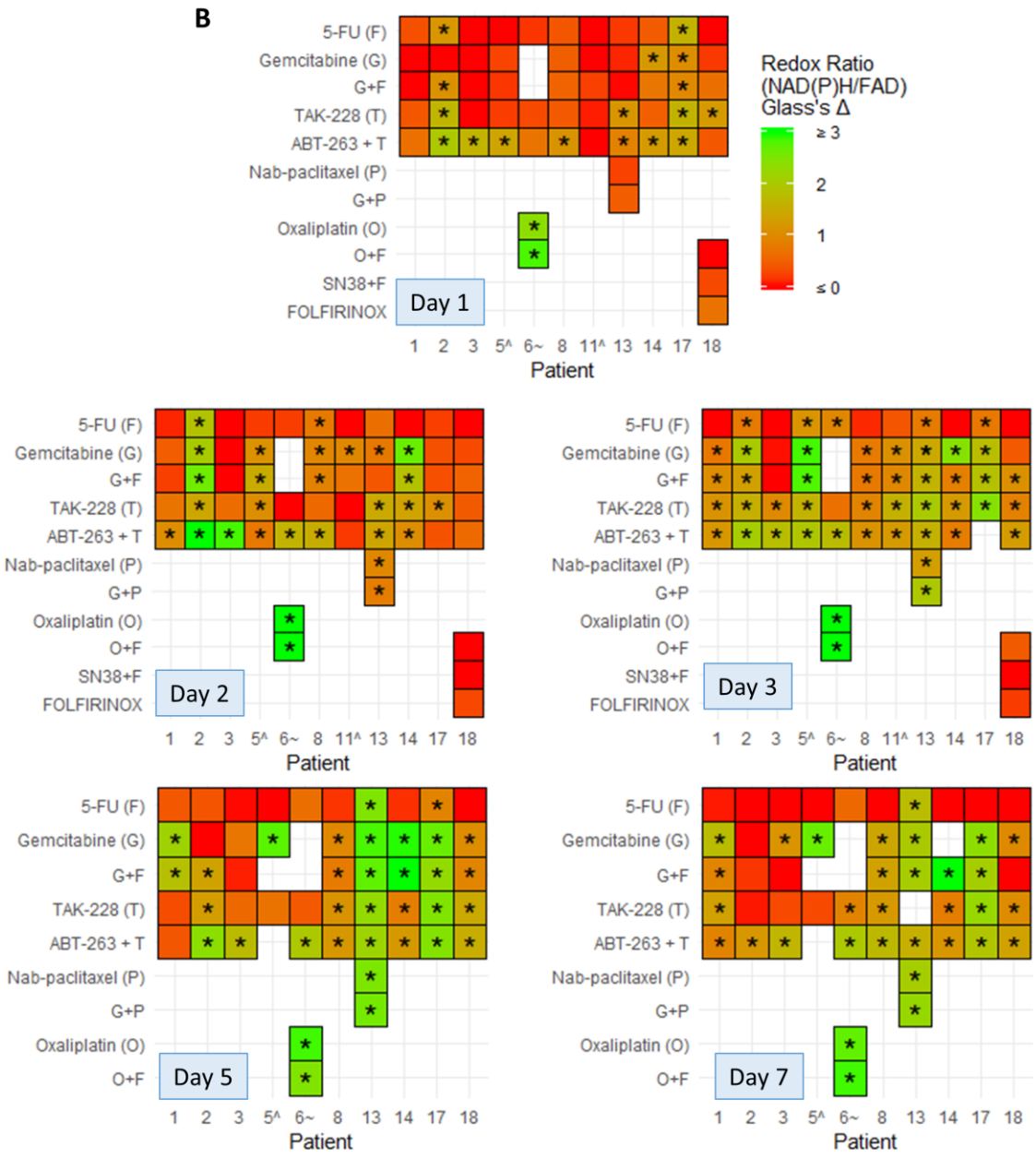
B
5-FU (F)
Gemcitabine (G)
G+F
TAK-228 (T)
ABT-263 + T
Nab-paclitaxel (P)
G+P
Oxaliplatin (O)
O+F
SN38+F
FOLFIRINOX
Day 1
Day 2
Day 3
Day 5
Day 7
1 2 3 5^ 6~ 8 11^ 13 14 17 18
Patient
Redox Ratio
(NAD(P)H/FAD)
Glass's Δ
≥ 3
2
1
≤ 0

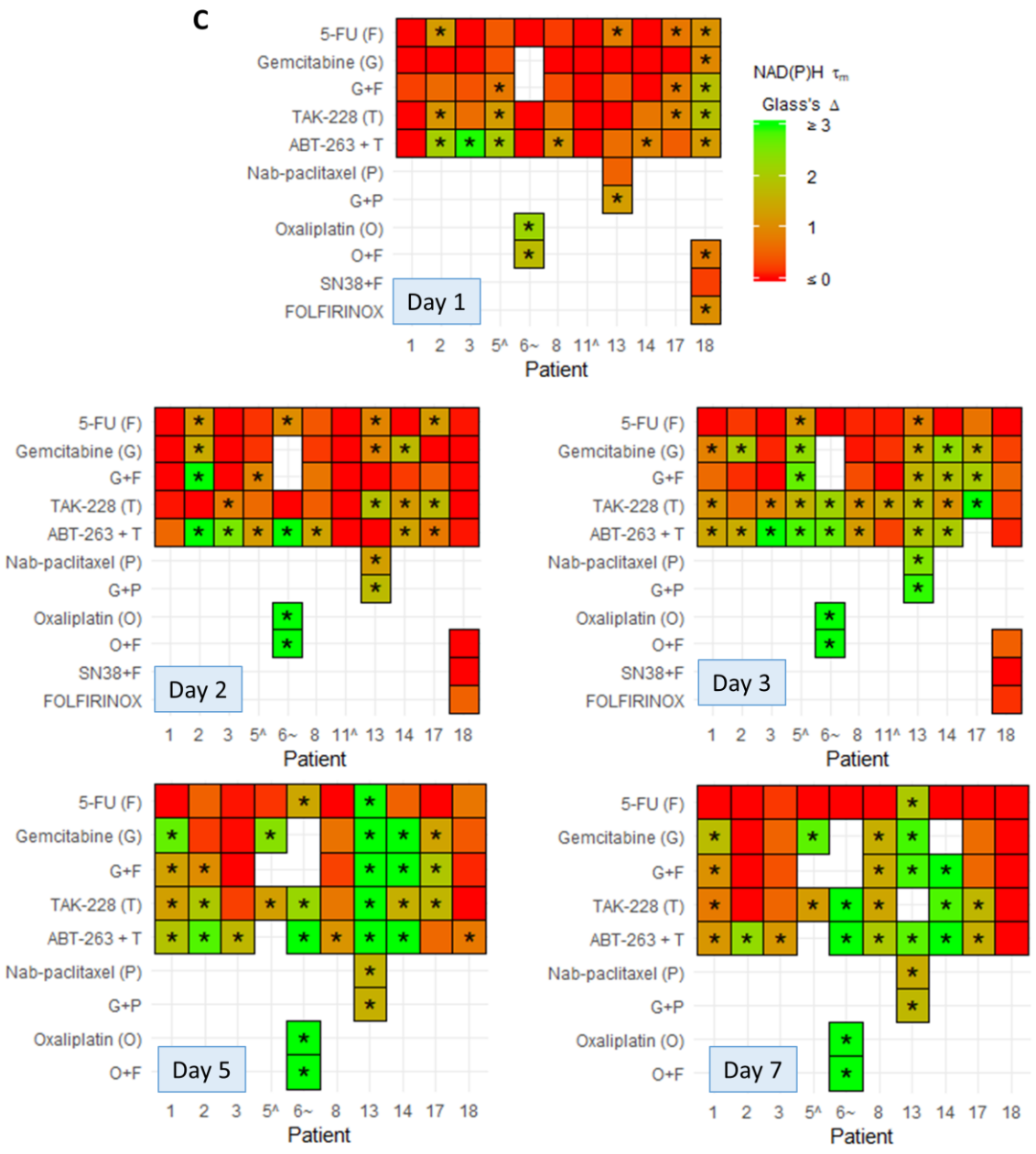
C
5-FU (F)
Gemcitabine (G)
G+F
TAK-228 (T)
ABT-263 + T
Nab-paclitaxel (P)
G+P
Oxaliplatin (O)
O+F
SN38+F
FOLFIRINOX
Day 1
Day 2
Day 3
Day 5
Day 7
1 2 3 5^ 6~ 8 11^ 13 14 17 18
Patient
NAD(P)H τm
Glass's Δ
≥ 3
2
1
≤ 0

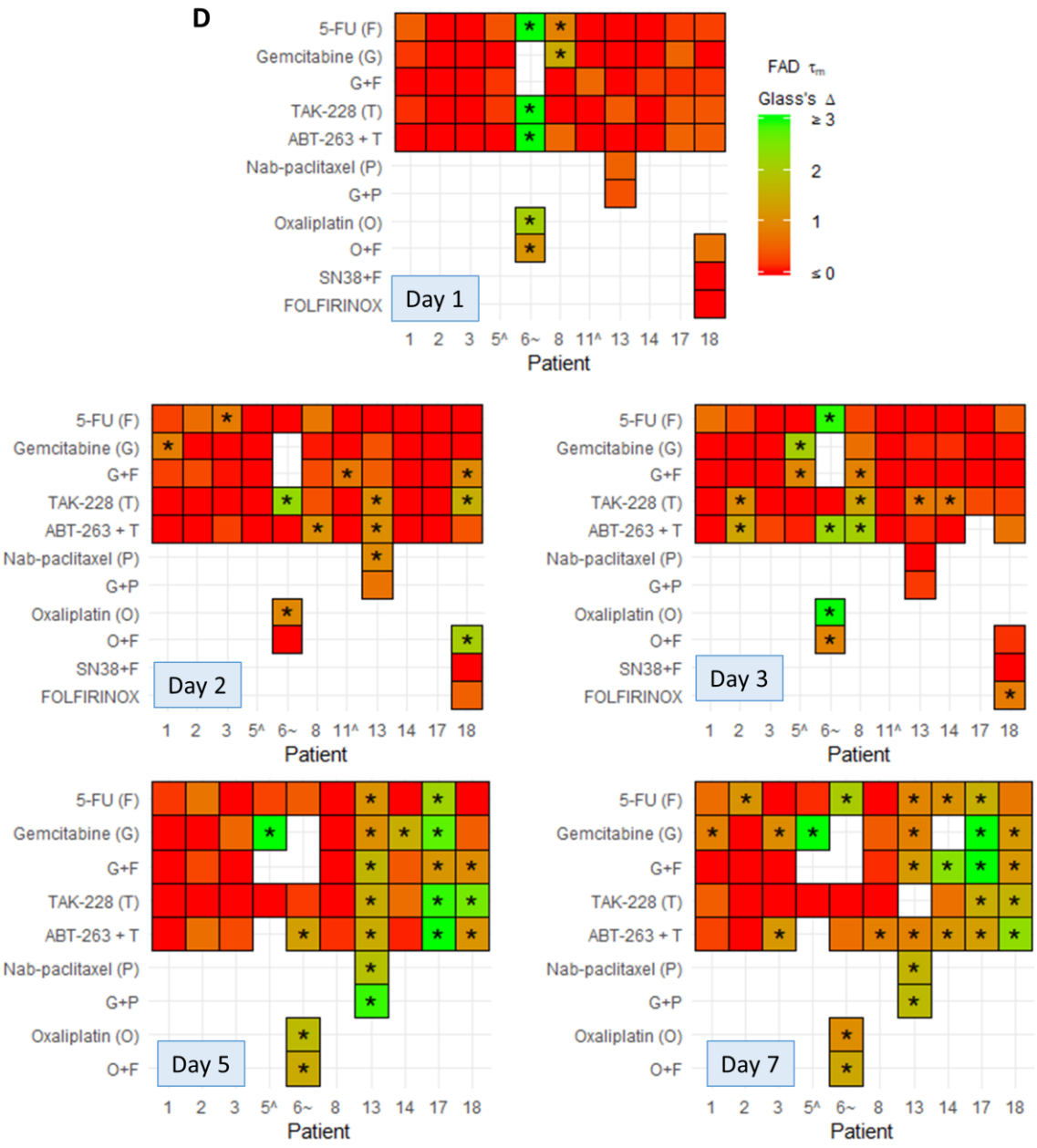


**Figure C.2. Effect sizes of drug treatment on individual OMI endpoints in organoids. A-D,** Heatmap representation of the treatment effect size (Glass's Δ) at each time point for the OMI index (**A**), redox ratio (**B**), NAD(P)H $\tau_m$ (**C**), and FAD $\tau_m$ (**D**). '^' indicates the patient lesion was diagnosed as PanIN. '~' indicates the patient lesion was diagnosed as ampullary cancer. * Glass's $\Delta \geq 0.75$ vs. control.

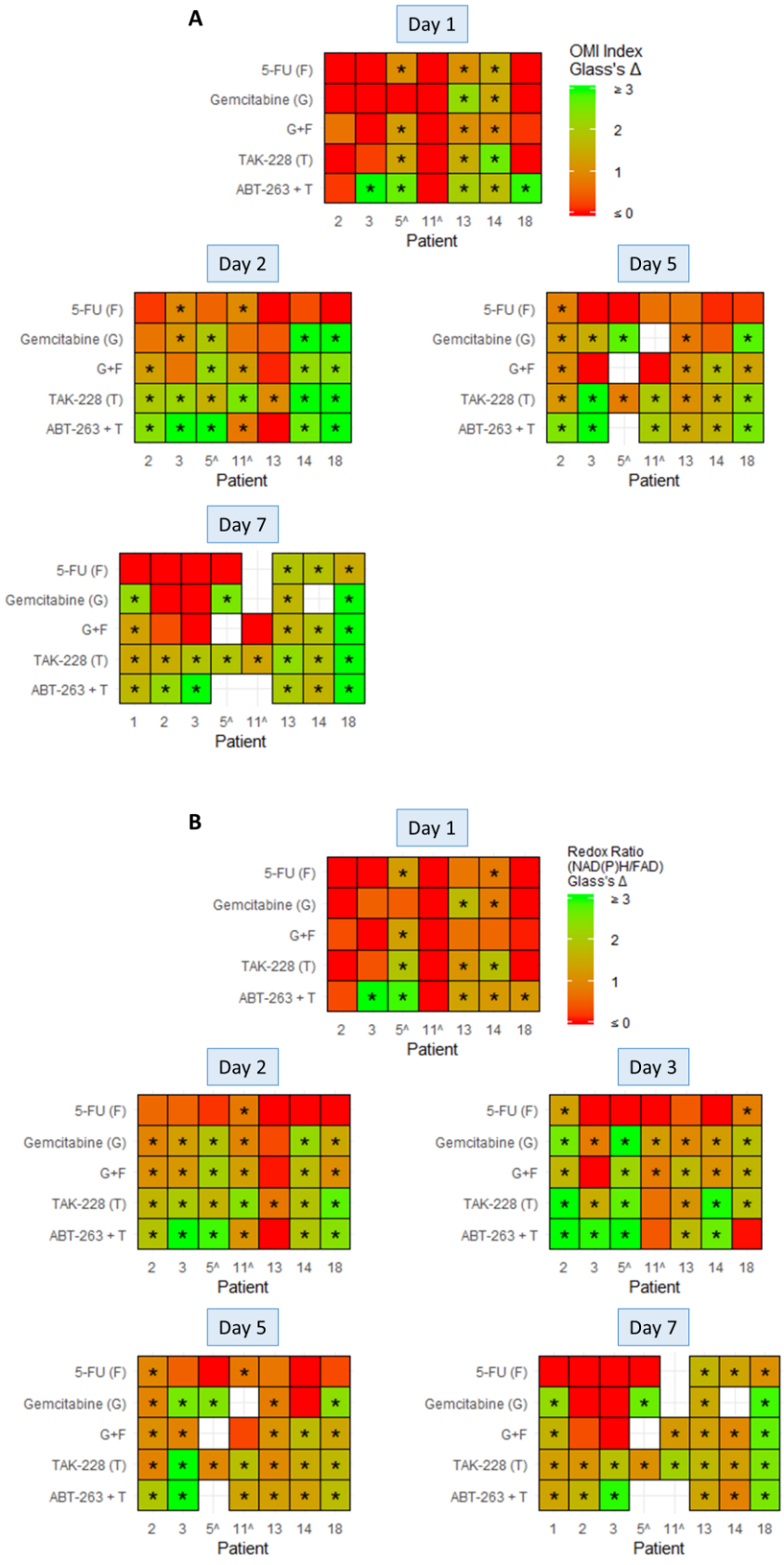
A
Day 1
Day 2
Day 5
Day 7
5-FU (F)
Gemcitabine (G)
G+F
TAK-228 (T)
ABT-263 + T
2 3 5^ 11^ 13 14 18
1 2 3 5^ 11^ 13 14 18
Patient
OMI Index
Glass's Δ
≥ 3
2
1
≤ 0
B
Day 1
Day 2
Day 3
Day 5
Day 7
Redox Ratio
(NAD(P)H/FAD)
Glass's Δ
≥ 3
2
1
≤ 0

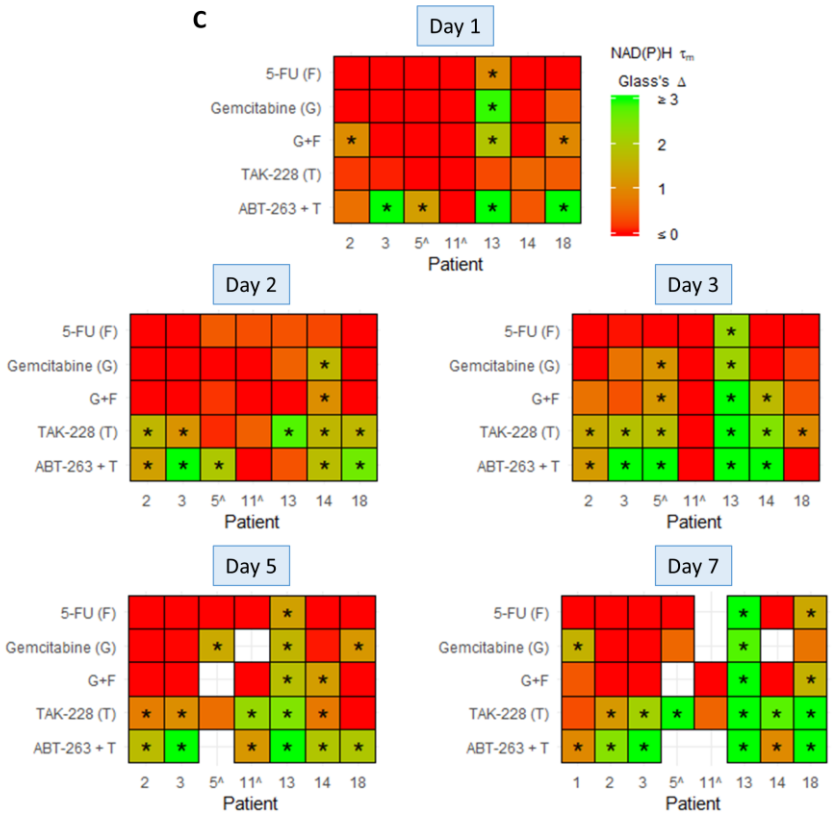
C
Day 1
Day 2
Day 3
Day 5
Day 7
5-FU (F)
Gemcitabine (G)
G+F
TAK-228 (T)
ABT-263 + T
NAD(P)H τm
Glass's Δ
≥ 3
2
1
≤ 0
2 3 5^ 11^ 13 14 18
1 2 3 5^ 11^ 13 14 18
Patient

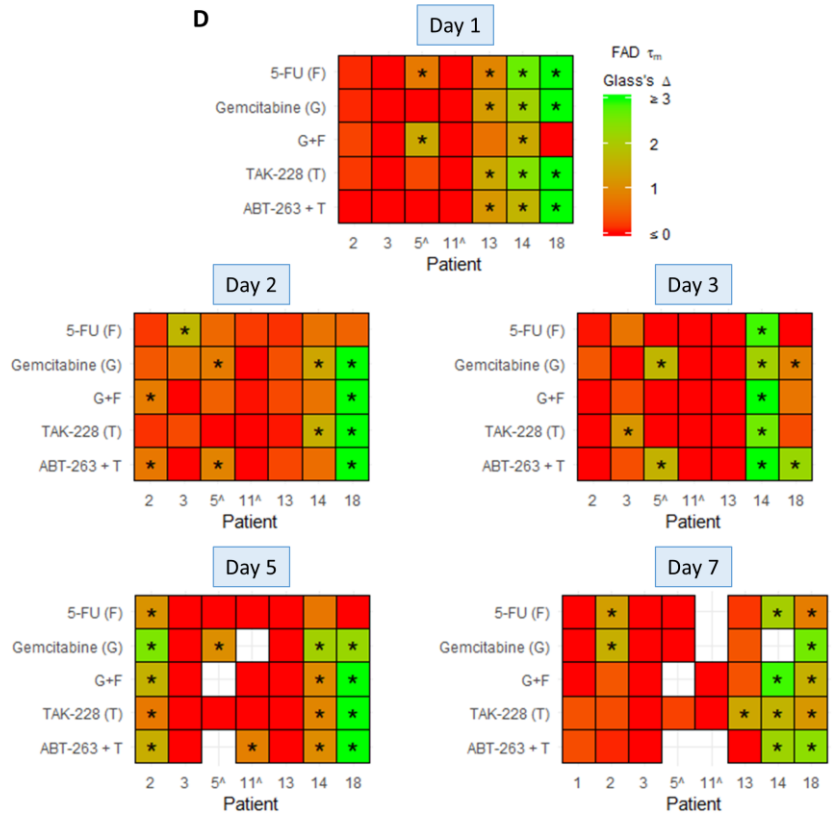
D
Day 1
Day 2
Day 3
Day 5
Day 7
5-FU (F)
Gemcitabine (G)
G+F
TAK-228 (T)
ABT-263 + T
FAD τm
Glass's Δ
≥ 3
2
1
≤ 0
2 3 5^ 11^ 13 14 18
1 2 3 5^ 11^ 13 14 18
Patient

**Figure C.3. Effect sizes of drug treatment on individual OMI endpoints in patient-derived fibroblasts co-cultured with organoids. A-D,** Heatmap representation of the treatment effect size (Glass's Δ) at each time point for the OMI index (**A**), redox ratio (**B**), NAD(P)H $\tau_m$ (**C**), and FAD $\tau_m$ (**D**). '^' indicates the patient lesion was diagnosed as PanIN. '~' indicates the patient lesion was diagnosed as ampullary cancer. * Glass's $\Delta \geq 0.75$ vs. control.

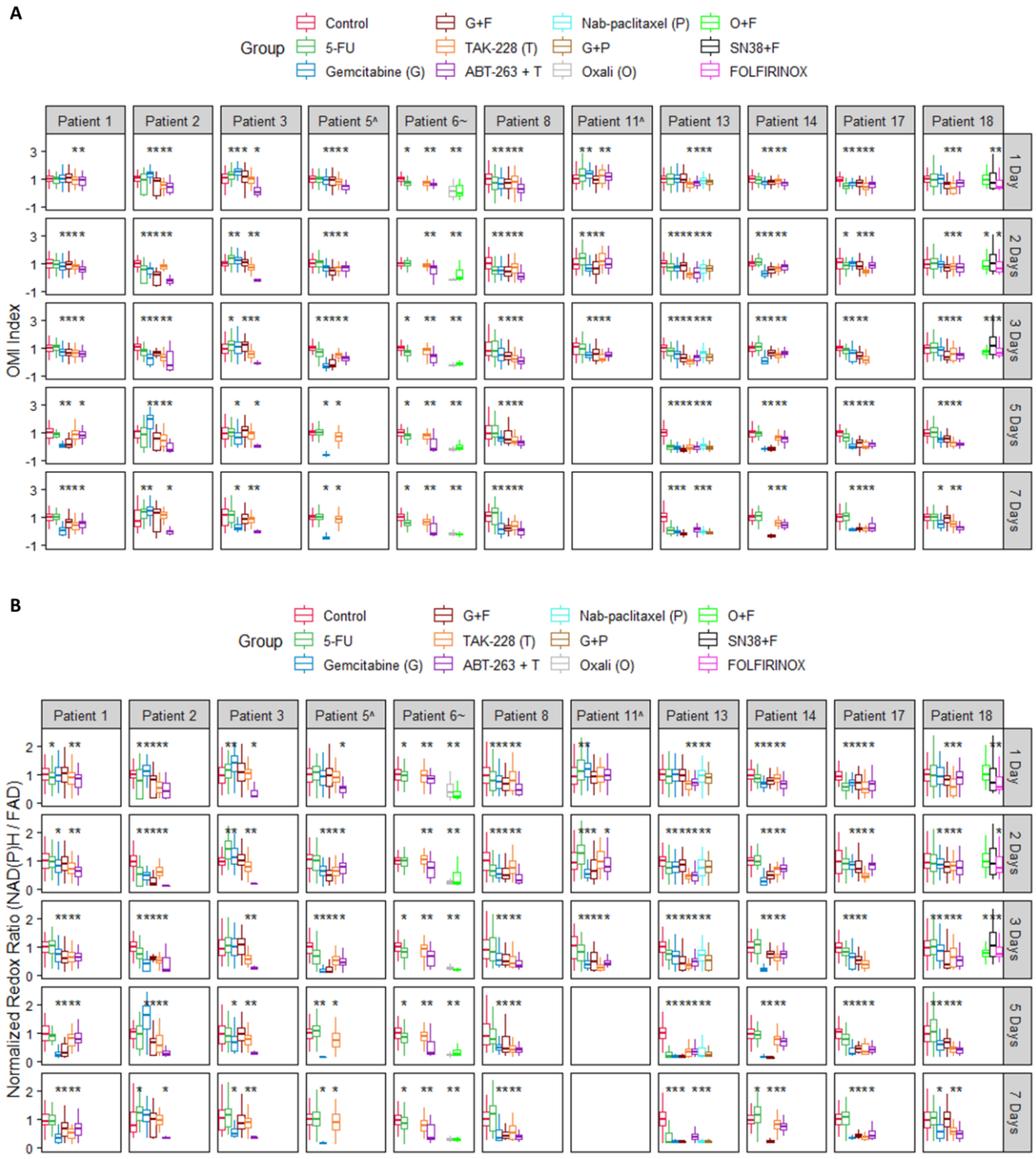

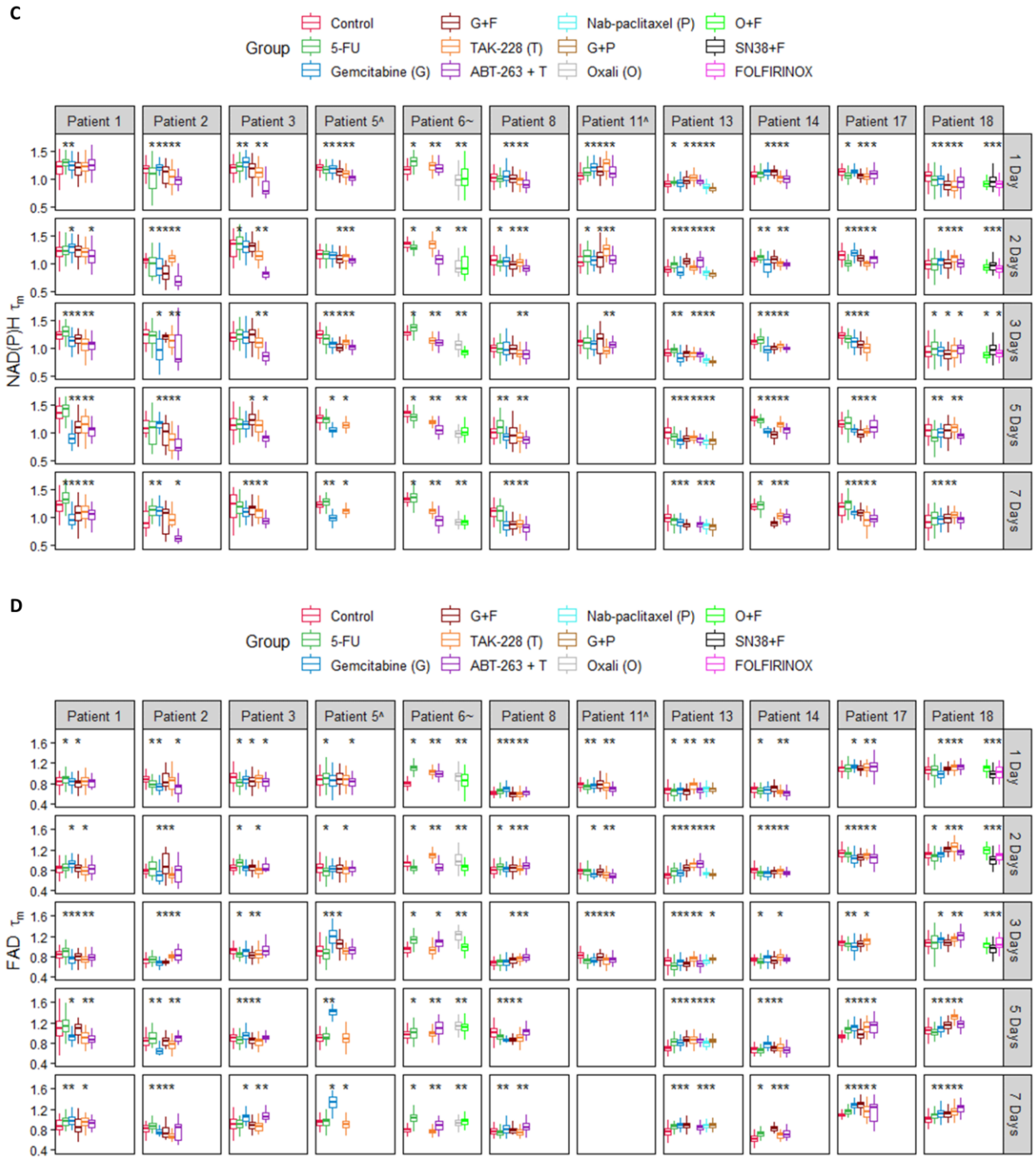


**Figure C.4. Significance of drug treatment effects on individual OMI endpoints in organoids.** **A-D,** Boxplot summaries comparing the effect of all drugs between patients and time points in organoids on the OMI index (**A**), redox ratio (**B**), NAD(P)H $\tau_m$ **(C)**, and FAD $\tau_m$ **(D)**. '^' indicates the patient lesion was diagnosed as PanIN. '~' indicates the patient lesion was diagnosed as ampullary cancer. * p<0.05 vs. control.

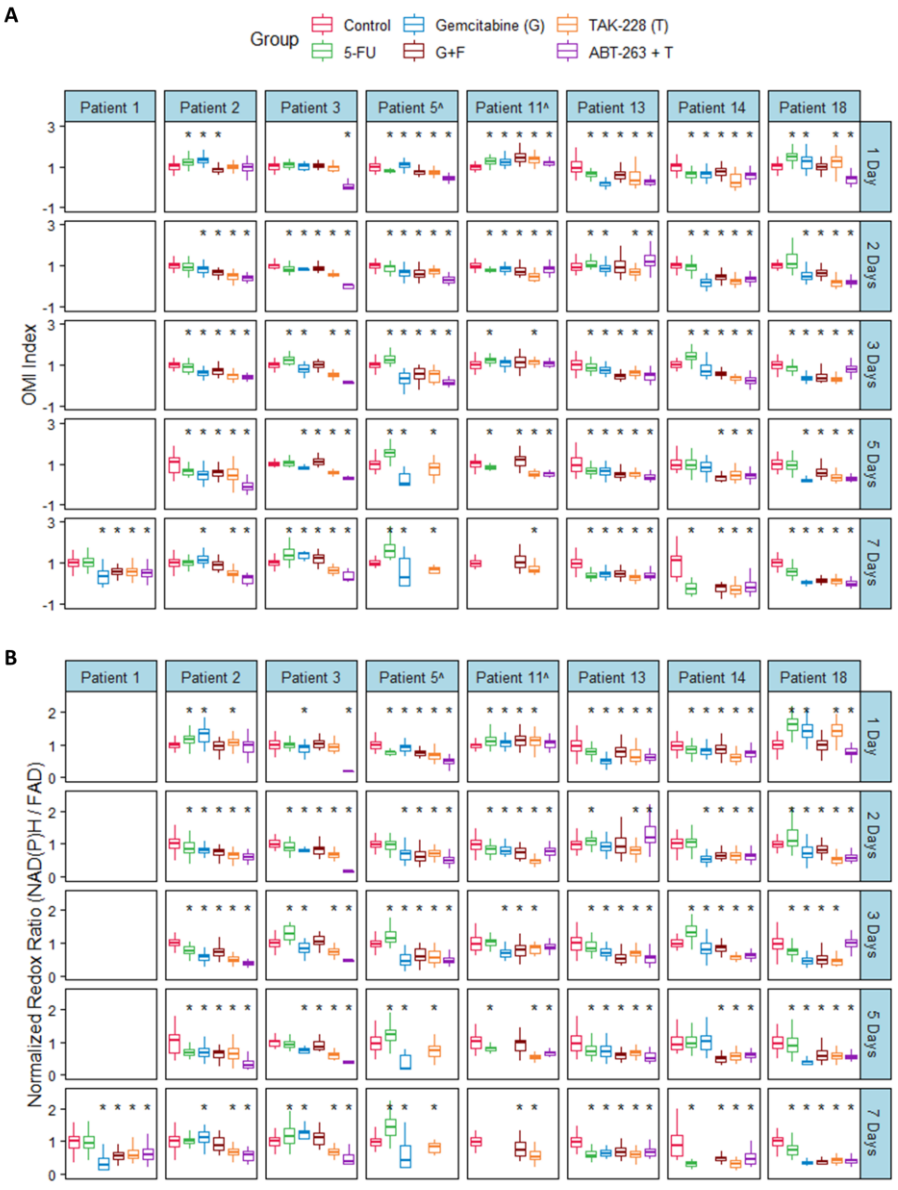
A
Group
Control
Gemcitabine (G)
TAK-228 (T)
5-FU
G+F
ABT-263 + T
Patient 1
Patient 2
Patient 3
Patient 5^
Patient 11^
Patient 13
Patient 14
Patient 18
1 Day
2 Days
3 Days
5 Days
7 Days
OMI Index
B
Normalized Redox Ratio (NAD(P)H / FAD)

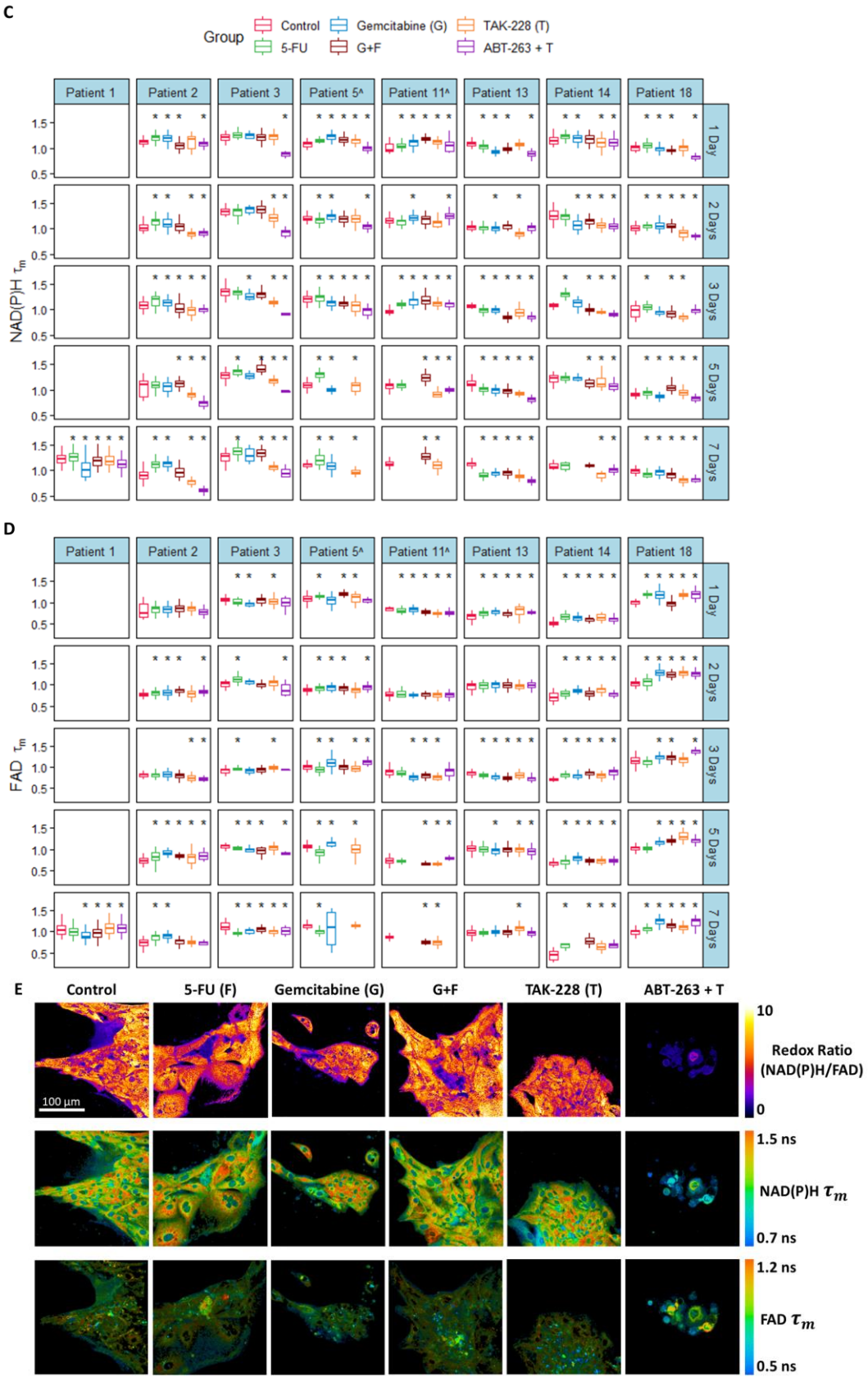
C
Group
Control
Gemcitabine (G)
TAK-228 (T)
5-FU
G+F
ABT-263 + T
Patient 1
Patient 2
Patient 3
Patient 5^
Patient 11^
Patient 13
Patient 14
Patient 18
1 Day
2 Days
3 Days
5 Days
7 Days
NAD(P)H τm
D
FAD τm
E
Control
5-FU (F)
Gemcitabine (G)
G+F
TAK-228 (T)
ABT-263 + T
100 µm
10
Redox Ratio
(NAD(P)H/FAD)
0
1.5 ns
NAD(P)H τm
0.7 ns
1.2 ns
FAD τm
0.5 ns

**Figure C.5. Significance of drug treatment effects on individual OMI endpoints in patient-derived fibroblasts co-cultured with organoids. A-D,** Boxplot summaries comparing the effect of all drugs on patient-derived fibroblasts at all time points for the OMI index (**A**), redox ratio (**B**), NAD(P)H $\tau_m$ (**C**), and FAD $\tau_m$ (**D**). '^' indicates the patient lesion was diagnosed as PanIN. '~' indicates the patient lesion was diagnosed as ampullary cancer. * $p<0.05$ vs. control. **E,** Representative OMI images of fibroblast monolayer co-cultured with organoids derived from Patient 3 at 24 hours of treatment.

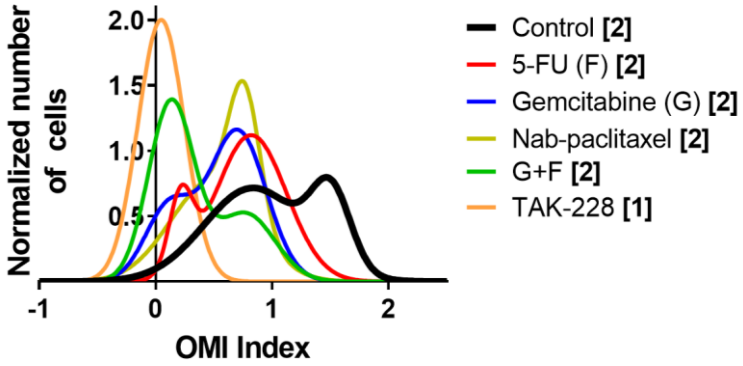


**Figure C.6. Population distribution modeling in response to additional drugs in Patient 13 organoids.** Normalized density distributions of the OMI index of individual cells after 72 hours. Bracketed number indicates number of subpopulations.

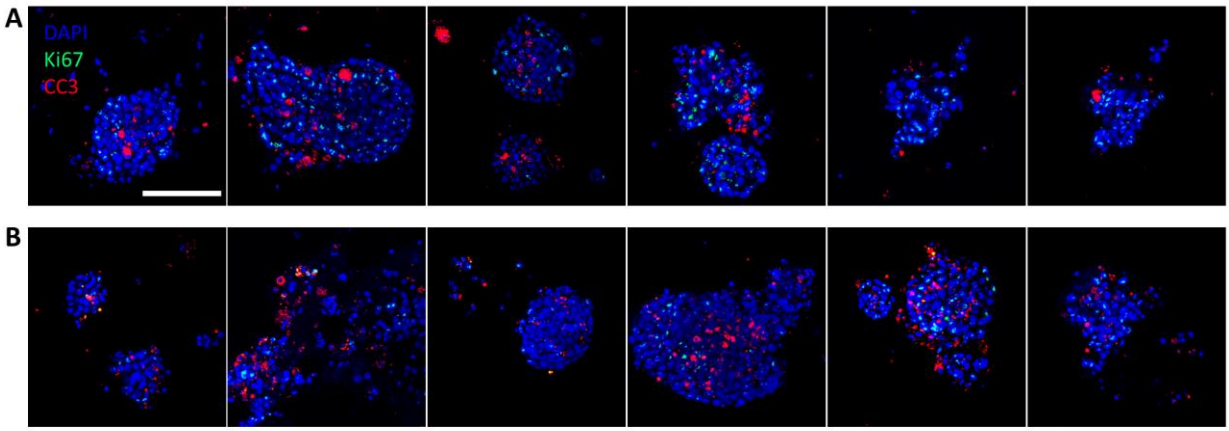


**Figure C.7. Dual immunofluorescence of cell fate in pancreatic organoids.** Composite images of Patient 13 organoids stained for Ki67 (green), cleaved caspase-3 (red), and DAPI (blue). **A,** Control organoids. Scale bar is 100 μm. **B,** organoids treated for 72 hours with the combination of TAK-228 and ABT-263.

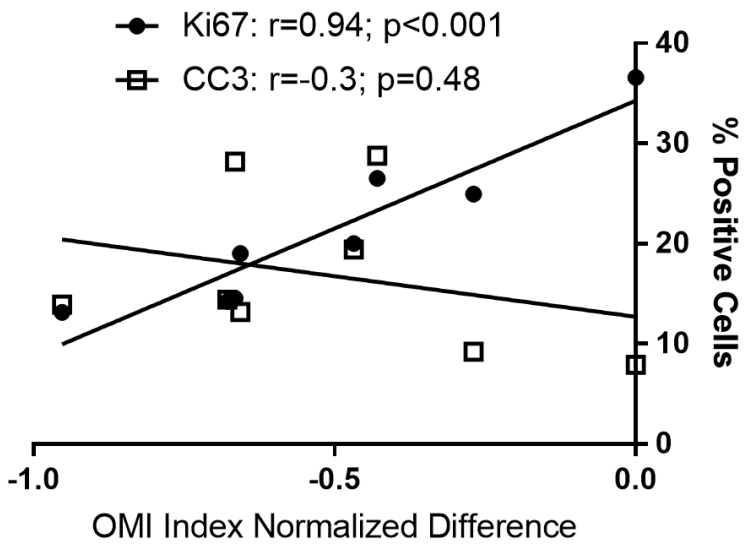


**Figure C.8. Correlation between OMI index, proliferation, and apoptosis in pancreatic organoids**. OMI index positively correlates with percentage of cells expressing Ki67 (filled circles). OMI index does not significantly correlate with percentage of cells expressing CC3 (open squares). Each dot represents the average value for one treatment group of Patient 13 organoids at 72 hours of treatment. N=8 conditions.

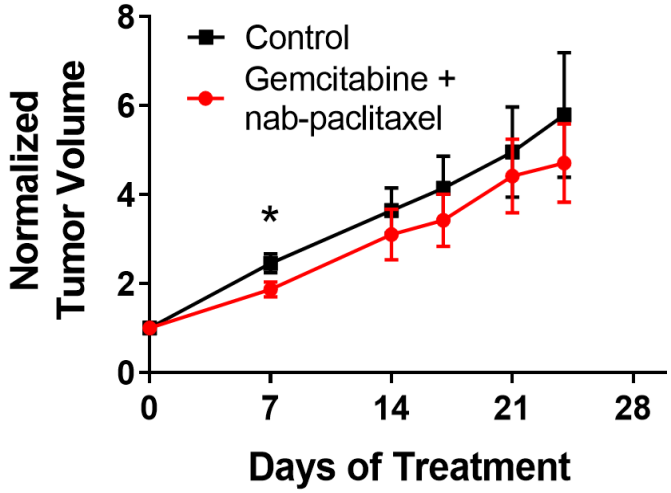


**Figure C.9. Growth response to gemcitabine and nab-paclitaxel combination therapy in tumors grown from Patient 13 organoids in athymic nude mice.** Error bars indicate mean ± SEM. * $p<0.05$ vs. control. N>20 tumors per group at day 7, N>13 tumors per group at day 14 and beyond.

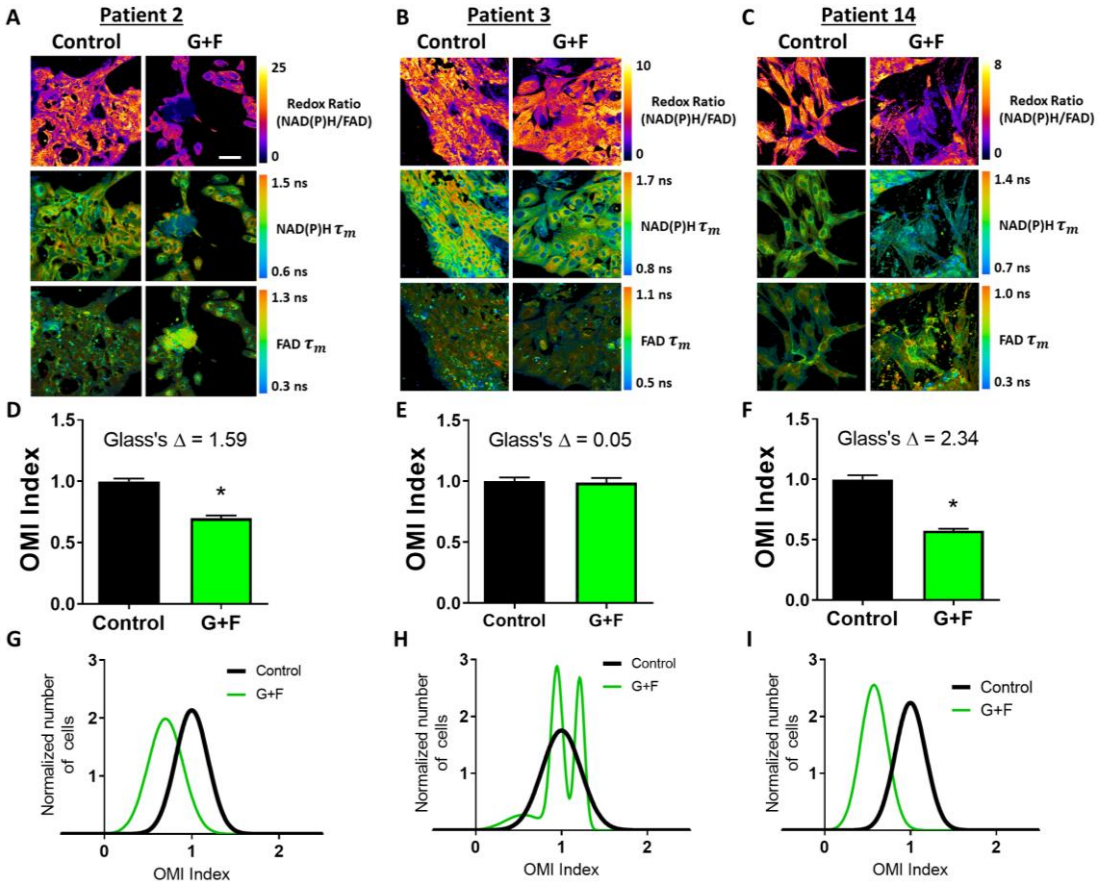


**Figure C.10. Response to patient adjuvant therapy in patient-derived fibroblasts. A-C**, Representative redox ratio, NAD(P)H $\tau_m$, and FAD $\tau_m$. images of fibroblasts co-cultured with organoids from Patients 2 (**A**), 3 (**B**), and 14 (**C**). Left columns indicate control fibroblasts, and right columns indicate fibroblasts treated with drugs matched to the patient's adjuvant treatment. G+F = gemcitabine + 5-FU. Scale bar is 50 μm. **D-F**, The effect of the same drugs on the OMI index averaged across all fibroblasts derived from Patient 2 (**D**), 3 (**E**), and 14 (**F**). Error bars indicate mean ± SEM. * p<0.0001. **G-I**, Single-cell OMI index subpopulation analysis of treatment response in fibroblasts from Patient 2 (**G**), 3 (**H**), and 14 (**I**).